Interfacial Electrochemical Kinetics

Chuhong Lin

Pembroke College

University of Oxford

A thesis submitted for the degree of

D.Phil. in Physical and Theoretical Chemistry

Trinity Term 2017

Interfacial Electrochemical Kinetics

Chuhong Lin
Pembroke College, University of Oxford

A thesis submitted for the degree of D.Phil. in Physical and Theoretical Chemistry
Trinity Term, 2017

Abstract

The first two chapters in this thesis introduce the fundamental knowledge underpinning electrochemistry and numerical simulation. The rest of the thesis comprises three parts: investigation of charge transfer at the electrode-electrolyte interface; a kinetic study of electrocatalytic reactions at micro- and nano-electrodes; and the evaluation of electrochemical detection of single enzymes.

In the first part the inner-sphere electron transfer is discussed under different situations where the breakage or formation of the chemical bond, the reorganization of the solvent and the influence of the electrical double layer are taken into consideration. Two important half-cell reactions in the field of fuel cells, the hydrogen oxidation reaction and the oxygen reduction reaction, are taken as examples and discussed in Chapter 3 and Chapter 4.

The second part focuses primarily on the influence of the electrode size and geometry on electrocatalytic reactions. The kinetics reflecting both the mass transport of the reacting species and the electrocatalytic reaction are investigated. The application of simulation enables the measurement of the kinetic parameters and the determination of rate-determining factors in different experimental situations. The hydrogen oxidation reaction on nanoparticles is investigated in Chapter 5. Homogeneous and heterogeneous EC' (E: electrochemical step; C': catalytic step) reactions are discussed in Chapter 6, respectively.

In the last section, the possible detection of single enzymes via the nano-impact electrochemical technique is explored in Chapter 7. The kinetics of the electrode system containing a freely-diffusing enzyme and a microelectrode is investigated and the experimental conditions required for the measurement of enzyme activity predicted.

Acknowledgements

I am extremely grateful to my supervisor, collaborators, colleagues, friends and families who have helped and supported me during my DPhil study.

I wish to first thank my supervisor, Prof. Richard G. Compton, whose selfless time and care kept me going. Thank you for your precious advice and inspiration in my DPhil study. You make me a qualified researcher in the three years. I still remember that at the first time I saw papers of this group, I was immediately attracted by their works. At that moment, I could not believe that one day I would become a team member!

I would like to thank everyone in Compton Group for making my research work productive and enjoyable. Many thanks to Dr. Christopher Batchelor-McAuley for his in-depth knowledge of electrochemistry; Dr. Enno Kätelhön for introducing me to the world of simulation; Dr. Eduardo Laborda for working together on crazy but exciting electron-transfer model; Dr. Lior Sepunaru for common enthusiasm on enzymes. I also would like to thank Dr. Qianqi Lin, Miss. Xiuting Li, Miss. Xue Jiao and Miss. Kamonwad Ngamchuea for allowing me to interpret their experimental results by my theories.

I thank all my friends who standing by me for the happy hours we spent together. Thank you for listening to me when I need company and convincing me when I felt upset.

I own my parents a lot of thanks for their invaluable love and support all the time. Since I was a kid, I have been keen on understanding the principles of nature and wishing that one day I could become a scientist like Dad and Grandma. I am very happy that now I can choose the same career! Thank you very much for always supporting and encouraging me in my way of chasing dreams!

Glossary Table

Symbol	Definition
a	a) activity (mol dm^{-3}) b) accurate value of a function (Eqn. 2.8)
c	concentration
c^{o}	standard concentration (1 mol dm^{-3})
d	distance (m)
d_0	bond length (m)
D	diffusion coefficient (m^2 s^{-1})
D_e	binding energy (eV)
e_0	elementary charge (1.602*10^{-19} C)
E	applied electrode potential (V)
E^{o}	standard potential (V)
E_f	formal potential (V)
f_{cutoff}	cutoff frequency
G	Gibbs free energy (J mol^{-1})
ΔG	Gibbs free energy difference (J mol^{-1})
$\Delta G^{\neq}$	activation energy (J mol^{-1})
H	Hamiltonian operator
h	Planck constant (6.626*10^{-34} m^2 kg s^{-1})
i	a) current density (A m^{-2}) b) index number in an array
I	current (A)
j	a) reaction flux (mol m^{-2}) b) index number in an array
k	a) rate constant (m s^{-1}, s^{-1}, mol m^{-2} s^{-1}, or mM^{-1} s^{-1}) b) force constant (Eqn. 1.41)

	c) index number in an array
k_B	Boltzmann constant (1.381*10^{-23} m^2 kg s^{-2} K^{-1})
K	equilibrium constant
K_M	Michealis-Menten constant (mM)
l	length (m)
n	a) stoichiometric number b) number of electrons
N	number of reactants
N_A	Avogadro's number (6.022*10^{23})
o	calculation error
p	a) momenta b) probability
P	probability
q	reaction coordinate
r	a) radius (m) b) coordinate in the cylindrical coordinate system
R	gas constant (8.3145 J mol^{-1} K^{-1})
S	area (m^2)
t	time (s)
T	temperature (K)
v	scan rate (V s^{-1})
V	volume (m^3)
x	distance from the electrode (m)
z	a) number of charge b) coordinate of the cylindrical coordinate system
α	a) transfer coefficient b) coefficient in an array or matrix

β	a) transfer coefficient b) coefficient in an array or matrix
γ	activity coeffient
Γ	surface coverage (mol m^{-2})
δ	a) diffusion layer thickness (m) b) Dirac delta function
Δ	energy level shift in the chemisorption (eV)
ε	a) dielectric constant (Eqn.1.14) b) energy level (eV, Eqn. 1.36)
ε_0	a) permittivity of the vacuum (8.854 F m^{-1}) b) ionisation energy (Eqn. 1.37)
ε_1	work function (eV)
ε_a	energy level of the valence orbital (eV)
κ	inverse of Debye length (m^{-1})
λ	reorganization energy (eV)
η	overpotential (V)
η_{vis}	dynamic viscosity (Pa·s)
ρ	charge density (C m^{-3})
ϕ	coordinate of the cylindrical coordinate system

Contents

Chapter 1 Electrode-Electrolyte Interface

The study of electrochemistry can be divided into two strongly-connected categories: ionically conducting solutions (ionics) and electrically charged interfaces (electrodics).[1] In this thesis, the kinetics of charge transfer at the electrode-electrolyte interface induced by a potential difference and the mechanism of electrochemically controlled surface processes are studied. The electrochemistry background of these areas is briefly introduced in this chapter.

1.1 Basic Concepts

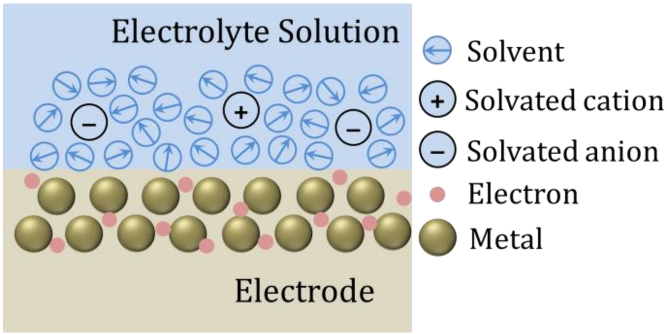

Figure 1.1 Structure of the electrode-electrolyte interface.

For an electrochemical reaction, metals, semiconductors, and insulators are all possible electrode materials, and aqueous solutions, ionic liquid, molten salts, and solid electrolytes can be used as ionic conductors. Thus, there are a variety of different classes of electrochemical interfaces. However in this thesis, the scope of the electrode-electrolyte interface is limited to metal (or other metallic materials)-aqueous solution systems. In practical terms whilst the metal is a good electrical conductor, extra supporting electrolyte (made of cations and anions) is usually added in the solution to conduct the electric current. Figure 1.1 shows a schematic diagram of the interfacial structure. The solvated ions are surrounded by solvent molecules. The solvent water has a dipole moment and this is represented by the circle with an arrow in the middle.

The metal, electrons, solvent, electrolyte and the redox species, either charged or neutral, comprise the electrode-electrolyte interface. The metal usually carries an excess charge at the surface, which is balanced by oppositely charged ions in the solution phase, creating a double layer.

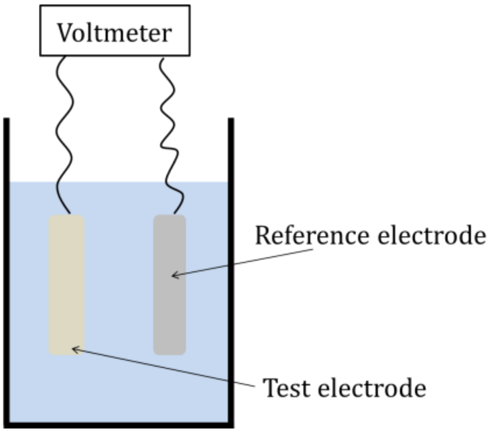

Figure 1.2 Illustration of the measurement of an electrode potential. The electrode under study and the reference electrode are immersed in the electrolyte solution and connected with a voltmeter in a closed electric circuit.

Due to the charge separation between the metal and the solution phase, there will be an electrical potential difference $\varphi_{\mathrm{M}} - \varphi_{\mathrm{S}}$ between the electrode (potential φ_{M}) and the solution (potential φ_{S}), which is called an electrode potential. Although the concept of potential difference at a single interface is used theoretically, the absolute value of the potential difference $\varphi_{\mathrm{M}} - \varphi_{\mathrm{S}}$ cannot be experimentally determined. To quantify the potential drop relating to any single electrode-solution interface, the potential at the standard hydrogen electrode (SHE) is assigned the standard potential of 0.000 V. In the SHE, the electrode is made of platinum with fine platinum black coated and all components in the solution at unit activity.[2] Potential drops of other interfaces can be determined with respect to the SHE acting as a reference electrode. The measurement of the electrode potential for a test electrode is illustrated in Figure 1.2. Due to the inconvenience of using a SHE in the experiment, the potential can be also referred to other reference electrodes, such as the *saturated calomel electrode* (SCE) made of

$Hg/Hg_2Cl_2/KCl$ (saturated in water) and the *silver-silver chloride electrode* made of $Ag/AgCl/KCl$ (saturated in water). As the reference electrode has a constant makeup, the potential of the reference electrode is fixed during the experiment.

The electrode potential in Figure 1.2 is measured under equilibrium conditions of the electrode-electrolyte interface, where no *external* potential is supplied to the electrode system and there is no current flow. In contrast, in electrolysis, the potential difference at the interface is applied by an external power supply so that the electrode system deviates from the equilibrium condition and electron transfer across the interface can be observed as current. In the case of electrochemical reactions, the electron transfer takes place between the redox species and the electrode, which is expressed as:

$$ox + e^- \rightleftharpoons red \tag{1.1}$$

or

$$red - e^- \rightleftharpoons ox \tag{1.2}$$

where the electrode works as an electron donor/acceptor. *ox* is the oxidised form of the redox couple and *red* is the reduced form.

1.2 Electrochemistry at Equilibrium

The equilibrium state of the electrode-electrolyte interface is introduced from two aspects: electrochemical reaction at equilibrium and the structure of the interface at equilibrium. At equilibrium, the net electron transfer across the interface is zero.

1.2.1 Electrochemical Reaction at Equilibrium

A simple redox reaction at the electrode can be expressed as:

$$n_\mathrm{A}\mathrm{A}^{z_\mathrm{A}}(\mathrm{sol}) + n_\mathrm{e}\mathrm{e}^- \rightleftharpoons n_\mathrm{B}\mathrm{B}^{z_\mathrm{B}}(\mathrm{sol}) \tag{1.3}$$

For a chemical reaction at equilibrium, the chemical potentials of both the reactant and product sides are required to be balanced. In electron transfer reactions, the concept of the electrochemical potential $\overline{\mu}$ is applied instead of the chemical potential μ. The electrochemical potential of species *j* is:

$$\overline{\mu}_{\mathrm{j}} = \mu_{\mathrm{j}} + z_{\mathrm{j}} F \varphi_{\mathrm{j}} \tag{1.4}$$

z is the charge carried by the species, *F* is the Faraday constant (96487 C mol^{-1}, the charge of one mole of electrons), and φ is the potential of the phase where the species resides. For the solution-phase species, $\varphi_{\mathrm{j}} = \varphi_{\mathrm{S}}$; for the electron, $\varphi_{\mathrm{j}} = \varphi_{\mathrm{M}}$. The chemical potential of species *j* can be calculated from the standard chemical potential μ_{j}^{o} (all unit activity, standard temperature), the temperature, and the activity of species *j*:

$$\mu_{\mathrm{j}} = \mu_{\mathrm{j}}^{o} + RT \ln\left(a_{\mathrm{j}}\right) \tag{1.5}$$

where *R* refers to the gas constant and *T* is the room temperature, a_{j} is the activity. In the solution phase, the activity if defined as:

$$a_{\mathrm{j}} = \gamma_{\mathrm{j}} \frac{c_{\mathrm{j}}}{c^{o}} \tag{1.6}$$

The concentration c_{j} is divided by the concentration $c^{o} = 1$ mol dm^{-3} of the standard state of a hypothetic ideal dilute solution. γ_{j} is the activity coefficient. In dilute solution, sometimes the activity coefficient is regarded as 1 and the activity is replaced by the concentration.

At equilibrium, the electrochemical potentials of Eqn.(1.3) are balanced:

$$n_{\mathrm{A}} \overline{\mu}_{\mathrm{A}} + n_{\mathrm{e}} \overline{\mu}_{\mathrm{e}^-} = n_{\mathrm{B}} \overline{\mu}_{\mathrm{B}} \tag{1.7}$$

$$n_{\mathrm{A}} \left(\mu_{\mathrm{A}} + z_{\mathrm{A}} F \varphi_{\mathrm{S}}\right) + n_{\mathrm{e}} \left(\mu_{\mathrm{e}^-} - F \varphi_{\mathrm{M}}\right) = n_{\mathrm{B}} \left(\mu_{\mathrm{B}} + z_{\mathrm{B}} F \varphi_{\mathrm{S}}\right) \tag{1.8}$$

Charge conservation of the redox reaction dictates:

$$n_{\mathrm{A}} z_{\mathrm{A}} - n_{\mathrm{B}} z_{\mathrm{B}} = n_{\mathrm{e}} \tag{1.9}$$

The potential difference can be derived from Eqn.(1.8):

$$\varphi_{\mathrm{M}} - \varphi_{\mathrm{S}} = \frac{1}{n_{\mathrm{e}}F}\left(n_{\mathrm{A}}\mu_{\mathrm{A}}^{o} + n_{\mathrm{e}}\mu_{\mathrm{e^-}}^{o} - n_{\mathrm{B}}\mu_{\mathrm{B}}^{o}\right) + \frac{RT}{n_{\mathrm{e}}F}\ln\left(\frac{{a_{\mathrm{A}}}^{n_{\mathrm{A}}}}{{a_{\mathrm{B}}}^{n_{\mathrm{B}}}}\right) \tag{1.10}$$

We use E to represent the electrode potential relative to a reference electrode and define the standard potential E^{o} of the redox couple A/B to be:

$$E_{\mathrm{A/B}}^{o} = \frac{1}{n_{\mathrm{e}}F}\left(n_{\mathrm{A}}\mu_{\mathrm{A}}^{o} + n_{\mathrm{e}}\mu_{\mathrm{e^-}}^{o} - n_{\mathrm{B}}\mu_{\mathrm{B}}^{o}\right) \tag{1.11}$$

As it is more convenient to use concentration rather than activity in practice, the formal potential which includes the effect by the activity coefficients is defined as:

$$E_{\mathrm{f,\ A/B}} = E_{\mathrm{A/B}}^{o} + \frac{RT}{n_{\mathrm{e}}F}\ln\left(\frac{{\gamma_{\mathrm{A}}}^{n_{\mathrm{A}}}}{{\gamma_{\mathrm{B}}}^{n_{\mathrm{B}}}}\right) \tag{1.12}$$

Therefore, Eqn.(1.10) can be written as:

$$E = E_{\mathrm{f,\ A/B}} + \frac{RT}{n_{\mathrm{e}}F}\ln\left(\frac{{c_{\mathrm{A}}}^{n_{\mathrm{A}}}}{{c_{\mathrm{B}}}^{n_{\mathrm{B}}}}\right) \tag{1.13}$$

This is called the Nernst equation to recognise the seminal contribution from W. Nernst in developing the thermodynamics of electrochemical reactions.[3] Note that although a solution phase redox couple was used as an example in the derivation of Nernst equation, the application of Nernst equation is not restricted to solution phase species but also suitable for adsorbates and solid-phase species.

1.2.2 The Interface at Equilibrium

At equilibrium, there is excess charge on each side of the electrode-electrolyte interface as shown in Figure 1.1, where, as shown, extra positive charge exists at the electrode surface and extra negative charge in the solution.

The physical properties of the electrical double layer were first developed by Gouy and Chapman in 1910s.[4, 5] The model was developed for the case of no specific adsorption at the electrode surface, in which the extra charge is only due to electrostatic attraction and repulsion of ions. In the Gouy-Chapman model, the solution comprises point ions embedded in a dielectric continuum solvent, the cation and anion of the electrolyte carry charge +z and −z, and the electrode is considered as a perfectly conductive planar electrode. When only considering the x direction perpendicular the electrode plane and set the electrode surface at x=0, the potential φ in the solution follows the Poisson equation:

$$\frac{\partial^2\varphi}{\partial x^2} = -\frac{\rho}{\varepsilon\varepsilon_0} \tag{1.14}$$

where ρ is the charge density in the electrolyte, ε is the dielectric constant of the solvent, and ε_0 is the permittivity of the vacuum. The charge density is related to the concentration of the cations (c_c) and anions (c_a) in the solution:

$$\rho = ze_0\left(c_\mathrm{c} - c_\mathrm{a}\right) \tag{1.15}$$

For the ion distribution fully driven by the electrostatic interaction, the concentration of the cations and anions is only dependent on the potential in the solution, which can be described by Boltzmann statistics:

$$c_\mathrm{c} = c^* \exp\left(-\frac{ze_0\varphi}{k_\mathrm{B}T}\right) \tag{1.16}$$

$$c_\mathrm{a} = c^* \exp\left(\frac{ze_0\varphi}{k_\mathrm{B}T}\right) \tag{1.17}$$

where c^* is the bulk concentration of the electrolyte and the potential in the bulk solution $\varphi_\mathrm{S}\left(x \to \infty\right)$ is defined to be zero as the reference.

Combining with Eqn.(1.15), (1.16) and (1.17), Eqn. (1.14) can be rewritten as:

$$\frac{\partial^2\varphi}{\partial x^2} = -\frac{ze_0c^*}{\varepsilon\varepsilon_0}\left(\exp\left(-\frac{ze_0\varphi}{k_\mathrm{B}T}\right) - \exp\left(\frac{ze_0\varphi}{k_\mathrm{B}T}\right)\right) \tag{1.18}$$

The exponential term can be expanded by the power series as:

$$\exp\left(-\frac{ze_0\varphi}{k_\mathrm{B}T}\right)=1+\left(-\frac{ze_0\varphi}{k_\mathrm{B}T}\right)+\frac{1}{2!}\left(-\frac{ze_0\varphi}{k_\mathrm{B}T}\right)^2+\ldots \tag{1.19}$$

$$\exp\left(\frac{ze_0\varphi}{k_\mathrm{B}T}\right)=1+\frac{ze_0\varphi}{k_\mathrm{B}T}+\frac{1}{2!}\left(\frac{ze_0\varphi}{k_\mathrm{B}T}\right)^2+\ldots \tag{1.20}$$

Therefore, in the condition of low potential where $ze_0\varphi/k_\mathrm{B}T \ll 1$, the exponentials can be linearized and an approximation of Eqn.(1.18) becomes:

$$\frac{\partial^2\varphi}{\partial x^2}=\kappa^2\varphi \tag{1.21}$$

where κ is expressed as:

$$\kappa=\left(\frac{2\left(ze_0\right)^2c^*}{\varepsilon\varepsilon_0k_\mathrm{B}T}\right)^{1/2} \tag{1.22}$$

and the inverse of κ is defined the Debye length, used to characterise the double layer thickness.

The potential distribution in the electrical double layer can be solved from Eqn.(1.21):

$$\varphi\left(x\right)=A\exp\left(-\kappa x\right) \tag{1.23}$$

where A is a constant to be determined by the boundary condition at the electrode surface.

Figure 1.3 shows a Gouy-Chapman potential distribution in the double layer. In the Gouy-Chapman model, the potential does not immediately change from the value at the electrode surface to the value in the bulk solution but varies as a function of distance in the electrical double layer. As there is a potential gradient as shown in Figure 1.3, any charged species located inside the double layer will be influenced by the electric field. From the expression of the Debye length in Eqn. (1.22), the Debye length is determined by the concentration of the supporting electrolyte added in the solution. For instance, the Debye length for an aqueous solution of a completely dissociated 1-1 electrolyte at room temperature is *ca.* 10 Å with an electrolyte concentration of 0.1 mol dm^{-3} and 30 Å with a 0.01 mol dm^{-3} concentration.[6]

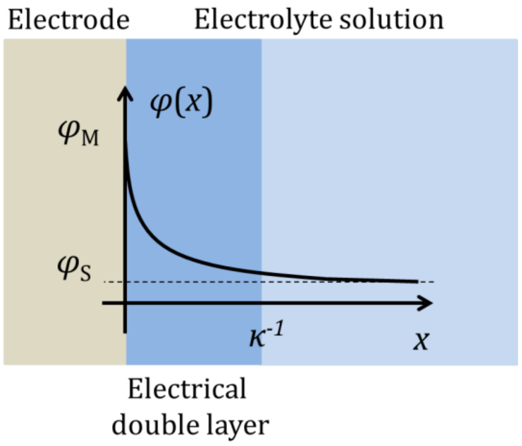

Figure 1.3 Gouy-Chapman model of the potential distribution in the electrical double layer. The potential φ in the solution varies exponentially as a function of the distance from the electrode x. φ_M and φ_S are the potentials of the electrode and the bulk solution. κ^{-1} is the Debye length.

More detailed models on the structure of charged interface were proposed later.[7] A layer of solvent molecules is recognised at the metal electrode surface, the location of which is called the *Inner Helmholtz Plane* (IHP). If an ion in the solution appears inside the Inner Helmholtz Plane, there is *specific adsorption* between the ion and the electrode. For the solvated ion and in the absence of specific adsorption, the electron exchange with the electrode is assumed to take place at a certain distance (outside the IHP) from the electrode surface, which is defined as the *Outer Helmholtz Plane* (OHP). The concept of Inner and Outer Helmholtz Planes will also be used in electron transfer theories discussed below.

1.3 Classical Electron-Transfer Theories

When applying an external potential to an electrode system, the electrochemical reaction deviates from the equilibrium Nernstian case and the net current flow across the interface is no longer zero. The current density is related to the electron transfer rate at the interface. Electron-transfer theories are developed to understand the relationship between the applied potential and the current.

1.3.1 Overpotential and Tafel Plot

The overpotential η is defined as the difference between the potential applied at the electrode E and the formal potential E_f, $\eta = E - E_f$. In the electrochemical reaction, the current of a redox reaction can be observed when there is an overpotential applied on the electrode. In early 20th century, an organic electrochemist J. Tafel found the overpotential linearly depended on the logarithm of the current in the experiments of hydrogen evolution:[8]

$$\eta = a + b\log|I| \tag{1.24}$$

where *a, b* are constants indicating the electrode kinetics. The slope $b = \dfrac{\partial \eta}{\partial \log|I|}$ is called the Tafel slope, which reflects how much overpotential is required to drive the charge transfer and indicates the efficiency of the electrochemical reaction. Note that the value of Tafel slope is determined by the slowest step in the overall reaction, which can be the electron transfer across the interface, the mass transport of the redox species, or even the influence of the reaction environment (supporting electrolyte, solvent, et al). When the electron transfer is relatively slow, the Tafel slope indicates the kinetics of the electrochemical reaction.

1.3.2 The Butler-Volmer equation

Following the footsteps of Nernst and Tafel, the next breakthrough in electrode kinetics appeared in 1920s and 1930s. The papers published by J. A. V. Butler on “heterogeneous equilibria” gave a kinetic explanation and contributed the idea of linking the electron transfer with the concentration change of the redox species.[9, 10] In the paper by Erdey-Gruz and Volmer, based on their experiments of hydrogen evolution reaction, they applied the laws of reaction kinetics to the current and recognized that the activation energy was connected with the applied electrode potential.[11] Erdey-Gruz and Volmer introduced the concept of the transfer coefficient to reflect the potential dependency of the electrode current. The physical meaning of the transfer coefficient was further explained later via the transition state theory.[12]

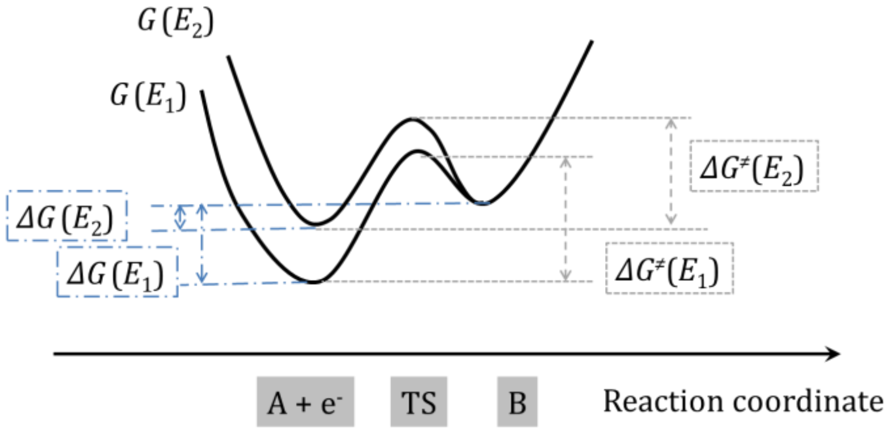

$$\frac{\Delta(\Delta G^{\neq})}{\Delta(\Delta G)} = \frac{\alpha F(E_2-E_1)}{F(E_2-E_1)}$$

Figure 1.4 Gibbs energy curves $G(E_1)$ and $G(E_2)$ for the reaction A + e$^-$ = B under potentials E_1 and E_2. α represents the transfer coefficient. ΔG (E_1) and ΔG (E_2) are the Gibbs energy differences between the reactant side and the product side. Δ$G^{\neq}$(E_1) and Δ$G^{\neq}$(E_2) are the activation energies. TS is the transition state.

An illustration is shown in Figure 1.4, where the potential energy curves for a simple electron transfer reaction A + e$^-$ = B under two different electrode potentials E_1 and E_2 are plotted. The Gibbs energy difference ΔG between the reactant side and the product side changes $F(E_2 - E_1)$ and the activation energy $\Delta G^{\neq}$, which is the Gibbs energy difference between the transition state and the reactant, shifts $\alpha F(E_2 - E_1)$ correspondingly. The transfer coefficient α is equivalent to the Bronsted coefficient in general chemical kinetics (Bronsted equation),[13] which also shows the dependency of the activation energy on the Gibbs energy:

$$\alpha = \frac{\partial\left(\Delta G^{\neq}\right)}{\partial\left(\Delta G\right)} \tag{1.25}$$

In the linear free energy correlation, the transfer coefficient is assumed to be independent of electrode potential and the temperature.

Another important contribution made by Erdey-Gruz and Volmer was to split the charge and discharge terms for the anodic (oxidation) and cathodic (reduction) processes. For the reaction A + e^- = B, the relationship of current and applied potential is expressed as:

$$i_{\mathrm{density}} = F\left(k_0 c_{\mathrm{A}}^{\mathrm{surf}} \exp\left(-\frac{\alpha F\eta}{RT}\right) - k_0 c_{\mathrm{B}}^{\mathrm{surf}} \exp\left(\frac{\beta F\eta}{RT}\right)\right) \tag{1.26}$$

where i_{density} is the current density, k_0 is the standard electron transfer rate constant, $c_{\mathrm{A}}^{\mathrm{surf}}$ and $c_{\mathrm{B}}^{\mathrm{surf}}$ are the surface concentration of A and B, α and β are the cathodic and anodic transfer coefficients. The sum of α and β is usually assumed to be 1 in the simple one-electron-transfer reaction. Eqn.(1.26) is called the Butler-Volmer equation. Although the Butler-Volmer equation is oversimplified and the physical meanings of the transfer coefficients and the pre-exponential term k_0 are ambiguous, as it rationalizes properly the electrochemical reaction in a clear and condensed way, the Butler-Volmer equation is still one of the most popular formulae used in the field of electrochemical kinetics.

The Butler-Volmer equation (1.26) can be transferred to the Tafel equation at high overpotential for the cathodic process ($\eta \ll 0$):

$$i_{\mathrm{density}} \approx F k_0 c_{\mathrm{A}}^{\mathrm{surf}} \exp\left(-\frac{\alpha F\eta}{RT}\right) \tag{1.27}$$

$$\frac{\partial\eta}{\partial\log\left|I\right|} = -\frac{2.303RT}{\alpha F} \tag{1.28}$$

for the anodic process ($\eta \gg 0$):

$$i_{\text{density}} = -Fk_0 c_{\text{B}}^{\text{surf}} \exp\left(\frac{\beta F \eta}{RT}\right) \tag{1.29}$$

$$\frac{\partial \eta}{\partial \log|I|} = \frac{2.303RT}{\beta F} \tag{1.30}$$

Apart from the surface concentration and the overpotential, the electrode current is also related to the number of electrons transferred in the electrochemical reaction. In the multi-electron transfer situation, the simultaneous transfer of more than one electron is highly improbable. For convenience, we can combine a series of fast electron transfer steps into one multi-electron transfer reaction, but there is at most one electron transfer in one rate-determining step. For the reaction with relatively simple mechanism, the Butler-Volmer equation can be applied to the overall reaction and the apparent Tafel slope can indicate the mechanism of the reaction.

Assume that a multi-electron transfer reaction A + n_ee$^-$ = B contains three parts: an electron transfer before the rate-determining step, a rate-determining step, and an electron transfer afterwards.

$$\begin{aligned} &\text{A} + n_{\text{f}}\text{e}^- \rightleftharpoons \text{A}' \\ &\text{A}' + \text{e}^- \rightleftharpoons \text{B}' \\ &\text{B}' + n_{\text{b}}\text{e}^- \rightleftharpoons \text{B} \end{aligned} \tag{1.31}$$

where n_f is the number of electrons transferred before the rate-determining step, n_b is that after the rate-determining step, and $n = n_\text{f} + 1 + n_\text{b}$. The reactions before and after the rate-determining step are regarded to be at equilibrium, where the concentrations of the reacting species follow the Nernst equation:

$$\frac{c_{\text{A}}^{\text{surf}}}{c_{\text{A}'}^{\text{surf}}} = \exp\left(\frac{n_{\text{f}} F \eta}{RT}\right) \tag{1.32}$$

$$\frac{c_{\text{B}'}^{\text{surf}}}{c_{\text{B}}^{\text{surf}}} = \exp\left(\frac{n_{\text{b}} F \eta}{RT}\right) \tag{1.33}$$

The reaction equation of the rate determining step is expressed as:

$$j_{\mathrm{A}^{'}/\mathrm{B}^{'}} = k_0 c_{\mathrm{A}^{'}}^{\mathrm{surf}} \exp\left(-\frac{\alpha F\eta}{RT}\right) - k_0 c_{\mathrm{B}^{'}}^{\mathrm{surf}} \exp\left(\frac{\beta F\eta}{RT}\right) \tag{1.34}$$

The current for the overall reaction can be derived:

$$i_{\mathrm{density}} = n_{\mathrm{e}} F\left(k_0 c_{\mathrm{A}}^{\mathrm{surf}} \exp\left(-\frac{(n_{\mathrm{f}}+\alpha)F\eta}{RT}\right) - k_0 c_{\mathrm{B}}^{\mathrm{surf}} \exp\left(\frac{(n_{\mathrm{b}}+\beta)F\eta}{RT}\right)\right) \tag{1.35}$$

and thus the Tafel slope can be used to detect the mechanism of the multi-electron transfer reaction.

1.3.3 Marcus-Hush theory

Different from the phenomenological Butler-Volmer equation, electrochemists have explored the electron transfer theory using the views of quantum mechanics. Starting with Gurney's paper in 1931,[14] which applied the quantum mechanics in the study of ion neutralisation at high overpotentials, the interaction between the hydrated ions and the electrons in the metal was taken into consideration. In an interval of time *dt* in any slab of the solution a certain number of ions will adsorb or release an electron and their places taken by ions flowing in. Thus the total current density *i* is given by:

$$i = \iint n(\varepsilon, E) \cdot N(\varepsilon, x) \cdot P(\varepsilon, x) \mathrm{d}\varepsilon \mathrm{d}x \tag{1.36}$$

where ε is the energy level of the ionic (the redox species side) or metallic (the electrode side) orbital, x is the distance between the electrode and the ion. n is the number of free metallic electrons or vacant sites, described by the Fermi-Dirac distribution; N is the number of ions (the redox species) per unit area at a distance x from the metal, following the Boltzmann distribution; P is the probability of electron transfer between the metallic orbital with energy level ε and the molecular orbital of the redox species located at the distance x from the electrode. The dependence of current density i on potential E and temperature T was derived as:

$$\log i = \frac{\varepsilon_0 - \varepsilon_1 + e_0 E}{\gamma k_\mathrm{B} T} + \log T + const \qquad (1.37)$$

ε_0 is the ionisation energy of the ion and ε_1 is equal to the value of work function. γ is a constant and γ is larger than unity. e_0 is the charge of one electron, k_B is the Boltzmann constant. The slope $e_0/(\gamma k_\mathrm{B} T)$ derived in the view of molecular dynamics is equivalent to $\alpha F/(RT)$ used in the Butler-Volmer equation and γ also has a similar physical meaning to α.

Gurney also commended on the role of water in the aspect of electron transfer at the interface: "Water molecules still cover the greater part of the metal surface…we shall have these water molecules being ousted by ions of both signs…no water molecules left in contact with the metal except those water molecules which are bound to the ions by the hydration forces…" But Gurney did not quantify the influence of solvent in his current formula and only chose the distance from the electrode surface as the reaction coordinate.

The solvent fluctuation model for electron transfer was introduced by R. A. Marcus and N. S. Hush in 1950s~60s[15-19], providing the electron transfer theory for heterogeneous (electrode) or homogeneous (inter-ion) reactions with valence change of the redox species. In the Marcus-Hush electron transfer model, the redox centre or the ion is surrounded by layers of ligand and solvent molecules. The reaction is accompanied by a reorganization of both the complex, or inner sphere, and the solvation sheath, or outer sphere (note that in Ref. 15, Marcus used "saturated sphere" and "unsaturated sphere" rather than the commonly-used "inner sphere" and "outer sphere").[15, 16] Figure 1.5 illustrates the inner sphere and the outer sphere during the electron transfer between a metal complex and an electrode. The inner sphere is the ligand layer closely coordinated with the ion centre and the outer sphere is the solvent molecules outside the inner coordinate shell. The electron transfer between a reactant and an electrode can be divided into two types: outer-sphere reaction and inner-sphere reaction. For an outer-sphere reaction, the configuration of the inner coordinate shell does not change between the reduced and oxidized forms of the redox species; while for an inner-sphere reaction, both the inner shell and the outer-sphere solvent reorient during the electron transfer.

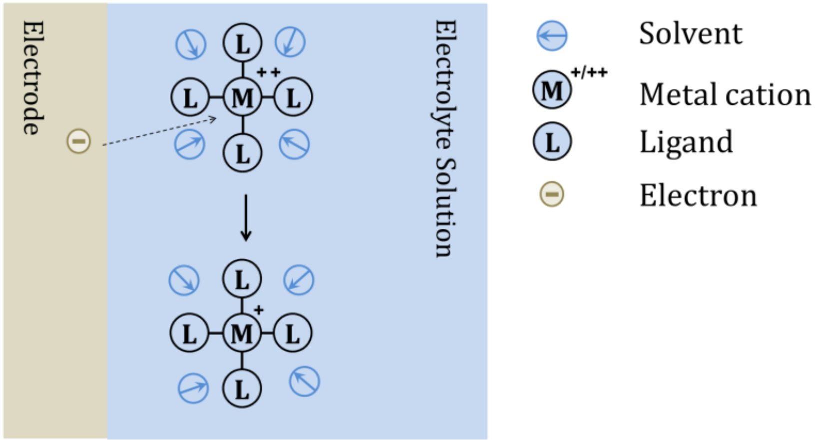

Figure 1.5 Illustration of the inner sphere and the outer sphere during the electron-transfer process between a metal complex and an electrode. The layer of ligands which closely coordinate with the metal cation is the inner sphere and the outside solvent molecules compose the outer sphere. The number of molecules used in the figure is for illustration, not the realistic situation.

The energy barrier for the reorientation of ligands or solvents slows the electron transfer reaction. The reaction coordinate for the electron transfer represents the length of the bond between the redox centre and the inner coordination shell and/or the change of separation distance between the redox centre and electrode, and/or the reorientation of polar solvent molecules in the medium.[17] The expressions of the reaction rate k_{el} and the activation energy $\Delta G^{\neq}$ are:[20]

$$k_{\mathrm{el}} = A\exp\left(-\frac{\Delta G^{\neq}}{k_{\mathrm{B}}T}\right) \tag{1.38}$$

$$\Delta G^{\neq} = \frac{\lambda}{4}\left(1+\frac{\Delta G_0}{\lambda}\right)^2 \tag{1.39}$$

where A is a constant, depending on the nature of the electron transfer. ΔG_0 is the free energy difference for the electron-transfer reaction. λ is the reorganization energy, which is defined as the energy needed for the rearrangement for the coordination shell from the initial state to the transition state. The reorganization energy λ is the sum of the outer-sphere contribution λ_o and the inner-sphere contribution λ_i. λ_o, reflecting the solvent reorganization, is determined by the radius of the inner-coordination shell of the redox ion r_{ion}, the separation distance between the redox ion and the electrode d, the optical and static dielectric constants (ε_{op} and ε_s) of the solvent:

$$\lambda_o = \frac{e_0}{2}\left(\frac{1}{r_{ion}} - \frac{1}{d}\right)\left(\frac{1}{\varepsilon_{op}} - \frac{1}{\varepsilon_s}\right) \tag{1.40}$$

where e_0 is the charge carried by one electron ($1.602*10^{-19}$ C mol^{-1}). λ_i is composed of the vibrational component arising from a stretching vibration in the innermost coordination shell, given by the following equation:

$$\lambda_i = \frac{1}{2}\sum_j \frac{2k_j^r k_j^p}{k_j^r + k_j^p}\left(q_j^r - q_j^p\right)^2 \tag{1.41}$$

where q_j is the equilibrium value of the jth normal mode coordinate and k_j is the force constant. The superscripts r and p refer to the reactant and the product. Bending modes can also contribute to λ_i.

In an electrode reaction, $\Delta G_0 = e_0\eta$. The physical insight is that the transfer coefficient is related to the reorganization energy. The transfer coefficient is expressed as:

$$\alpha = \frac{1}{2}\left(1 \pm \frac{F\eta}{2\lambda_m}\right) \tag{1.42}$$

where + and – correspond to the cathodic and anodic process, respectively.

More discussion on electron transfer theory can be found in Chapters 3 and 4 of this thesis. In Chapter 3, the Butler-Volmer model and the Marcus theory are compared in the study of hydrogen oxidation reaction. In Chapter 4, a model for the inner-sphere electron transfer is built with the consideration of both ion-electrode interaction and solvent fluctuation, where the potential dependence of the activation energy is calculated and the effects of the electrical double layer on the charge transfer process is also emphasized.

1.4 Mass Transport in the Electrolyte Solution

1.4.1 Three Mass Transport Phenomena

The concentration mentioned in the reaction rate equation refers to the surface concentration of the redox species. If the redox species stay at the electrode as adsorbates, the surface concentration is the surface coverage. But for the solution-phase species, the surface concentration is not identical to the value in the bulk solution. Therefore, if we want to quantify the electrode kinetics, it is necessary to take the mass transport of the redox species into consideration. There are three types of mass transport phenomena in electrochemistry: diffusion, migration and convection. Diffusion and migration are caused by concentration differences and potential differences in the solution. Convection is the movement of the whole or part of solution driven by either an external mechanical force or density gradients.

In the electrode systems of this thesis, only the diffusion phenomenon is involved. The other two types of mass transport, the migration and the convection, are not taken into consideration in this thesis. The electrochemical measurements mentioned in the thesis are implemented in still solution and the measurement time is usually short enough to avoid the occurrence of natural convection.[21] As for the migration, the electrode system is always regarded to be fully supported by the highly-concentrated electrolyte in the solution. The spatial range of the electrical double layer is limited to a very small region and will not affect the mass transport of the charged species in the solution. [22]

We need to identify the possible influence of migration and the electrical double layer on an electrochemical reaction. Migration only needs to be considered in solution of low supporting electrolyte, where the double layer is broad and the potential gradient plays an important role in the mass transport of the redox species toward the electrode. However, for highly-supported electrolyte solutions, the double layer thickness is very small and will not influence the mass transport of the redox species toward the region close to the electrode surface. But the influence of the electrical double layer can be found in the electron transfer process for certain inner-sphere reactions, where the reactant locates inside the double layer and the Gibbs energy of the ion is thus influenced by the potential distribution in the double layer. It will be discussed in Chapter 4 that in modelling a redox reaction coupled with chemical adsorption, the effects of the electrical double layer are involved in the charge transfer process but not included in the description of the mass transport of the charged redox species.

1.4.2 Diffusion Equations

Diffusion is caused by a concentration difference in the solution. For a solution-phase species, the flux per unit area *j* of the solute at an imaginary plane perpendicular to the direction *x* is proportional to the concentration gradient in *x* direaction:

$$j = -D\frac{\partial c}{\partial x} \tag{1.43}$$

where *D* is diffusion coefficient, relating to the temperature and the identities of all present substances in the solution. A. Fick analysed and quantified the diffusion phenomenon in the paper title with "On the liquid" in 1855.[23] Eqn.(1.43) is called Fick's first law. In Figure 1.6, the flux in the solution is illustrated at the two dashed planes at positions x and $x + \Delta x$. The rate of the change of the amount of solute in the slab bounded by the two imaginary planes x and $x + \Delta x$ is the excess of the input flux over the output flux:

$$\frac{\Delta n}{\Delta t} = S\left(j(x) - j(x+\Delta x)\right) \tag{1.44}$$

n is the amount of the solute and *S* is the area of the plane. The amount of the solute in the imaginary slab relates to the concentration change in Δt and the slab volume $S \cdot \Delta x$:

$$\Delta n = \Delta c \cdot S \cdot \Delta x \tag{1.45}$$

Thus Eqn.(1.44) can be rewritten as:

$$\frac{\partial c}{\partial t} = -\frac{\partial j}{\partial x} \tag{1.46}$$

Combining with Eqn.(1.43), the change of concentration in the solution follows:

$$\frac{\partial c}{\partial t} = D\frac{\partial^2 c}{\partial x^2} \tag{1.47}$$

In general, the diffusion equation, which is called Fick's second law, is expressed as:

$$\frac{\partial c}{\partial t} = D\nabla^2 c \tag{1.48}$$

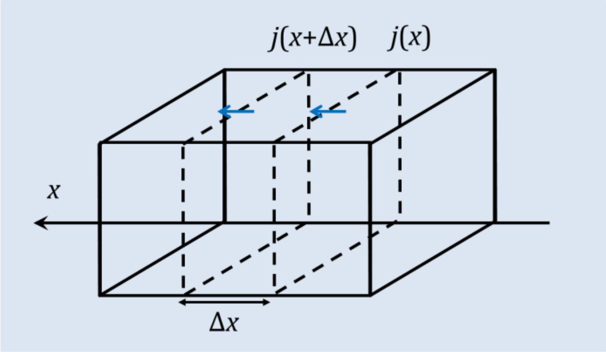

Figure 1.6 Illustration of the flux density *j* at *x* direction in the solution. For the imaginary slab located between *x* and *x* + Δ*x*, the flux importing to the slab and exporting from the slab are *j*(*x*) and *j*(*x* + Δ*x*).

Recognising molecular movement, diffusion is driven by Brownian motion, which is the random motion of particles suspended in a fluid (a liquid or a gas) resulting from their collision with the fast-moving atoms or molecules in the medium. In Einstein's theory of Brownian motion, when the random movement of a particle is only considering one space dimension x, the mean squared displacement of a Brownian particle $<\Delta x>^2$ in terms of the elapsed time Δt and the diffusivity, which is represented by the diffusion coefficient D, is expressed as:[24]

$$\langle \Delta x \rangle^2 = 2D\Delta t \tag{1.49}$$

For spherical particles suspended in a liquid of radius r_P, the diffusion coefficient can be calculated from:[24]

$$D = \frac{k_B T}{6\pi\eta_{vis} r_P} \tag{1.50}$$

where k_B is the Boltzmann constant, T is the temperature, η_{vis} is the dynamic viscosity of the solution.

1.4.3 The Diffusion Layer

At the electrode-electrolyte interface, the current density is proportional to the flux of the electroactive species toward the electrode surface, described by the Fick's first law (1.43). When the electrochemical reaction occurs at the electrode surface, the concentration of the reactant at the electrode surface is consumed and a concentration gradient develops over a certain distance from the electrode surface into the bulk solution. The solution layer within which the concentration gradient appears is termed as *diffusion layer* or *diffusion domain*. The size of the diffusion layer represents the spatial region in the solution phase which is affected by the electrochemical reaction. The diffusion layer thickness δ for the planar semi-infinite diffusion follows the relationship:[25]

$$\delta = \sqrt{2Dt} \tag{1.51}$$

where t is the reaction time. For a redox species with a diffusion coefficient of 10^{-9} m^2 s^{-1}, the diffusion layer thickness is about 10 μm after undergoing the reaction for 0.1 s. Note that except the reaction time and the diffusion coefficient, the diffusion layer thickness also depends on the electrode geometry. Eqn.(1.51) is only valid for the macro-size planar electrode, where only the diffusion on one dimension, the dimension perpendicular to the plane, is taken into consideration. For the electrode with other geometry, the diffusion layer thickness is different, which will be discussed in Chapters 3, 5 and 6.

1.5 Electrochemical Techniques

1.5.1 The Three-Electrode System

It was mentioned in section 1.1 that the potential difference between a metal surface and the solution phase can be only determined or controlled in presence of the reference electrode. In electrochemistry experiments, in addition to the working and reference electrodes, a counter electrode is also needed to measure the current flow in the electric circuit. The potential E and the current I of the working electrode are controlled by an instrument called a potentiostat. The scheme of a three-electrode cell used in electrochemistry measurement is shown in Figure 1.7. A potential E is applied between the working electrode and the reference electrode. The electrochemical reaction of interest occurs at the working electrode and the current flows between the working electrode and the counter electrode. There is no current passing the reference electrode as the potential of the reference electrode needs to always stay at the equilibrium value in the experiment.

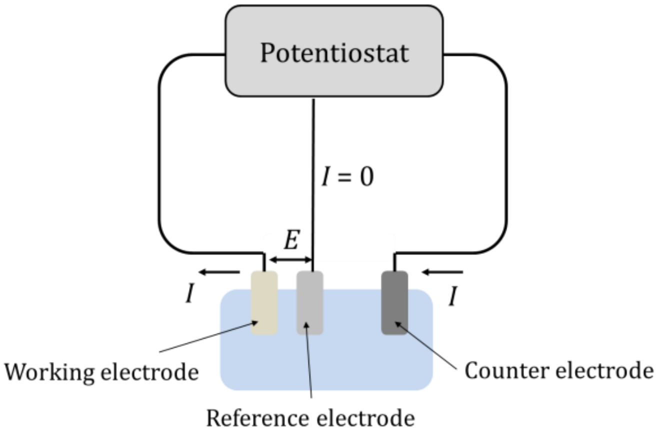

Figure 1.7 A three-electrode cell controlled by a potentiostat.

1.5.2 Macro- and Micro-electrodes

Based on the magnitude of the electrode size, there are two types of working electrodes used in the electrochemistry experiments: macroelectrodes and microelectrodes. The size of commonly-used macroelectrode is of the scale of a millimetre. As the size of the macroelectrode is much larger than the diffusion layer thickness, the current density is regarded as identical at every point of the electrode surface and the diffusion toward to a planar macroelectrode is regarded as linear. A microelectrode is defined as the electrode which has at least one dimension on the scale of tens of micrometres or less, down to the submicrometre range.[26] The tiny size of the microelectrode brings additional advantages in the measurement, such as the enhanced mass transport, the rapidly attained steady state, the reduced ohmic drop, the improved signal-to-noise level, et al. In contrast with the macroelectrode, the diffusion layer thickness is usually comparable with the size of the microelectrode and the diffusion toward the electrode surface is radial. The comparison between the linear and radial diffusion is shown in Figure 1.8. Note that we distinguish the two limiting cases by comparing the diffusion layer thickness with the size of the electrode. As the diffusion layer thickness is dependent on reaction time, the differentiation also depends on time. At extremely short reaction durations, any micro-size or even nano-size electrode can behave as a macroelectrode as the diffusion mode is actually linear rather than radial, and vice versa.

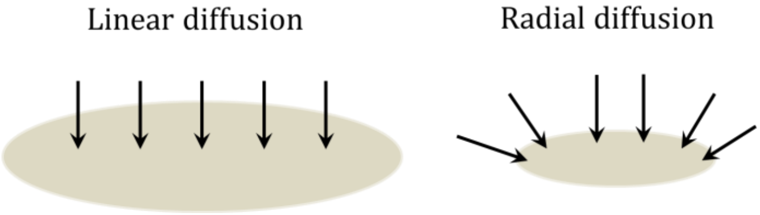

Figure 1.8 Comparison between the linear diffusion and radial diffusion at the planar electrode.

An ensemble of microelectrodes in a conductive, inert substrate comprises a microelectrode array. Compared to a single microelectrode, the microelectrode array increases the total current magnitude; compared to a macroelectrode, the signal-to-noise level is improved and the use of electrode materials, which are usually nobel metals, is minimised in the microelectrode array. But the diffusion on the microelectrode array is more complicated, due to the overlap of the diffusion fields of two adjacent microelectrodes. The current measured from the overall array is not only determined by the redox reaction and the diffusion, but also influenced by the overlap degree between two nearby electrodes. The different diffusion modes in the microelectrode array will be further discussed in Chapter 5 and 6, where a microelectrode array is applied in the study of electrocatalytic reactions.

1.5.3 Chronoamperometry

Chronoamperometry is a technique which records current as a function of time. In the experiment, the electrode potential is changed from an initial potential E_1, which is inactive to the redox reaction, to the reacting potential E_2, where the redox reaction occurs. The current at the constant potential E_2 is measured. Figure 1.9 shows the variation of electrode potential and current in the chronoamperometry.

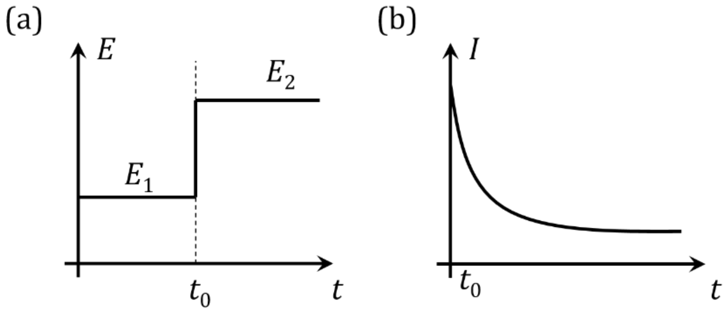

Figure 1.9 In the chronoamperometry, (a) the electrode potential changes from E_1 to E_2 at time t_0; (b) the electrode current is recorded as a function of time.

The current expression as a function of time can be solved for planar electrodes at high overpotentials. Assuming the electrochemical reaction is fully driven at high overpotentials, the surface concentration of the reactant is approximately zero. For a simple one-electron-transfer reaction at a planar macroelectrode, by solving Fick's second law, the current is calculated as a function of time:

$$I = \frac{n_e F S \sqrt{D} c^*}{\sqrt{\pi t}} \tag{1.52}$$

where n_e is the number of electrons transferred in the reaction, S is the area of the electrode, D and c^* are the diffusion coefficient and the bulk concentration of the redox species. Eqn.(1.52) is known as the Cottrell equation. [27]

The current at a planar microdisc electrode can be expressed as:[25]

$$I = 4n_e FDc^* r_{el} f(\tau)$$
$$f(\tau) = \left(\frac{\pi}{4\tau}\right)^{1/2} + \frac{\pi}{4} + 0.094\tau^{1/2} + \ldots,\ \ \tau = 4Dt/r_{el}^2 \qquad (1.53)$$

where r_{el} is the radius of the microdisc electrode. At macroelectrode, the current decreases to zero after long reaction time. But for microelectrode, there is a non-zero electrode current at long times and it is called 'steady state' when the current stops changing with time. The steady-state current at a planar microelectrode is:[25]

$$I_{ss} = 4n_e FDc^* r_{el} \qquad (1.54)$$

1.5.3 Cyclic Voltammetry

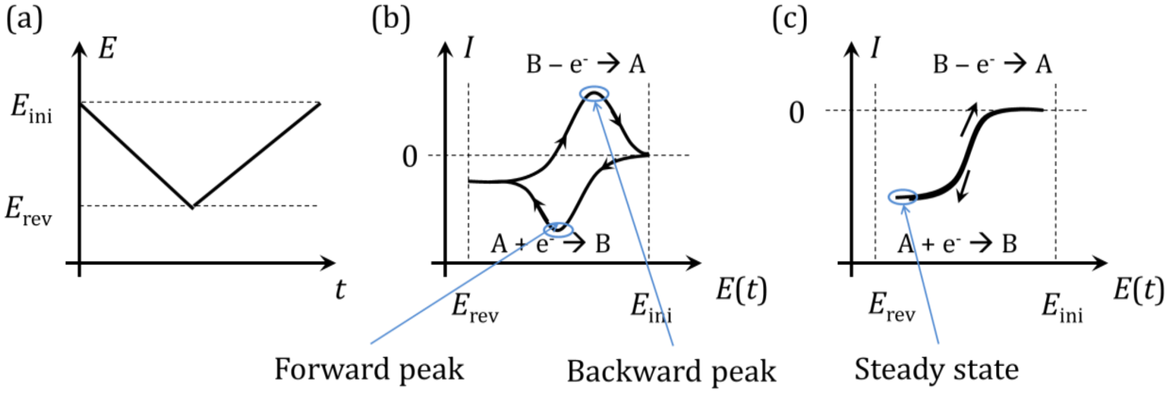

Figure 1.10 (a) Cyclic potential sweep; (b) Current-potential plot recorded at a planar macroelectrode; (c) Current-potential plot recorded at a planar microelectrode.

In cyclic voltammetry, the electrode potential linearly sweeps in a scan rate v between the initial potential E_{ini} and the reverse potential E_{rev}, as illustrated in Figure 1.10a. The potential window between E_{ini} and E_{rev} is chosen to allow the target redox reaction occur as well as avoid the decomposition of solvent and interference from other coexisting redox species. For a simple one-electron-transfer reaction $A + e^- = B$, a typical current-potential curve at a planar macroelectrode and a current-potential curve at a planar microelectrode are shown in Figure 1.10b and 1.10c, respectively. In the forward scan from E_{ini} to E_{rev}, the electrode reaction is $A + e^- \rightarrow B$ and in the backward scan, the electrode reaction is $B - e^- \rightarrow A$.

In Figures 1.10 b and c, a peak shape is observed in the cyclic voltammogram of the macroelectrode and a steady state is found at the microelectrode, as the consequence of the interplay between the diffusion and the electron transfer. The diffusion speed is independent of the electrode potential but the electrode transfer rate is affected. At high overpotential, as the rate of electron transfer increases, the diffusion becomes relatively slow and the overall reaction rate is limited by the diffusion, reflected by the peak at the macroelectrode and the steady state at the microelectrode.

For a simple electrode system, the cyclic voltammetric behaviour depends on the electrochemical reversibility of the reaction. Electrochemically reversible and irreversible correspond to 'fast' and 'slow' electrode kinetics, respectively. In electron transfer theories, the reversible electron transfer is usually represented by a large electron transfer rate constant k_0 and the electron transfer with small k_0 is irreversible. But the reversibility is not determined by the absolute value of the reaction rate, it needs to be compared with the other rate-determining factor, diffusion. The distinction between reversible and irreversible electron transfer, relating to the prevailing rate of diffusion, is given by:[25]

$$k_0 \gg \sqrt{\frac{FvD}{RT}} \qquad \text{(reversible)} \qquad (1.55)$$

$$k_0 \ll \sqrt{\frac{FvD}{RT}} \qquad \text{(irreversible)} \qquad (1.56)$$

$\sqrt{\frac{FvD}{RT}}$ reflects the diffusion rate with the consideration of the time taken to scan the voltammogram. In both reversible and irreversible electron transfer conditions, a square root dependence between the forward peak current and the scan rate is found at the planar macroelectrode for reaction A + e^- = B:[25]

$$I_{\mathrm{p,rev}} = 0.446FSc^{*}\sqrt{\frac{FDv}{RT}} \tag{1.57}$$

$$I_{\mathrm{p,irr}} = 0.496\sqrt{\alpha}FSc^{*}\sqrt{\frac{FDv}{RT}} \tag{1.58}$$

At a planar microelectrode, the reversibility of the electrochemical reaction does not influence the value of the steady-state current of the cyclic voltammogram. For an one-electron-transfer reaction, the steady-state current has the same expression as Eqn.(1.54).

1.5.4 The Nano-particle Impact (Nano-Impact) Technique

The traditional method to analyse the electroactivity of nanoparticles is to immobilize the nanoparticles on a supporting electrode surface and measure the current response contributed by the ensemble of the nanoparticles. However, it is difficult to know the structure of the immobilized nanoparticle layer, such as the distribution of the nanoparticles at the surface and the extent of any agglomeration, if any. Thus, the diffusion towards the nanoparticle ensemble is unclear. In addition, the current measured from such nanoparticle modified electrode can only qualitatively reflect the electroactivity of the nanoparticles and the number of the active nanoparticles cannot be determined, as there is a high chance of the nanoparticles to aggregate during the immobilization process or drop off the electrode during the measurement.[28]

The nanoparticle impact technique is an electroanalytical method to characterise the physical and chemical properties of single nanoparticles.[29, 30] For an electrode-electrolyte system, particles suspended in a solution undergo Brownian motion and will stochastically reach the electrode surface. Under a suitable potential, the electrochemical reaction related to the nanoparticle via either direct or mediated electron transfer can be observed. The principles of three types of nano-impact experiments are shown in Figure 1.11. In Figure 1.11 a, the nanoparticle itself is consumed in the redox reaction when it collides with the electrode surface and the corresponding current signal is a sharp spike. Figure 1.11 b shows the case of the electron transfer mediated by the nanoparticle, where the redox species are added in the electrolyte solution and the supporting electrode is inert to the redox reaction in the absence of the nanoparticle. The current signal of the mediated redox reaction is usually a step. In Figure 1.11 c, some solution species are catalysed to react by the nanoparticle in the solution phase, forming electroactive products. The potential of the electrode is set as the value which only enables the electron exchange with the product species in the latter case. The current increases when the nanoparticle moves towards the electrode as it can collect more products and the current decreases when the nanoparticle moves away from the electrode. Fluctuating currents are recorded in this case. The application of the nano-impacts in understanding electrode-electrolyte kinetics and the analysis of the nano-impact results will be further discussed in Chapter 5, 6 and 7.

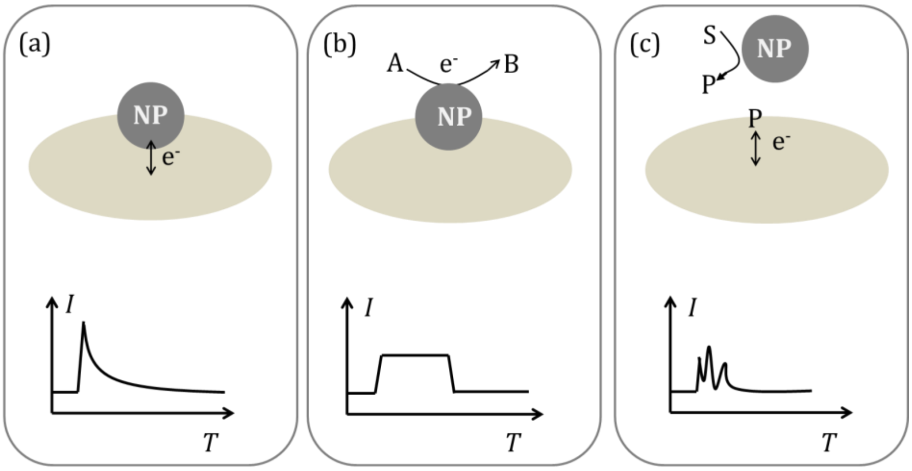

Figure 1.11 Principles of nanoparticle impact methods under different conditions: (a) the nanoparticle is consumed at the electrode surface via direct electron transfer; (b) the nanoparticle mediates the electron transfer at the supporting electrode; (c) the collection electrode detects the product catalysed by the nanoparticle in the solution phase.

The nano-impact technique has been proved to be an efficient method for measurement of physical properties of nanoparticles, such as size, concentration and aggregation/agglomeration state.[30] In addition, when the nanoparticle mediates electrochemical reaction, it acts as a "nanoelectrode" for the duration of impact. Due to the small size of the nanoparticle, the diffusion towards the nanoparticle surface is faster compared to the macro- or even micro-electrodes and the nano-impact method enables the study of ultrafast kinetic processes, of which the influence at macro- and micro-electrodes is usually covered by the relatively slow diffusion speed.

References

1. J. O. M. Bockris, A. K. N. Reddy and M. E. Gamboa-Aldeco, *Modern electrochemistry*, Plenum Press, New York, 1998.
2. S. Trasatti, *Journal*, 1986, **58**, 955.
3. A. J. Bard and L. R. Faulkner, *Electrochemical Methods: Fundamentals and Applications*, Wiley, 2000.
4. G. Gouy, *J.Phys.*, 1910, **9**, 457-468.
5. D. L. Chapman, *Philos. Mag.*, 1913, **25**, 475-481.
6. W. Schmickler and E. Santos, *Interfacial Electrochemistry*, Springer Berlin Heidelberg, 2010.
7. J. O. M. Bockris, M. A. V. Devanathan and K. Müller, *Proceedings of the Royal Society of London. Series A. Mathematical and Physical Sciences*, 1963, **274**, 55.
8. J. Tafel, *Zeitschrift für physikalische Chemie*, 1905, **50**, 641-712.
9. J. A. V. Butler, *Transactions of the Faraday Society*, 1924, **19**, 729-733.
10. J. A. V. Butler, *Transactions of the Faraday Society*, 1924, **19**, 734-739.
11. T. Erdey-Grúz and M. Volmer, *Journal*, 1930, **150A**, 203.
12. J. Horiuti and M. Polanyi, *Journal of Molecular Catalysis A: Chemical*, 2003, **199**, 185-197.
13. J. N. Bronsted, *Chemical Reviews*, 1928, **5**, 231-338.
14. R. W. Gurney, *Proceedings of the Royal Society of London. Series A*, 1931, **134**, 137-154.
15. R. A. Marcus, *The Journal of Chemical Physics*, 1956, **24**, 966-978.
16. R. A. Marcus, *Annual Review of Physical Chemistry*, 1964, **15**, 155-196.

17. R. A. Marcus, *The Journal of Chemical Physics*, 1965, **43**, 679-701.

18. N. S. Hush, *The Journal of Chemical Physics*, 1958, **28**, 962-972.

19. N. S. Hush, *Transactions of the Faraday Society*, 1961, **57**, 557-580.

20. R. A. Marcus, *Angewandte Chemie (International Edition in English)*, 1993, **32**, 1111-1121.

21. K. Ngamchuea, S. Eloul, K. Tschulik and R. G. Compton, *Analytical Chemistry*, 2015, **87**, 7226-7234.

22. E. J. F. Dickinson, J. G. Limon-Petersen, N. V. Rees and R. G. Compton, *The Journal of Physical Chemistry C*, 2009, **113**, 11157-11171.

23. A. Fick, *Journal of Membrane Science*, 1995, **100**, 33-38.

24. A. Einstein, *Annalen der Physik*, 1906, **324**, 371-381.

25. R. G. Compton and C. E. Banks, *Understanding Voltammetry*, Imperial College Press, 2nd edn., 2011.

26. K. Stulík, C. Amatore, K. Holub, V. Marecek and W. Kutner, *Journal*, 2000, **72**, 1483.

27. F. G. Cottrell, *Z.Phys.Chem.*, 1902, **42**, 385.

28. H. S. Toh, C. Batchelor-McAuley, K. Tschulik, M. Uhlemann, A. Crossley and R. G. Compton, *Nanoscale*, 2013, **5**, 4884-4893.

29. A. J. Bard, H. Zhou and S. J. Kwon, *Israel Journal of Chemistry*, 2010, **50**, 267-276.

30. W. Cheng and R. G. Compton, *Angewandte Chemie - International Edition*, 2016, **55**, 2545-2549.

Chapter 2 Simulation of Electrochemistry

In this chapter the modelling of electrode systems is introduced. The aim of these simulations is to translate the real-world problem into mathematical models and utilise the conclusions drawn from the model for the actual situation at hand.[1] In an electrode system, by solving the partial differential equations used to describe the mass transport of the reactive species, the concentration change at the electrode-electrolyte interface can be calculated and the current response can be simulated under given conditions.

2.1 Geometry of the Electrode System: Cylindrical Coordinates

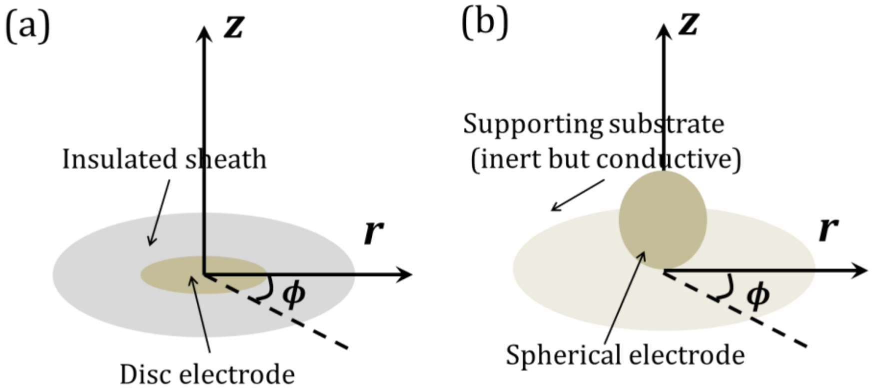

Figure 2.1 Cylindrical coordinates used in modelling (a) a disc electrode surrounded by an insulated sheath; (b) a spherical electrode attached on the supporting substrate. The supporting substrate is conductive to electron transfer but inert to any chemical or electrochemical reactions. r, ϕ and z represent the three dimensions.

The cylindrical coordinates are applied in the simulation of disc electrodes and surface-attached sphere electrodes, as illustrated in Figure 2.1. The cylindrical coordinates have three dimensions (r, ϕ, z). The electrode is usually placed on the plane where the r and ϕ axes cross and the z axis is the direction perpendicular to the electrode surface.

The line element $\mathrm{d}\vec{l}$ of the cylindrical coordinates is:

$$\mathrm{d}\vec{l} = \mathrm{d}r\hat{r} + r\mathrm{d}\phi\phi + \mathrm{d}z\hat{z} \tag{2.1}$$

where $\hat{r}, \hat{\phi}, \hat{z}$ are the unit vectors. The volume element $\mathrm{d}V$ is:

$$\mathrm{d}V = r\mathrm{d}r\mathrm{d}\phi\mathrm{d}z \tag{2.2}$$

For any function f in the cylindrical coordinates, the gradient operator and the Laplace operator are written:

$$\nabla f = \frac{\partial f}{\partial r}\hat{r} + \frac{1}{r}\frac{\partial f}{\partial \phi}\phi + \frac{\partial f}{\partial z}\hat{z} \tag{2.3}$$

$$\nabla^2 f = \frac{1}{r}\frac{\partial}{\partial r}\left(r\frac{\partial f}{\partial r}\right) + \frac{1}{r^2}\frac{\partial^2 f}{\partial \phi^2} + \frac{\partial^2 f}{\partial z^2} \tag{2.4}$$

The coordinates can be further simplified into two dimensions or even one dimension, according to the symmetry of the electrode system. If the size of the electrode is relatively large compared with the diffusion layer, the influence at the edge of the electrode can be ignored and each position at the electrode surface is treated evenly, $\frac{\partial f}{\partial r} = \frac{\partial f}{\partial \phi} = 0$. Therefore, the concentration varies only along the dimension z perpendicular to the electrode plane. On the other hand, if the electrode radius is comparable with the diffusion layer thickness, the concentration is no longer uniform at the electrode surface and the variation along the radial direction r needs to be taken into consideration. But for the disc or sphere electrodes, the geometry is axially symmetric with the z axis and thus the concentration does not change with the angle ϕ, $\frac{\partial f}{\partial \phi} = 0$.

2.2 Normalisation and Dimensionless Parameters

For real-world problems, the variables and parameters have their individual physical meanings and units. But in a simulation, it is usually more convenient to transform the given physical variables into dimensionless ones. According to Buckingham's theorem, different systems that share the same description in terms of the dimensionless numbers are equivalent.[1] The normalization provides convenience for simulation, as the dimensionless parameters are independent of any specific situations. Therefore, the dimensionless conclusion can be easily and rapidly applied to similar systems with different parameters.

In addition, normalization can provide extra physical interpretation which helps to analyse the kinetics of an electrode system and understand the hierarchy of the significance among a series of influencing factors. In modelling and simulation, it is important to decide which effects are relevant to the problem to be solved. The relevant effects need to be included in the model while the irrelevant ones are ignored to reduce the complexity of the programme. By using dimensionless parameters, the set of variables can be effectively reduced to a smaller set of independent, dimensionless variables. In the following chapters, the importance of using dimensionless variables and parameters will be emphasized again with detailed examples in various electrode systems.

2.3 Partial Differential Equation

Equations with derivatives with respect to more than one variable are called *partial differential equations* (PDE). For instance, the diffusion equation (Fick's Second Law) is a partial differential equation describing the concentration change as a function of space positon and time.[2] A PDE of the function $u(x, y, \ldots)$ can be expressed as:

$$f\left(x, y, \ldots, u, \frac{\partial u}{\partial x}, \frac{\partial u}{\partial y}, \ldots, \frac{\partial^2 u}{\partial x^2}, \frac{\partial^2 u}{\partial y^2}, \frac{\partial^2 u}{\partial x \partial y}, \ldots\right) = 0 \tag{2.5}$$

If f is a linear function of u and its derivatives, the PDE is called *linear*; otherwise is *non-linear*.

To solve a PDE, we also need to know the boundary conditions, which refer to the states of the system under certain conditions, usually at the boundary of the simulation domain. There are three main boundary conditions: the Dirichlet, Neumann and Robin conditions.[3] With the Dirichlet condition, which is also called a 'fixed boundary condition', the function is constrained to a constant value at the boundary. The Neumann condition, also called a 'derivative boundary condition', is one where the first derivative of the function is a constant value at the boundary. The Robin condition, a mixed boundary condition, is the linear combination of the Dirichlet condition and the Neumann condition.

There are two types of solutions to the PDE: one is the analytical solution, the other is the numerical solution. For certain PDEs with relatively simple geometry and boundary conditions, the analytical solution can be directly derived via mathematical methods.[4] For instance, the Cottrell equation, which describes potential step chonoamperometry for a reversible electrochemical reaction at a planar macroelectrode by F. G. Cottrell in 1902,[5] is analytically derived from the Fick's second law. The analytical solution of the PED is not only applied in the simulation, but also widely used to examine the validation of the numerical results, as discussed in section 2.8.

However, in most cases, limited by the complexity of geometry and boundary conditions, as well as the number of variables involved in PDEs, it is rather difficult to obtain the analytical solution. Instead, the numerical solution is proposed as an approximation. In chapters 3 to 7 of this thesis, the complicated electrode systems are simulated via the numerical technique and several numerical methods will be introduced in the following sections.

2.4 The Finite Difference Method

As it is usually difficult to find the mathematical solution for a PDE, especially in the case of complicated boundary conditions, the numerical method is often employed to obtain an approximate solution. The simplest way is to define a discrete analogue of the continuous PDE and the differential is then replaced by a finite difference approximation in the simulation domain.[1] Here the one-dimension (one spatial dimension) Fick's second law is used as an example:

$$\frac{\partial c}{\partial t} = D\frac{\partial^2 c}{\partial x^2} \tag{2.6}$$

As illustrated in Figure 2.2, the sets of points $\{t_k\}$ and $\{x_i\}$ are called the *grid* or the *mesh*. *i* and *k* refer to the index of the grid points. The continuous function $c\ (t, x)$ is then expressed as $\{c_i^k \coloneqq c(t_k, x_i)\}$. When discretising the diffusion equation, a first derivative of time ($\frac{\partial c}{\partial t}$) and first- or second- order derivatives of the space coordinates ($\frac{\partial c}{\partial x}$ or $\frac{\partial^2 c}{\partial x^2}$) are required.

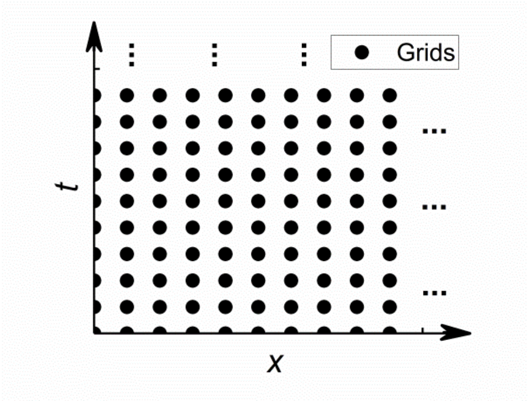

Figure 2.2 The illustration of the interested domain containing the discrete space dimension {*x*i} and time dimension {*t*k}.

2.4.1 Space Derivation

In order to obtain the derivative of *c* at $x = x_i$, the two adjacent positions i+1 and i-1 may also need to be taken into consideration. The first-order space derivative at x_i can be expressed in three ways: forward difference, backward difference and centre difference:6

$$
\begin{aligned}
\frac{\partial c}{\partial x} &= \frac{c_{i+1}^k - c_i^k}{x_{i+1} - x_i} \quad (\text{forward difference}) \\
\frac{\partial c}{\partial x} &= \frac{c_i^k - c_{i-1}^k}{x_i - x_{i-1}} \quad (\text{backward difference}) \qquad (2.7) \\
\frac{\partial c}{\partial x} &= \frac{c_{i+1}^k - c_{i-1}^k}{x_{i+1} - x_{i-1}} \quad (\text{central difference})
\end{aligned}
$$

The schemes of the forward difference, the backward difference and the centre difference are shown in Figure 2.3.

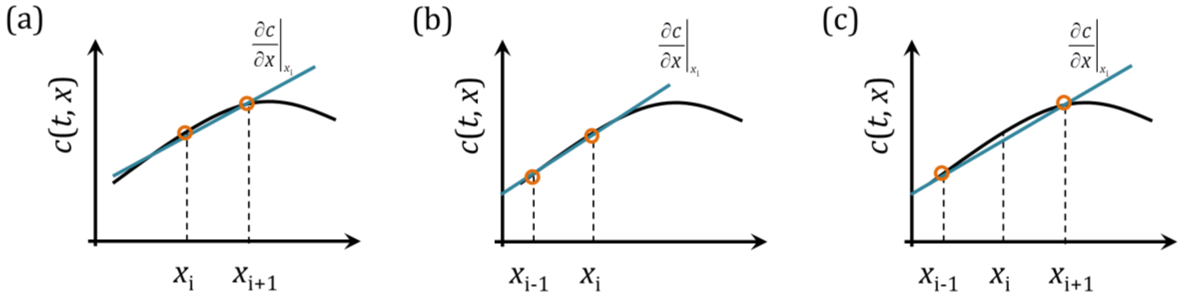

Figure 2.3 Schemes of (a) forward difference, (b) backward difference, and (c) central difference.

It is clear from Figure 2.3 that all the first-order differences, indicated by the slope of the blue lines, deviate from the real gradient at x_i. Assuming the accurate solution in the absence of any error of the PDE is given by $a(t, x)$, the Taylor expansion of $a\left(t, x_{i+1}\right)$ at x_i can be expressed as:

$$a\left(t, x_{i+1}\right) = a\left(t, x_i\right) + \left(x_{i+1} - x_i\right)\left.\frac{\partial a}{\partial x}\right|_{x_i} + \frac{\left(x_{i+1} - x_i\right)^2}{2!}\left.\frac{\partial^2 a}{\partial x^2}\right|_{x_i} + \frac{\left(x_{i+1} - x_i\right)^3}{3!}\left.\frac{\partial^3 a}{\partial x^3}\right|_{x_i} + \ldots \quad (2.8)$$

The first derivative at x_i is then rewritten as:

$$\left.\frac{\partial a}{\partial x}\right|_{x_i} = \frac{a\left(x_{i+1}\right) - a\left(x_i\right)}{x_{i+1} - x_i} - \frac{x_{i+1} - x_i}{2!}\left.\frac{\partial^2 a}{\partial x^2}\right|_{x_i} - \frac{\left(x_{i+1} - x_i\right)^2}{3!}\left.\frac{\partial^3 a}{\partial x^3}\right|_{x_i} - \ldots \quad (2.9)$$

Similarly, if considering the two points x_{i-1} and x_i, the first derivative is:

$$\left.\frac{\partial a}{\partial x}\right|_{x_i} = \frac{a\left(x_i\right) - a\left(x_{i-1}\right)}{x_i - x_{i-1}} - \frac{x_{i-1} - x_i}{2!}\left.\frac{\partial^2 a}{\partial x^2}\right|_{x_i} - \frac{\left(x_{i-1} - x_i\right)^2}{3!}\left.\frac{\partial^3 a}{\partial x^3}\right|_{x_i} - \ldots \quad (2.10)$$

Comparing (2.7) with (2.9) and (2.10), the truncation error, which is the miscalculation resulting from cutting off a numerical calculation before it is finished,[3] is the first order of the space increment in the case of the forward/backward difference.

However, by combining (2.9) and (2.10) together, the first-order derivative is expressed as:

$$\begin{aligned}\left.\frac{\partial a}{\partial x}\right|_{x_\mathrm{i}} &= \frac{1}{2}\left(\frac{a(x_\mathrm{i+1})-a(x_\mathrm{i})}{x_\mathrm{i+1}-x_\mathrm{i}}+\frac{a(x_\mathrm{i})-a(x_\mathrm{i-1})}{x_\mathrm{i}-x_\mathrm{i-1}}\right)-\frac{1}{2}\left(\frac{x_\mathrm{i+1}-x_\mathrm{i}}{2!}+\frac{x_\mathrm{i-1}-x_\mathrm{i}}{2!}\right)\left.\frac{\partial^2 a}{\partial x^2}\right|_{x_\mathrm{i}} \\ &\quad -\frac{1}{2}\left(\frac{(x_\mathrm{i+1}-x_\mathrm{i})^2}{3!}+\frac{(x_\mathrm{i}-x_\mathrm{i-1})^2}{3!}\right)\left.\frac{\partial^3 a}{\partial x^3}\right|_{x_\mathrm{i}}\end{aligned} \qquad (2.11)$$

In even spatial grids, where the spatial increment between two adjacent grid points is always the same Δx, Eqn.(2.11) can be further simplified as:

$$\left.\frac{\partial a}{\partial x}\right|_{x_\mathrm{i}} = \frac{a(x_\mathrm{i+1})-a(x_\mathrm{i-1})}{\Delta x}-\frac{1}{2}\frac{\Delta x^2}{3!}\left.\frac{\partial^3 a}{\partial x^3}\right|_{x_\mathrm{i}} \qquad (2.12)$$

From (2.11) and (2.12), it is found that the truncation error is of second order in the space increment when applying the central difference. In (2.11), we know that if the grid points are distributed unevenly, the expanding degree $\left|(x_\mathrm{i+1}-x_\mathrm{i})/(x_\mathrm{i}-x_\mathrm{i-1})\right|$ needs to be controlled as a small value to minimize the error. If the spatial increment ($x_\mathrm{i+1}-x_\mathrm{i}$) is small enough, the higher-order error increases the accuracy of the calculation. Therefore, the central difference is preferred for the space difference in most cases except the boundaries where the forward/backward difference needs to be applied.

Based on the midpoint rule, the second-order space derivative can be written as:

$$\left(\frac{\partial^2 c}{\partial x^2}\right)_{x_i} = \frac{\dfrac{c_{i+1}-c_i}{x_{i+1}-x_i}-\dfrac{c_i-c_{i-1}}{x_i-x_{i-1}}}{x_{i+1}-x_{i-1}} = \frac{c_{i+1}-c_i}{(x_{i+1}-x_i)(x_{i+1}-x_{i-1})}+\frac{c_i-c_{i-1}}{(x_i-x_{i-1})(x_{i+1}-x_{i-1})} \qquad (2.13)$$

Here note that if more points are applied in the approximation, so that the first-order derivative at x_i can include 2k+1 points from $x_\mathrm{i-k}$ to $x_\mathrm{i+k}$, the accuracy can be increased as the error becomes higher-order. However, since the accuracy of the two-point approximation is enough with small space intervals and the multi-point derivative is not convenient to implement, all the simulations involved in this thesis only consider two points in the calculation of the first derivative.

2.4.2 Time Evolution: Explicit and Implicit Methods

If the concentration value c_i^k at time level t_k can be computed independently from the other values at the same time level, the computational approach is defined as an explicit method; otherwise it is called an implicit method.[6] Figure 2.4 illustrates the difference between the explicit and implicit methods in the (*x*, *t*) mesh.

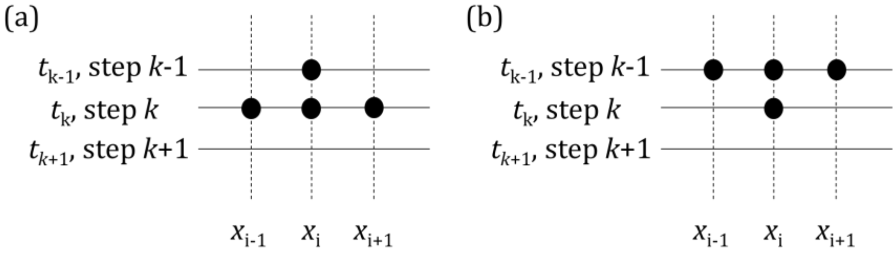

Figure 2.4 Schemes of (a) an explicit method; (b) an implicit method in a (*x*, *t*) mesh.

In terms of the one-dimension diffusion equation, the explicit approach can be written as:

$$\frac{c_i^k - c_i^{k-1}}{t_k - t_{k-1}} = D\left(\frac{c_{i+1}^{k-1} - c_i^{k-1}}{(x_{i+1}-x_i)(x_{i+1}-x_{i-1})} - \frac{c_i^{k-1} - c_{i-1}^{k-1}}{(x_i - x_{i-1})(x_{i+1}-x_{i-1})}\right) \tag{2.14}$$

where c_i^k only depends on the concentration values calculated from the last time step c_{i+1}^{k-1}, c_i^{k-1} and c_{i-1}^{k-1}. On the other hand, the implicit expression is:

$$\frac{c_i^k - c_i^{k-1}}{t_k - t_{k-1}} = D\left(\frac{c_{i+1}^{k} - c_i^{k}}{(x_{i+1}-x_i)(x_{i+1}-x_{i-1})} - \frac{c_i^{k} - c_{i-1}^{k}}{(x_i - x_{i-1})(x_{i+1}-x_{i-1})}\right) \tag{2.15}$$

where c_i^k is not only dependent on the last time calculation results c_i^{k-1} but also related with the other two unknown variables c_{i+1}^k and c_{i-1}^k. In the explicit method, each unknown concentration can be solved independently of the spatial position. But in the implicit method, the concentration cannot be calculated separately. Instead, the set of equations at each position needs to be solved simultaneously:

$$
\begin{aligned}
&\cdots\\
&-\frac{(t_k-t_{k-1})(c_i^k-c_{i-1}^k)}{(x_i-x_{i-1})(x_i-x_{i-2})}-\frac{(t_k-t_{k-1})(c_{i-1}^k-c_{i-2}^k)}{(x_{i-1}-x_{i-2})(x_i-x_{i-2})}+c_{i-1}^k=c_{i-1}^{k-1}\\
&-\frac{(t_k-t_{k-1})(c_{i+1}^k-c_i^k)}{(x_{i+1}-x_i)(x_{i+1}-x_{i-1})}-\frac{(t_k-t_{k-1})(c_i^k-c_{i-1}^k)}{(x_i-x_{i-1})(x_{i+1}-x_{i-1})}+c_i^k=c_i^{k-1}\\
&-\frac{(t_k-t_{k-1})(c_{i+2}^k-c_{i+1}^k)}{(x_{i+2}-x_{i+1})(x_{i+2}-x_i)}-\frac{(t_k-t_{k-1})(c_{i+1}^k-c_i^k)}{(x_{i+1}-x_i)(x_{i+2}-x_i)}+c_{i+1}^k=c_{i+1}^{k-1}\\
&\cdots
\end{aligned}
\tag{2.16}
$$

where the first and the last equations are given by the boundary conditions.

The explicit approximation is more convenient in programming than the implicit one. However, via the Fourier stability analysis (also known as von Neumann stability analysis), the explicit method is found to be only conditionally stable.[7] For evenly spaced grids where $\Delta t = t_\mathrm{k} - t_\mathrm{k-1}$ and $\Delta x = x_\mathrm{i} - x_\mathrm{i-1}$ are constants for each k and i, the mass transport equation can be approximated numerically as:

$$c_i^k = c_i^{k-1} + \frac{D\Delta t}{\Delta x^2}\left(c_{i+1}^{k-1} - 2c_i^{k-1} + c_{i-1}^{k-1}\right) \tag{2.17}$$

Defining the error o_i^k as $a_i^k - c_i^k$ where a is the accurate solution while c is the numerical solution, the error at each grid point also follows:

$$o_i^k = o_i^{k-1} + \frac{D\Delta t}{\Delta x^2}\left(o_{i+1}^{k-1} - 2o_i^{k-1} + o_{i-1}^{k-1}\right) \tag{2.18}$$

For the Fick's second law, the error contributed from both time and space grids can be expanded in a finite Fourier series as:

$$o_i^k = \sum_{m=1}^{M} \exp\left(\alpha t_\mathrm{k}\right)\exp\left(\iota \cdot \beta_\mathrm{m} x_\mathrm{i}\right) \tag{2.19}$$

α is a contant, ι is the imaginary unit, β_m is the wavenumber. In the space arrange L ($x \in L$), the wavenumber $\beta_\mathrm{m} = \pi m/L$ with m = 1, 2, … , M ($M = L/\Delta\mathrm{x}$). Since Eqn.(2.18) is linear, we only need to consider one typical term in Eqn.(2.19):

$$o_i^k = \exp\left(\alpha t_{\mathrm{k}}\right)\exp\left(\iota \cdot \beta_{\mathrm{m}} x_{\mathrm{i}}\right) \tag{2.20}$$

Similarly, after replacing o_{i+1}^{k-1}, o_i^{k-1} and o_{i-1}^{k-1} by:

$$\begin{aligned} o_{i+1}^{k-1} &= \exp\left(\alpha\left(t_{\mathrm{k}} - \Delta t\right)\right)\exp\left(\iota \cdot \beta_{\mathrm{m}}\left(x_{\mathrm{i}} + \Delta x\right)\right) \\ o_i^{k-1} &= \exp\left(\alpha\left(t_{\mathrm{k}} - \Delta t\right)\right)\exp\left(\iota \cdot \beta_{\mathrm{m}} x_{\mathrm{i}}\right) \\ o_{i+1}^{k-1} &= \exp\left(\alpha\left(t_{\mathrm{k}} - \Delta t\right)\right)\exp\left(\iota \cdot \beta_{\mathrm{m}}\left(x_{\mathrm{i}} - \Delta x\right)\right) \end{aligned} \tag{2.21}$$

Eqn. (2.18) becomes:

$$\begin{aligned} \exp\left(\alpha \Delta t\right) &= 1 + \frac{D\Delta t}{\Delta x^2}\left(\exp\left(\iota \cdot \beta_{\mathrm{m}} \Delta x\right) + \exp\left(\iota \cdot \beta_{\mathrm{m}}\left(-\Delta x\right)\right) - 2\right) \\ &= 1 - \frac{4D\Delta t}{\Delta x^2}\sin^2\left(\frac{\beta_{\mathrm{m}} \Delta x}{2}\right) \end{aligned} \tag{2.22}$$

To keep solution stable, the error amplification, defined as $\left|\frac{o_i^{k+1}}{o_i^k}\right|$, needs to remain less than 1:

$$\left|\frac{o_i^{k+1}}{o_i^k}\right| = \left|\exp\left(\alpha \Delta t\right)\right| \le 1 \tag{2.23}$$

Combining (2.22) and (2.23), considering that $\frac{4D\Delta t}{\Delta x^2}\sin^2\left(\frac{\beta_{\mathrm{m}} \Delta x}{2}\right) > 0$, the stable condition for the explicit method is:

$$\frac{D\Delta t}{\Delta x^2} < \frac{1}{2} \tag{2.24}$$

To meet the requirement of stability, the time interval Δ*t* needs to be significantly small and the computation is very inefficient. On the other hand, by means of the Fourier stability analysis, the implicit finite difference is shown to be unconditionally stable:

$$\text{Implicit}: \exp\left(\alpha \Delta t\right) = \left(1 + \frac{4D\Delta t}{\Delta x^2}\sin^2\left(\frac{\beta_{\mathrm{m}} \Delta x}{2}\right)\right)^{-1} \tag{2.25}$$

which means that there is no restriction between Δt and Δx. Due to its stability, the implicit method is applied in the simulation of the following chapters.

2.5 Algorithms for Linear and Non-linear Problems

In the finite difference method, one-dimensional space is separated by finite points $\vec{x} = \{x_1, x_2, \ldots\}$ and the concentration function at time t is expressed as $\vec{c}(t, \vec{x}) = \{c(t, x_1), c(t, x_2), \ldots\}$. To numerically calculate $\vec{c}\left(t, \vec{x}\right)$, two typical algorithms, the LU decomposition for linear PDEs and the Newton method for non-linear PDEs, are adopted and are introduced in this section.

2.5.1 LU Decompositon

For a linear PDE, the equation is expressed in the matrix format $\mathbf{A}\vec{c} = \vec{b}$ where **A**, b contain the coefficients to calculate the concentration function. The set of equations in (2.16) is written as:

$$\begin{pmatrix} \alpha_{1,1} & \alpha_{1,2} & \alpha_{1,3} & \cdots & \alpha_{1,n} \\ \alpha_{2,1} & \alpha_{2,2} & \alpha_{2,3} & \cdots & \alpha_{2,n} \\ & \ddots & \ddots & \ddots & \\ \alpha_{n-1,1} & \cdots & \alpha_{n-1,n-2} & \alpha_{n-1,n-1} & \alpha_{n-1,n} \\ \alpha_{n,1} & \cdots & \alpha_{n,n-2} & \alpha_{n,n-1} & \alpha_{n,n} \end{pmatrix} \begin{pmatrix} c_1^k \\ c_2^k \\ \vdots \\ c_{n-1}^k \\ c_n^k \end{pmatrix} = \begin{pmatrix} \beta_1 \\ \beta_2 \\ \vdots \\ \beta_{n-1} \\ \beta_n \end{pmatrix} \tag{2.26}$$

At each time step t, the values of the coefficients in **A** and b are known.

The $n \times n$ matrix **A** can be decomposed into a lower triangular matrix **L** and an upper triangular matrix **U**:

$$\mathbf{A}\vec{c} = \mathbf{L}\mathbf{U}\vec{c} = \mathbf{L}\vec{y} = \vec{b}, \qquad \vec{y} = \mathbf{U}\vec{c} \tag{2.27}$$

The solution of c contains two steps: the first is to solve the equation $\mathbf{L}\vec{y} = \vec{b}$, the second is to solve $\vec{y} = \mathbf{U}\vec{c}$.

The matrices **L** and **U** have the format as:

$$\mathbf{L} = \begin{pmatrix} 1 & 0 & 0 & \cdots & 0 \\ l_{21} & 1 & 0 & \cdots & 0 \\ & \ddots & \ddots & \ddots & \\ l_{n-1,1} & \cdots & l_{n-1,n-2} & 1 & 0 \\ l_{n,1} & \cdots & l_{n,n-2} & l_{n,n-1} & 1 \end{pmatrix} \tag{2.28}$$

$$\mathbf{U} = \begin{pmatrix} u_{1,1} & u_{1,2} & u_{1,3} & \cdots & u_{1,n} \\ 0 & u_{2,2} & u_{2,3} & \cdots & u_{2,n} \\ & \ddots & \ddots & \ddots & \\ 0 & \cdots & 0 & u_{n-1,n-1} & u_{n-1,n} \\ 0 & \cdots & 0 & 0 & u_{n,n} \end{pmatrix} \tag{2.29}$$

where the coefficients in **L** and **U** are given by:[6]

$$\begin{aligned} &\text{for } j = 1,2,\ldots,n \\ &u_{i,j} = \begin{cases} \alpha_{i,j} - \sum_{k=1}^{i} l_{i,k} u_{k,j}, & i = 1,2,\ldots,j \\ 0, & i = j+1, j+2,\ldots n \end{cases} \\ &l_{i,j} = \begin{cases} 0, & i = 1,2,\ldots j-1 \\ \dfrac{1}{u_{j,j}} \left(\alpha_{i,j} - \sum_{k=1}^{j} l_{i,k} u_{k,j} \right), & i = j, j+1, j+2,\ldots n \end{cases} \end{aligned} \tag{2.30}$$

As **L** is a lower triangular matrix, the solution of $\mathbf{L}\vec{y} = \vec{b}$ is easily derived as:

$$y_i = \beta_i - \sum_{k=1}^{i} l_{i,k} y_k, \qquad i = 1,2,\ldots,n \tag{2.31}$$

By solving $\vec{y} = \mathbf{U}\vec{c}$ through the backward substitution, the concentration function at each time *t* is determined as:

$$c_i = \frac{1}{u_{i,i}} \left(y_i - \sum_{k=i+1}^{n} u_{i,k} c_k \right), \qquad i = n, n-1,\ldots,1 \tag{2.32}$$

2.5.2 Newton-Raphson Method

A non-linear PDE in the electrochemical reaction related mass transport problem corresponds to the case of a coupled second-order chemical reaction in the electrolyte solution or the case where mass transport phenomena rather than diffusion is also taken into consideration. There are two methods to solve a non-linear PDE. One is the linearization of the non-linear term[2], which is easier to implement but usually takes long time to reach the required accuracy, as the time interval studied is forced to be very small. The other is multidimensional root finding. A simple algorithm for the root finding is called the Newton-Raphson method.[8]

Considering a function f as $f(c)=0$, the Newton-Raphson method determines the root of $f = 0$ by iteration. We first start with an initial guess c_0. After each iteration, the value of c_s is optimised until it reaches the real value of the root. c_s is the result after s steps of iteration and we use δc_s to represent the variation of c after step s. At step s+1, the function $f(c_s+\delta c_s)$ can be expanded as:

$$f(c_s+\delta c_s)=f(c_s)+f^{'}(c_s)\delta c_s+f^{''}(c_s)\delta {c_s}^2+\cdots \tag{2.33}$$

If high-order terms are ignored, $f(c_s+\delta c_s)$ can be approximated as:

$$f(c_s+\delta c_s)\approx f(c_s)+f^{'}(c_s)\delta c_s=0 \tag{2.34}$$

which is equal to:

$$f^{'}(c_s)\delta c_s=-f(c_s) \tag{2.35}$$

By solving the set of equations in the same format as Eqn.(2.35), the correction term δc_s can be calculated for each iteration. The difference between two iteration results δc_s is treated as a ‘residual’ error. When solving a non-linear equation, the iteration needs to be repeated several times until the residual error falls below a specified tolerance.

2.6 Two-Dimensional Systems

The microelectrode (or so called 'ultramicroelectrode') is widely applied due to the advantages of having a relatively large current density and improved mass transport efficiency. In contrast with the uniform current distribution at a macroelectrode surface, the microelectrode shows strong edge effects. Taking the microdisc electrode as an example, as the current densities along the radius of the electrode are very uneven, in addition to the dimension perpendicular to the electrode surface, the dimension along the electrode radius also needs to be considered. A two-dimensional cylindrical system, as the coordinates (r, z) shown in Figure 2.1, is applied to simulate the electrochemistry at the microdisc electrode. The diffusion equation with the (r, z) coordinates is expressed as:

$$\frac{\partial c}{\partial t} = D\left(\frac{\partial^2 c}{\partial z^2} + \frac{1}{r}\frac{\partial c}{\partial r} + \frac{\partial^2 c}{\partial r^2}\right) \tag{2.36}$$

To solve the above equation, an alternating direction implicit method (the ADI method) was proposed.[9, 10] The aim of the ADI method is to split the finite difference equations into two, one with the z-derivative taken implicitly ('z sweep') and the next with the r-derivative taken implicitly ('r sweep'). Assuming there is a 'half step' between two time steps k and k+1, at the z sweep, Eqn.(2.36) is approximated as:

$$\begin{aligned}
&\frac{c_{i,j}^{k+0.5} - c_{i,j}^{k}}{t_{k+0.5} - t_k} = D\left(\frac{2}{z_{j+1} - z_{j-1}}\left(\frac{c_{i,j+1}^{k+0.5} - c_{i,j}^{k+0.5}}{z_{j+1} - z_j} - \frac{c_{i,j}^{k+0.5} - c_{i,j-1}^{k+0.5}}{z_j - z_{j-1}}\right) + f\left(\{r_i\},\{c_{i,j}^{k}\}\right)\right)\\
&f\left(\{r_i\},\{c_{i,j}^{k}\}\right) = \frac{1}{r_i}\frac{c_{i+1,j}^{k} - c_{i-1,j}^{k}}{r_{i+1} - r_{i-1}} + \frac{2}{r_{i+1} - r_{i-1}}\left(\frac{c_{i+1,j}^{k} - c_{i,j}^{k}}{r_{i+1} - r_i} - \frac{c_{i,j}^{k} - c_{i-1,j}^{k}}{r_i - r_{i-1}}\right)
\end{aligned} \tag{2.37}$$

where $t_{k+0.5}$ is the 'half step'. k, i and j are the index for the coordinates t, r and z. Similarly, at the r sweep, the equation is:

$$\begin{aligned}
&\frac{c_{i,j}^{k+1} - c_{i,j}^{k+0.5}}{t_{k+1} - t_{k+0.5}} = D\left(\frac{1}{r_i}\frac{c_{i+1,j}^{k+1} - c_{i-1,j}^{k+1}}{r_{i+1} - r_{i-1}} + \frac{2}{r_{i+1} - r_{i-1}}\left(\frac{c_{i+1,j}^{k+1} - c_{i,j}^{k+1}}{r_{i+1} - r_i} - \frac{c_{i,j}^{k+1} - c_{i-1,j}^{k+1}}{r_i - r_{i-1}}\right) + f\left(\{z_j\},\{c_{i,j}^{k+0.5}\}\right)\right)\\
&f\left(\{z_j\},\{c_{i,j}^{k+0.5}\}\right) = \frac{2}{z_{j+1} - z_{j-1}}\left(\frac{c_{i,j+1}^{k+0.5} - c_{i,j}^{k+0.5}}{z_{j+1} - z_j} - \frac{c_{i,j}^{k+0.5} - c_{i,j-1}^{k+0.5}}{z_j - z_{j-1}}\right)
\end{aligned}$$

(2.38)

Figure 2.5 illustrates the alternation between the z sweep and the r sweep in the ADI method.

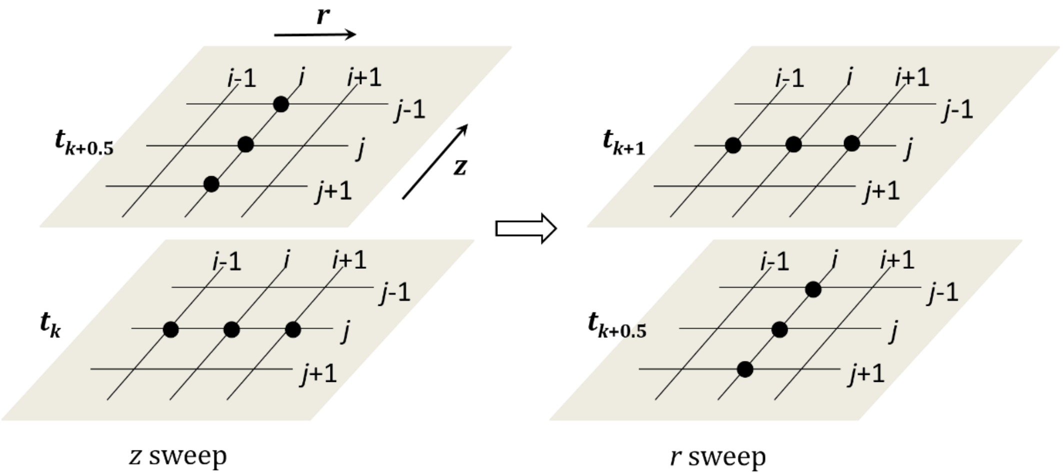

Figure 2.5 The z sweep and the r sweep of the alternating direction implicit method in a two-dimensional (*r, z*) system.

2.7 Validation and Convergence Tests

The global error in the simulation of an electrode system is a composite of the truncation error, which is caused by the numerical approximation, and the rounding error, which occurs due to a computer's finite precision arithmetic.[1] The truncation error contributes most to the global error. By refining the mesh used in the simulation domain, the truncation error can be diminished to an appropriate tolerance, where the current evaluated from the calculated concentration profile tends to the 'true' value. This phenomenon is referred as 'convergence'. The convergence of the simulation is achieved by consecutively decreasing the grid interval in both spatial and temporal dimensions.[6] The convergence of all the simulation results presented in this thesis is tested. The tolerance for a one-dimensional simulation is set to be 0.1 % and that of a two-dimensional simulation is 0.5 %, because of the compromise between the accuracy and the computation time. In practice, keeping the other variables and parameters constant, if the current at a microdisc electrode changes less than 0.5 % when the space interval Δx decrease from 10^{-5} to 10^{-6}, the simulation is regarded to be convergent with the spatial interval < 10^{-5}. The convergence with the temporal dimension can be tested in a similar way.

The validation of the simulation can be examined by comparing the simulation result with the analytic solution solved under the certain conditions. For instance, the peak current and the peak-to-peak separation are commonly used in the simulation of the macroelectrode (one-dimensional simulation); the steady-state current and the half-wave potential are used in the two-dimensional simulation.[11] If the analytical solution is not available, the mass balance (the sum of the present species and the consumed species should be constant) and the concentration distribution are also used to characterise the reasonableness of the simulation of an electrode system.

2.8 Summary

Digital simulation has been widely applied as an important tool to analyse electrochemical systems. This chapter introduced basic concepts in modelling and simulation, such as the need for dimensionless variables, partial differential equations and boundary conditions. The numerical solution of the diffusion equation via the finite difference method was discussed for both the one-dimensional (macroelectrode) and two-dimensional (microelectrode) systems. Validation and convergence testing was also introduced as a necessary procedure to examine the reasonableness of any simulation.

References

1. R. M. M. Mattheij, S. W. Rienstra and J. H. M. T. Boonkkamp, *Partial Differential Equations: Modeling, Analysis, Computation*, Society for Industrial and Applied Mathematics, 2005.
2. A. C. Fisher and R. G. Compton, *Electroanalysis*, 1992, **4**, 311-315.
3. D. Britz, *Digital Simulation in Electrochemistry*, Springer Berlin Heidelberg, 2005.
4. J. Kevorkian, *Partial Differential Equations: Analytical Solution Techniques*, Springer New York, 2010.
5. F. G. Cottrell, *Z.Phys.Chem.*, 1902, **42**, 385.
6. R. G. Compton, E. Laborda and K. R. Ward, *Understanding voltammetry: simulation of electrode processes*, Imperial College Press, London, U.K., 2013.
7. E. Isaacson and H. B. Keller, *Analysis of Numerical Methods*, Dover Publications, 1994.
8. T. J. Ypma, *SIAM Review*, 1995, **37**, 531-551.
9. D. W. Peaceman and J. H. H. Rachford, *Journal of the Society for Industrial and Applied Mathematics*, 1955, **3**, 28-41.
10. J. Douglas and D. W. Peaceman, *AIChE Journal*, 1955, **1**, 505-512.
11. E. Kätelhön and R. G. Compton, *Analyst*, 2015, **140**, 2592-2598.

Chapter 3 Electron Transfer with Coupled Chemical Adsorption

In this chapter, electron transfer with coupled chemical adsorption is explored. The effects of solvent reorganization and coupled chemical adsorption are examined via simulation. The Tafel-Volmer type mechanism, which describes the hydrogen oxidation reaction,[1] is taken as an example. A typical Tafel-Volmer reaction embraces a preceding chemisorption step and a following electron transfer:

$$\mathrm{A(sol)} + \mathrm{M} \rightleftharpoons \mathrm{A}\left(\mathrm{ads}\right) \tag{3.1}$$

$$\mathrm{A}\left(\mathrm{ads}\right) \rightleftharpoons \mathrm{B(sol)} + \mathrm{e}^{-} + \mathrm{M} \tag{3.2}$$

A and B are the solution-phase redox partners, M is the active site on the electrode/electrocatalyst, A(ads) is the adsorbate. Two different electron transfer formalisms, Butler-Volmer and a Marcus-Hush like approach, are utilised to interpret the potential-dependent kinetics of the electrochemical process. This chapter contains the work of two papers published in the *Journal of Physical Chemistry C*[2, 3] and the experimental part in 3.8 is from the work done by Miss. Xue Jiao.

3.1 Introduction

The Butler-Volmer (BV) equation, although phenomenological in its description of electron transfer, has historically been and continues to be successful in describing a wide variety of electrochemical data.[4] However, significant work has been focused upon both providing a more physically correct description of the interfacial electron transfer process[5, 6] and determining experimental conditions under which the Butler-Volmer equation is found to be inadequate in describing the electron transfer process.[7, 8]

It was with the publication of Chidsey's work in 1991 that the first direct evidence for the limitations of the Butler-Volmer equation was obtained, highlighting how at high overpotentials the rate of electron transfer is significantly below that predicted by the BV equation.[7] This work utilised a surface bound ferrocene group as the electroactive species. Importantly, it is the use of the such a 'diffusionless' system that facilitated the interrogation of the electron transfer kinetics at potentials significantly away from the formal potential for the redox couple, evidencing the validity of the Marcus-Hush (MH) description of electron transfer kinetics. For an outer-sphere diffusional (solution phase) electrochemical system, evidencing distinctions between models of electron transfer becomes inherently challenging in part due to the rate of electrochemical reaction commonly being under mass-transport (diffusion) control at high overpotentials. Recent advancements in the theory of interfacial electron transfer have demonstrated how, for outer-sphere diffusional redox processes, deviations from Butler-Volmer electron transfer kinetics are predicted to be observable under conditions of extremely high mass-transport.[9] Such conditions may be achievable with the use of an electrode with nanoscopic dimensions, however under most experimental conditions the electrochemical response is found to be relatively insensitive to the mechanism of electron transfer (BV vs MH).[10]

Between the limits of the two above cases (surface bound and outer-sphere diffusional) exists a third class of interfacial electrochemical reactions, inner-sphere heterogeneous electrode reactions.[11] Here for inner-sphere reactions, the electroactive species is present in the solution phase however, electron transfer proceeds via one or more surface adsorbed intermediates. This class of reactions encompasses a diverse range of systems including some of the most technological and industrially relevant.[12] Hence, questions arise: are 'inner-sphere' heterogeneous reactions sensitive to the electron transfer mechanism (for example BV vs MH) and the chemical sorption? And under what conditions can the influence of chemical adsorption and the electron transfer kinetics be observed from the current response of such reactions? Addressing these questions presents two significant difficulties, first an appropriate electrochemical mechanism needs to be selected and second the form of the kinetic formalism requires consideration. In terms of the overall operative electrochemical mechanism, a host of possible reaction routes may be considered, however within this work the Tafel-Volmer reaction mechanism is taken as a paradigmatic example of an inner-sphere heterogeneous electrochemical process. This reaction path is one route by which hydrogen may be oxidised on some electrodes[1, 13] and so is both a 'simple' example of an inner-sphere heterogeneous reaction and is of further academic interest.

On returning to the question of whether the electrochemical response of an inner-sphere heterogeneous reaction is more or less sensitive to the electron transfer mechanism, within this chapter the Marcus-Hush model of electron transfer is applied, such that the deviation from the Butler-Volmer equation due to the solvent reorganization is suitably described by the model. As a first approach, a MH-like model will be employed. A potential energy curve method with a single reaction coordinate and a (symmetric) Marcusian description of the energy profile; that is, a quadratic variation of the energy with the reaction coordinate that results in a quadratic relationship between the activation energy and the applied potential. This quadratic relationship is in contrast with the linear dependence predicted by the semiempirical BV model. However, strict physical interpretation of the potential energy curve utilised in this work would require inclusion of an understanding of the influence of the inter analyte/electrode distance upon the reaction coordinate. Therefore, application of the Marcus-Hush model within the Tafel-Volmer electrochemical mechanism provides an objective route by which the sensitivity of this paradigmatic 'inner-sphere' reaction pathway towards the electron transfer mechanism can be assessed. In light with the influence of the chemical adsorption, a simple Langmuir type adsorption is assumed to describe the pre-adsorption step. With the Langmuir adsorption hypothesis, the electrode is treated as a smooth plane with uniform active sites, there is no interaction between two adsorbates, and only one monolayer of the adsorbate forms at the surface.

The current response of the Tafel-Volmer reaction is simulated under various adsorption and electron transfer conditions. The theoretical model of the whole electrode reaction is built and the kinetics of the reaction is characterised. Experiments on the hydrogen oxidation reaction at platinum microelectrodes are used as an example to show how to analyse the kinetics of such electrochemical systems.

3.2 Theoretical Model of Tafel-Volmer Reaction

In this study, the electrode reaction which includes a preceding adsorption step and a following electron transfer step is taken into consideration. The hydrogen oxidation reaction is utilised as an example to explore the adsorption coupled inner-sphere electrode reaction. Two electron transfer models, the Butler-Volmer and a Marcus-Hush like approach, are applied in the description of the kinetics of the electron transfer process. The definition of the kinetic parameters and its influence on the simulation are also discussed.

3.2.1 Tafel-Volmer Mechanism

As demonstrated in previous works[1, 2, 13], the hydrogen oxidation reaction (3.3) on Pt electrodes can be regarded as the combination of a chemical adsorption step ((3.4), the Tafel reaction) and an electron transfer step ((3.5), the Volmer reaction):

$$\mathrm{H_2} \rightleftarrows \mathrm{2H^+ + 2e^-} \tag{3.3}$$

$$\mathrm{H_2 + 2M} \underset{k_\mathrm{d}}{\overset{k_\mathrm{a}}{\rightleftarrows}} \mathrm{2H(ads)} \tag{3.4}$$

$$\mathrm{H(ads)} \underset{k_\mathrm{red}}{\overset{k_\mathrm{ox}}{\rightleftarrows}} \mathrm{H^+ + e^- + M} \tag{3.5}$$

where H(ads) is an adsorbed hydrogen atom, M is an available adsorption site on the electrode surface, k_a (m s^{-1}) and k_d (mol m^{-2} s^{-1}) are the adsorption and desorption rate constants for the Tafel reaction, k_ox (mol m^{-2} s^{-1}) and k_red (m s^{-1}) are the oxidative and reductive electron transfer rate constants for the Volmer reaction.

The values of k_ox and k_red are dependent on the applied electrode potential E (V) and the formal potential of the electron transfer step $E_{\mathrm{f,\ H^+/H(ads)}}$, which is *not* identical with the formal potential of the whole reaction $E_{\mathrm{f,\ H^+/H_2}}$. From the Gibbs energy balance, $E_{\mathrm{f,\ H^+/H(ads)}}$ can be expressed in terms of $E_{\mathrm{f,\ H^+/H_2}}$ and the adsorption equilibrium constant K_ads (unitless):

$$E_{\mathrm{f,\ H^+/H(ads)}} = E_{\mathrm{f,\ H^+/H_2}} + \frac{RT}{2F}\ln\left(K_\mathrm{ads}\right) \tag{3.6}$$

$$K_\mathrm{ads} = \frac{k_\mathrm{a} c^o}{k_\mathrm{d}} \tag{3.7}$$

where the standard concentration c^o = 1 mol dm^{-3}.

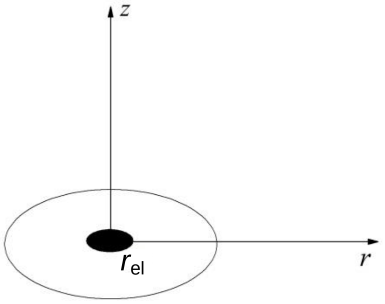

Figure 3.1 Illustration of the microdisk electrode considered in the simulation. The microdisc electrode (black) is surrounded by an insulating sheath (white). r_{el} is the radius of the electrode. *z* and *r* are the cylindrical coordinates.

According to the mechanism of Eqn.(3.4) and Eqn.(3.5), the fluxes of the electroactive species on the electrode surface can be described as:

$$j_{H_2}(r,z=0,t) = -k_a c_{H_2}(r,z=0,t)\left[\frac{\Gamma_M(r,t)}{\Gamma_{max}}\right]^2 + k_d\left[\frac{\Gamma_{H(ads)}(r,t)}{\Gamma_{max}}\right]^2 \tag{3.8}$$

$$\begin{aligned}\frac{\partial \Gamma_{H(ads)}(r,t)}{\partial t} &= 2k_a c_{H_2}(r,z=0,t)\left[\frac{\Gamma_M(r,t)}{\Gamma_{max}}\right]^2 - 2k_d\left[\frac{\Gamma_{H(ads)}(r,t)}{\Gamma_{max}}\right]^2 \\ &\quad - k_{ox}\left[\frac{\Gamma_{H(ads)}(r,t)}{\Gamma_{max}}\right] + k_{red}\left[\frac{\Gamma_M(r,t)}{\Gamma_{max}}\right] c_{H^+}(r,z=0,t)\end{aligned} \tag{3.9}$$

$$j_{H^+}(r,z=0,t) = k_{ox}\left[\frac{\Gamma_{H(ads)}(r,t)}{\Gamma_{max}}\right] - k_{red} c_{H^+}(r,z=0,t)\left[\frac{\Gamma_M(r,t)}{\Gamma_{max}}\right] \tag{3.10}$$

$\Gamma_i(r, t)$ is the surface coverage (mol m^{-2}) and $\Gamma_i(r, t)/\Gamma_{max}$ is the fractional surface coverage (unitless). Γ_{max} is the maximum surface coverage at the electrode surface and $\Gamma_{max} = \Gamma_{H(ads)}(r, t) + \Gamma_M(r, t)$. The discussion about the differences between applying $\Gamma_i(r, t)$ or $\Gamma_i(r, t)/\Gamma_{max}$ in the rate equations can be found in section 3.2.2. The parameters *r*, *z* are the cylindrical coordinates used to model a microdisc electrode as shown in Figure

3.1, and t is the time of applying the electrical perturbation. For linear sweep voltammetry, t and the applied electrode potential E follows:

$$\begin{aligned} &t < t_{\mathrm{switch}}, E = E_{\mathrm{ini}} + vt \\ &t > t_{\mathrm{switch}}, E = E_{\mathrm{switch}} - v(t - t_{\mathrm{switch}}) \end{aligned} \tag{3.11}$$

where E_{ini} and E_{switch} are the initial potential and the switching potential, t_{switch} is the time at which the direction of sweep is switched, and v is the scan rate.

The reaction fluxes of H_2 and H^+ follow Fick's first law:

$$j_{\mathrm{H_2}}\left(r,z,t\right) = -D_{\mathrm{H_2}} \frac{\partial c_{\mathrm{H_2}}\left(r,z,t\right)}{\partial z} \tag{3.12}$$

$$j_{\mathrm{H^+}}\left(r,z,t\right) = -D_{\mathrm{H^+}} \frac{\partial c_{\mathrm{H^+}}\left(r,z,t\right)}{\partial z} \tag{3.13}$$

Adsorption is considered to follow a dissociative Langmuir isotherm. Thus, the initial surface coverage fractions ($\Gamma_i(r, t)/\ \Gamma_{\max}$) for H(ads) and M are:

$$\frac{\Gamma_{\mathrm{H(ads)}}\left(r,t=0\right)}{\Gamma_{\max}} = \frac{\sqrt{c^{*}_{\mathrm{H_2}} k_{\mathrm{a}} / k_{\mathrm{d}}}}{1+\sqrt{c^{*}_{\mathrm{H_2}} k_{\mathrm{a}} / k_{\mathrm{d}}}} \tag{3.14}$$

$$\frac{\Gamma_{\mathrm{M}}\left(r,t=0\right)}{\Gamma_{\max}} = \frac{1}{1+\sqrt{c^{*}_{\mathrm{H_2}} k_{\mathrm{a}} / k_{\mathrm{d}}}} \tag{3.15}$$

where $c^{*}_{\mathrm{H_2}}$ is the bulk concentration of the hydrogen molecule.

In addition to the reaction on the electrode surface, the diffusion process of the reactant H_2 and the product H^+ are also considered in the simulation. Given the electrode geometry shown in Figure 3.1, the diffusion equations for solution species can be described as:

$$\frac{\partial c_{\mathrm{H_2}}\left(r,z,t\right)}{\partial t} = D_{\mathrm{H_2}}\left(\frac{\partial^2 c_{\mathrm{H_2}}\left(r,z,t\right)}{\partial r^2} + \frac{1}{r}\frac{\partial c_{\mathrm{H_2}}\left(r,z,t\right)}{\partial r} + \frac{\partial^2 c_{\mathrm{H_2}}\left(r,z,t\right)}{\partial z^2}\right) \tag{3.16}$$

$$\frac{\partial c_{H^+}(r,z,t)}{\partial t} = D_{\mathrm{H}^+}\left(\frac{\partial^2 c_{\mathrm{H}^+}(r,z,t)}{\partial r^2} + \frac{1}{r}\frac{\partial c_{\mathrm{H}^+}(r,z,t)}{\partial r} + \frac{\partial^2 c_{\mathrm{H}^+}(r,z,t)}{\partial z^2}\right) \tag{3.17}$$

3.2.2 Electron Transfer Kinetics

In the Butler-Volmer model, k_{ox} and k_{red} are dependent on the standard heterogeneous rate constant k_0, the transfer coefficient α or β ($\alpha + \beta = 1$), and the applied potential E:

$$k_{\mathrm{ox}}^{\mathrm{BV}} = k_0 c^o \exp\left(\frac{\beta F}{RT}\left(E - E_{\mathrm{f,\ H^+/H(ads)}}\right)\right) \tag{3.18}$$

$$k_{\mathrm{red}}^{\mathrm{BV}} = k_0 \exp\left(-\frac{\alpha F}{RT}\left(E - E_{\mathrm{f,\ H^+/H(ads)}}\right)\right) \tag{3.19}$$

$E_{\mathrm{f,\ H^+/H(ads)}}$ is the formal potential associated with the Volmer reaction. $E - E_{\mathrm{f,\ H^+/H(ads)}}$ is the overpotential of the electron transfer step, which is different from the overpotential for the whole reaction $E - E_{\mathrm{f,\ H^+/H_2}}$. Here notice that Eq.(3.18) is not the common expression for the oxidative electron transfer rate, which reflects the stoichiometry of the reaction and the different standard states defined for solution species and adsorbates on the left and right sides of the electron transfer reaction Eq.(3.5).

In the Marcus-Hush model, for an electrochemical reaction $\mathrm{R} \underset{k_{\mathrm{red}}}{\overset{k_{\mathrm{ox}}}{\rightleftarrows}} \mathrm{P} + e^-$, the expression for a rate constant k is derived from a transition state theory approach:[5, 14, 15]

$$k_{\mathrm{ox/red}}^{\mathrm{MH}}(\varepsilon) = A\exp\left(-\frac{\Delta G_{\mathrm{ox/red}}^*}{k_{\mathrm{B}}T}\right) \tag{3.20}$$

$$\Delta G_{\mathrm{ox/red}}^*(\varepsilon) = \frac{\lambda}{4}\left(1 \mp \frac{e\left(E - E_{\mathrm{f,\ H^+/H(ads)}}\right) + \varepsilon}{\lambda}\right)^2 \tag{3.21}$$

where A is the pre-exponential term, which is assumed to be independent on E and ε. $\Delta G_{\mathrm{ox/red}}^*$ (eV) is the activation energy for the oxidative (-) or the reductive (+) process of the electrochemical reaction. ε (eV) is the energy level of the metal electrode. λ (eV) is the reorganization energy. It is worth noting that, within the present context, the "reorganization energy" λ has a parametric character, its value being related to the curvature/shape of the energy profile with the reaction coordinate. Thus, in this case the physical meaning of λ is likely not only associated with the reorganization of the configuration of the electroactive species and the solvation shell (as for outer-sphere processes), but also with interactions with the electrode, (partial) desolvation and coulombic forces that the molecule undergoes along the reaction pathway.[12]

For the electron transfer between a reactant and a metal electrode, as there is not a single energy level but an energy band for the metal electrode, the overall rate constant should be the sum of all energy levels, that is $k = \sum k(\varepsilon)$. Since there are only small intervals $k_{\mathrm{B}}T$ among these energy levels, the probability of this transfer varies very little over two nearby different energy levels in the metal electrode. Therefore, the rate constant expression can be written as:[7]

$$k_{\mathrm{ox}}^{\mathrm{MH}} = A\int_{-\infty}^{+\infty} \frac{1}{1+\exp\left(\varepsilon^{*}\right)} \exp\left(-\frac{\lambda^{*}}{4}\left(1-\frac{\left(E-E_{\mathrm{f,\ H^{+}/H(ads)}}\right)^{*}+\varepsilon^{*}}{2\lambda^{*}}\right)^{2}\right) d\varepsilon^{*} \tag{3.22}$$

$$k_{\mathrm{red}}^{\mathrm{MH}} = A\int_{-\infty}^{+\infty} \frac{1}{1+\exp\left(-\varepsilon^{*}\right)} \exp\left(-\frac{\lambda^{*}}{4}\left(1+\frac{\left(E-E_{\mathrm{f,\ H^{+}/H(ads)}}\right)^{*}+\varepsilon^{*}}{2\lambda^{*}}\right)^{2}\right) d\varepsilon^{*} \tag{3.23}$$

where $f_{\mathrm{ox/red}}\left(\varepsilon^{*}\right) = \frac{1}{1+\exp\left(\pm\varepsilon^{*}\right)}$ is the Fermi-Dirac distribution for the electron occupancy (+) or the vacancy (-). For convenience, the dimensionless parameters are applied in Eqs. (3.20) and (3.21):

$$\lambda^{*} = \lambda F/\left(RT\right) \tag{3.24}$$

$$\varepsilon^{*} = \varepsilon F/\left(RT\right) \tag{3.25}$$

$$\left(E-E_{\mathrm{f,\ H^{+}/H(ads)}}\right)^{*} = \left(E-E_{\mathrm{f,\ H^{+}/H(ads)}}\right)F/\left(RT\right) \tag{3.26}$$

Considering k_0 is the standard rate constant at the formal potential, for the Volmer reaction, the MH rate constants can be expressed in a more general way:

$$k_{\mathrm{ox}}^{\mathrm{MH}} = k_0 c^o \frac{\int_{-\infty}^{+\infty} \frac{1}{1+\exp\left(\varepsilon^*\right)} \exp\left(-\frac{\lambda^*}{4}\left(1-\frac{\left(E-E_{\mathrm{f,\ H^+/H(ads)}}\right)^* + \varepsilon^*}{2}\right)^2\right) d\varepsilon^*}{\int_{-\infty}^{+\infty} \frac{1}{1+\exp\left(\varepsilon^*\right)} \exp\left(-\frac{\lambda^*}{4}\left(1-\frac{\varepsilon^*}{2}\right)^2\right) d\varepsilon^*} \tag{3.27}$$

$$k_{\mathrm{red}}^{\mathrm{MH}} = k_0 \frac{\int_{-\infty}^{+\infty} \frac{1}{1+\exp\left(-\varepsilon^*\right)} \exp\left(-\frac{\lambda^*}{4}\left(1+\frac{\left(E-E_{\mathrm{f,\ H^+/H(ads)}}\right)^* + \varepsilon^*}{2}\right)^2\right) d\varepsilon^*}{\int_{-\infty}^{+\infty} \frac{1}{1+\exp\left(-\varepsilon^*\right)} \exp\left(-\frac{\lambda^*}{4}\left(1+\frac{\varepsilon^*}{2}\right)^2\right) d\varepsilon^*} \tag{3.28}$$

Similar to $k_{\mathrm{ox}}^{\mathrm{BV}}$, k_0 has been replaced by $k_0 c^0$ in the expression of $k_{\mathrm{ox}}^{\mathrm{MH}}$.

3.3 Numerical Simulation of the Tafel-Volmer Reaction

3.3.1 Dimensionless Expressions

Dimensionless parameters are applied in the simulation, as listed in Table 3.1. Under the dimensionless format, the diffusion equations for the reactive species in the solution can be described as:

$$\frac{\partial C_{\mathrm{H_2}}(R,Z,T)}{\partial T} = d_{\mathrm{H_2}}\left(\frac{\partial^2 C_{\mathrm{H_2}}(R,Z,T)}{\partial R^2} + \frac{1}{R}\frac{\partial C_{\mathrm{H_2}}(R,Z,T)}{\partial R} + \frac{\partial^2 C_{\mathrm{H_2}}(R,Z,T)}{\partial Z^2}\right) \tag{3.29}$$

$$\frac{\partial C_{\mathrm{H^+}}(R,Z,T)}{\partial T} = d_{\mathrm{H^+}}\left(\frac{\partial^2 C_{\mathrm{H^+}}(R,Z,T)}{\partial R^2} + \frac{1}{R}\frac{\partial C_{\mathrm{H^+}}(R,Z,T)}{\partial R} + \frac{\partial^2 C_{\mathrm{H^+}}(R,Z,T)}{\partial Z^2}\right) \tag{3.30}$$

The dimensionless boundary conditions for solving diffusion equations can be expressed as:

$$\left.\begin{array}{l} T=0,\forall R,Z \\ T>0,R,Z\to\infty \end{array}\right\} \quad C_{\mathrm{H_2}}=C^*_{\mathrm{H_2}}=1\,, \quad C_{\mathrm{H^+}}=C^*_{\mathrm{H^+}}=0 \tag{3.31}$$

$$T=0,\, Z=0,\, 0\le R\le 1\text{:} \quad \Theta_{\mathrm{H(ads)}}=\frac{\sqrt{K_{\mathrm{a}}/K_{\mathrm{d}}}}{1+\sqrt{K_{\mathrm{a}}/K_{\mathrm{d}}}} \tag{3.32}$$

$T>0,\, Z=0,\, 0\le R\le 1$:

$$-d_{\mathrm{H_2}}\left(\frac{\partial C_{\mathrm{H_2}}}{\partial Z}\right)_{Z=0}=K_{\mathrm{d}}\Theta^2_{\mathrm{H\,(ads)}}-K_{\mathrm{a}}\left(1-\Theta_{\mathrm{H\,(ads)}}\right)^2 C_{\mathrm{H_2}} \tag{3.33}$$

$$-\mathrm{d}_{\mathrm{H^+}}\left(\frac{\partial C_{\mathrm{H^+}}}{\partial Z}\right)_{Z=0}=K_{\mathrm{ox}}\Theta_{\mathrm{H\,(ads)}}-K_{\mathrm{red}}\left(1-\Theta_{\mathrm{H\,(ads)}}\right)C_{\mathrm{H^+}} \tag{3.34}$$

$$\begin{aligned}\left(\frac{\partial\Theta_{\mathrm{H\,(ads)}}}{\partial T}\right)&=2K_{\mathrm{a}}\gamma\left(1-\Theta_{\mathrm{H\,(ads)}}\right)^2 C_{\mathrm{H_2}}-2K_{\mathrm{d}}\gamma\Theta^2_{\mathrm{H\,(ads)}}\\ &\quad+K_{\mathrm{red}}\gamma\left(1-\Theta_{\mathrm{H\,(ads)}}\right)C_{\mathrm{H^+}}-K_{\mathrm{ox}}\gamma\Theta_{\mathrm{H\,(ads)}}\end{aligned} \tag{3.35}$$

$T>0,\, Z=0,\, R>1$:

$$\left(\frac{\partial C_{\mathrm{H_2}}}{\partial Z}\right)_{Z=0}=0\ ;\ \left(\frac{\partial C_{\mathrm{H^+}}}{\partial Z}\right)_{Z=0}=0 \tag{3.36}$$

$T>0,\, Z,\, R=0$:

$$\left(\frac{\partial C_{\mathrm{H_2}}}{\partial R}\right)_{R=0}=0\ ;\ \left(\frac{\partial C_{\mathrm{H^+}}}{\partial R}\right)_{R=0}=0 \tag{3.37}$$

where the dimensionless parameter γ is equal to $c^*_{\mathrm{H_2}}r_{\mathrm{el}}\big/\Gamma_{\max}$. From Table 3.1, it is found that γ is the only constant parameter that contains $\Gamma_{\max}$ ($\Theta_i = \Gamma_i/\Gamma_{\max}$ works as a variable not a constant parameter during the simulation). Under steady state conditions, as $\partial\Theta_{\mathrm{H\,(ads)}}/\partial T=0$, the parameter γ cancels out in Eq.(3.35) such that the response of the system is independent of its value. It also indicates that for transient voltammetry where $\partial\Theta_{\mathrm{H\,(ads)}}/\partial T\neq 0$, the value of γ cannot be cancelled out from Eq.(3.35) and consequently the voltammogram will be influenced by the magnitude of $\Gamma_{\max}$.

The resulting problem was solved numerically by means of the Newton-Raphson method and according to the alternating direction implicit (ADI) method. The simulation was written in C++ with OpenMP for multithreading and simulations were performed using an Intel(R) Xeon(R) 3.60G CPU and the runtime was approximately 10 minutes *per* voltammogram.

Table 3.1 Dimensionless parameters employed in the simulations

SI unit parameters	Dimensionless parameters
c_j	$C_\mathrm{j} = c_\mathrm{j} / c^*_{\mathrm{H_2}}$
$\Gamma_\mathrm{i} / \Gamma_\mathrm{max}$	$\Theta_\mathrm{i} = \Gamma_\mathrm{i} / \Gamma_\mathrm{max}$
D_j	$d_\mathrm{j} = D_\mathrm{j} / D_{\mathrm{H_2}}$
r	$R = r / r_\mathrm{el}$
z	$Z = z / r_\mathrm{el}$
t	$T = D_{\mathrm{H_2}} t / r_\mathrm{el}{}^2$
E	$\theta = (F/RT)(E - E_{\mathrm{f,\ H^+/H_2}})$
$E_{\mathrm{f,\ H^+/H(ads)}}$	$\theta_{\mathrm{f,\ H^+/H(ads)}} = (F/RT)(E_{\mathrm{f,\ H^+/H(ads)}} - E_{\mathrm{f,\ H^+/H_2}})$
v	$\sigma = (r_\mathrm{el}{}^2 / D_{\mathrm{H_2}})(F/RT)v$
I	$J = I / (2\pi r_\mathrm{el} F D_{\mathrm{H_2}} c^*_{\mathrm{H_2}})$
k_a	$K_\mathrm{a} = k_\mathrm{a} r_\mathrm{el} / D_{\mathrm{H_2}}$
k_d	$K_\mathrm{d} = k_\mathrm{d} r_\mathrm{el} / \left(D_{\mathrm{H_2}} c^*_{\mathrm{H_2}}\right)$
$K_\mathrm{ads} = k_\mathrm{a} c^o / k_\mathrm{d}$	$K_\mathrm{ads} = K_\mathrm{a} c^o / \left(K_\mathrm{d} c^*_{\mathrm{H_2}}\right)$
k_0	$K_0 = k_0 r_\mathrm{el} / D_{\mathrm{H_2}}$
k_ox	$K_\mathrm{ox} = k_\mathrm{ox} r_\mathrm{el} / \left(D_{\mathrm{H_2}} c^*_{\mathrm{H_2}}\right)$
k_red	$K_\mathrm{red} = k_\mathrm{red} r_\mathrm{el} / D_{\mathrm{H_2}}$
λ^*	$\lambda F / (RT)$
ε^*	$\varepsilon F / (RT)$
	$\gamma = c^*_{\mathrm{H_2}} r_\mathrm{el} / \Gamma_\mathrm{max}$

3.3.2 Surface Coverage and Fractional Surface Coverage

If $\Gamma_{\mathrm{H(ads)/M}}/\Gamma_{\max}$ is applied to represent the amount of surface-bonded species, the rate equations (dimensional) for the three reactive species are:

$$j_{\mathrm{H_2}} = -D_{\mathrm{H_2}}\frac{\partial c_{\mathrm{H_2}}(r,z=0,t)}{\partial z} = -k_{\mathrm{a}}\left[c_{\mathrm{H_2}}(r,z=0,t)\right]\left[\frac{\Gamma_{\mathrm{M}}(r,t)}{\Gamma_{\max}}\right]^2 + k_{\mathrm{d}}\left[\frac{\Gamma_{\mathrm{H(ads)}}(r,t)}{\Gamma_{\max}}\right]^2 \quad (3.38)$$

$$\begin{aligned}\frac{\partial \Gamma_{\mathrm{H(ads)}}(r,t)}{\partial t} &= 2k_{\mathrm{a}}\left[c_{\mathrm{H_2}}(r,z=0,t)\right]\left[\frac{\Gamma_{\mathrm{M}}(r,t)}{\Gamma_{\max}}\right]^2 - 2k_{\mathrm{d}}\left[\frac{\Gamma_{\mathrm{H(ads)}}(r,t)}{\Gamma_{\max}}\right]^2 \\ &\quad - k_{\mathrm{ox}}\left[\frac{\Gamma_{\mathrm{H(ads)}}(r,t)}{\Gamma_{\max}}\right] + k_{\mathrm{red}}\left[\frac{\Gamma_{\mathrm{M}}(r,t)}{\Gamma_{\max}}\right]\left[c_{\mathrm{H^+}}(r,z=0,t)\right]\end{aligned} \quad (3.39)$$

$$j_{\mathrm{H^+}} = -D_{\mathrm{H^+}}\frac{\partial c_{\mathrm{H^+}}(r,z=0,t)}{\partial z} = k_{\mathrm{ox}}\left[\frac{\Gamma_{\mathrm{H(ads)}}(r,t)}{\Gamma_{\max}}\right] - k_{\mathrm{red}}\left[c_{\mathrm{H^+}}(r,z=0,t)\right]\left[\frac{\Gamma_{\mathrm{M}}(r,t)}{\Gamma_{\max}}\right] \quad (3.40)$$

where k_{a} (m s^{-1}), k_{d} (mol m^{2} s^{-1}), k_{ox} (mol m^{2} s^{-1}) and k_{red} (m s^{-1}) are defined as combined parameters (combined with $\Gamma_{\max}$). The rate equations used in the main text are defined in this way and all the parameters mentioned in discussion are combined with $\Gamma_{\max}$.

Alternatively, $\Gamma_{\mathrm{H(ads)/M}}$ is used, the rate equations become:

$$j_{\mathrm{H_2}} = -D_{\mathrm{H_2}}\frac{\partial c_{\mathrm{H_2}}(r,z=0,t)}{\partial z} = -k_{\mathrm{a,n}}\left[c_{\mathrm{H_2}}(r,z=0,t)\right]\left[\Gamma_{\mathrm{M}}(r,t)\right]^2 + k_{\mathrm{d,n}}\left[\Gamma_{\mathrm{H(ads)}}(r,t)\right]^2 \quad (3.41)$$

$$\begin{aligned}\frac{\partial \Gamma_{\mathrm{H(ads)}}(r,t)}{\partial t} &= 2k_{\mathrm{a,n}}\left[c_{\mathrm{H_2}}(r,z=0,t)\right]\left[\Gamma_{M}(r,t)\right]^2 - 2k_{\mathrm{d,n}}\left[\Gamma_{\mathrm{H(ads)}}(r,t)\right]^2 \\ &\quad - k_{\mathrm{ox,n}}\left[\Gamma_{\mathrm{H(ads)}}(r,t)\right] + k_{\mathrm{red,n}}\left[c_{\mathrm{H^+}}(r,z=0,t)\right]\left[\Gamma_{\mathrm{M}}(r,t)\right]\end{aligned} \quad (3.42)$$

$$j_{\mathrm{H^+}} = -D_{\mathrm{H^+}}\frac{\partial c_{\mathrm{H^+}}(r,z=0,t)}{\partial z} = k_{\mathrm{ox,n}}\left[\Gamma_{\mathrm{H(ads)}}(r,t)\right] - k_{\mathrm{red,n}}\left[c_{\mathrm{H^+}}(r,z=0,t)\right]\left[\Gamma_{\mathrm{M}}(r,t)\right] \quad (3.43)$$

where $k_{\mathrm{a,n}}$, $k_{\mathrm{d,n}}$, $k_{\mathrm{ox,n}}$, $k_{\mathrm{red,n}}$ are defined as non-combined parameters (independent of $\Gamma_{\max}$).

Table 3.2 Non-combined and combined parameters

Non-combined parameters	Combined parameters	Dimensionless non-combined parameters	Dimensionless combined parameters
$k_{\mathrm{a,n}}$ ($\mathrm{m^5\,mol^{-2}\,s^{-1}}$)	$k_{\mathrm{a}} = k_{\mathrm{a,n}}\Gamma_{\max}^2$ ($\mathrm{m\,s^{-1}}$)	$K_{\mathrm{a,n}} = \dfrac{k_{\mathrm{a,n}}\Gamma_{\max}^2 r_{\mathrm{el}}}{D_{\mathrm{H_2}}}$	$K_{\mathrm{a}} = \dfrac{k_{\mathrm{a}} r_{\mathrm{el}}}{D_{\mathrm{H_2}}}$
$k_{\mathrm{d,n}}$ ($\mathrm{m^2\,mol^{-1}\,s^{-1}}$)	$k_{\mathrm{d}} = k_{\mathrm{d,n}}\Gamma_{\max}^2$ ($\mathrm{mol\,m^{-2}\,s^{-1}}$)	$K_{\mathrm{d,n}} = \dfrac{k_{\mathrm{d,n}}\Gamma_{\max}^2 r_{\mathrm{el}}}{D_{\mathrm{H_2}} c_{\mathrm{H_2}}^*}$	$K_{\mathrm{d}} = \dfrac{k_{\mathrm{d}} r_{\mathrm{el}}}{D_{\mathrm{H_2}} c_{\mathrm{H_2}}^*}$
$k_{\mathrm{ox,n}}$ ($\mathrm{s^{-1}}$)	$k_{\mathrm{ox}} = k_{\mathrm{ox,n}}\Gamma_{\max}$ ($\mathrm{mol\,m^{-2}\,s^{-1}}$)	$K_{\mathrm{ox,n}} = \dfrac{k_{\mathrm{ox,n}}\Gamma_{\max} r_{\mathrm{el}}}{D_{\mathrm{H_2}} c_{\mathrm{H_2}}^*}$	$K_{\mathrm{ox}} = \dfrac{k_{\mathrm{ox}} r_{\mathrm{el}}}{D_{\mathrm{H_2}} c_{\mathrm{H_2}}^*}$
$k_{\mathrm{red,n}}$ ($\mathrm{m^3\,mol^{-1}\,s^{-1}}$)	$k_{\mathrm{red}} = k_{\mathrm{red,n}}\Gamma_{\max}$ ($\mathrm{m\,s^{-1}}$)	$K_{\mathrm{red,n}} = \dfrac{k_{\mathrm{red,n}}\Gamma_{\max} r_{\mathrm{el}}}{D_{\mathrm{H_2}}}$	$K_{\mathrm{red}} = \dfrac{k_{\mathrm{red}} r_{\mathrm{el}}}{D_{\mathrm{H_2}}}$
		$\gamma = \dfrac{c_{\mathrm{H_2}}^* r_{\mathrm{el}}}{\Gamma_{\max}}$	$\gamma = \dfrac{c_{\mathrm{H_2}}^* r_{\mathrm{el}}}{\Gamma_{\max}}$

The above two definitions have the same dimensionless rate equations as shown in Eqs.(3.33), (3.34) and (3.35). However the expressions for the non-combined and combined dimensionless parameters are different, as listed in Table 3.2. Among the combined parameters, only γ is related to $\Gamma_{\max}$ and γ cancels out when the true steady-state condition is achieved. But all the non-combined parameters are dependent on $\Gamma_{\max}$, which makes the steady-state voltammogram change with different $\Gamma_{\max}$. Under steady-state conditions, the combined parameters allow investigation of the voltammetric responses of the Tafel-Volmer reaction without assumptions regarding the magnitude of $\Gamma_{\max}$.

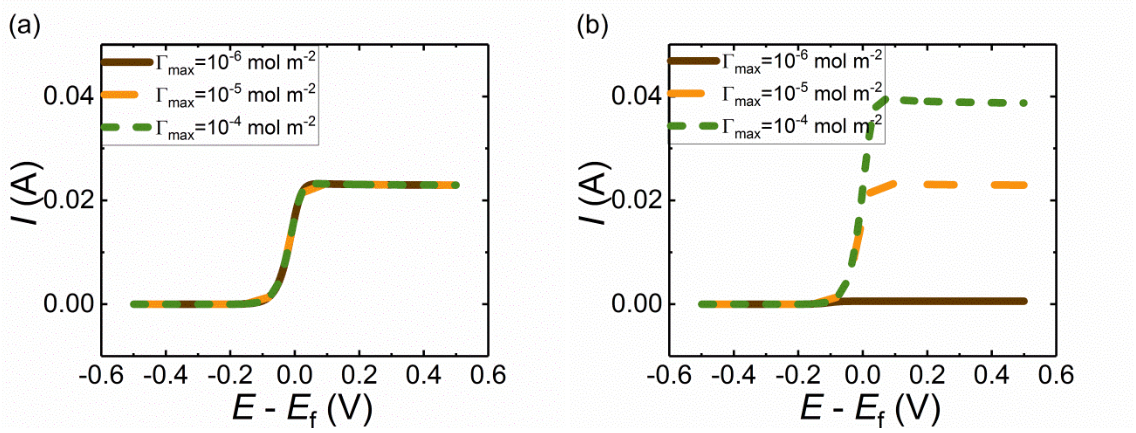

Figure 3.2 Influence of the maximum surface coverage Γ_{max} on the current-potential response at a 10 μm microdisc electrode. (a) The combined kinetic parameters (k_a = 0.001 m s^{-1}, k_d = 1 mol m^{-2} s^{-1} and k_0 = 1 m s^{-1}) are kept identical with three different Γ_{max} of 10^{-6}, 10^{-5} and 10^{-4} mol m^{-2}. The three lines overlap with each other; (b) The non-combined kinetic parameters (k_a = 0.001 m s^{-1}, k_d = 1 mol m^{-2} s^{-1} and k_0 = 1 m s^{-1}) are kept identical with different Γ_{max}. Other simulation parameters are: $c^*_{H_2}$ = 0.73 mol m^{-3}, D_{H_2} = 5*10^{-9} m^2 s^{-1}, D_{H^+} = 8.3*10^{-9} m^2 s^{-1}.

Figure 3.2 shows the difference of combined parameters and non-combined parameters. In Figure 3.2a, the combined parameters are applied and the key kinetic parameters keep constant when the maximum surface coverage varies. Due to the definition of the combined parameters, these kinetic parameters are independent of the value of Γ_{max}. Γ_{max} used in Figure 3.2a are 10^{-6}, 10^{-5}, and 10^{-4} mol m^{-2} but there is no discernible difference among the three corresponding voltammograms. In Figure 3.2b, the non-combined parameters are used, of which the values does not change with Γ_{max}. As predicted before, when the value of Γ_{max} varies from 10^{-6} to 10^{-4}, the voltammgrams show the dependence of Γ_{max} with the same second-order kinetic parameters (non-combined).

When the influence of the surface coverage is involved in the catalytic ability of the electrode/catalyst, combined parameters should be applied. However, when comparing the amount of active sites among different materials or when the maximum surface coverage of the electrode needs to be specified, non-combined parameters need to be used. The example of non-combined parameters can be found in the study of oxygen reduction reaction at the glassy carbon electrode,[16] where the surface adsorbate $O_2^{-\cdot}$ plays an important role in understanding the mechanism at high pH.

3.4 Influence of the Electron Transfer Reversibility

In the following sections, the empirical Butler-Volmer model of the electron transfer is compared with the Marcus-Hush like model in respect of their effects on the Tafel-Volmer mechanism and associated voltammetry. The steady-state voltammetric responses at microdisc electrodes of the two electron transfer models are examined under different electron transfer kinetics and adsorption behaviour.

Figure 3.3 shows the variation of the steady-state voltammograms with a series of standard dimensionless heterogeneous rate constants K_0. The electron transfer models used in Figure 3.3a and 3.3b are described by the BV and the MH formulas, respectively. The value of the adsorption equilibrium constant K_{ads} is always set to unity such that the formal potential of the electron transfer reaction $\theta_{\mathrm{f,\ H^+/H(ads)}}$ coincides with the formal potential of the whole hydrogen oxidation reaction $\theta_{\mathrm{f,\ H^+/H_2}}$ (Eq.(3.6)). Also, the adsorption and desorption rate constants K_{a}, K_{d} are considered to be so fast as not to be the limiting factor of the overall reaction. The value of K_0 varies from 10^8 to 10^{-3}, covering the transition from electrochemical reversibility to slow (“non-reversible”) electron transfer. As expected, the electrochemically reversible reactions (i.e. $K_0 = 10^8$ and $K_0 = 10^3$), the voltammograms obtained with the two kinetic models coincide because they both follow the Nernst equation that along with the diffusive mass transport define the voltammograms. On the other hand, important differences between the BV and MH models are found for electrochemically non-reversible processes. Thus, under the same diffusion conditions, slow electrode kinetics affects the steady-state voltammogram by increasing the overpotential required to drive the current. Also, a decrease of the limiting current is predicted by the MH formalism.

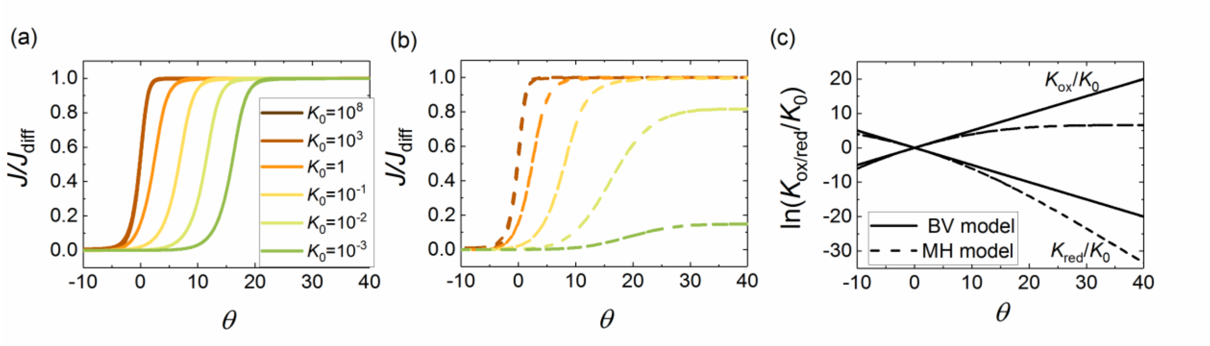

Figure 3.3 Effects of the dimensionless standard heterogeneous rate constants K_0 on the voltammmograms obtained with: (a) The Butler-Volmer model; (b) The Marcus-Hush model; (c) The comparison of the electron transfer constants between the two kinetic models. The dimensionless current is normalized by the diffusion limited current J_{diff}. Simulation parameters for the adsorption step are: $K_a = K_d = 10^8$. In the BV model, $\alpha = \beta = 0.5$; in the MH model, $\lambda^* = 20$. θ is the dimensionless overpotential for the overall reaction.

In the BV model (Figure 3.3a), for the reaction with small K_0 values, the voltammograms shift to higher overpotentials while the limiting current is the same as the reversible value, which is the diffusion limited current J_{diff}. This is because the electrooxidation rate $K_{\text{ox}}^{\text{BV}}$ increases ad infinitum with overpotential (Figure 3.3c). Therefore by increasing the overpotential, it is always possible to achieve electron transfer kinetics that is not rate limiting and only a potential shift is observed in the voltammograms. Compared with the BV voltammograms in Figure 3.3a, the decrease of K_0 in the MH model in Figure 3.3b leads to much more apparent changes. The overall reaction rates under the MH model are obviously slower than those under the BV models as shown in Figure 3.3c, reflected both in the decline of the limiting current and the increase of the overpotential. This can be explained as a consequence of a limiting electron transfer rate constant at high overpotentials predicted by the MH model. As shown in Figure 3.3c, these two models predict similar electron transfer rate constants only at the overpotentials near $\theta_{\text{f, H}^+/\text{H(ads)}}$, which is equal to $\theta_{\text{f, H}^+/\text{H}_2}$ in this case. $K_{\text{ox/red}}^{\text{BV}}$ varies exponentially with the overpotential while $K_{\text{ox/red}}^{\text{MH}}$ tends to reach a limiting value at high overpotentials, which kinetically controls the maximum rate of the whole reaction. This trend for the Tafel-Volmer type of reaction is consistent with that reported for a simple one-electron-transfer reaction.[9, 17]

In the MH kinetics, the parameter λ^* plays a key role as well. Figure 3.4 shows the voltammetric responses of a Tafel-Volmer reaction for different λ^* values. As shown in Figure 3.4a, the decrease of λ^* leads to the decline in the limiting current. Figure 3.4b provides details about the electron transfer rates varying with different λ^*. It is found that the maximum rate constant for the electron transfer step falls with decreasing λ^*, which explains the voltammograms in Figure 3.4a.

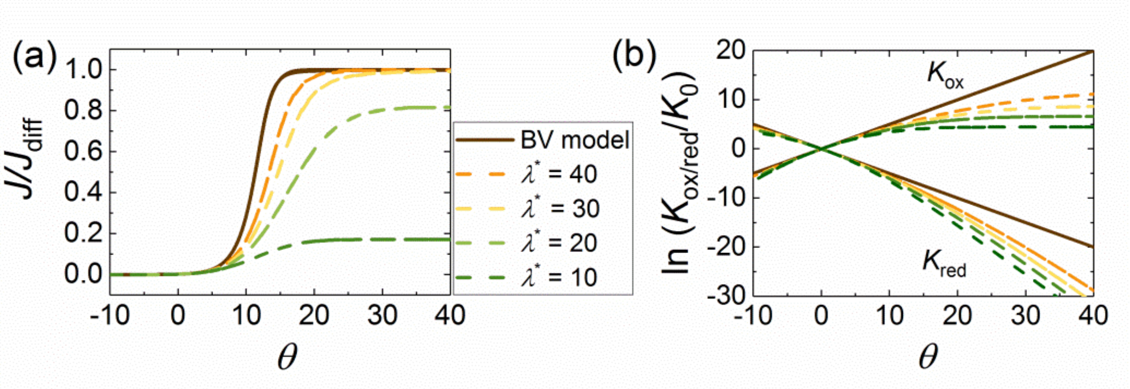

Figure 3.4 Effects of the "reorganization energy" λ^* on: a) Steady-state voltammograms; b) Oxidative and reductive electron transfer rates. Dashed lines correspond to results obtained from the MH model and solid lines are from the BV model. $K_0 = 10^{-2}$ and $K_a = K_d = 10^8$. θ is the dimensionless overpotential for the overall reaction.

3.5 Influence of Adsorption on Reversible Electron Transfer

In this section, the influence of adsorption is studied under reversible electron transfer conditions ($K_0 \gg 1$). K_{ads} is not constrained to being unity. K_a and K_d change over a large range. When the electron transfer step is fast (reversible, $K_0 \gg 1$), the surface concentrations of the reactive species should follow the Nernst equation and hence the BV and MH formulas lead to identical voltammetric responses. The main features of a steady-state voltammogram (that is, the limiting current J_{lim} and the half-wave overpotential $\theta_{1/2}$) are controlled by either the diffusion or the adsorption/desorption rates.[1, 2, 13, 18] Figure 3.5 shows the voltammograms of an electrochemically reversible Tafel-Volmer reaction for different adsorption or desorption rate constants. In Figure 3.5a, the decrease of K_d shifts the wave to higher overpotentials. When K_a varies from 10^3 (shown by the solid lines) to 10^7 (shown by the open circles), changes in K_a (and so K_{ads}) have no influence on the position of the voltammograms. The potential shift is attributed only to the decreasing of K_d. Similarly, in Figure 3.5b, for K_d equal to 10^7 (solid lines) and 10^{-1} (open circles), the normalized limiting current is only dependent on the value of K_a.

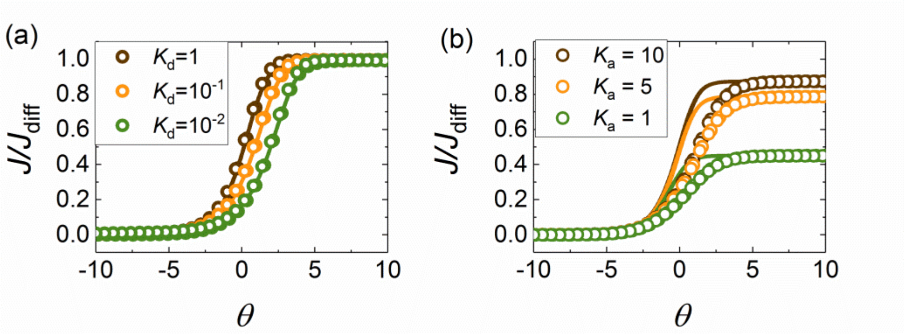

Figure 3.5 Voltammograms of the electrochemically reversible HOR under different adsorption conditions. (a) Half-wave potential shift with decreasing K_d (solid lines: K_a = 10^3, open circles: K_a = 10^7); (b) Normalized limiting current decline with decreasing K_a (solid lines: K_d = 10^7, open circles: K_d = 10^{-1}). K_0 = 10^8. θ is the dimensionless overpotential for the overall reaction.

Figure 3.6 provides a general view on the change of the normalized limiting current J_{lim}/J_{diff} and the half-wave overpotential $\theta_{1/2}$ under various adsorption/desorption rate constants. From Figures 3.5, 3.6, it is found that for the electrochemically reversible Tafel-Volmer reaction, the normalized limiting current J_{lim}/J_{diff} is only dependent on the value of K_a. Figure 3.6b shows the half-wave overpotential varying with different K_a and K_d. In general, based on the thermodynamic arguments, the half-wave overpotential should not be smaller than the reversible value. However, considering that small adsorption rate constants can cause a decrease in the limiting current, this leads to an artificial shift of the half-wave potential. Except for this interference from slow adsorption rate constants, the half-wave potential is mainly determined by the value of K_d rather than K_{ads}, indicating that changing the thermodynamics of the preceding adsorption step will not cause any significant differences on the voltammogram for an electrochemically reversible Tafel-Volmer reaction.

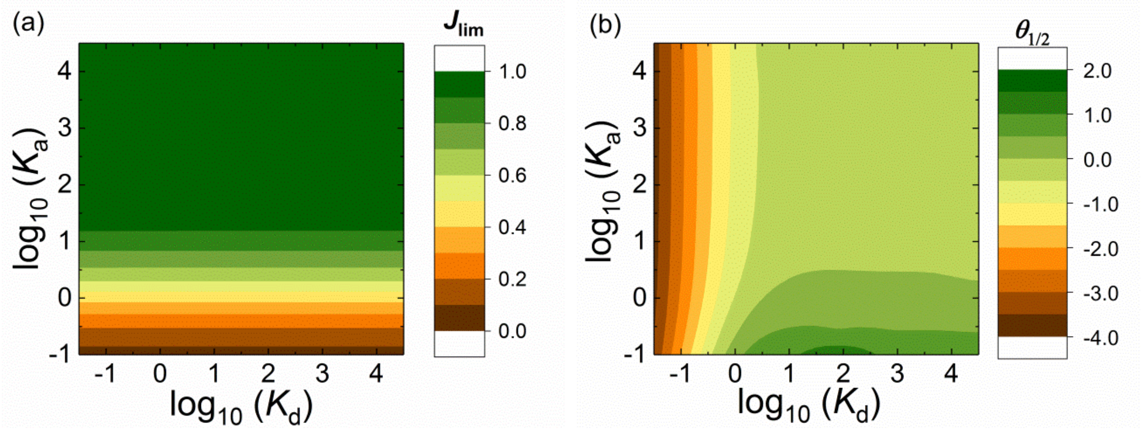

Figure 3.6 Voltammetric features, (a) The normalized limiting current; (b) The half-wave overpotential, under different adsorption conditions for reversible electron transfer. The heterogeneous standard rate constant $K_0 = 10^8$. θ is the dimensionless overpotential for the overall reaction.

3.6 Influence of Adsorption on Non-Reversible Electron Transfer

For the electrochemically non-reversible case (small K_0), apart from the effects from slow adsorption/desorption kinetics (K_a, K_d), the whole reaction is expected to be sensitive to the adsorption thermodynamics (K_{ads}) as well. Although the formal potential of the electron transfer step $\theta_{f,\ H^+/H(ads)}$ is always dependent on K_{ads}, only when K_0 is small, is the change of formal potential (and hence the overpotential) expected to have an apparent influence on the overall reaction rate.

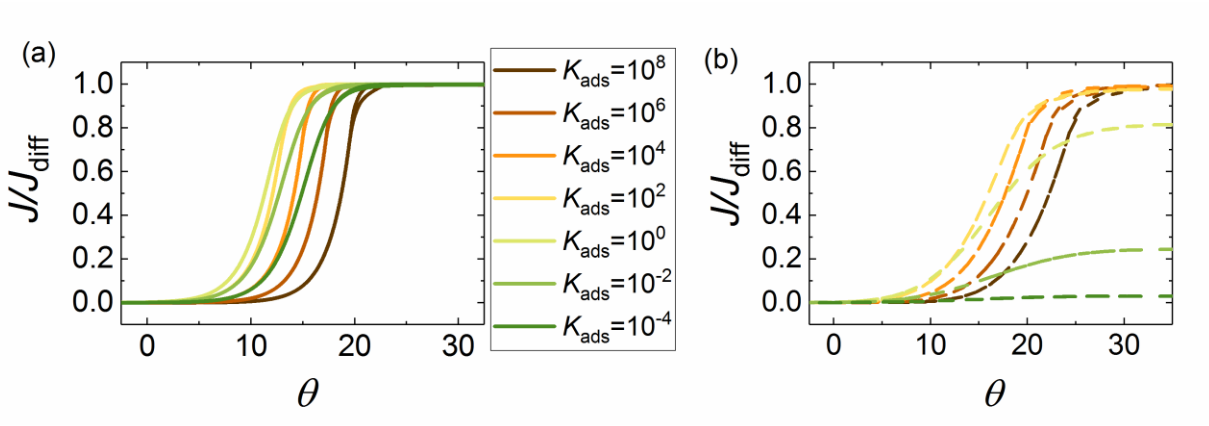

Figure 3.7 Voltammograms of electrochemically non-reversible Tafel-Volmer reaction with different adsorption conditions. (a) Butler-Volmer electron transfer model (K_0 = 10^{-2} and α = β = 0.5); (b) Marcus-Hush electron transfer model (K_0 = 10^{-2} and λ^*= 20). The parameters of the adsorption step used in the simulation are listed in Table 3.3.

Table 3.3 Adsorption/desorption rate constants used in Figure 3.7

K_{ads}	K_a	K_d
10^8	10^8	10^0
10^6	10^8	10^2
10^4	10^8	10^4
10^2	10^8	10^6
10^0	10^8	10^8
10^{-2}	10^8	10^{10}
10^{-4}	10^8	10^{12}

Figure 3.7 shows the effects of the adsorption thermodynamics (K_{ads}) on the voltammograms simulated in the BV model (Figure 3.7a) and the MH model (Figure 3.7b). In order to distinguish this case from the electrochemically reversible reactions discussed above, the standard heterogeneous constant K_0 is selected as 10^{-2} and λ^* used in the MH model is 20. As shown in Figure 3.7a, in the BV model, the normalized limiting current is always unity (diffusion controlled) but the overpotential changes with K_{ads}.

Both strong (large K_{ads}) and weak (small K_{ads}) chemical adsorptions make the overpotential shift positively. In the MH model, strong adsorption leads to a similar overpotential shift while weak adsorption significantly decreases the limiting current, which is visibly different from that predicted by the BV model (Figure 3.7a). Here to avoid any additional effect from slow adsorption/desorption, the values of the applied K_{a} and K_{d} for Figure 3.7 are relatively fast, as listed in Table 3.3. Compared with Figure 3.6, it is found that these K_{a}, K_{d} applied in Figure 3.7 should not lead to any extra potential shift. Therefore, the changes of the waveshape in Figure 3.7 are only attributed to the value of K_{ads}.

Figure 3.8 provides a general view on the effect of the Tafel step under electrochemically non-reversible conditions, covering the adsorption and desorption rate constants from 10^{-2} to 10^{8}. The results are calculated from the BV model ($K_0 = 10^{-2}$ and $\alpha = \beta = 0.5$) and the MH model ($K_0 = 10^{-2}$ and $\lambda^* = 20$). Unlike in Figure 3.7, the additional effect of slow adsorption and desorption is also taken into consideration in Figure 3.8 where the variation of the normalized limiting current $J_{\mathrm{lim}}/J_{\mathrm{diff}}$ and the overpotential corresponding to $0.01J_{\mathrm{diff}}$ ($\theta_{0.01J_{\mathrm{diff}}}$) are studied as the characteristic magnitudes of the voltammetric responses. The reason for using $\theta_{0.01J_{\mathrm{diff}}}$ rather than $\theta_{1/2}$ in Figure 3.8 (and also Figure 3.9) is that when the adsorption *thermodynamics* effect (K_{ads}) on the electron transfer kinetics is explored, the comparison of the overpotential at the same current corresponding to the foot of the wave can clearly reveal the change of the formal potential of the electron transfer step, without the interference of the adsorption/desorption *kinetics* discussed in section 3.3.2. On the other hand, in Figure 3.6 (and Figure 3.10 as well), the kinetics of the adsorption step (K_{a}, K_{d}) is explored and its effect on the whole voltammogram, such that the half-wave overpotential is chosen as the measurement of the wave position.

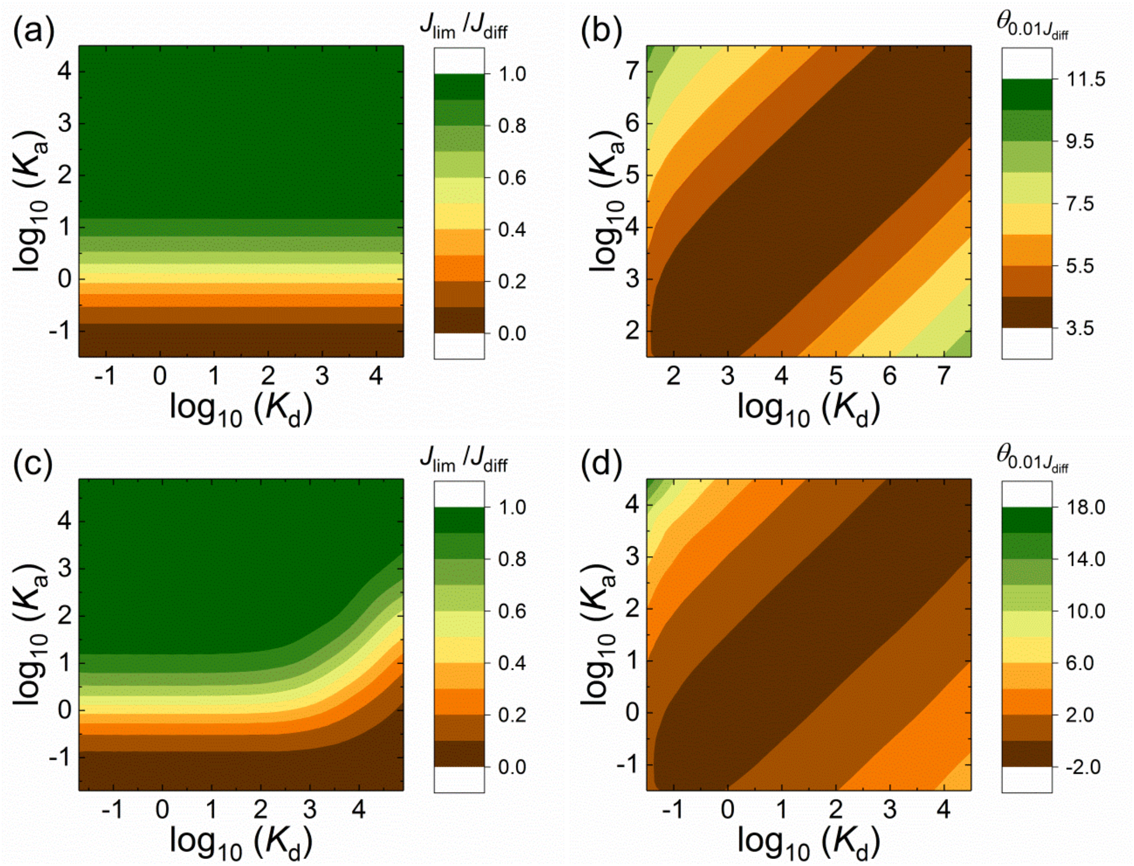

Figure 3.8 Voltammetric features under different adsorption conditions and electron transfer models for non-reversible electron transfer. (a) Normalized limiting current under the BV model; (b) The overpotential when $J = 0.01J_{\mathrm{diff}}$ under the BV model; (c) Normalized limiting current under the MH model; (d) The overpotential when $J = 0.01J_{\mathrm{diff}}$ under the MH model. For the BV model, $K_0 = 10^{-2}$ and $\alpha = \beta = 0.5$; for the MH model, $K_0 = 10^{-2}$ and $\lambda^* = 20$. θ is the dimensionless overpotential for the overall reaction.

From Figure 3.8a and 3.8b simulated in the BV model, it can be seen that the limiting current of the BV model is only related to the value of K_{a}, similarly to that observed for reversible electron transfers in Figure 3.6a. However, the overpotential shift is not solely determined by K_{d} but instead mainly dependent on the value of $K_{\mathrm{a}}/K_{\mathrm{d}}$ (K_{ads}). Figure 3.8c and 3.8d are simulated under the MH model. In contrast to the BV model, the limiting current of the MH model is determined by both K_{a} and K_{d} and higher overpotential is needed to obtain the same current in the MH model.

In both the BV and MH models, when the electron transfer step is not reversible, the value of $\theta_{0.01J_{\mathrm{diff}}}$ changes parabolically with K_{ads} (see Figure 3.8b and 3.8d), which implies that both strong and weak adsorption can impede the reaction. According to the Sabatier principle,[19] optimal electrocatalysis happens when the adsorption is neither strong nor weak. In the Tafel-Volmer mechanism, strong adsorption makes the formal potential for the electron transfer step $\theta_{\mathrm{f,\ H^+/H(ads)}}$ move positively and hence the overpotential has to increase in order to drive the electrochemical reaction. Therefore, the voltammetric wave shifts to higher potentials when the interaction between the hydrogen and the electrode is stronger. For weak adsorption, although the electron transfer reaction is more favourable thermodynamically, the voltammogram also shift to higher overpotentials as a result of the low availability of adsorbed hydrogen on the electrode surface. Moreover, compared with the BV model, in the MH model, the limiting current decreases and higher overpotential is required to obtain the same current, especially under weak adsorption conditions (small K_a/K_b). This can be explained as follows: the amount of adsorbed hydrogen becomes insufficient for the Volmer reaction and the lack of H(ads) accentuates the limitation by the electron transfer rate constants $K_{\mathrm{ox}}^{\mathrm{MH}}$. Interestingly, the BV and MH models give almost the same voltammetric responses when the adsorption is strong (large K_a/K_b), indicating that the discrepancies between the two kinetic models can be more clearly observed under weak adsorption conditions whereas strong adsorption can partially compensate the loss of the reaction rate caused by slow electron transfer rate at high overpotentials. Thus, the maximum reaction rate for a Tafel-Volmer reaction is directly linked with the electron transfer rate, given by $K_{\mathrm{ox}}\Theta_{\mathrm{H(ads)}}$ at high overpotentials. For the Tafel-Volmer reaction with a slow MH electron transfer kinetics, although K_{ox} reaches a limiting value, there are more adsorbed hydrogen atoms on the electrode surface under strong adsorption conditions rather than weak adsorption, as the initial amount of adsorbed hydrogen is determined by K_{ads} (Eqn.(3.32)).

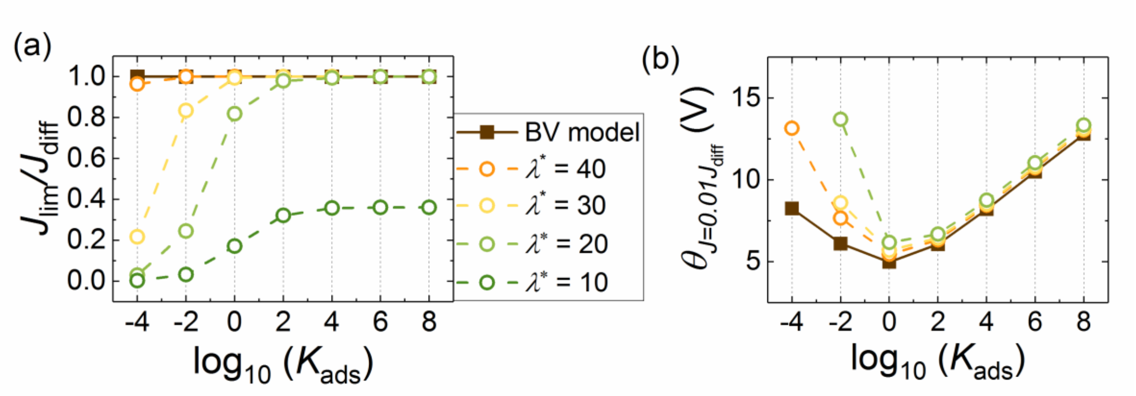

Figure 3.9 Voltammetric features of electrochemically non-reversible HOR with different adsorption conditions. (a) Normalized limiting current; (b) Overpotential where J = $0.01J_{diff}$. K_a, K_d are the same as listed in Table 3.3. θ is the dimensionless overpotential for the overall reaction.

Figure 3.9 shows the variation of the limiting current and the overpotential corresponding to $0.01J_{diff}$ with the value of K_{ads} for λ^* = 10, 20, 30, 40. In Figure 3.9a, as the applied K_a and K_d are the same as in Figure 3.7, it is clear that under any adsorption conditions, the values of the limiting current simulated from the BV model are equal to the diffusion limited current. For the MH model, as discussed in Figure 3.4, the values of the limiting currents calculated from small reorganization energies are much lower than the diffusion limited value. It is also shown in Figure 3.9a that the decrease of J_{lim} caused by non-reversible electron transfer can be partially compensated by a strong adsorption step. Here the adsorption equilibrium constant K_{ads} at which the electron transfer limitation of the MH model starts to be detectable is dependent on the reversibility of the electron transfer step. When the electron transfer becomes more irreversible (e.g. small K_0 and/or small λ^*), for the MH model, the deviation from the diffusion limited current can be observed for stronger adsorption.

3.7 Influence of Diffusion on Different Limiting Factors

In the BV model, the slow adsorption rate constant (small K_a) can determine the maximum current of the whole reaction, while in the MH model, even with fast adsorption (large K_a), the reorganization energy has similar effects as shown in Figure 3.7. Therefore, for the Tafel-Volmer type of reaction, if the limiting current of a steady-state voltammogram is less than the diffusion controlled value, it can be limited by either a slow preceding adsorption or a sluggish electron transfer step that follows a MH type kinetics. In order to examine if these two limiting factors can be experimentally distinguished, voltammograms for the two situations are simulated under different diffusion conditions. In experiments this corresponds to the use of electrodes of different sizes.

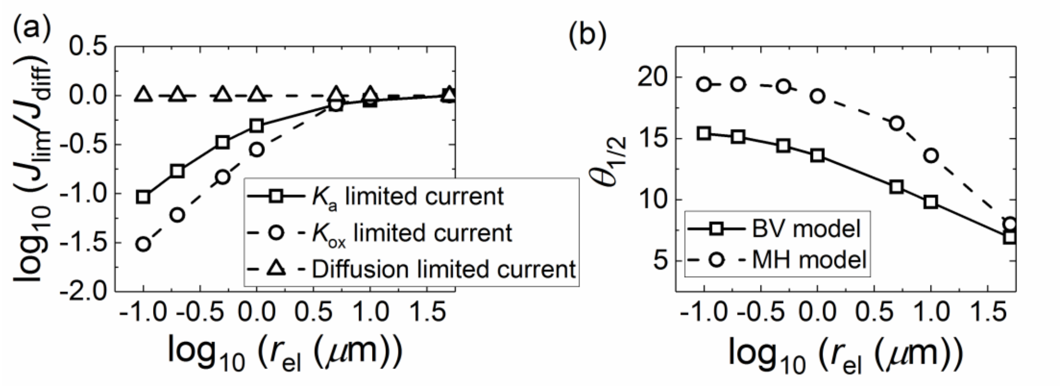

Figure 3.10 Diffusion effects of the adsorption and the electron transfer limited reactions. (a) Normalized limiting current; (b) Half-wave potential. The adsorption limited reaction is simulated in the BV model with $K_0 = 10^{-2}$, $K_a = 60$ and $K_{ads} = 1$. The electron transfer limited reaction is simulated in the MH model with K_0 = 10^{-2}, $\lambda^* = 20$, and $K_{ads} = 1$ ($K_a = K_d \gg 1$). The radii of the electrode change from 50.0 μm to 0.1 μm. θ is the dimensionless overpotential for the overall reaction.

In Figure 3.10, an adsorption limited reaction in the BV model with K_0 = 10^{-2} and K_a = 60 and an electron transfer limited reaction in the MH model with K_0 = 10^{-2} and λ^*=20 are taken as examples, the variations of J_{lim}/J_{diff} and $\theta_{1/2}$ with the radius of the electrode being explored. Note that to clearly show the results, a real dimensional radius with the unit of μm is considered. Other parameters are still dimensionless to remain consistent with other figures. At "large" microdisc electrodes (i.e., r_{el} = 50.0 μm), due to the relatively slow diffusion, the reaction rate is controlled by mass transport and the two limiting factors above mentioned have little discrepancies in the voltammetric features. With the decrease of the electrode size, diffusion becomes more efficient and the limiting factors have different behaviours: The limiting current decreases faster in the MH model (electron transfer controlled) than in the BV model (adsorption controlled) and the half-wave overpotential shifts more positively for the MH model as well. However, the general trends of their responses to the diffusion change are the same for limitations associated with both adsorption and electron transfer kinetics. The two mechanisms are unable to be distinguished as they are both slower than the diffusion process. In Figure 3.10, decreasing the electrode radius also improves the efficiency of the diffusion and thus cannot help to distinct the two models.

3.8 Example: Hydrogen Oxidation Reaction on Platinum Microdisc Electrodes

The application of the Tafel-Volmer model in understanding the kinetics of the hydrogen oxidation reaction on platinum microdisc electrodes is shown in this section. The experimental part was implemented by Miss Xue Jiao. Cyclic voltammograms for HOR at bright polycrystalline platinum electrodes with radii of 64.9 μm, 12.3 μm and 5.0 μm were measured in experiments and simulated on the basis of the Tafel-Volmer mechanism. At each electrode, three different concentrations of the hydrogen gas are applied (0.78, 0.55, 0.34 mM). As the voltammetric feature shows that the electron transfer in HOR is not the rate-determining step in the reaction, the Tafel-Volmer model in section 3.5 is applied, containing the reversible electron transfer and the reactant adsorption. A smaller steady-state current is observed in experiment as compared to that anticipated for a diffusion limited process. Under conditions of reversible electron transfer the adsorption kinetics k_a and k_d are found to have distinctly different influences upon the voltammetry responses. Correspondence between the simulated and the experimental voltammograms is found, confirming the decrease of the steady-state current is caused by the slow adsorption process.

3.8.1 Theory for Reversible Hydrogen Oxidation Reaction at Microdisc Electrodes

In this section, in accordance with the previous work of Jiao *et al.* on proton reduction,[18] an idealised current expression for the reversible hydrogen oxidation reaction is derived via the Nernst equation and Fick's first law. As the simulation is compared with the experimental results, the dimensional variables and parameters are applied in section 3.8.

The electrochemical reaction between the proton/hydrogen redox pair is:

$$\mathrm{H^+} + e^- \rightleftarrows \frac{1}{2}\mathrm{H_2} \tag{3.44}$$

The electrode potential written in terms of the formal potential of the proton/hydrogen redox pair $E^{\mathrm{o}}_{\mathrm{f,H^+/H_2}}$ is:

$$E = E^{\mathrm{o}}_{\mathrm{f,H^+/H_2}} + \frac{RT}{F}\ln\frac{c_{\mathrm{H^+}}}{c_{\mathrm{H_2}}^{\frac{1}{2}}\left(c^{\mathrm{o}}\right)^{\frac{1}{2}}} \tag{3.45}$$

where $c_{\mathrm{H^+}}$ is the proton concentration (mol dm^{-3} or M), $c_{\mathrm{H_2}}$ is the hydrogen concentration (mol dm^{-3} or M), c$^{\mathrm{o}}$ is the standard state concentration (equal to 1 M). For the experimental conditions used within this work the formal potential has a value of (-0.0991 V vs SHE)[18]. Note the predominant difference between the formal and standard potential is that the SHE is defined to be at standard conditions, in this case defined by 1 bar pressure of hydrogen, and not the standard concentration.

For the hydrogen oxidation reaction, at the electrode surface, the reaction flux of electrons *j* can be defined from the conservation of mass:

$$j = -j_{\mathrm{H^+}} = 2j_{\mathrm{H_2}} \tag{3.46}$$

where $j_{\mathrm{H_2}}$ is the flux of hydrogen gas and $j_{\mathrm{H^+}}$ is the flux of protons. (Note: the reaction flux of the electrons *j* has a unit of mol m^{-2} s^{-1}. $j = -I/(AF)$, *I* is the reaction current, *A* is the area of the electrode and *F* is the Faraday constant.)

Consequently, applying the Fick's first law to Eqn.(3.46):

$$j = -2D_{\mathrm{H_2}} \left(\frac{\partial c_{\mathrm{H_2}}}{\partial z} \right)_{z=0} \tag{3.47}$$

For a reversible hydrogen oxidation reaction, assuming that the concentration profile in the diffusion layer changes lineally, Eqn.(3.47) can be rewritten as:

$$j = 2D_{\mathrm{H_2}} \left(\frac{c^*_{\mathrm{H_2}} - c_{\mathrm{H_2}}(z=0)}{\delta_{\mathrm{H_2}}} \right) \tag{3.48}$$

where $\delta_{\mathrm{H_2}}$ is the diffusion layer thickness for *H2* in the reversible hydrogen oxidation reaction.

Similarly, the flux of the electrons can also be expressed by the flux of the protons:

$$j = D_{\mathrm{H^+}} \left(\frac{c^*_{\mathrm{H^+}} - c_{\mathrm{H^+}}(z=0)}{\delta_{\mathrm{H^+}}} \right) = -\frac{D_{\mathrm{H^+}} c_{\mathrm{H^+}}(z=0)}{\delta_{\mathrm{H^+}}} \tag{3.49}$$

where the bulk concentration of the protons $c^*_{\mathrm{H^+}}$ is regarded as 0. $\delta_{\mathrm{H^+}}$ is the diffusion layer thickness for H^+ in the reversible hydrogen oxidation reaction.

From Eqn. (3.48) and Eqn. (3.49), the surface concentrations of the hydrogen gas and the protons are:

$$c_{\mathrm{H_2}}(z=0) = c^*_{\mathrm{H_2}} + \frac{\delta_{\mathrm{H_2}}}{2D_{\mathrm{H_2}}} j \tag{3.50}$$

$$c_{\mathrm{H^+}}(z=0) = -\frac{\delta_{\mathrm{H^+}}}{D_{\mathrm{H^+}}} j \tag{3.51}$$

The Nernst equation (3.45) is used to link the electrode potential with the surface concentrations of the electroactive species ($c_{\mathrm{H_2}}(z=0)$, $c_{\mathrm{H^+}}(z=0)$):

$$\exp\left(\frac{2F}{RT} \left(E - E^{\mathrm{o}}_{\mathrm{f,H^+/H_2}} \right) \right) = \frac{\left(c_{\mathrm{H^+}}(z=0)/c^{\mathrm{o}} \right)^2}{\left(c_{\mathrm{H_2}}(z=0)/c^{\mathrm{o}} \right)} \tag{3.52}$$

Using the concentration expressions (3.50) and (3.51), the flux of electrons *j* as a function of the electrode potential *E* for reversible steady-state voltammograms can be derived as:

$$\frac{\delta_{\mathrm{H^+}}^2}{D_{\mathrm{H^+}}^2} j^2 - \exp\left(\frac{2F}{RT}\left(E - E^{\mathrm{o}}_{\mathrm{f,H^+/H_2}}\right)\right)\frac{\delta_{\mathrm{H_2}}}{2D_{\mathrm{H_2}}} j - \exp\left(\frac{2F}{RT}\left(E - E^{\mathrm{o}}_{\mathrm{f,H^+/H_2}}\right)\right) c^{\mathrm{o}} c^*_{\mathrm{H_2}} = 0 \qquad (3.53)$$

In order to get a clear understanding of the current-potential curve in steady-state voltammetry, the expression for the diffusion layer thicknesses $\delta_{\mathrm{H_2}}$ and $\delta_{\mathrm{H^+}}$ needs to be further derived.

For the steady-state voltammogram, the limiting current appears at high overpotentials, where the surface concentration of the reactant species equals zero ($c_{\mathrm{H_2}}(z=0)=0$). When the current reaches the steady-state limitation, the flux of electrons *j* becomes:

$$j_{\mathrm{lim}} = -\frac{2D_{\mathrm{H_2}} c^*_{\mathrm{H_2}}}{\delta_{\mathrm{H_2}}} \qquad (3.54)$$

The limiting current expression for the steady-state voltammogram can be derived directly from solving the diffusion equation of Fick's second law:[20]

$$j_{\mathrm{lim}} = -\frac{I_{\mathrm{lim}}}{\pi r_{\mathrm{el}}{}^2} = -\frac{8D_{\mathrm{H_2}} c^*_{\mathrm{H_2}}}{\pi r_{\mathrm{el}}} \qquad (3.55)$$

Therefore, the diffusion layer thickness of hydrogen gas on microelectrodes can be calculated from (3.54) and (3.55):

$$\delta_{\mathrm{H_2}} = \frac{\pi r_{\mathrm{el}}}{4} \qquad (3.56)$$

Similarly, for the protons, there is:

$$\delta_{\mathrm{H^+}} = \frac{\pi r_{\mathrm{el}}}{4} \qquad (3.57)$$

Therefore Eqn.(3.53) can be solved and the flux of electrons *j* is written as:

$$j = \frac{C - \sqrt{\left(C - 2j_{\mathrm{lim}}\right)^2 - 4j_{\mathrm{lim}}^2}}{2} \tag{3.58}$$

and the parameter C is:

$$C = \frac{\delta_{\mathrm{H_2}} D_{\mathrm{H^+}}^2 c^{\mathrm{o}} \exp\left(\frac{2F}{RT}\left(E - E_{\mathrm{f,H^+/H_2}}^{\mathrm{o}}\right)\right)}{2D_{\mathrm{H_2}} \delta_{\mathrm{H^+}}^2} = c^{\mathrm{o}} \left(\frac{2D_{\mathrm{H^+}}^2}{\pi r_{\mathrm{el}} D_{\mathrm{H_2}}}\right) \exp\left(\frac{2F}{RT}\left(E - E_{\mathrm{f,H^+/H_2}}^{\mathrm{o}}\right)\right) \tag{3.59}$$

From Eqn.(3.58) it is possible to analytically define the half-wave potential ($E_{1/2}$) for the oxidation. The half-wave potential is defined as the potential at which the electrochemical flux is half of its limiting value. Hence, $E_{1/2}$ can be calculated by substituting $j = 0.5j_{\mathrm{lim}}$ into Eqn.(3.58):

$$\exp\left(\frac{F\left(E_{1/2} - E_{\mathrm{f,H^+/H_2}}^{\mathrm{o}}\right)}{RT}\right) = \left(\frac{2c_{\mathrm{H_2}}^*}{c^{\mathrm{o}}}\right)^{\frac{1}{2}} \frac{D_{\mathrm{H_2}}}{D_{\mathrm{H^+}}} \tag{3.60}$$

Consequently, use of Eqn.(3.60) theoretically predicts the half-wave potential for hydrogen oxidation within this work to occur at -0.194 V vs SHE. It is worth considering that this potential is significantly different from the formal potential (-0.0991 V vs SHE). This discrepancy arises due to the non-unity stoichiometry of the reaction, as well as the contributions of non-unity $c_{\mathrm{H_2}}^*$, $D_{\mathrm{H_2}}$ (5.0×10^{-9} m^2 s^{-1}) and $D_{\mathrm{H^+}}$ (8.1×10^{-9} m^2 s^{-1}) used in this work.[18, 21] The half-wave potential varies as a function of the hydrogen concentration. This is in contrast to the case for reactions of unity stoichiometry where the half-wave and formal potentials are found to be regularly comparable and only differ by an amount which depends upon the diffusion coefficients of the electroactive species. Moreover, if the electron transfer is not reversible, the half-wave potential will deviate from the reversible value given by Eqn.(3.60). Therefore, by comparing the experimental half-wave potential with the reversible $E_{1/2}$, the reversibility of the electron transfer of such reaction is found.

3.8.2 Adsorption Limited Current

In contrast to the reversible HOR, if the electron transfer is reversible but the whole reaction is limited by the slow adsorption of the reactant hydrogen, the limiting current at the steady state will deviate from the theoretical diffusion limited value as indicated in Eqn.(3.55).

At the steady state of HOR, as the electron transfer step is much faster than the adsorption step, the adsorbate H(ads) can be quickly consumed and thus the surface coverage of H(ads) can be treated as zero. Therefore, Eqn.(3.8) can be rewritten as:

$$j_{\mathrm{H_2}} = -k_{\mathrm{a}} c_{\mathrm{H_2}}(z=0) \tag{3.61}$$

Combined with the linear concentration profile assumption as applied in Eqn.(3.48), the hydrogen adsorption rate at the electrode surface can be expressed as:

$$D_{\mathrm{H_2}} \frac{c^*_{\mathrm{H_2}} - c_{\mathrm{H_2}}\left(z=0\right)}{\delta_{\mathrm{H_2}}} = 2k_{\mathrm{a}} c_{\mathrm{H_2}}\left(z=0\right) \tag{3.62}$$

The surface concentration of hydrogen under the adsorption limitation is calculated:

$$c_{\mathrm{H_2}}\left(z=0\right) = \frac{c^*_{\mathrm{H_2}}}{1+\dfrac{\pi r_{\mathrm{el}} k_{\mathrm{a}}}{4D_{\mathrm{H_2}}}} \tag{3.63}$$

By substitution in Eqn.(3.61), one obtains the steady state limiting current:

$$\frac{j_{\mathrm{lim}}}{j_{\mathrm{diff}}} = \frac{-j_{\mathrm{H_2}}}{j_{\mathrm{diff}}} = \frac{\dfrac{\pi r_{\mathrm{el}} k_{\mathrm{a}}}{4D_{\mathrm{H_2}}}}{1+\dfrac{\pi r_{\mathrm{el}} k_{\mathrm{a}}}{4D_{\mathrm{H_2}}}} \tag{3.64}$$

3.8.3 Cyclic Voltammetry of Hydrogen Oxidation Reaction at Platinum Electrodes

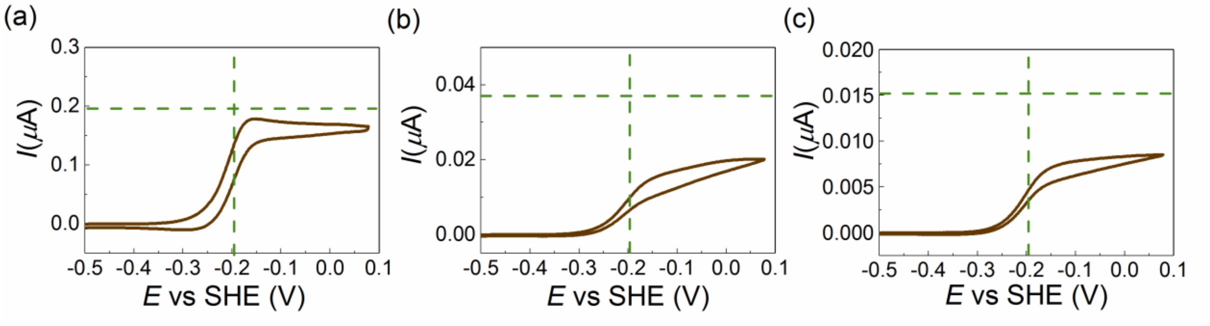

Figure 3.11 Diffusion limited currents and experimental steady-state voltammograms of the hydrogen oxidation reaction. $c^*_{H_2}$ and $c^*_{H^+}$ are 0.78 mM and 0 mM. D_{H_2} is 5.0×10^{-9} m^2 s^{-1}, D_{H^+} is 8.1×10^{-9} m^2 s^{-1}, T is 298.2 K and v is 25 mV s^{-1}. The solid lines are the experimental voltammograms. The parallel dashed lines are the diffusion limited currents calculated from Eqn.(3.55), which are 0.195 μA, 0.370 μA and 0.0151 μA for (a), (b) and (c), respectively. The vertical dashed lines are the theoretical half-wave potentials calculated from Eqn.(3.60), which are -0.194 V vs SHE for all of the three voltammograms. (a) r_{el} is 64.9 μm. (b) r_{el} is 12.3 μm. (c) r_{el} is 5.0 μm.

Figure 3.11 shows the diffusion limited currents calculated from Eqn.(3.55), the theoretical half-wave potentials calculated from Eqn.(3.60) and the voltammograms measured from experiment for the three microelectrodes of different radii (64.9, 12.3, and 5.0 μm). Importantly, for each microelectrode, the half-wave potentials in Figure 3.11 do not deviate significantly from the theoretical value, indicating that the electron transfer process for the hydrogen oxidation reaction can be regarded as fast and nearly reversible. Moreover the position of half-wave potential also indicates that the combined desorption rate constant k_d used in simulation should not be less than the value used in simulating the reversible reaction as in Figure 3.6 b. Conversely in light of the simulated results, a slow adsorption process can lead to a decrease of the limiting current as shown in Figure 3.6 a. Therefore, within the framework of the Tafel-Volmer reaction under an electrochemically reversible reaction, the decreased limiting current observed in experiments is consistent with a slow hydrogen adsorption process (a rate determining k_a).

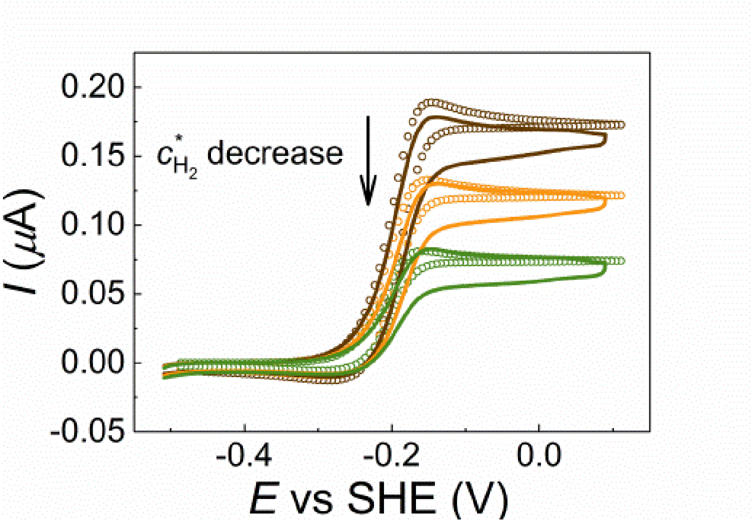

Figure 3.12 Experimental voltammograms (solid lines) and simulated voltammograms (open circles) for hydrogen oxidation reaction. The bulk concentrations of the hydrogen gas $c^*_{H_2}$ are 0.78 mM (brown), 0.55 mM (yellow) and 0.34 mM (green). In the experiment, $c^*_{H^+}$ is 0 mM, D_{H_2} is 5.0×10^{-9} m^2 s^{-1}, D_{H^+} is 8.1×10^{-9} m^2 s^{-1}, r_{el} is 64.9 μm, T is 298.2 K and v is 25 mV s^{-1}. In the simulation, the same parameters are used together with k_a is 5.0×10^{-4} m s^{-1}, k_d is 10^3 mol m^{-2} s^{-1}, k_{ox} is 1×10^3 mol m^{-2} s^{-1}, k_{red} is 1×10^3 m s^{-1}.

Figure 3.12 shows the measured experimental voltammograms (solid lines) and simulated voltammograms (open circles) for the 64.9 μm microelectrode at the three hydrogen concentrations. For each concentration, the simulated voltammogram fits well with the experimental result, indicating that the Tafel-Volmer mechanism under the electrochemically reversible limit is able to describe the hydrogen oxidation reaction at bright polycrystalline Pt microelectrodes. Here it needs to be noticed that although the conclusions from the last section are also valid in this section, the steady-state voltammograms here deviate slightly from the idealized steady states. In the simulation voltammogram, the hysteresis between forward and backward scans is caused by the effect of the relatively large electrode radii and scan rate, which lead to a change in the diffusion efficiency. As for the experiment voltammograms, this difference is caused by both the diffusion change and the capacitance current effect. For the forward scans, the capacitance effect is minimized by subtracting the background signal. However, for the backward scan, it is difficult to reduce such capacitance effect (or any other unknown effect as discussed later in this paper). Therefore, there is greater hysteresis between forward and backward scans in the experimental voltammograms than that in the simulation results.

Table 3.4 Comparison of the diffusion limited current I_{diff} and the experimental limiting current $I_{lim,exp}$. I_{diff} and $I_{lim,exp}$ are obtained from Figure 3.7.

r_{el} /μm	I_{diff} /μA	$I_{lim,exp}$ /μA
5	0.0151	0.00814±0.0006
12.3	0.0370	0.0182±0.002
64.9	0.195	0.171±0.007

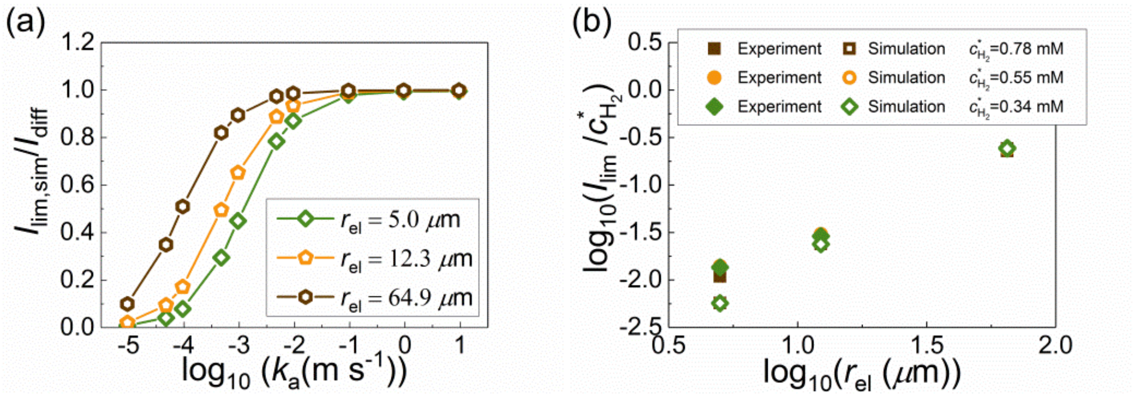

Figure 3.13 (a) The variation of the normalized steady-state currents with the combined adsorption rate constants. k_a changes from 10 m s^{-1} to 10^{-5} m s^{-1}. Other simulation conditions are the same as used in Figure 3.8. $I_{lim,sim}$ is the adsorption limited steady-state current and I_{diff} is the diffusion limited steady-state current. (b) The variation of experimental and simulated limiting currents (I_{lim}) with the hydrogen concentration ($c^*_{H_2}$ = 0.78, 0.55, 0.34 mM) and the electrode radius (r_{el} = 64.9, 12.3, 5.0 μm).

Table 3.4 shows the comparison between the diffusion limited currents and the experimental limiting currents $I_{lim,exp}$. Figure 3.13 shows the change of the simulated adsorption limited steady-state current $I_{lim,sim}$, which is then normalized by the diffusion limited current I_{diff}, as a function of k_a for these three differently sized electrodes. In

Figure 3.13, when k_a is small enough, the limiting current deviates from the diffusion controlled limit. From the comparison of $I_{\text{lim,exp}}$ / I_{diff} in Table 3.4 and $I_{\text{lim,sim}}$ / I_{diff} in Figure 3.13, a suitable simulated value for k_a can be found from our experimental results. Due to the uncertainty in the experiment and the simulation model, we can estimate an approximate range of k_a from 2.5×10^{-4} m s^{-1} to 2.5×10^{-3} m s^{-1} and a k_a equal to 5.0×10^{-4} m s^{-1} is selected in Figure 3.12 to make the Tafel-Volmer model better fit our experimental results.

Using the selected k_a, Figure 3.13 b shows the values of the experimental and simulated limiting currents for different hydrogen bulk concentrations ($c^*_{H_2}$ = 0.78, 0.55, 0.34 mM) and different electrode radii (r_{el} = 64.9, 12.3, 5.0 μm). For the 12.3 μm and the 64.9 μm electrode, the currents from experimental voltammograms and simulated voltammograms exhibit similar values, demonstrating that the Tafel-Volmer model is suitable for simulating the hydrogen oxidation reaction on these electrodes. However, for the smallest electrode, our simulation results deviate from the experimental ones, indicating that apart from the diffusion and the adsorption effect, the decreased electrode size and hence the enhanced mass-transport leads to further kinetic parameters influencing the voltammetry rate. The simulated limiting current is smaller than the experimental ones for the 5.0 um microelectrode, showing that the adsorption may be faster at the smallest microdisc electrode than the others. The study of HOR on platinum nanoparticles will be discussed in Chapter 6, where the similar trend is observed when comparing the kinetic parameters measured from the platinum microelectrodes and the platinum nanoparticles.

3.9 Summary

In this chapter, the effects of surface adsorption on Butler-Volmer and Marcus-Hush electron transfer theories have been explored in the context of the Tafel-Volmer mechanism. The voltammetric responses to the change of various kinetic and thermodynamic parameters (K_0, λ, K_a, K_d, K_{ads}) are examined for both BV and MH electron transfer models. When the preceding adsorption step is fast (K_a, $K_d \gg 1$), a slow electron transfer step (small K_0 and/or small λ^*) changes the voltammogram of the

Tafel-Volmer reaction consistently as it does for a simple unity-stoichiometry, one-electron-transfer reaction.

When the preceding adsorption is taken into consideration as a limiting factor of the overall reaction, different electron transfer kinetics show distinct voltammetric responses, depending on the reversibility of the electron transfer step and kinetic models used to describe the electron transfer step. For an electrochemically reversible Tafel-Volmer reaction ($K_0 \gg 1$), the limiting current can be expressed as a function of the adsorption rate constant K_a while it is independent of the thermodynamics of the adsorption step (K_{ads}).

For a non-reversible electron transfer step (relatively small K_0), if the electron transfer step is described in terms of the BV model, the limiting current is only dependent on diffusion and the value of K_a. But for the MH model, the limiting current is determined by both K_a and K_{ads}, especially under weak adsorption conditions (small K_{ads}). Therefore, when analysing the voltammograms of a Tafel-Volmer reaction with a weak preceding adsorption step, it is important to consider the kinetic description of the electron transfer in order to correctly understand the mechanism. It is also found that for non-reversible electron transfer, the overpotential changes parabolically with the adsorption equilibrium constant, indicating that both strong and weak adsorption can cause a decrease on the overall reaction rate for the Tafel-Volmer reaction.

This work has also concluded out that the non-diffusion control of the limiting current of steady-state voltammograms is consistent, not only with slow adsorption kinetics, but also with the deviation of the potential variation of the rate constants from the BV formalism. Indeed, the variation of the rate constants with the applied potential predicted by the MH model leads to non-diffusion controlled limiting currents for slow electron transfer kinetics and/or very small electrodes.

The Tafel-Volmer model of reversible electron transfer and limiting adsorption is applied in the study of HOR on platinum electrodes. The theoretical model successfully provides a method to analyse the electrode kinetics and measure the adsorption rate constant for such reactions.

References

1. A. N. Frumkin and E. A. Aikazyan, *Bulletin of the Academy of Sciences of the USSR Division of Chemical Science*, 1960, **8**, 188-197.

2. C. Lin, X. Jiao, K. Tschulik, C. Batchelor-McAuley and R. G. Compton, *The Journal of Physical Chemistry C*, 2015, **119**, 16121-16130.

3. C. Lin, C. Batchelor-McAuley, E. Laborda and R. G. Compton, *The Journal of Physical Chemistry C*, 2015, **119**, 22415-22424.

4. C. Batchelor-McAuley, E. Kätelhön, E. O. Barnes, R. G. Compton, E. Laborda and A. Molina, *ChemistryOpen*, 2015, **4**, 224-260.

5. R. A. Marcus, *The Journal of Chemical Physics*, 1965, **43**, 679-701.

6. N. S. Hush, *Journal of Electroanalytical Chemistry*, 1999, **470**, 170-195.

7. C. E. D. Chidsey, *Science*, 1991, **251**, 919-922.

8. S. Chen and Y. Liu, *Physical Chemistry Chemical Physics*, 2014, **16**, 635-652.

9. S. W. Feldberg, *Analytical Chemistry*, 2010, **82**, 5176-5183.

10. E. Laborda, M. C. Henstridge, C. Batchelor-McAuley and R. G. Compton, *Chemical Society Reviews*, 2013, **42**, 4894-4905.

11. A. J. Bard, *Journal of the American Chemical Society*, 2010, **132**, 7559-7567.

12. W. Schmickler and E. Santos, in *Interfacial Electrochemistry*, Springer Berlin Heidelberg, 2010, ch. 13, pp. 145-162.

13. K. J. Vetter and D. Otto, *Z.Elektrochem.*, 1956, **60**, 1072-1080.

14. R. A. Marcus, *Annual Review of Physical Chemistry*, 1964, **15**, 155-196.

15. R. A. Marcus, *Angewandte Chemie (International Edition in English)*, 1993, **32**, 1111-1121.

16. H. Zhang, C. Lin, L. Sepunaru, C. Batchelor-McAuley and R. G. Compton, *Journal of Electroanalytical Chemistry*, 2017, **799**, 53-60.

17. E. E. L. Tanner, L. Xiong, E. O. Barnes and R. G. Compton, *Journal of Electroanalytical Chemistry*, 2014, **727**, 59-68.

18. X. Jiao, C. Batchelor-McAuley, E. Kätelhön, J. Ellison, K. Tschulik and R. G. Compton, *The Journal of Physical Chemistry C*, 2015, **119**, 9402-9410.

19. R. Parsons, in *Catalysis in Electrochemistry*, John Wiley & Sons, Inc., 2011, DOI: 10.1002/9780470929421.ch1, pp. 1-15.

20. R. G. Compton and C. E. Banks, *Understanding Voltammetry*, Imperial College Press, 2nd edn., 2011.

21. J. V. Macpherson and P. R. Unwin, *Analytical Chemistry*, 1997, **69**, 2063-2069.

Chapter 4 Electrical Double Layer Effects on Ion Transfer Reactions

In contrast to the large-distance electron transfer assumed in the Butler-Volmer or symmetric Marcus-Hush theories, the reaction occurs over a short distance from the electrode in the electron exchange between an adsorbed species and the metallic electrode. For such "ion transfer" reactions, the interactions among the electrode, the electrolyte, the redox species become more complicated. The factors governing variation of reaction rate constant with distance need to be taken into consideration.

In this Chapter, the potential dependence of the thermodynamics and kinetics of ion transfer reactions are modelled via Gibbs energy surfaces calculated with an extension of the Anderson-Newns Hamiltonian. The electrical double layer effects on ion transfer reactions are explored. The work presented in this chapter has been published as part of two separate papers in the *Journal of Physical Chemistry Letter*[1] and the *Physical Chemistry Chemical Physics*.[2] The experiments mentioned in section 4.6 were performed by Miss Xiuting Li.

4.1 Gibbs Energy Surface

The understanding and modelling of heterogeneous inner-sphere reactions is of fundamental importance in electrocatalysis and a major challenge in electrochemistry. These processes are present in a number of systems of fundamental and practical interests such as metal underpotential deposition,[3] the hydrogen evolution reaction,[4] and the oxygen reduction reaction. The kinetics of ion-transfer reactions have been frequently described by making use of the empirical Butler-Volmer formalism as in the case of outer-sphere electron transfer processes. Previous experimental and theoretical studies show that such a phenomenological approach can provide a satisfactory parameterization of the variation of the electrochemical rate constants with the applied potential and, therefore, of the voltammetric response.[5, 6] Nevertheless, the Butler-Volmer model provides very limited physical insight into the electron transfer process and it has been shown to be unable to explain certain experimental behaviours.[7-9] Furthermore, as will be shown in this work, the limitation of the Butler-Volmer model can lead to misinterpretations of experimental data in terms of the reversibility of the charge transfer reaction.

First-principles modelling at the molecular level of the various phenomena mentioned above is far from straightforward and has been tackled in the past with different "refinement levels".[10-12] It is worth noting that the (semi-)quantum theories developed for outer-sphere reactions are not directly applicable to an ion transfer reaction given the very distinct nature of the physical phenomena.[13-15] Thus, in this work an extension of the model proposed in the literature[16] for ion transfer reactions will be applied to study the voltammetry by including the electrostatic potential distribution across the electrical double layer according to the Gouy-Chapman model. To understand the electronic coupling between the adsorbate and the metal substrate, the chemisorption of an atom on a transition-metal surface has been treated theoretically on the basis of the Anderson-Newns Hamiltonian and a Lorentzian shape density-of-states function is solved.[17-19]

The free energy surface of the system is calculated as a function of two coordinates: a single solvent coordinate q, which reflects the partial charge carried by the ion during the electron-transfer process,[20, 21] and the distance to the electrode surface in the direction perpendicular to the interface, d. The minimum energy path and the energy barrier will be studied under different conditions, identifying the main contributions to the energy barrier.

4.2 Model

The interfacial ion transfer reaction studied in this work can be given by the following chemical reactions:

$$\mathrm{X^{+}(sol)} + e^{-} \rightleftarrows \mathrm{X(ads)} \tag{4.1}$$

$$\mathrm{X(sol)} + e^{-} \rightleftarrows \mathrm{X^{-}(ads)} \tag{4.2}$$

In reaction (4.1) X^+(sol) is a charged species in the electrolyte solution, hydrated by the solvent and X(ads) is a neutral species adsorbed on the electrode surface. In reaction (4.2), the hydrated X(sol) is neutral and the adsorbate X^-(ads) carries a negative charge. Typical examples for reactions (4.1) and (4.2) are the Volmer reaction H^+/H and the first step of the oxygen reduction reaction $O_2/O_2^{-\bullet}$, respectively. The "mirror" systems of the redox species in reactions (4.1) and (4.2), which are X(ads)/X^-(sol) and X^+(ads)/X(sol) respectively, can be calculated with the same approach described below.

The Gibbs energies for the redox processes X^+(sol)/X(ads) and X(sol)/X^-(ads) are calculated in the (q,d) space: the solvent coordinate q [10] and the spatial coordinate d, which is the perpendicular distance between the centre of the redox species and the electrode surface. The value of $-q$ is related with the charge carried by the redox species upon considering that a given solvent configuration characterized by a value q will be in equilibrium with a reactant's charge of $-q$.[20, 22] Note that q can take fractional values within the model, reflecting that the valence orbital is partially filled, as a result of the Heisenberg uncertainty principle.[23, 24] Thus the solvent coordinate q varies continuously in the simulation, connected to the partial charge transferred as the ion becomes adsorbed.

The change in the free energy upon the above reactions will be modelled based on the extension of the Hamiltonian proposed in the literature[22] that can be written in three parts:

$$H = H_{\text{sol}} + H_{\text{el}} + H_{\text{int}} \tag{4.3}$$

where H_{sol} is the contribution of the solvation energy and its interaction with the ion, H_{el} the electronic energy taking into account the interaction between the metallic and reagent's levels, and H_{int} other electrostatic and non-covalent interactions. In contrast to the Hamiltonian applied in the literature,[22] the electrical double layer in the interfacial electrochemical environment is considered and the influence is introduced in the third component in Eqn.(4.3).

The solvent reorientation process coupled with the electron transfer can be described by:[10, 25]

$$H_{\mathrm{sol}} = \frac{1}{2}\sum_{v} \hbar\omega_{v}\left(p_{v}^{2}+q_{v}^{2}\right)+\left(z - n_{\mathrm{a}}\right)\sum_{v}\hbar\omega_{v}g_{v}q_{v} \tag{4.4}$$

v represents the different phonon modes and ω_v the frequency, p_v and q_v the dimensionless momenta and coordinates, z the charge of the oxidized state (z = 1 in reaction (4.1) and z = 0 in reaction (4.2)), n_a the occupation number of the reactant's valence orbital and g_v the coupling between the phonon and the redox centre. The reorganization of solvent molecules surrounding the redox species can be divided into the contributions from fast and slow solvent modes. The fast and slow modes describe different sorts of reorientation, which are related to the solvent loosely or strongly interacting with the redox species.[26] The values of λ_f and λ are equivalent in this model. As the fast reorientation process is considered to be faster than the charge transfer rate, λ_f does not explicitly appear in the Hamiltonian expression (4.4) but it is included in the expression of the reactant energy level as shown in Eqns. (4.18) and (4.19). The values of λ_f and λ are equivalent in this model, as we assume the . The reorganization energy is defined by:[27]

$$\lambda = \frac{1}{2}\sum_{v}\hbar\omega_{v}g_{v}^{2} \tag{4.5}$$

The solvent coordinate q is defined as $q = q_\mathrm{v}/g_\mathrm{v}$, representing not only the vibration modes but also the charge carried by the hydrated redox species. Assuming the ion is fully discharged, the q-value varies from -1 (corresponding to X^+(sol)) to 0 (X(ads)) for reaction (4.1) and from 0 (X(sol)) to 1 (X^-(sol)) for reaction (4.2).

The electrostatic and non-covalent interactions between the redox species and the metal electrode are included in H_int. The expressions for reactions (4.1) and (4.2) are given by Eqns. (4.6) and (4.7):[11, 28]

$$H_{\mathrm{int}} = \left(1-n_{\mathrm{a}}\right)G_{\mathrm{X^{+}(sol)\ \&\ M}} + n_{\mathrm{a}}G_{\mathrm{X(ads)\ \&\ M}} \tag{4.6}$$

$$H_{\mathrm{int}} = \left(1-n_{\mathrm{a}}\right) G_{\mathrm{X(sol)\ \&\ M}} + n_{\mathrm{a}} G_{\mathrm{X^{-}(ads)\ \&\ M}} \tag{4.7}$$

where M represents the metal electrode. $G_{\mathrm{X\ \&\ M}}$ is the Gibbs energy for the electrostatic and non-covalent interaction between the redox species and the metal electrode.

The Gouy-Chapman model[29] is applied to describe the electrostatic potential in solution as a function of the distance to the electrode surface:

$$G_{\mathrm{X^{+},EDL}}(d) = e_0 \left(E - E_{\mathrm{pzc}}\right) \exp\left(-\kappa d\right) \tag{4.8}$$

$$G_{\mathrm{X^{-},EDL}}(d) = -e_0 \left(E - E_{\mathrm{pzc}}\right) \exp\left(-\kappa d\right) \tag{4.9}$$

where κ (unit: Å^{-1}) is the Debye constant, E is the applied potential on the working electrode, E_{pzc} the potential of zero charge and e_0 is the elementary charge, approximately 1.60×10^{-19} C. The reciprocal of the Debye constant is called the Debye length κ^{-1}, which is applied as a simulation parameter that gives an estimation (not quantitatively) of the thickness of the double layer.

Morse-like potentials enable us to obtain a qualitative, simple and manageable view of the non-covalent interactions between the redox species and the metal electrode.[30, 31]. The latter is regarded to implement a force which accounts for the Morse-like potential of the adsorbates X(ads) and X^{-}(ads), and a repulsive force for the reactant species in the electrolyte solution X^{+}(sol) and X(sol) is considered:

$$G_{\mathrm{Morse}} = D_e \left\{ \left[1 - \exp\left(-a\left(d - d_0\right)\right) \right]^2 - 1 \right\} \tag{4.10}$$

$$G_{\mathrm{repulsive}} = D_e \exp\left(-a\left(d - d_0\right)\right)^2 \tag{4.11}$$

where D_{e} is the binding energy for the hypothetical X-metal bond, a is a constant with an approximate value of 1 Å^{-1} and d_0 is the equilibrium bond length.

For any charged species, the image interaction caused by the induced image charge on the electrode surface as the ion approaches the metal is also taken into account in the model:[32]

$$G_{\mathrm{X^+(sol),im}}\left(d\right) = -\frac{1}{4\pi\varepsilon_{\mathrm{s}}}\frac{e_0^2}{4d} \tag{4.12}$$

$$G_{\mathrm{X^-(ads),im}}\left(d\right) = -\frac{1}{4\pi\varepsilon_{\mathrm{s}}}\frac{e_0^2}{4d} \tag{4.13}$$

where ε_{S} is dielectric constant of the solvent. The dielectric constant varies a function of distance in the area close to the electrode surface. The effective dielectric constant is used in Eqn.(4.12) and (4.13) as suggested in the literature:[21]

$$\begin{aligned} &\varepsilon_s\left(d\right) = \left(1+3.9p\left(d\right)\right)\varepsilon_s\left(\infty\right) \\ &p\left(d\right) = \begin{cases} 0 & d/L<0 \\ \left(3-2d/L\right)\left(d/L\right)^2 & 0<d/L<1 \\ 1 & d/L>1 \end{cases} \end{aligned} \tag{4.14}$$

L is the distance where the dielectric constant is assumed to be the same as the bulk value. L is set to be 4 Å in the following simulation, taken from the case of iodide ion adsorption.

Under the one-electron approximation where a single electron on the reactant is considered, the electronic Hamiltonian H_{el} is given by:[18, 19]

$$H_{\mathrm{el}} = n_{\mathrm{a}}\varepsilon_{\mathrm{a}}^0 + \sum_{\mathrm{k}}\left(\varepsilon_{\mathrm{k}}n_{\mathrm{k}} + V_{\mathrm{ak}}c^+c\ \right) \tag{4.15}$$

where $\varepsilon_{\mathrm{a}}^0$ is the energy of the valence level on the reactant in the absence of interactions and relative to the Fermi level of the electrode (which is taken as the zero reference value). n_{a} is the electron occupancy of the bonding/antibonding orbital of the redox species. ε_{k} and n_{k} are the energy and electron occupancy of the k metallic levels, respectively. V_{ak} is the hopping integral that characterizes the strength of the interaction between the redox system and the electrode. c^+ and c are the creation and annihilation operators. The spin of the electron is ignored in Eqn. (4.15), as it is considered that there is only one electron involved in the bonding/antibonding orbital.[19, 33]

The density of states for the reactant valence level is broadened due to the interaction between the valence orbital and the metallic levels and a simple qualitative expression is given by:[17-19]

$$\rho_{\mathrm{a}}(\varepsilon)=\frac{1}{\pi}\frac{\Delta(d)}{\left(\varepsilon-\varepsilon_{\mathrm{a}}(q,d)-\Lambda\right)^2+\Delta(d)^2} \tag{4.16}$$

where Λ and Δ are the chemisorption functions: the original energy level is shifted by Λ and broadened by Δ due to the interaction with the electrons in the metal electrode. Within the wide-band approximation, Δ is independent on ε. Δ is a function of the distance to the electrode surface and it shows an approximately exponential decay.[34, 35]

$$\Delta(d)=\Delta_0\exp(-\beta d) \tag{4.17}$$

Δ_0 is the energy broadening at the electrode surface, β is a constant approximately 1 Å^{-1} and d is the position of the centre of the reactant from the electrode surface.

$\varepsilon_{\mathrm{a}}(q, d)$ corresponds to the 'effective' energy of the valence level relative to the Fermi level after considering the interactions with the solvent, the metal electrode and the electrical double layer. Thus, for reactions (4.1) and (4.2), the effective energy levels are:

$$\varepsilon_{\mathrm{a}}(q,d)=\varepsilon_{\mathrm{a}}^0+\lambda_{\mathrm{f}}q^2_{\mathrm{X^+(sol)}}-2\lambda q-G_{\mathrm{X^+(sol)\ \&\ M}}(q,d)+G_{\mathrm{X(ads)\ \&\ M}}(q,d) \tag{4.18}$$

$$\varepsilon_{\mathrm{a}}(q,d)=\varepsilon_{\mathrm{a}}^0+\lambda_{\mathrm{f}}q^2_{\mathrm{X(sol)}}-2\lambda q-G_{\mathrm{X(sol)\ \&\ M}}(q,d)+G_{\mathrm{X^-(ads)\ \&\ M}}(q,d) \tag{4.19}$$

where $q_{\mathrm{X^+(sol)}}$ and $q_{\mathrm{X(sol)}}$ are the values of the solvent coordinates for X$^+$(sol) and X(sol), which equal 1 and 0, respectively. Given that the Fermi level is taken as reference, $\varepsilon_{\mathrm{a}}^{0}$ is dependent on the applied overpotential η and the energy level at equilibrium potential $\varepsilon_{\mathrm{a,eq}}$:

$$\varepsilon_{\mathrm{a}}^{0} = \varepsilon_{\mathrm{a,eq}} + e_0\eta \tag{4.20}$$

In order to calculate the occupation probability n_{a} and the electronic energy, the distribution function of the metallic levels must be considered. Here a step distribution function is applied:

$$f(\varepsilon) = \begin{cases} 1, & \varepsilon_{\mathrm{C}} \le \varepsilon \le \varepsilon_{\mathrm{F}} \\ 0, & \varepsilon > \varepsilon_{\mathrm{F}} \end{cases} \tag{4.21}$$

where ε_{C} is the bottom of the conduction band and ε_{F} is the Fermi level. Therefore the electronic free energy expression and the electron occupancy can be calculated from:

$$G_{\mathrm{el}} = n_{\mathrm{a}}(q,d)\varepsilon_{\mathrm{a}}(q,d) + \frac{\Delta(d)}{2\pi}\ln\left(\frac{\varepsilon_{\mathrm{a}}(q,d)^2 + \Delta(d)^2}{\left(\varepsilon_{\mathrm{a}}(q,d) - \varepsilon_{\mathrm{C}}\right)^2 + \Delta(d)^2}\right) \tag{4.22}$$

$$n_a(q,d) = \frac{1}{2} + \frac{1}{\pi}\tan^{-1}\left(\frac{-\varepsilon_{\mathrm{a}}}{\Delta(d)}\right) \tag{4.23}$$

Finally, the Gibbs energy for the whole electrochemical system can be expressed as:

$$\begin{aligned} G_{\mathrm{tot}}(q,d) = {} & G_{\mathrm{sol}}(q,d) + G_{\mathrm{el}}(q,d) + \{1 - n_{\mathrm{a}}(q,d)\}G_{\mathrm{X_{red}\ \&\ M}}(q,d) \\ & + n_{\mathrm{a}}(q,d)G_{\mathrm{X_{ox}\ \&\ M}}(q,d) \end{aligned} \tag{4.24}$$

where $\mathrm{X_{red}}$ and $\mathrm{X_{ox}}$ are the reduced and oxidized species of the redox couples in the reactions (4.1) and (4.2).

Based on the Gibbs energy surfaces calculated from Eqn.(4.24), the minimum energy path and the local extreme points (stationary points) on such path are determined. The local extreme points characterize the initial, final and intermediate states.[36] For reactions (4.1) and (4.2), usually only one intermediate state is found and thus the activation energies for the reductive and oxidative processes can be calculated as:

$$\Delta G_{\mathrm{red}}^{\mathrm{act}} = G_{\mathrm{TS}} - G_{\mathrm{X_{ox}}} \tag{4.25}$$

$$\Delta G_{\mathrm{ox}}^{\mathrm{act}} = G_{\mathrm{TS}} - G_{\mathrm{X_{red}}} \tag{4.26}$$

G_{TS} is the energy of the transition state, corresponding to the saddle point on the energy surface. $G_{\mathrm{X_{red}}}$ and $G_{\mathrm{X_{ox}}}$ are local energy minima corresponding to the reduced and oxidized states, respectively.

The reaction rate constants calculated from Eqns. (4.25) and (4.26) have the following form:

$$k_{\mathrm{ox/red}} = k_0 \exp\left(-\frac{\Delta G_{\mathrm{ox/red}}^{\mathrm{act}}}{k_{\mathrm{B}} T} \right) \tag{4.27}$$

where k_0 is the standard heterogeneous rate constant, which is considered as a constant for a given temperature. k_{B} is the Boltzmann constant and T is the absolute temperature. The equilibrium potential E_{eq} is defined as the potential where the reaction rates of the reduction and oxidation processes are equal. Thus, the activation energies under different overpotential $E - E_{\mathrm{eq}}$ are defined as:

$$\Delta G_{\mathrm{ox/red}}^{\mathrm{act}} \left(E - E_{\mathrm{eq}} \right) = \Delta G_{\mathrm{ox/red}}^{\mathrm{act}} \left(E \right) - \Delta G_{\mathrm{ox/red}}^{\mathrm{act}} \left(E_{\mathrm{eq}} \right) \tag{4.28}$$

The reaction rates of (4.1) and (4.2) for the redox species in the solution and the adsorbates on the electrode surface can be expressed by:

$$j_{\mathrm{X_{red}}} = -k_{\mathrm{red}} c_{\mathrm{X_{red}}} \left(1 - \Gamma_{\mathrm{X_{ox}}} \right) + k_{\mathrm{ox}} \Gamma_{\mathrm{X_{ox}}} \tag{4.29}$$

$$\frac{\partial \Gamma_{X_{ox}}}{\partial t} = k_{red} c_{X_{red}} \left(1 - \Gamma_{X_{ox}}\right) - k_{ox} \Gamma_{X_{ox}} \tag{4.30}$$

where t is the time upon which the perturbation is applied. Γ represents the surface coverage with only a monolayer adsorption being considered on the electrode surface.

For the species moving freely in the electrolyte solution, the mass transport is described by Fick's second law for linear diffusion:

$$\frac{\partial c}{\partial t} = D \frac{\partial^2 c}{\partial z^2} \tag{4.31}$$

with z being the coordinate perpendicular to the electrode surface.

4.3 Characteristic Free Energy Surfaces for X^+(sol)/X(ads) and X(sol)/X^-(ads)

Figure 4.1 shows a typical Gibbs energy surface (Figure 4.1a) and the change in the electron occupancy (Figure 4.1b) for the reduction of the charged species X^+ from solution (reaction (4.1)), together with the changes in the Gibbs energy and in the occupation probability of the reactant's orbital as the reactant approaches the electrode surface along the minimum energy path. The latter shows a minimum in the 'ionic channel' and it reaches the adsorption site along the path plotted by the white dashed lines in Figure 4.1a and 4.1b. Before the charged reactant X^+(sol) (corresponding to q = −1) is electrodeposited to the adsorbate state X(ads) (corresponding to the minimum on the energy surface closer to the electrode surface), the ion can experience a weak adsorption on the way to the electrode surface due to the attractive forces of electrostatic and covalent (electronic) character. Thus, a stable intermediate can be found in Figures 4.1a and 4.1c, symbolized by X^+(surf). The energy well corresponding to the weak adsorption site of the solvated ion X^+(surf) precedes the charge transfer: q = −1 for X^+(surf). As the reaction proceeds, variations in both the q and d dimensions are observed, indicating that the reaction is governed by both the approach of the ion towards the surface and by the reorganization of the solvent. In the region where the charge transfer takes place (*i.e.*, where most of the change in the electron occupancy n_a occurs along the minimum energy path), the Gibbs energy reaches a stationary point that is regarded as the transition state (TS).

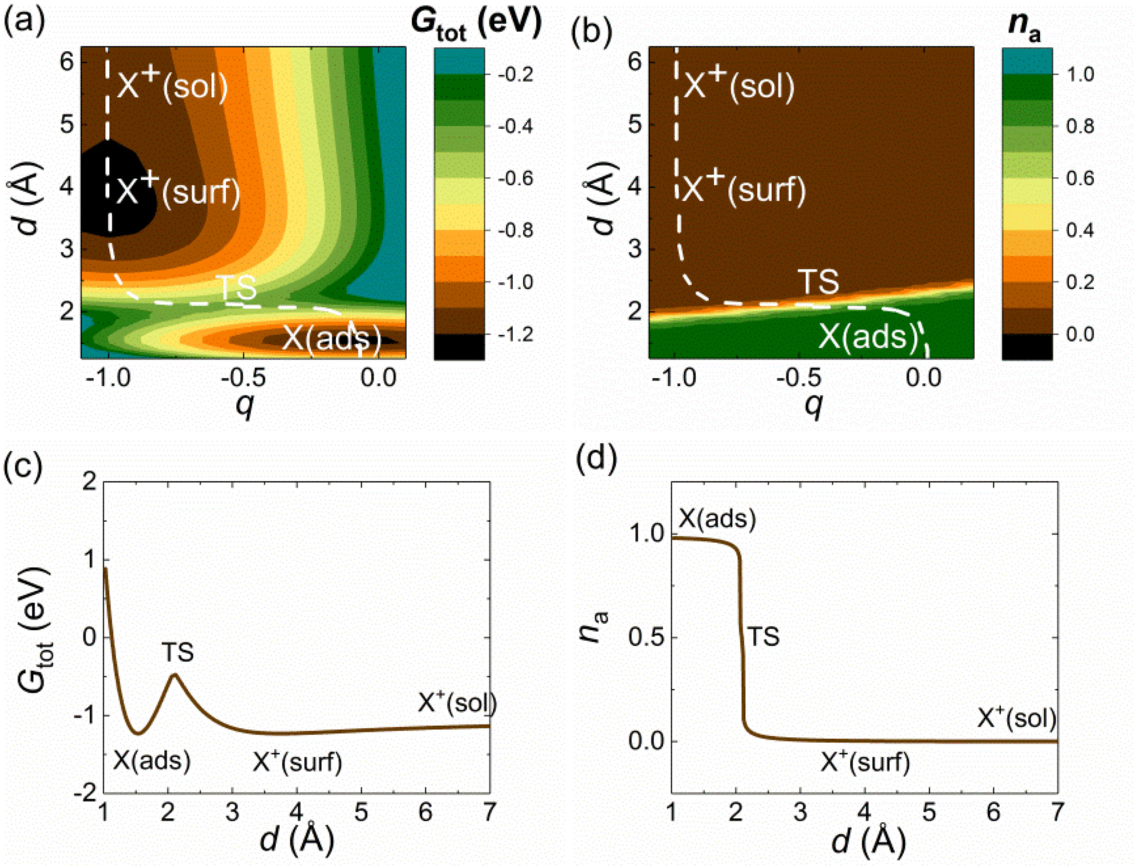

Figure 4.1 Example of the Gibbs energy surface for reaction (4.1): a) Gibbs energy surface, b) electron occupancy, c) Gibbs energy and d) occupation probability of the reactant orbital as the reactant approaches the electrode surface along the minimum energy path. $E = E_{eq}$, $\kappa^{-1} = 10.0$ Å, $E_{pzc} = 0.2$ V, $D_e = 5$ eV, $d_0 = 1.5$ Å, $\Delta_0 = 2.0$ eV, $\lambda = 1.0$ eV.

Figure 4.1d shows the change in the electron occupancy of the reactant's orbital with the distance to the electrode along the minimum energy path. As the ion approaches the metal surface, the electron occupancy in its bonding orbital is increased and the effective charge it carries is reduced. This takes place mainly in the region around the transition state where the occupation number varies from 0 (corresponding to the ion X^+) to a final value close to 1. It can be inferred from this figure that the charge transfer occurs between the state X^+(surf) and the adsorbate X(ads). Hence, the transfer process from the ion in solution to the adsorbed species can be described by the following two steps:

$$\mathrm{X^+(sol)} \rightleftharpoons \mathrm{X^+(surf)} \tag{4.32}$$

$$\mathrm{X^+(surf)} + \mathrm{e^-} + \mathrm{M} \rightleftharpoons \mathrm{X(ads)} \tag{4.33}$$

When the repulsive forces dominate (for instance, when the applied potential is much more positive than the potential of zero charge), the weak adsorption well can vanish (not shown) and step (4.33) will not be operative. Both conditions where the preceding adsorption takes place or not will be discussed below. In the preceding adsorption case, reaction (4.1) follows the above two-step mechanism. If there is no preceding adsorption, the electron transfer directly occurs between X^+(sol) and X(ads).

Figure 4.2 shows a typical Gibbs energy surface for the reduction of the neutral species X(sol) from the solution (reaction (4.2)). In contrast with X^+(sol)/X(ads) in reaction (4.1), there is no preceding adsorption on the reaction path when X(sol) moves close to the electrode surface under the simulation conditions considered. The electron transfer occurs near the transition state (TS), where both the electron occupancy of the antibonding orbital and the absolute value of the charge carried by the redox species vary from 0 to 1.

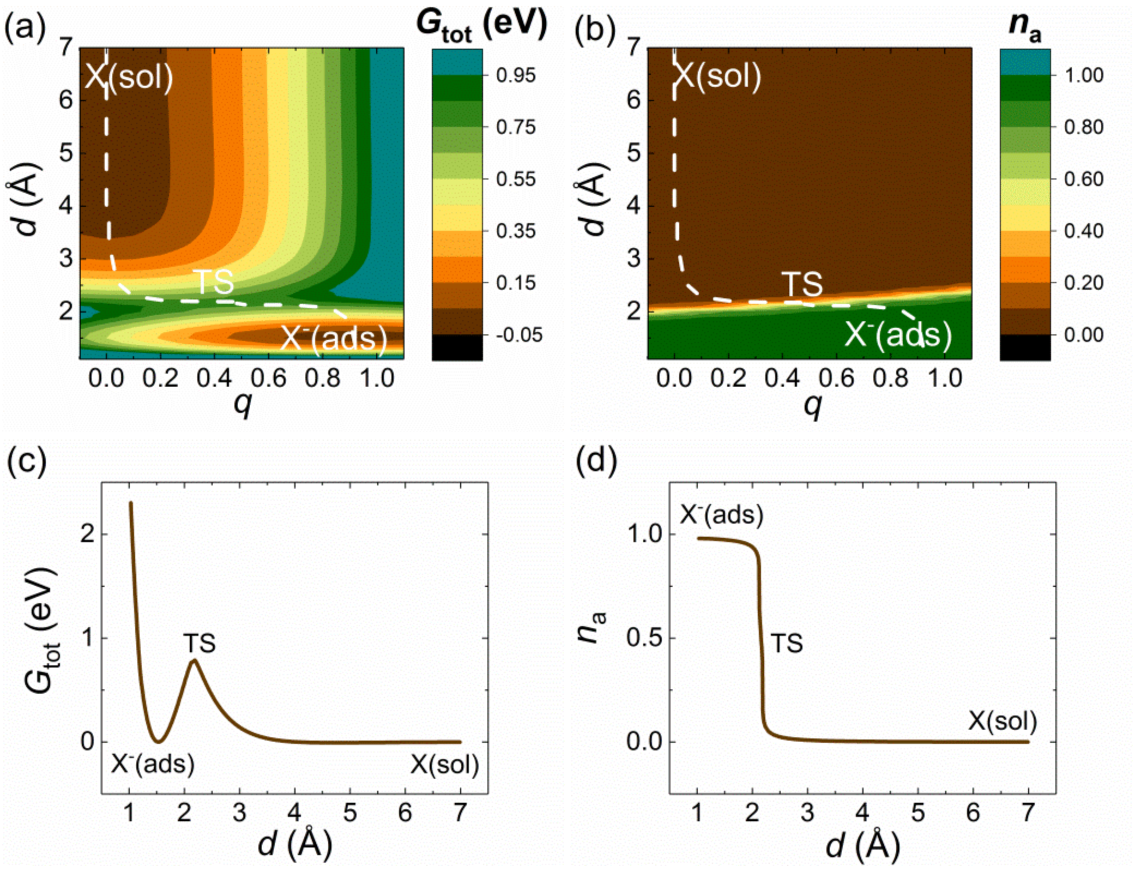

Figure 4.2 Example of the Gibbs energy surface for reaction (4.2): a) Gibbs energy surface, b) electron occupancy, c) Gibbs energy and d) occupation probability of the reactant orbital as the reactant approaches the electrode surface along the minimum energy path. $E = E_{eq}$, κ^{-1} = 2.0 Å, E_{pzc} = 0.2 V, D_e = 5 eV, d_0 = 1.5 Å, Δ_0 = 2.0 eV, λ = 1.0 eV. TS is short for transition state.

Compared to reaction (4.1), changing the simulation parameters will not cause any apparent energy well. This is because the energy well in Figure 4.1 is mainly due to the coulombic attraction. The reactant X(sol) in reaction (4.2) is neutral but X^+(sol) in reaction (4.1) carries a positive charge. Therefore, the energy well is only observed for X^+(sol)/X(ads).

4.4 Electrical Double Layer Effects on X$^+$(sol)/X(ads)

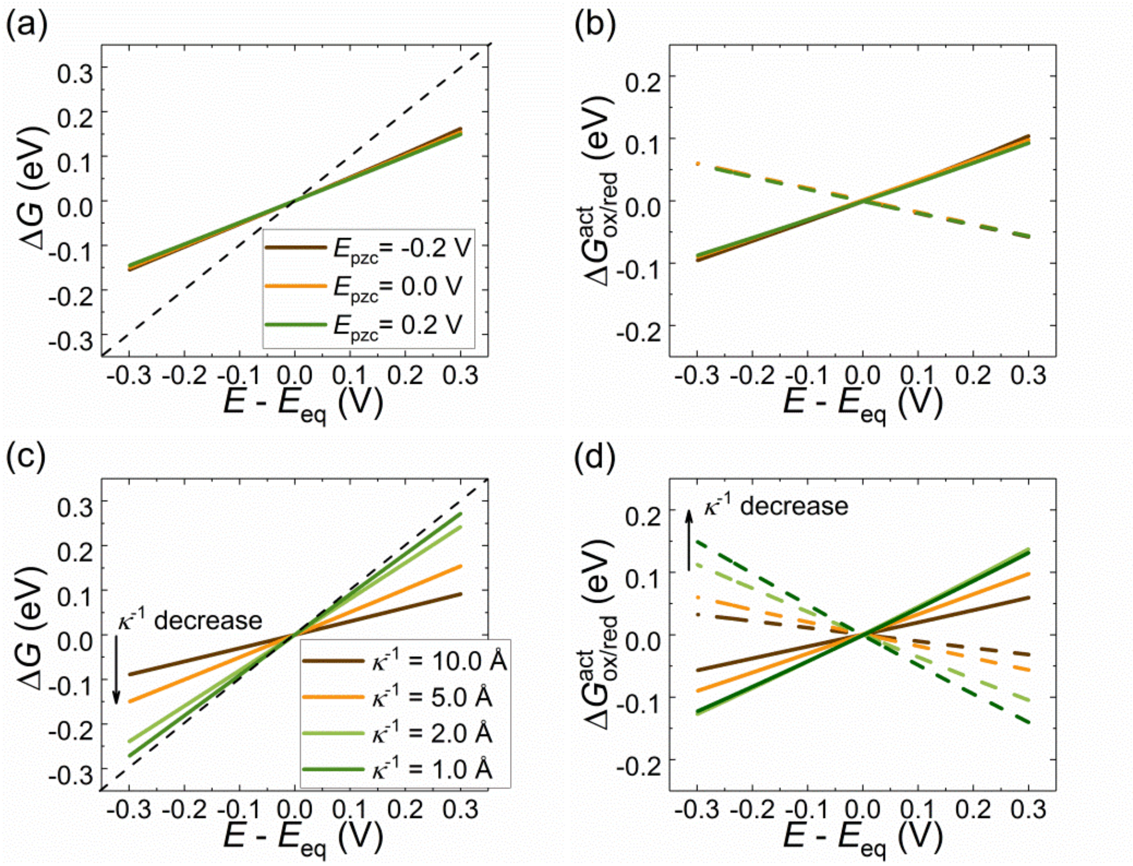

Figure 4.3 Calculated Gibbs energies for X$^+$(surf)/X(ads) under different electrical double layers: (a) ΔG as a function of E_{pzc}, where the dashed black lines are the Nernstian Gibbs energy differences, (b) $\Delta G^{act}_{ox/red}$ as a function of E_{pzc}, (c) ΔG as a function of κ^{-1}, (d) $\Delta G^{act}_{ox/red}$ as a function of κ^{-1}. In (a) and (b), E_{pzc} = -0.1V, 0, 0.1V and κ^{-1} = 5.0 Å; in (c) and (d), E_{pzc} = 0 V and κ^{-1} = 10.0, 5.0, 2.0 and 1.0 Å. Other simulation conditions are the same as in Figure 4.1.

The influence of the electrical double layer on ion transfer reactions is studied in this and the next sections. The potential of zero charge E_{pzc} and the Debye length κ^{-1} are the two key parameters in the current model to account for the double layer structure and the electric potential distribution. The Debye length reflects the thickness of the electrical double layer and the value depends on the electrolyte concentration.[37] Figure 4.3 shows the thermodynamics and kinetics of the charge transfer step for X^+(surf)/X(ads) for different E_{pzc} and κ^{-1}. The thermodynamics of X^+(surf)/X(ads) is characterized by the Gibbs energy difference ΔG between X^+(surf) and X(ads), and the kinetics by the reductive and oxidative activation energies calculated from $\Delta G_{\mathrm{ox/red}}^{\mathrm{act}} = G_{\mathrm{TS}} - G_{\mathrm{X(ads)/X^+(surf)}}$. The black dashed lines in Figures 4.3a and 4.3c represent the Gibbs energy difference according to the Nernst equation, which is $\Delta G_{\mathrm{Nernst}} = F(E\text{-}E_{\mathrm{eq}})$. Note that when discussing the Gibbs energy changes of the charge transfer step, E_{eq} is the equilibrium potential for X^+(surf)/X(ads), which is defined as:

$$G_{\mathrm{X^+(surf)}}\left(E_{\mathrm{eq}}\right) = G_{\mathrm{X(ads)}}\left(E_{\mathrm{eq}}\right) \tag{4.34}$$

In Figure 4.3a, although ΔG for X^+(surf)/X(ads) deviates from the ideal Nernstian case, this deviation is insensitive to the value of the E_{pzc}-value. The activation energies of the charge transfer step (4.33) in Figure 4.3b are also independent on E_{pzc}, reflecting that the variation of E_{pzc} does not cause any significant change on the potential dependence of the thermodynamic and kinetic parameters considered.

However, the thermodynamics and kinetics of X^+(surf)/X(ads) show a strong dependence on the size of the electrical double layer, as can be seen in Figures 4.3c and 4.3d. At large Debye lengths, corresponding to wide double layers, the driving force applied to the charge transfer step is smaller than the Gibbs energy difference following the Nernst equation. When the double layer is relatively small (that is, a small Debye length), the Gibbs energy difference ΔG between X^+(surf) and X(ads) almost coincides with the Nernstian one (Figure 4.3c) and the energy transfer efficiency from the applied overpotential to the activation energies increases (Figure 4.3d). This can be understood considering that the influence of the electric field on the energy of the charged species X^+(surf) and the charged transition state. Therefore, the Gibbs energy of X^+(surf) and TS vary with the Debye lengths.

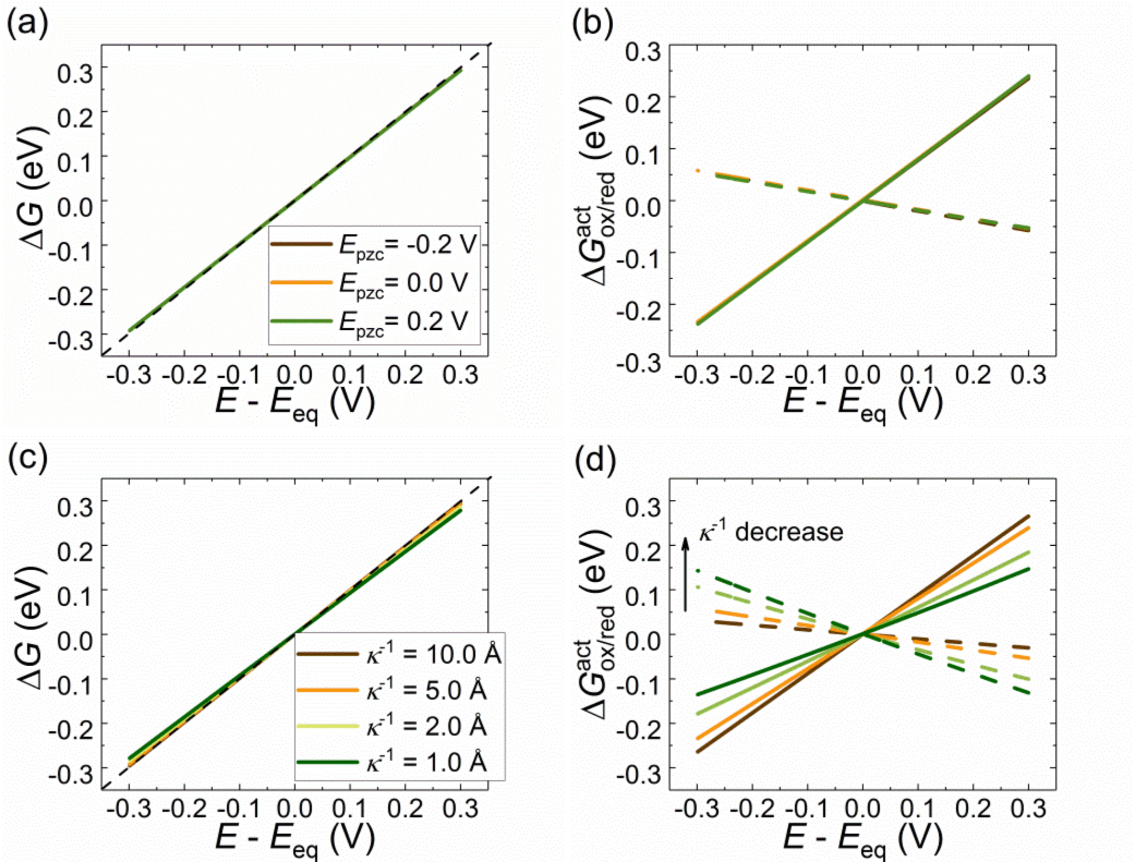

Figure 4.4 Calculated Gibbs energies for X^+(sol)/X(ads) under different electrical double layers: (a) Δ*G* as a function of E_{pzc}, where the dashed black lines is the Nernst Gibbs energy difference, (b) $\Delta G^{act}_{ox/red}$ as a function of E_{pzc}, (c) ΔG as a function of κ^{-1}, (d) $\Delta G^{act}_{ox/red}$ as a function of κ^{-1}. In (a) and (b), E_{pzc} = -0.1V, 0, 0.1V and κ^{-1} = 5.0 Å; in (c) and (d), E_{pzc} = 0 V and κ^{-1} = 10.0, 5.0, 2.0 and 1.0 Å. Other simulation conditions are the same as in Figure 4.1.

Figure 4.4 displays the energy changes for the whole reaction between X^+(sol) and X(ads). Here, the apparent equilibrium potential E_{eq} for reaction (4.1) is defined on the basis of the reactant X^+(sol) and the product X(ads):

$$G_{X^+(sol)}\left(E_{eq}\right) = G_{X(ads)}\left(E_{eq}\right) \tag{4.35}$$

Similar to the case of X^+(surf)/X(ads), the potential dependence of the Gibbs energy difference and the activation energies are independent of the E_{pzc}-value. Also, the Gibbs energy difference for X^+(sol)/X(ads) is not sensitive to the change of the Debye length. On the other hand, the activation energies are notably affected by the electrical double layer thickness. As shown in Figure 4.4d, the profiles of $\Delta G_{\mathrm{red}}^{\mathrm{act}}$ and $\Delta G_{\mathrm{ox}}^{\mathrm{act}}$ are symmetric for small Debye lengths and the symmetry is broken when the Debye length increases (the double layer becomes broader). As the Gibbs energy for the species X^+(sol) is independent of the electrical double layer influence, the Nernstian ΔG indicates that the external electric field almost has no effects on the neutral adsorbate X(ads). However, as the transition state carries a charge, the activation energies for the reductive and the oxidative directions show a strong dependence on the external electric field.

Figures 4.5 and 4.6 show the effects of the electrical double layer parameters on the current-potential curve obtained in the cyclic voltammetry for X^+(sol)/X(ads). The Gibbs energy differences ΔG and the activation energies $\Delta G_{\mathrm{ox/red}}^{\mathrm{act}}$ used in the simulation are based on the results shown in Figure 4.4.

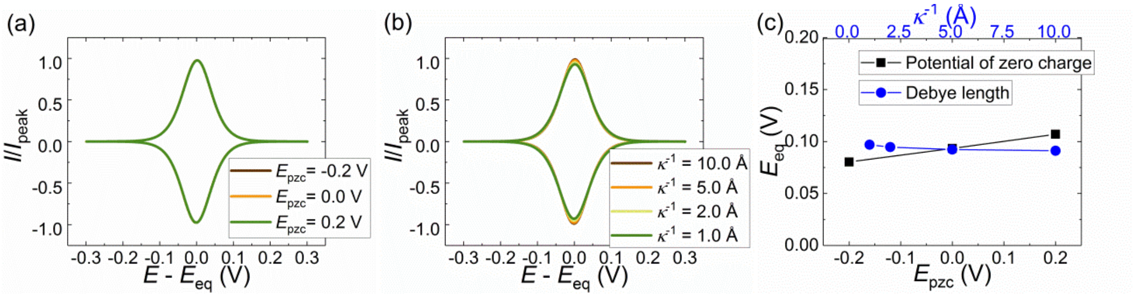

Figure 4.5 Simulated reversible cyclic voltammograms for X^+(sol)/X(ads) under different electrode double layers: (a) with various E_{pzc}, the pre-exponential parameter k_0 is 1 m/s, (b) with various κ^{-1}, the standard heterogeneous rate constant k_0 is 1 m/s. (c) shows the equilibrium potentials for the voltammograms in (a) and (b). Other simulation conditions are the same as used in Figure 1.

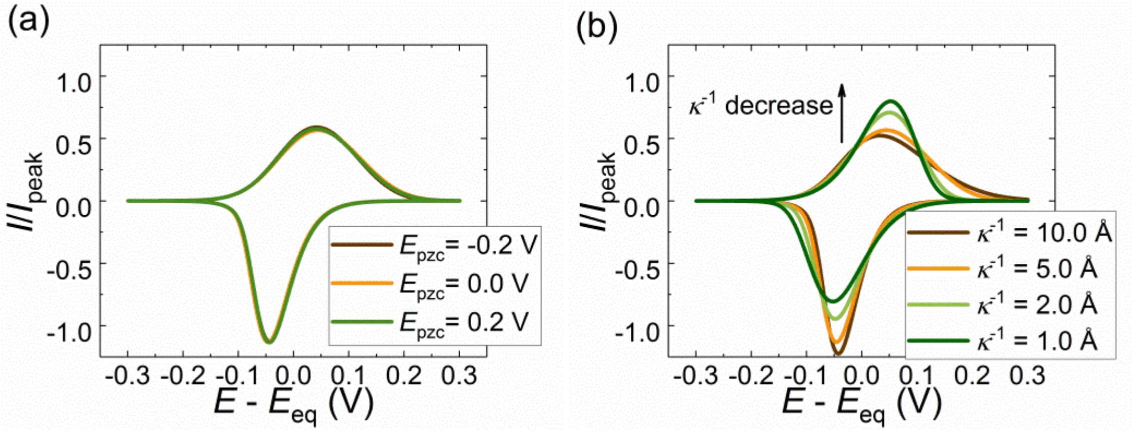

Figure 4.6 Simulated cyclic voltammograms for a quasi-reversible X^+(sol)/X(ads) reaction: (a) for several E_{pzc}-values, the standard heterogeneous rate constant k_0 is 10^{-5} m/s, (b) for several κ^{-1}-values, the standard heterogeneous rate constant k_0 is 10^{-5} m/s. Other simulation conditions are the same as used in Figure 4.1.

The deviation of ΔG from the Nernstian case can be detected from the deviations of the waveshapes from that corresponding to the cyclic voltammogram of reversible interfacial electrochemical reactions (Figure 4.5). The variations of $\Delta G^{\mathrm{act}}_{\mathrm{ox/red}}$ can be detected on the cyclic voltammograms as well when the charge transfer is not reversible (Figure 4.6). For interfacial electrochemical reactions (4.1) and (4.2), assuming that the mass transport is fast enough for not being rate determining and that the charge transfer is reversible, the forward and backward peaks should be symmetric under Nernstian condition and the reversible adsorption peak current be given by:

$$I_{\mathrm{peak}} = \frac{F^2}{4RT} vS\Gamma_{\mathrm{max}} \tag{4.36}$$

where v is the scan rate, S is the area of the electrode and $\Gamma_{\max}$ is the maximum surface coverage on the electrode surface. For convenience, all the simulated currents of reactions (4.1) and (4.2) are normalized with respect to the theoretical peak current (4.36).

Figure 4.5 shows the cyclic voltammograms of a fast (reversible) ion transfer reaction X^+(sol)/X(ads) under different electrical double layer parameters. The voltammograms for various E_{pzc} (Figure 4.5a) and κ^{-1} (Figure 4.5b) values overlap with those predicted for a Nernstian behavior, indicating that the thermodynamics of reaction (4.1) for the redox couple X^+(sol)/X(ads) follows the Nernst equation even under the influence of the electrical double layer. The equilibrium potential E_{eq} changes a little with the variation of the double layer parameters as shown in Figure 4.5c, indicating that the peak position may shift under large change of E_{pzc} or κ^{-1} values. But the external electric field does not have any significant influence on the waveshape of the reversible cyclic voltammograms for the case X^+(sol)/X(ads) in reaction (4.1), which is consistent with the Nernstian behavior of ΔG discussed in Figures 4.4a and 4.4c.

In contrast to the above results, when the ion transfer is quasi-reversible, the voltammograms reflect the transfer energy barrier and kinetics and so, according to the results shown in Figure 4.4d, they will be dependent on the thickness of the electrical double layer. As a consequence of the asymmetric activation energies caused by strong electric fields, the presence of the electrical double layer breaks the symmetry between the forward and backward voltammetric peaks, reflecting that the effects of the double layer on the reductive and oxidative half reactions for reaction (4.1) are not the same. On the other hand, as observed in Figure 6.6a, under quasi-reversible kinetics, the change of E_{pzc} does not influence the shape of the voltammogram.

In summary, for the reduction of the charged ion X^+(sol), when there is no preceding adsorption of the reactant X^+ or the two-step mechanism can be ignored, the double layer does have an influence on the ion transfer reaction. The potential of zero charge has contributions to the equilibrium potential for X^+(sol)/X(ads) while has no effects on the current-potential waveshape. With respect to the electrical double layer thickness not only does it affect the value of the equilibrium potential, but it also plays an important role in determining the activation energies for X^+(sol)/X(ads), which can reflect on the cyclic voltammogram when the charge transfer rate is no longer considered as infinitely fast. It is also found that the electrical double layer cannot change the thermodynamics of the ion transfer reaction in X^+(sol)/X(ads), and thus the cyclic voltammograms under fast charge transfer rates are insensitive to neither of the double layer parameters.

4.5 Electrical Double Layer Effects on X(sol)/X^-(ads)

In comparison with the case of X^+(sol)/X(ads) in reaction (4.1), the ion transfer process of X(sol)/X^-(ads) in reaction (4.2) is expected to be more sensitive to the variation of the electrical double layer, as the external electric field will strongly affect the charged adsorbate X^-(ads). Figure 4.7 shows the Gibbs energy difference ΔG and the activation energies $\Delta G_{\mathrm{ox/red}}^{\mathrm{act}}$ for the reductive and oxidative half-reactions of reaction (4.2), which change as a function of E_{pzc} and κ^{-1}. As there is not any preceding adsorption step in reaction (4.1) as shown in Figure 4.2, the equilibrium potential, the Gibbs energy differences and the activation energies are all calculated between the states X(sol) and X^-(ads). In Figure 4.7, the Gibbs energy differences and the activation energies are independent of the value of E_{pzc} but dependent on the Debye length. Unless the thickness of the electrical double layer is compressed to be nearly zero, the existence of the double layer can drive ΔG deviating significantly from the Nernst value, which causes the decrease of $\Delta G_{\mathrm{ox/red}}^{\mathrm{act}}$.

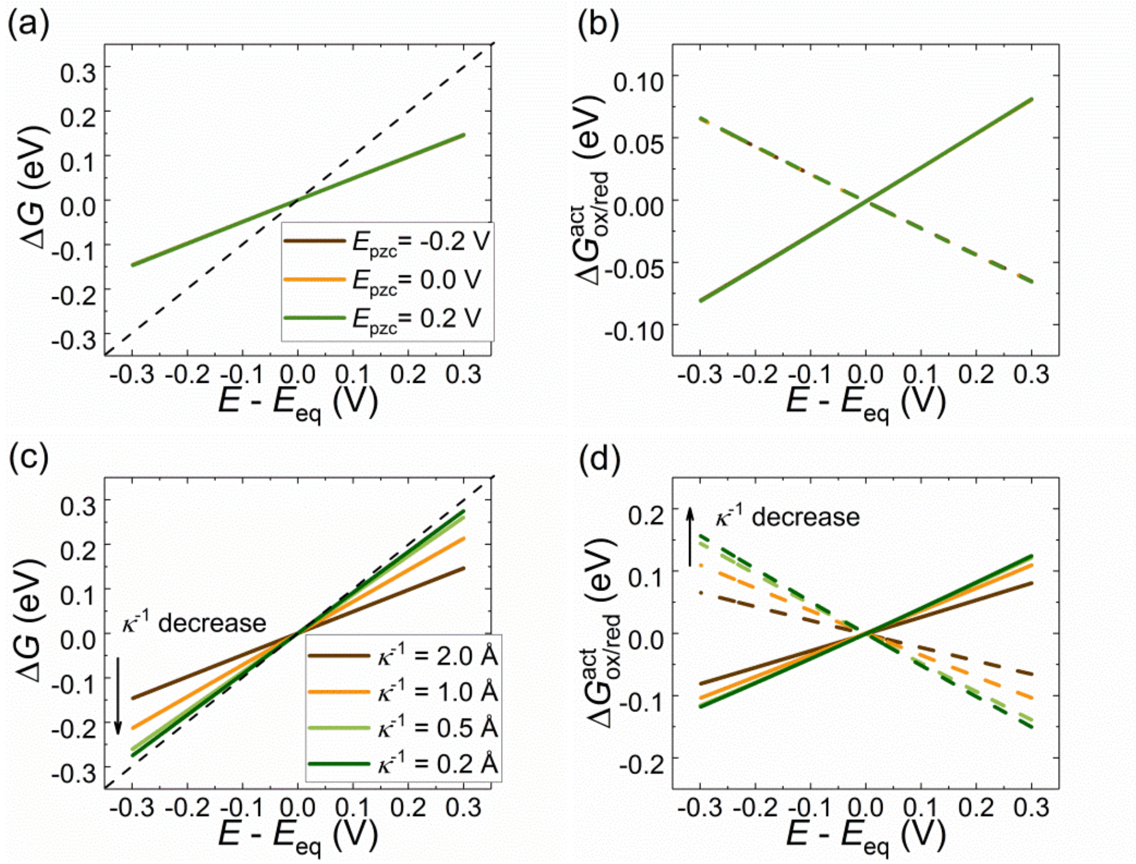

Figure 4.7 Calculated Gibbs energies for X(sol)/X^-(ads) under different conditions of the electrical double layers: (a) ΔG as a function of E_{pzc}, where the dashed black lines is the Nernst Gibbs energy difference, (b) $\Delta G_{ox/red}^{act}$ as a function of E_{pzc}, where the solid lines are the reductive activation energies and the dashed lines the oxidative ones, (c) ΔG as a function of κ^{-1}, (d) $\Delta G_{ox/red}^{act}$ as a function of κ^{-1}. In (a) and (b), E_{pzc} = -0.2V, 0, 0.2V and κ^{-1} = 2.0 Å; in (c) and (d), E_{pzc} = 0 V and κ^{-1} = 2.0, 1.0, 0.5, 0.2 Å. Other simulation conditions are the same as in Figure 4.1.

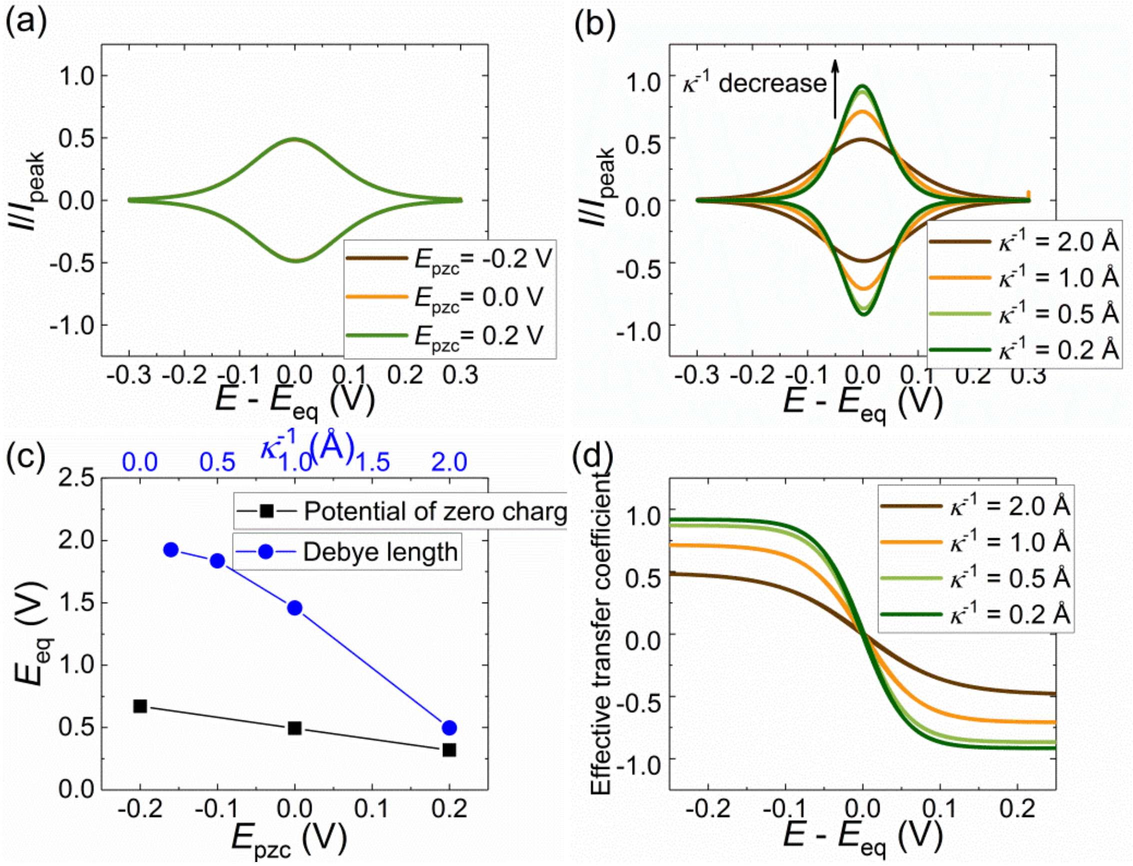

Figure 4.8 Simulated cyclic voltammograms for a reversible X(sol)/X$^-$(ads) process: (a) for several E_{pzc}-values, the standard heterogeneous rate constant k_0 is 1 m/s, (b) for several κ^{-1}-values, the standard heterogeneous rate constant k_0 is 1 m/s. (c) shows the equilibrium potentials for the voltammograms in (a) and (b). (d) shows the potential-dependence of the effective transfer coefficient calculated from the curves in (b). Other simulation conditions are the same as used in Figure 4.2.

Note that the double layer electric field shows similar influences on X(sol)/X$^-$(ads) and X$^+$(surf)/X(ads) with respect to, the Gibbs energy differences ΔG of the two systems (Figure 4.3c and Figure 4.8c), which changes as a function of the Debye length. A large electrical double layer can cause the decrease of the driving force for both X$^+$(surf)/X(ads) and X(sol)/X$^-$(ads). This reinforces the idea that the effects of the electrical double layer on the ion transfer processes like reactions (4.1) and (4.2) are mainly related with the charge carried by the redox species and the location of the charged species with respect to the electrical double layer.

Figure 4.8 shows the electrical double layer dependence in the cyclic voltammograms of reaction (4.2). The potential of zero charge does not affect the waveshape of the voltammogram for X(sol)/X^-(ads). However even for the ultra-fast transfer kinetics considered in Figure 4.8, the cyclic voltammograms and the Tafel slopes calculated from the current-voltage curve show a strong dependence on the value of the Debye length, which is totally different from the reversible X^+(sol)/X(ads) case shown in Figure 4.5. This is somewhat expected considering that for the redox couple X(sol)/X^-(ads) the adsorbate carries a charge such that the electrical double layer will have a more apparent influence on the ion transfer reaction than for X^+(sol)/X(ads) in reaction (4.1), where the adsorbate is almost neutral and the charged reactant is relatively far away from the electrode.

The different current-potential responses between X^+(sol)/X(ads) and X(sol)/X^-(ads) are also reflected by the equilibrium potential calculated for various values of the double layer parameters given in Figures 4.5c and 4.8c. Thus, the equilibrium potential for X(sol)/X^-(ads) apparently depends on the double layer parameters while there is only little influence on the E_{eq}-values for X^+(sol)/X(ads). Figure 4.8d shows the effective transfer coefficients calculated from the cyclic voltammograms in Figure 4.8b. The effective transfer coefficient is calculated by $\left(RT/F\right)\times\left(\partial\ln|I|/\partial\left(E-E_{\mathrm{eq}}\right)\right)$. The ideal calculated results for the fully-reversible reaction (4.2) should equal 1 at low overpotentials and -1 at high overpotentials, which is a widely-used as criterion to judge the reversibility of the electrochemical process.[38, 39] However, even for an artificially fast reaction rate constant k_0 to assure full electrochemical reversibility of the reaction, the presence of the electrical double layer can lead to a non-unity effective transfer coefficient at low overpotentials that takes a value smaller than 1. The results in Figure 4.8d indicate that even for reversible charge transfer kinetics, the external electric field can lead to an apparently "irreversible" behaviour via affecting the driving force of the charge transfer step.

4.6 Example: Oxygen Reduction Reaction on Palladium Modified Carbon Nanotubes

The oxygen reduction reaction (ORR) is an important reaction in living processes and in energy converting systems.[40] The mechanism of ORR is much studied but still under debate. In aqueous solution, two common system dependent overall routes have been proposed: either a direct four electron reduction to H_2O[41] or a series pathway via two electron transfer to form hydrogen peroxide (H_2O_2) and subsequent reduction of H_2O_2 to H_2O.[42]

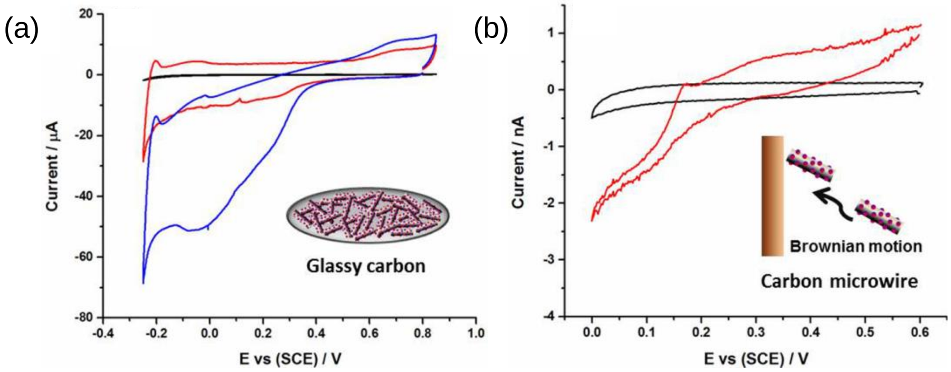

Figure 4.9. (a) Voltammogram of the bare GC electrode (diameter 3.0 mm) in 0.5 M H_2SO_4 saturated with O_2 (black line); voltammogram of the N-CNT-Pd modified GC electrode in 0.5 M H_2SO_4 saturated with Ar (red line) and with O_2 (blue line), 50 mV/s. (b) Voltammogram in 0.5 M H_2SO_4 saturated with O_2 of the carbon microwire electrode before (black line) and after (red line) collision and immobilized with N-CNT-Pd.

To seek new insights into electron transfer most generally, the ‘nano-impacts’ method is applied to study the reduction of oxygen at palladium in aqueous acid. The experiments shown in this section were implemented by Miss Xiuting Li. Experiments of ORR catalyzed by palladium (Pd) nanoparticle modified nitrogen-doped-multiwalled carbon nanotubes, N-CNT-Pd (length ca. 5 μm; width 130 nm; diameter of Pd nanoparticles ca. 1.4 nm), were implemented with ensemble and single Pd modified nanotubes. In the experiment, the role of the nanotube is assumed to be effectively graphitic in nature and acts solely as a conductive substrate, facilitating electrical connection to the palladium nanoparticles.

The ability of the N-CNT-Pd to catalyse the ORR was evaluated by drop-casting onto a glassy carbon (GC) macroelectrode (ca. 3.0 mm in diameter). As shown in Figure 4.9a (black line), no voltammetric signal from ORR was observed at the bare GC electrode in an O_2-saturated solution. The GC electrode was then drop-cast with a 20 μL suspension of N-CNT-Pd (4.6×10^{-12} M) and dried under a N_2 atmosphere. Assuming homogeneous coverage over the electrode surface constitutes ~5 layers of carbon nanotubes on the surface. Figure 4.9a shows the CV profiles of the N-CNT-Pds modified GC electrode in 0.5 M H_2SO_4 saturated with Ar (red line) and with O_2 (blue line). It proves that N-CNT-Pd in combination with a carbon electrode allows the investigation of the O_2 reduction at single N-CNT-Pd tubes via the nano-impact method.

The nano-impact method is introduced in Chapter 1 and an illustration of the single nanotube impact experiment can be found in the inner panel of Figure 4.9b. It has been proved that the long residence time of the N-CNT-Pd permits the recording of a cyclic voltammogram at individual CNTs.[43] After the N-CNT-Pd lands on the electrode within a few minutes of adding a known concentration of N-CNT-Pd suspension into an O_2-saturated solution with 0.5 M H_2SO_4 contained, the CV signal of ORR during the initial impact event of N-CNT-Pd which lands on the electrode, as shown in Figure 4.9b.

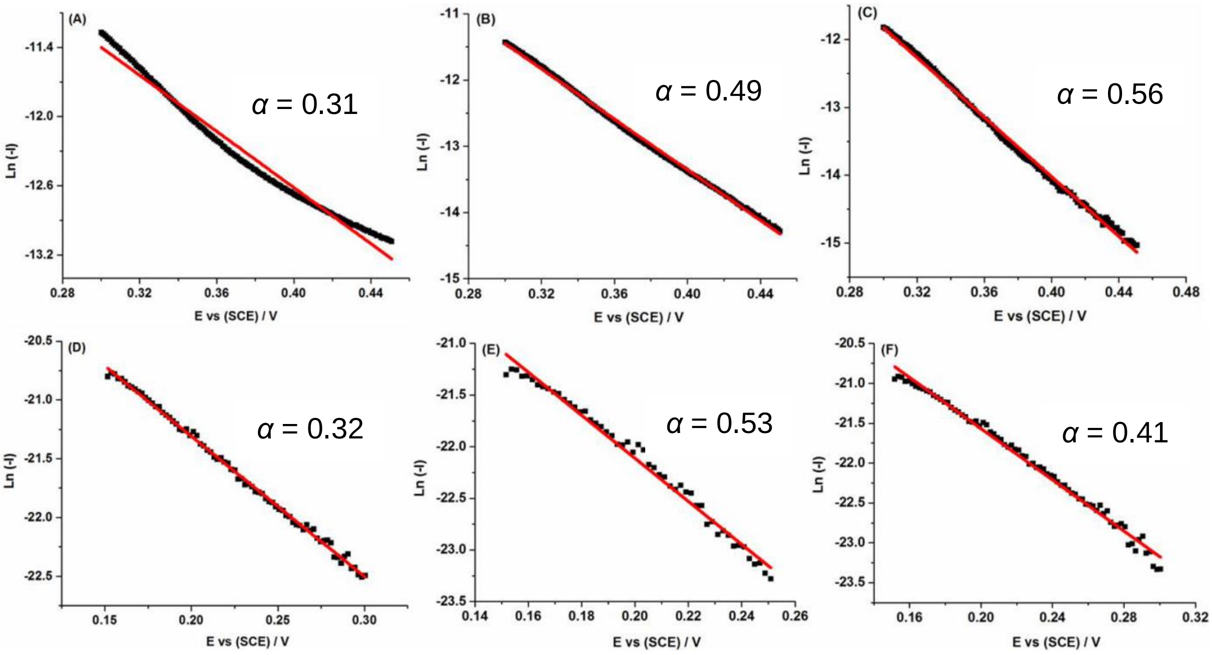

Figure 4.10. Tafel plots of (A) the raw CV of ORR on the N-CNT-Pd modified GC electrode (the blue line in Figure 4.9a), (B) the raw CV after baseline correction, (C) the raw CV after blank subtraction (the red line in Figure 4.9a as a blank); (D) the raw CV of ORR on the single N-CNT-Pd (the red line in Figure 4.9b), (E) the raw CV after baseline correction, (F) the raw CV after blank subtraction (the black line in Figure 4.9b as a blank).

In Figure 4.10, the effective transfer coefficient (calculated from $\left(RT/F\right)\times\left(\partial \ln\left|I\right|/\partial\left(E-E_{\mathrm{eq}}\right)\right)$) is measured by plotting ln|I| for the forward sweep versus E with the data directly from CV experiments with linear fitting to get the slopes. For more accurate measurement, two background correction strategies including baseline correction and blank subtraction are employed. The resulting value of transfer coefficient varies from 0.31 to 0.56 for the N-CNT-Pd modified GC electrode and from 0.32 to 0.53 for the single N-CNT-Pd depending on the background technique used. This effective transfer coefficient is consistent with the reported Tafel slopes in the literature where a value of 120 mV dec^{-1} or greater (equivalent transfer coefficient $\alpha \leq 0.49$) is reported for the ORR on Pt(111) supported Pd film electrodes.

For an irreversible electron transfer, the mass transport constant of a planar GC macroelectrode (of ca. 3.0 mm in diameter) and a single N-CNT-Pd acting as a cylindrical 'nanoelectrode' (of ca. 5 μm in length and ca. 130 nm in diameter) can be estimated as 2×10^{-5} m s^{-1} and 4×10^{-3} m s^{-1} respectively, which according to the Butler-Volmer equation would result in a higher overpotential of single N-CNT-Pd than the modified GC macroelectrode by ca. 0.32 V (calculation details can be found in the appendix of this chapter). Comparing Figure 4.9a and Figure 4.9b, it is observed that the voltammetric waves shifts negatively about 0.1 V (the quarter-wave potential as the characteristic potential[44]: ~0.3V for modified GC electrode and ~0.2V for the single CNT) when the size of the electrode drops from millimeter scale of GC to sub-micrometer scale of the CNTs. This slight potential shift might reflect the "reversibility" of the first electron transfer step (reduction of O_2 to the superoxide ion $O_2^{-\bullet}$):

$$O_2(\text{sol}) + e^- \rightleftarrows O_2^{-\bullet}(\text{ads}) \tag{4.37}$$

However, this step is usually thought to be the rate-determining step and the low transfer coefficient seen in the CV signal of ORR is commonly believed to signal "electrochemical irreversibility".[23] Under reversible conditions the apparent transfer coefficient of a one-electron transfer is one, and the wave-shape reflects a redox process under Nernstian control not any underlying electron transfer kinetics.

Over the potential range used for Tafel analysis neither transport effects nor substantial changes in k_0 between dropcast ensembles and single nanotubes are expected, therefore the observed kinetic limitation must have a more "complicated" cause. It is necessary to revisit the fundamentals of electron transfer theory in the light of these unexpected data. As discussed in the ion transfer model X(sol)/X$^-$(ads), in particular for reactions where the product of the electron transfer is an adsorbed species, the electrical double layer is expected to have a significant effect on the kinetics of the electron transfer. It is reasonable to assume that the small value of the transfer coefficient is caused by other factors, such as the electrical double layer effect. Figure 4.8 shows the effective transfer coefficient as a function of κ^{-1} with a fast standard heterogeneous rate constant k_0. Under reversible Nernstian condition, an ideal effective transfer coefficient should equal 1 as the relatively large k_0 leads to reversibility of the reaction. However, it is found that even for an artificially fast k_0 (in order to achieve full electrochemical reversibility) as applied in Figure 4.8, the presence of the electrical double layer leads the effective transfer coefficient deviating from 1. Figure 4.7c shows the Gibbs energy difference $G_{\mathrm{X^{-}(ads)}} - G_{\mathrm{X(sol)}}$ varying as a function of the Debye length, demonstrating that the apparent "irreversibility" inferred from the transfer coefficient can be caused by the decrease of the driving force as a consequence of the interaction between the electric field within the double layer and the charged species participating in the reaction.

4.7 Summary

Gibbs energy surfaces are generated to describe the energy change in ion transfer reactions based on an extension of the Anderson–Newns Hamiltonian that includes the potential distribution within the double layer according to the Gouy-Chapman model. For the redox couple X^{+}(sol)/X(ads), it is found that the charged reactant can experience a preceding adsorption step on its way to the electrode surface, while the charge it carries does not change and the charge transfer occurs between the "weakly-adsorbed" state X^{+}(surf) and the electrode. For X(sol)/X^{-}(ads), no apparent preceding adsorption of X(sol) is inferred from the Gibbs energy surfaces.

The electrical double layer is described by the values of the potential of zero charge E_{pzc} and the Debye length κ^{-1}. From the simulation results, it is concluded that the value of E_{pzc} has no significant effects on the waveshapes of the voltammograms but it can affect the equilibrium potential. The thickness of the electrical double layer is the main factor influencing the voltammetric waveshapes. Comparing the charge transfer processes X^+(sol)/X(ads) and X(sol)/X^-(ads), it is found that X(sol)/X^-(ads) is more vulnerable to the double layer effects, including significant deviations from the Nernstian peak current and the effective transfer coefficients. When the "preceding adsorption" X^+(sol)/X(ads) is not taken into consideration, the voltammograms for X^+(sol)/X(ads) does not reflect the influence of the electrical double layer under reversible kinetics. But the waveshape for X^+(sol)/X(ads) can change significantly with the increase of the Debye length when the charge transfer kinetics is not reversible. Therefore, for the electrochemical systems here considered, the effects of the external electric field can have a profound influence on the cyclic voltammograms. Consideration is required for the correct interpretation and modeling of the voltammetric response.

In the example of the oxygen reduction reaction on palladium, the data obtained at single nanoparticle catalysts has under conditions of extreme rates of mass transport coupled with theoretical modeling, allowed the key insight that the voltammetric characteristics of the ORR at Pd are likely dominated by double layer effects. As a consequence of the proposed model even for fast electron transfer reactions the illusion of slower kinetics is induced. The reduction of oxygen on Pd involves the initial formation of absorbed superoxide $O_2^{-\cdot}$ (ads) with fast electron transfer kinetics but with an apparent transfer coefficient of 0.3~0.5 due to double layer effects arising from the coulombic interactions of the adsorbed superoxide species inside the double layer.

Appendix

For the irreversible process of one electron transfer, the mass transport constant at the voltammetry peak current, k_{MT}, of a planar macro electrode is:[45]

$$k_{\mathrm{MT(macro)}} = 0.496\sqrt{\alpha}\sqrt{\frac{FDv}{RT}} \tag{4.38}$$

where α is the electron transfer coefficient and 0.43 is taken as a representative value in this work for oxygen, F is the Faraday constant (96485 C mol^{-1}), D is the diffusion coefficient of O_2 (1.96×10^{-9} m^2 s^{-1}),[46] v is the voltage scan rate (0.05 V s^{-1}), R is the gas constant (8.314 J mol^{-1} K^{-1}) and T is the temperature (298 K). Therefore, the mass transport constant of a planar macro electrode, $k_{\mathrm{MT(macro)}}$, is calculated as 2×10^{-5} m s^{-1}.

While the mass transport constant, $k_{\mathrm{MT(CNT)}}$, of a single carbon nanotube as a cylindrical micro electrode at the voltammetry peak current is approximately:[47]

$$k_{\mathrm{MT(CNT)}} = \frac{D}{r_0}\left(0.446p + 0.335p^{0.15}\right),\ \text{with } p = \sqrt{\frac{Fr_0^2 v}{RTD}} \tag{4.39}$$

where r_0 is the radius of the carbon nanotube (ca. 6.4×10^{-8} m) and the other parameters are as the same as the above. The mass transport constant of the carbon nanotube as a cylindrical micro electrode, is then estimated to be 4×10^{-3} m s^{-1}.

Using the Butler-Volmer equation:

$$i = FSk_0\left(C_{\mathrm{O}} \exp\left(-\frac{\alpha F\eta}{RT}\right) - C_{\mathrm{R}} \exp\left(\frac{(1-\alpha)F\eta}{RT}\right)\right) \tag{4.40}$$

where S is the area of the electrode, k_0 is the standard rate constant, C_{O} and C_{R} are respectively the concentration of the species O and R at the electrode surface in O + e ↔ R and η is the overpotential. From this the change in the overpotential due to the altered mass transport can be estimated to be:

$$\frac{k_{\mathrm{MT(CNT)}}}{k_{\mathrm{MT(macro)}}} = \exp\left(-\frac{\alpha F}{RT}\left(\eta_{\mathrm{(CNT)}} - \eta_{\mathrm{(macro)}}\right)\right) \tag{4.41}$$

Therefore, the overpotential difference, shown as the potential shift in the voltammogram, can be derived from the ratio of $k_{\mathrm{MT(CNT)}}$ and $k_{\mathrm{MT(macro)}}$, giving a value of 0.32 V.

References

1. X. Li, C. Lin, C. Batchelor-McAuley, E. Laborda, L. Shao and R. G. Compton, *The Journal of Physical Chemistry Letters*, 2016, **7**, 1554-1558.

2. C. Lin, E. Laborda, C. Batchelor-McAuley and R. G. Compton, *Physical Chemistry Chemical Physics*, 2016, **18**, 9829-9837.

3. E. Herrero, L. J. Buller and H. D. Abruña, *Chemical Reviews*, 2001, **101**, 1897-1930.

4. J. Durst, A. Siebel, C. Simon, F. Hasché, J. Herranz and H. A. Gasteiger, *Energy and Environmental Science*, 2014, **7**, 2255-2260.

5. Y. Wang, E. Laborda, M. C. Henstridge, F. Martinez-Ortiz, A. Molina and R. G. Compton, *Journal of Electroanalytical Chemistry*, 2012, **668**, 7-12.

6. E. E. L. Tanner, L. Xiong, E. O. Barnes and R. G. Compton, *Journal of Electroanalytical Chemistry*, 2014, **727**, 59-68.

7. J. M. Savéant and D. Tessier, *Journal of Electroanalytical Chemistry and Interfacial Electrochemistry*, 1975, **65**, 57-66.

8. C. E. D. Chidsey, *Science*, 1991, **251**, 919-922.

9. M. C. Henstridge, N. V. Rees and R. G. Compton, *Journal of Electroanalytical Chemistry*, 2012, **687**, 79-83.

10. W. Schmickler, *Journal of Electroanalytical Chemistry*, 1986, **204**, 31-43.

11. M. T. M. Koper and G. A. Voth, *Chemical Physics Letters*, 1998, **282**, 100-106.

12. P. Quaino, E. Santos, G. Soldano and W. Schmickler, *Advances in Physical Chemistry*, 2011, **2011**.

13. R. A. Marcus, *The Journal of Chemical Physics*, 1965, **43**, 679-701.

14. N. S. Hush, *Transactions of the Faraday Society*, 1961, **57**, 557-580.

15. R. R. Dogonadze, A. M. Kuznetsov and M. A. Vorotyntsev, *Journal of Electroanalytical Chemistry*, 1970, **25**, A17-A19.

16. E. Santos and W. Schmickler, in *Catalysis in Electrochemistry*, John Wiley & Sons, Inc., 2011, DOI: 10.1002/9780470929421.ch6, pp. 197-222.

17. P. W. Anderson, *Physical Review*, 1961, **124**, 41-53.

18. D. M. Newns, *Physical Review*, 1969, **178**, 1123-1135.

19. J. P. Muscat and D. M. Newns, *Progress in Surface Science*, 1978, **9**, 1-43.

20. N. S. Hush, *The Journal of Chemical Physics*, 1958, **28**, 962-972.

21. W. Schmickler, *Electrochimica Acta*, 1996, **41**, 2329-2338.

22. W. Schmickler and E. Santos, *Interfacial Electrochemistry*, Springer Berlin Heidelberg, 2010.

23. S. Fletcher, *Journal of Solid State Electrochemistry*, 2009, **13**, 537-549.

24. W. Schmickler and R. Guidelli, *Electrochimica Acta*, 2014, **127**, 489-505.

25. N. S. Hush, *Journal of Electroanalytical Chemistry*, 1999, **470**, 170-195.

26. A. Declemy, C. Rulliere and P. Kottis, *Laser Chemistry*, 1990, **10**, 413-429.

27. E. Santos, M. T. M. Koper and W. Schmickler, *Chemical Physics*, 2008, **344**, 195-201.

28. A. Ignaczak and W. Schmickler, *Journal of Electroanalytical Chemistry*, 2003, **554–555**, 201-209.

29. P. H. Rieger, *Electrochemistry*, Prentice-Hall, Englewood Cliffs, 1987.

30. J. R. Smith, S. C. Ying and W. Kohn, *Physical Review Letters*, 1973, **30**, 610-613.

31. J. M. Savéant, *Accounts of Chemical Research*, 1993, **26**, X1-460.

32. J. O. M. Bockris, A. K. N. Reddy and M. E. Gamboa-Aldeco, *Modern Electrochemistry 2A: Fundamentals of Electrodics*, Springer US, 2000.

33. E. Santos, A. Lundin, K. Pötting, P. Quaino and W. Schmickler, *Physical Review B*, 2009, **79**, 235436.

34. A. Calhoun and G. A. Voth, *Journal of Electroanalytical Chemistry*, 1998, **450**, 253-264.

35. M. T. M. Koper and G. A. Voth, *The Journal of Chemical Physics*, 1998, **109**, 1991-2001.

36. G. Henkelman, G. Jóhannesson and H. Jónsson, in *Theoretical Methods in Condensed Phase Chemistry*, ed. S. Schwartz, Springer Netherlands, 2002, vol. 5, ch. 10, pp. 269-302.

37. A. J. Bard and L. R. Faulkner, *Electrochemical Methods: Fundamentals and Applications*, Wiley, 2000.

38. R. Guidelli, R. G. Compton, J. M. Feliu, E. Gileadi, J. Lipkowski, W. Schmickler and S. Trasatti, *Pure and Applied Chemistry*, 2014, **86**, 245-258.

39. R. Guidelli, R. G. Compton, J. M. Feliu, E. Gileadi, J. Lipkowski, W. Schmickler and S. Trasatti, *Pure and Applied Chemistry*, 2014, **86**, 259-262.

40. C. Song and J. Zhang, in *PEM Fuel Cell Electrocatalysts and Catalyst Layers: Fundamentals and Applications*, ed. J. Zhang, Springer London, London, 2008, DOI: 10.1007/978-1-84800-936-3_2, pp. 89-134.

41. L. Sepunaru, E. Laborda and R. G. Compton, *Chemistry – A European Journal*, 2016, **22**, 5904-5908.

42. A. Damjanovic, M. A. Genshaw and J. O. Bockris, *The Journal of Chemical Physics*, 1966, **45**, 4057-4059.

43. X. Li, C. Batchelor-McAuley, S. A. I. Whitby, K. Tschulik, L. Shao and R. G. Compton, *Angewandte Chemie International Edition*, 2015, **55**, 4296-4299.

44. L. Meites, *Pure and Applied Chemistry*, 1985, **57**, 1491-1505.

45. R. G. Compton and C. E. Banks, *Understanding Voltammetry*, Imperial College Press, 2nd edn., 2011.

46. P. Han and D. M. Bartels, *The Journal of Physical Chemistry*, 1996, **100**, 5597-5602.

47. K. Aoki, K. Honda, K. Tokuda and H. Matsuda, *Journal of Electroanalytical Chemistry*, 1985, **182**, 267-279.

Chapter 5 Hydrogen Oxidation Reaction on Platinum Nanoparticles

In Chapters 3 and 4, the charge transfer of the electrode reaction was analysed with the consideration of the electrode environment, including the solvent reorganization, the external electrical field, the chemical bond. Apart from the electron transfer process, as an electrode reaction occurs at the interface, physical (mass transport) and chemical (solution-phase chemical reactions) processes of the redox species in the electrolyte solution also play important roles in determining the overall reaction rate. In the following chapters, the physical and chemical processes in the interface and their influence on the electrode reaction will be discussed.

In this Chapter, the kinetics of the hydrogen oxidation reaction (HOR) on platinum nanoparticles (PtNPs) is explored. The steady-state current for HOR on individual PtNPs is measured via the nano-impact approach. Adopting the Tafel-Volmer mechanism as discussed before, the adsorption rate constant for HOR on PtNPs can be calculated. The HOR is also studied on electrodes where PtNPs are immobilized via drop-casting on the supporting substrate prior to experimentation and the kinetic parameters contrasted with those from the nano-impact experiments. The experimental work was performed by Miss Xue Jiao and the work has been published in the Journal of Physical Chemistry C.[1]

5.1 Introduction

The physical and chemical properties of a material can change dramatically when the size decreases from the macro-scale to the nano-scale, leading to potential applications for nanoparticles in the fields of biotechnology, catalysis and energy.[2-5] In the area of catalysis, the small size provides large surface-to-volume ratio and often a high density of defects, which may alter the catalytic properties of nano-scale materials. Furthermore, investigations of nanoparticles lead to new insights into the structure-activity relationship of catalysts and help to understand the principles of the catalysis and heterogeneous reactions.[6, 7]

The electrocatalytic activity of nanoparticles is commonly studied as an ensemble effect by immobilising a large number of nanoparticles on an inert, conductive substrate.[8] Inherent in such work is the assumption that the structure and the morphology of the nanoparticles on the surface are well known. However, the coverage of the nanoparticles may change in the experiment due to the aggregation or loss of the nanoparticles, misleading the analysis of experimental phenomena observed on the nanoparticle ensemble.[9, 10] On the other hand, the so-called "nano-impact" or "single nanoparticle collision" technique allows the detection of the reaction at the single nanoparticle scale, providing more direct and detailed information on the nanoparticle electrocatalysis.

In this work, the kinetics of the hydrogen oxidation reaction (HOR) on Pt nanoparticles (PtNPs) is investigated. This reaction system is selected because it is a paradigmatic example of an inner sphere reaction and is of both fundamental and commercial interest.[11] The study of the hydrogen oxidation reaction is implemented both on ensembles of PtNPs and at individual PtNPs. The adsorption rate constant for the hydrogen oxidation reaction on individual PtNPs is measured to be 0.020 ± 0.008 m s^{-1}. It is further found that the kinetics for HOR on PtNPs detected from an ensemble of PtNPs is significantly underestimated, emphasizing the importance of applying the nano-impact technique to correctly understand electrocatalytic reactions on nanoparticles. Physical insights into the differences between single nanoparticle and ensemble behaviour are drawn.

5.2 Simulation of HOR on PtNP Modified Electrode

The hydrogen oxidation reaction occurs at the PtNP surface and follows the Tafel-Volmer mechanism as discussed in Chapter 3. The electrode reaction at the nanoparticle surface is described by the Langmuir adsorption and the Butler-Volmer electron transfer reaction. By solving the diffusion equations, the concentration profiles of the product H_2 and the product H^+ are calculated and the current-response of HOR on PtNP is then simulated. Different nanoparticle geometries are compared in order to explore a suitable and simple simulation model for the HOR on PtNPs.

5.2.1 Sphere and Disc Nanoparticle Model

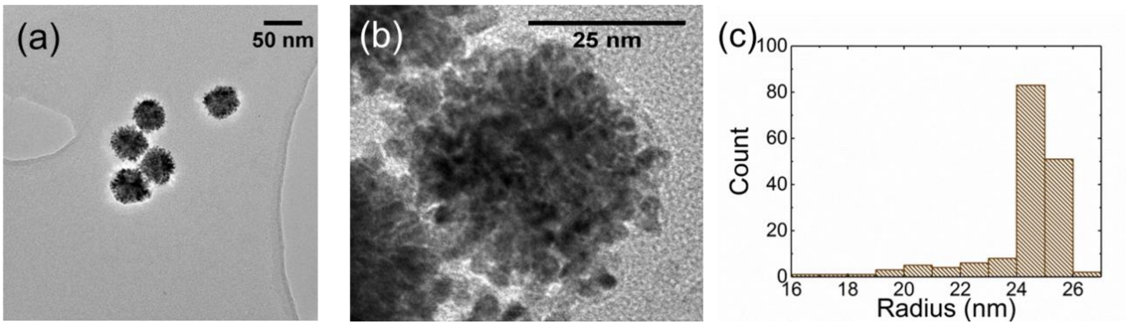

Figure 5.1 (a) TEM bright field image of PtNPs. (b) High-resolution TEM image of one PtNP. (c) Size distribution of the PtNPs with an average radius of 24.3 ± 1.6 nm.

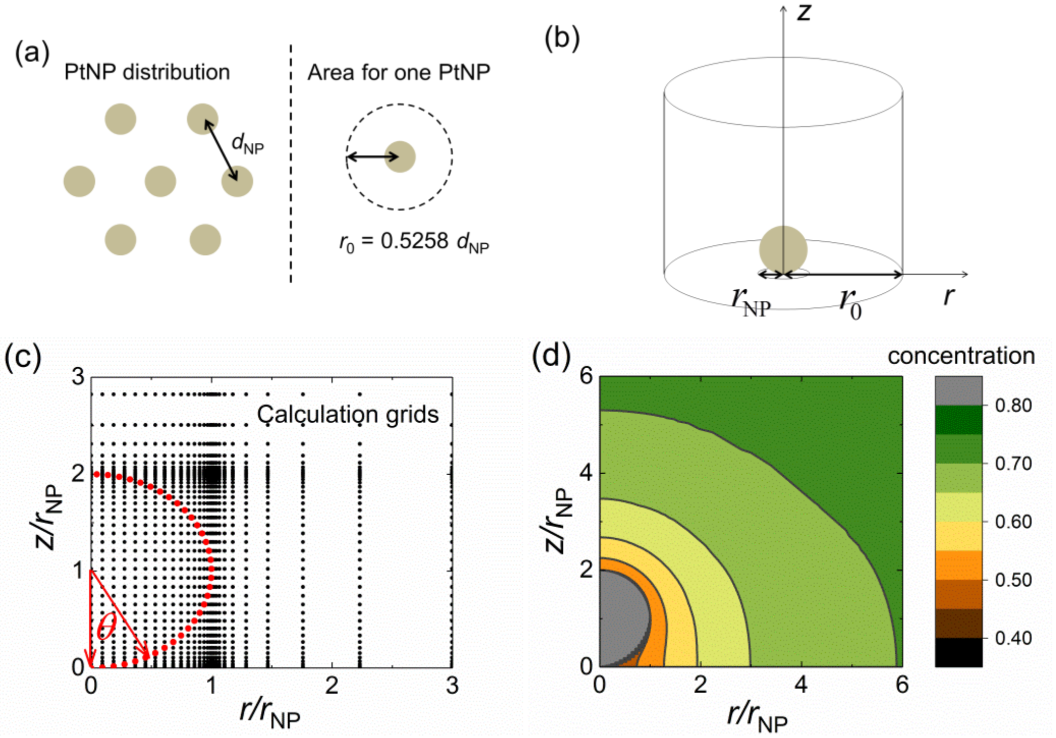

Figure 5.2 Simulation for the PtNPs modified electrode with the sphere model. (a) Distribution of the PtNPs on the supporting electrode, where the blue circles are PtNPs and the dashed line shows the simulation area for each PtNP; (b) Simulation space for one PtNP, where the blue sphere is the PtNP; (c) Calculation grids applied in a simulation cell, where the red points are the boundary of a PtNP; (d) An example concentration profile of the reactant.

The PtNP used in the experiment is regarded as a sphere with an average radius of 25 nm, of which the radius distribution can be observed from the TEM image, as shown in Figure 5.1. For the PtNP modified electrode, the PtNPs are assumed to be regularly dispersed on a supporting substrate. Although a regular distribution of the PtNPs is an idealised model, it has been previously applied successfully in the simulation for the drop-casting experiments, especially at low nanoparticle coverage.[12, 13] Therefore, the PtNP modified electrode is treated as a regular array in this work. For a nanoparticle array, the geometry of the nanoparticle also plays a crucial role. There is previous work discussing the influence of the particle geometry in the simulation for nanoparticle modified electrodes.[14] Here two geometries are discussed in the study of HOR on PtNPs: a 'sphere model' and a 'disc model'.

Figure 5.2 illustrates the 'sphere model' for the PtNP modified electrode. Figure 5.2a shows the regular distribution of the spherical PtNPs dispersed on the supporting substrate. The simulation space for each individual PtNP is estimated on the basis of the diffusion domain approximation.[15, 16] It has been shown that the diffusion domain approximation turns the 3-dimensional problem into a simpler 2-dimensional problem while attaining similar accuracy.[12, 16, 17] Figure 5.2b shows the simulation space under a 2-dimensional cylindrical coordinate for a spherical PtNP. In the cylindrical coordinate system, r is the coordinate parallel to the supporting electrode surface and z is that perpendicular to the supporting electrode. d_{NP} is the average centre-to-centre distance between two adjacent PtNPs, which can be inferred from the particle coverages used in the experiment. The distribution of the particles is approximated by a hexagonal packing arrangement and the simulating area for an individual PtNP on the supporting substrate is considered as a circular cell with a radius of 0.5258 d_{NP}.[18] The radius of the particle is r_{NP} and the radius of the simulation cell is r_0. Thus the d_{NP} and the coverage of PtNPs have the relationship:

$$\text{coverage} = \frac{r_{\mathrm{NP}}{}^2}{\left(0.5258 d_{\mathrm{NP}}\right)^2} \tag{5.1}$$

As the simulation area for one PtNP is symmetric, only half of the space needs to be calculated and the three-dimensional space in Figure 5.2b can be converted to a two-dimensional cell as shown in Figure 5.2c. Figure 5.2c displays the simulation geometry and the calculation grids for a PtNP, based on the approach in the literature.[19, 20] Within the area where $r < r_{\mathrm{NP}}$ and $z < 2*r_{\mathrm{NP}}$, the grids are given by:

$$\begin{aligned} r_m &= r_{\mathrm{NP}}\sin(\theta_m), \theta_m = 0, \frac{\pi}{200}, \ldots, \frac{99\pi}{200}, \frac{\pi}{2} \\ z_n &= r_{\mathrm{NP}}\left(1-\cos(\theta_n)\right), \theta_n = 0, \frac{\pi}{200}, \ldots, \frac{199\pi}{200}, \pi \end{aligned} \tag{5.2}$$

where m, n are the indexes of r and z directions. θ is the angle shown in Figure 2c. In our simulation, the angle from 0 to π in the sphere is evenly separated into 200 parts. For the rest, general expanding grids are applied. Figure 5.2d is an example of the concentration profile for an individual spherical PtNP, showing how the concentration of the reactant gradually changes from the bulk solution to the electroactive surface.

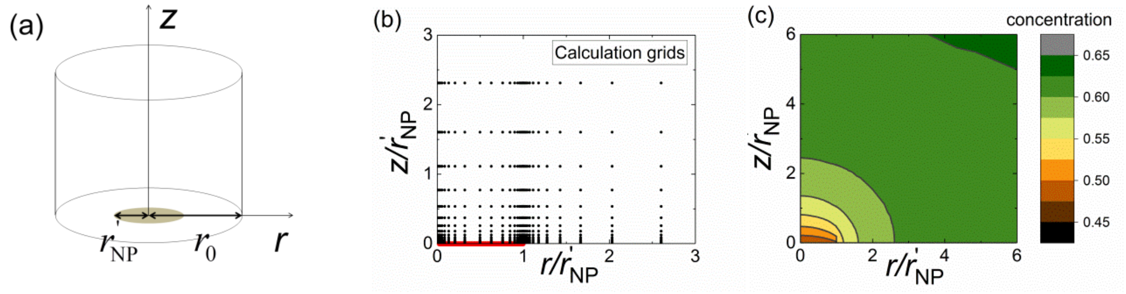

Figure 5.3 Simulation for the PtNPs modified electrode with the disc model. (a) Simulation space for one PtNP disc, where the blue sphere is the electroactive area for the PtNP; (b) Calculation grids applied in the simulation cell, where the red line shows the position of the electroactive area; (c) An example concentration profile of the reactant.

An alternative but more approximate approach to simulate the PtNPs modified electrode is to apply a disc geometry for the PtNP and keep the equivalent electroactive surface area to the PtNP sphere.[14] For the sphere model, the radius of the PtNP sphere r_{NP} is the average radius for real PtNPs, 25 nm. But as the PtNP disc should have the same surface area with the spherical one, the radius of the PtNP disc r_{NP}' is taken as equal to $2r_{\mathrm{NP}}$, 50 nm. The simulation space and the calculation grids are shown in Figure

5.3, also with an example of the concentration profile for the reactant on an individual disc PtNP. As the geometry is relatively simple in the disc model, general expanding grids are applied in the (r, z) space. In the r direction, as the boundaries are located at r = 0 and $r = r_{\mathrm{NP}}'$, the grids symmetrically expand from both 0 and r_{NP}' to the middle point $0.5r_{\mathrm{NP}}'$.

5.2.2 Numerical Simulation and Validation Test

The resulting problem was solved numerically by means of the Newton-Raphson method and the alternating direction implicit (ADI) method. In this chapter, cyclic voltammograms are simulated for the HOR on PtNP modified electrodes. The differences between the sphere model and the disk model will be discussed in next subsection. The simulation is written in C++ with OpenMP for multithreading and simulations are performed using an Intel(R) Xeon(R) 3.60G CPU.

The simulation results shown in this chapter are tested to be convergent. The validation of the simulation programs is also checked. The simulated steady-state currents with a fast reaction kinetics applied are compared with the theoretical diffusion-controlled currents. In the steady state, the analytical diffusion-controlled steady-state currents for HOR on the isolated sphere and the isolated disk can be expressed by:[18, 21]

$$I_{\mathrm{diff,\ disk}} = 4nFr_{\mathrm{NP}}^{'}c_{\mathrm{H_2}}^{*}D_{\mathrm{H_2}} \tag{5.3}$$

$$I_{\mathrm{diff,\ sphere}} = 4\pi nFr_{\mathrm{NP}}c_{\mathrm{H_2}}^{*}D_{\mathrm{H_2}}\ln 2 \tag{5.4}$$

where r_{NP} in Eqn.(5.4) is the average radius of the PtNP sphere and r_{NP}' is the radius of the disc. The steady-state currents for the disc and the sphere geometry are used in the validation test of the simulation programs.

5.2.3 HOR on PtNP Arrays

In contrast with the case of isolated PtNP, the diffusion to the PtNP array is not only influenced by the electrode size and geometry, but also related to the distribution of the nanoparticles on the supporting substrate. For the electrode modified by an ensemble of nanoparticles, typical current responses are simulated with different nanoparticle coverages.

Generally the diffusion conditions, determined by the experimental timescale and the coverages of the nanoparticles, can be divided into four limiting categories, defined as "cases 1~4".[14, 18] In cases 1 and 2, the diffusion zones for each particle are separated. But the diffusion zone is perpendicular to the surface of each individual particle for case 1 (short diffusion time) while it is radial from the surface for case 2 (long diffusion time). In cases 3, the radial diffusion zones for each individual particle overlap somewhat. In case 4, the diffusion zones for each particle fully overlap such that the overall diffusion region becomes planar and linear to the whole electrode. However, as in our experiments the size of the PtNP (25 nm) and the scan rate for HOR in the cyclic voltammetry (0.1 V s^{-1}) is fixed, the diffusion condition is determined by the coverage of the PtNPs on the supporting substrate and the reaction kinetics. Thus the case 1 which only occurs under an ultrashort experimental timescale will not be discussed in this work, while cases 2~4 are shown in the Figure 5.4. The diffusional cases for the three situations are distinct and thus lead to various voltammetric features. In addition to the diffusion mode, different reaction kinetics are considered as well: one where the reaction rate of HOR is fast and the limiting factor for the reaction rate is diffusion, the other where that the reaction rate of the HOR is limited by slow adsorption. From the previous study of HOR on Pt in Chapter 3, it is known that on microsize electrodes, the reaction rate of HOR is limited by the slow dissociative adsorption of H_2 and the electron transfer rate is relatively fast. Therefore, only the adsorption kinetics and the diffusion of the reactant are taken into consideration as possible limiting factors for the HOR on the PtNP.

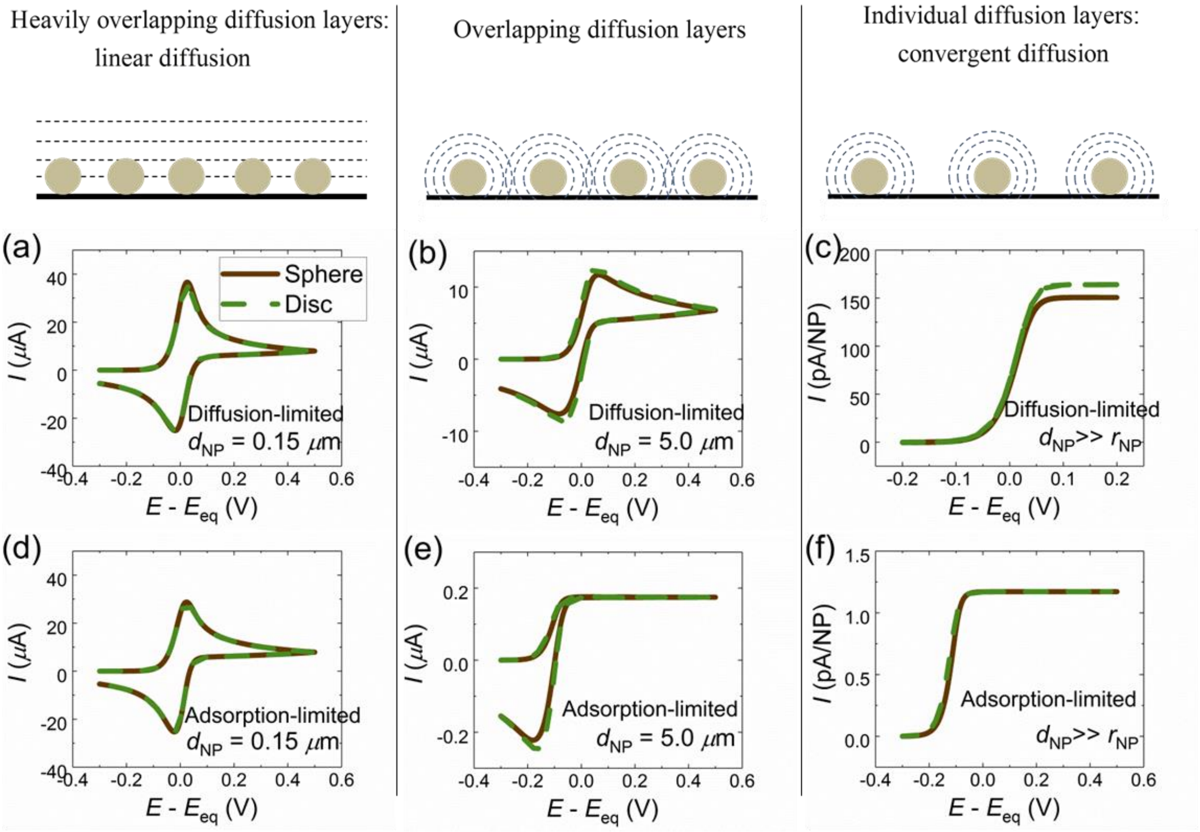

Figure 5.4 Comparison between the voltammograms with the sphere model (shown by the brown lines) and the disc model (shown by the green lines). The reaction rates in (a), (b) and (c) are limited only by the diffusion process and the electrochemical reaction is reversible. The reaction rates in (d), (e) and (f) are limited by the adsorption of H_2 and k_a = 0.001 m s^{-1}. k_d is 1.0 mol m^{-2} s^{-1} and k_0 is 1.0 m s^{-1}. r_{NP} in the nano-sphere model is 25 nm and r_{NP}' in the nano-disk model is 50 nm. $c^*_{H_2}$ is 0.78 mM. D_{H_2} is 5.0×10^{-9} m^2 s^{-1}. D_{H^+} is 8.1×10^{-9} m^2 s^{-1}.

Figures 5.4 a-c and Figures 5.4 d-f are simulated with different kinetics: the electrochemical reaction is "fast" but the current is limited by the diffusion of the reactant in Figures 5.4 a-c; the reaction is limited by the slow adsorption process in Figure 5.4 d-f. When the reaction is fast and the reaction rate is only limited by the diffusion of the reactant, these diffusion-controlled voltammograms change with different PtNP coverages, as shown in Figures 5.4 a-c. The "case 4" voltammetry of Figure 5.4a appears when the centre-to-centre distance between two adjacent PtNPs is small (compared to the diffusion layer thickness) and the diffusion layers for each PtNP are overlapped. In contrast, the fully steady-state ("case 2") voltammetry of Figure 5.4c can be observed when the distance between particles is large (compared to the diffusion layer thickness) and the diffusion regions for each particle are separated. The "case 3" voltammetric waveshape is between the "case 4" voltammetry and the "case 2" one, as shown in Figure 5.4b.

Figures 5.4d, 5.4e and 5.4f show the "case 4", "case 3" and "case 2" voltammograms under the adsorption-limited reactions. Although the diffusion-controlled voltammograms and the adsorption-limited ones have similar voltammetric features under the same PtNP coverage, the formation of the waveshapes and the steady-state currents are distinct. In the voltammograms of Figures 5.4a, 5.4b and 5.4c, the diffusion process is the limiting factor for the reaction while in Figures 5.4d, 5.4e and 5.4f, the slow adsorption process of H_2 prevents the increase of the current with the overpotential. Compared to the diffusion-controlled situation for one-electron-transfer reaction on nanoparticle arrays, which has been well-established in the literature,[22] the HOR has a more complex CE mechanism (C: chemical step; E: electrochemical step). As can be seen from Figure 5.4, the voltammetric responses for the CE reaction on nanoparticle arrays are strongly dependent on the reaction kinetics.

In Figure 5.4, the two simulation geometries, the spherical model of Figure 5.2 and the disc model of Figure 5.3, are also compared with respect to various distribution densities of the nanoparticles and different reaction kinetics. The simulated voltammograms based on the sphere model are shown in brown lines while those from the disc are in green. The electroactive areas for HOR on spherical and disc PtNPs are the same in the two simulation models. The voltammograms of the HOR in Figures 5.4a, 5.4b, 5.4c are simulated with fast and reversible reaction kinetics. The waveshapes for PtNP spheres and discs are very similar in "case 4" (Figure 5.4a) and "case 3" (Figure 5.4b) voltammograms. But in "case 2" (Figure 5.4c) the diffusion-limited steady-state currents for the sphere nanoparticle and the disc nanoparticle are different. In case 2, the nanoparticle coverage is so small that the diffusion zone of each nanoparticle is totally independent. As shown in Eqn. (5.3) and (5.4), the diffusion-controlled steady-state currents are related to the geometry of the electrode.

The “case 4”, “case 3” and “case 2” voltammetries, for cases where the reaction rate is limited by the adsorption kinetics, are shown in Figures 5.4d, 5.4e and 5.4f. When the coverage density of the particles is high on the supporting substrate, the forward peaks of the two simulated geometries overlap and the backward peaks have similar waveshapes and peak currents, as shown in Figures 5.4d and 5.4e. For the steady-state voltammetry in Figure 5.4f, in contrast to the results of Figure 5.4c, the kinetics-limited steady-state current is insensitive to the change of the geometry of the electroactive PtNP. Therefore, the alternative of the sphere model by the disc one is suitable for the kinetics-limited steady-state voltammetry. In steady state, when the adsorption process is a limiting factor, the adsorption-limited current I_{ad} on a disc microelectrode or nanoelectrode can be expressed as a function of k_{a}:[23]

$$I_{\mathrm{ad}} = I_{\mathrm{diff}} \frac{\dfrac{k_{\mathrm{a}} r_{\mathrm{NP}}}{D_{\mathrm{H_2}}}}{\dfrac{4}{\pi} + \dfrac{k_{\mathrm{a}} r_{\mathrm{NP}}}{D_{\mathrm{H_2}}}} \qquad (5.5)$$

which is also valid for an isolated PtNP sphere. But when applying to an isolated PtNP sphere it needs to be noted that I_{diff} used in Eqn.(5.5) is the diffusion current in the planar geometry model, calculated from Eqn.(5.3).

5.3 Hydrogen Oxidation Reaction on Single Platinum Nanoparticles

5.3.1 Nano-impact Experiments

The nano-impact experiment was performed by Miss Xue Jiao. All nano-impact electrochemical experiments were measured on a three electrode system in a Faraday cage. The working electrode was a gold microdisc electrode of diameter 10.0 μm from ALS, Tokyo, Japan and the electrode was polished with alumina powders from Buehler, Lake Bluff, IL, U.S.A of decreasing sizes: 1.0 μm, 0.3 μm and 0.05 μm. A leakless silver/silver chloride electrode [Ag/AgCl, 1.0 M KCl] from Cypress Systems, Lawrence, KS, U.S.A functioned as a reference electrode (measured as −0.006 V vs saturated calomel electrode, SCE, [Hg/Hg_2Cl_2, KCl (saturated)], which is equivalent to +0.235 V vs SHE). A platinum foil from Goodfellow, Cambridge, U.K. acted as a counter electrode.

All solutions were thoroughly saturated with hydrogen prior to experiments. All measurements were made under thermostatted conditions at 25.0 ± 0.5 °C.

An in-house built low noise potentiostat[8] was employed for both potentiostatic control and impact current measurement. A computer interface allowed analogue-digital conversion via a USB connected NI USB-6003 data acquisition (DAQ) device from National Instruments, Austin, TX, U.S.A. The DAQ device was controlled by a script written in Python 2.7 and run through the IDE Canopy from Enthought, Austin, TX, U.S.A. A low-noise current amplifier LCA-4K-1G from FEMTO, Messtechnik GmbH, Germany measured currents at the working electrode (running to ground), where its output bandwidth was limited by two cascaded passive RC-filters (100 Hz). The outcoming analogue signal was oversampled and digitized by the DAQ device at a stream rate of 4 kHz. A highly stabilized (1 kHz bandwidth) classic adder potentiostat[24] provided potentiostatic control. It is noted that a high quality operational amplifier, LMC6001 from Farnell, Leeds, U.K, with an ultra-low-input bias (25 fA) was used for the reference buffer; and a high quality low-noise operational amplifier, AD797 from Farnell, Leeds, U.K, controlled the potential at the counter electrode.

In the experimental data used below, all potentials are converted to the SHE scale.

5.3.2 HOR Kinetics on Individual Nanoparticles

The nano-impact technique enables the study of electrochemical reactions at individual nanoparticles. In this work, the hydrogen oxidation reaction on individual PtNPs is explored via the nano-impact approach. A gold micro-disc electrode (radius 5.0 μm) was employed and immersed in a 20 mM KNO_3 solution saturated with hydrogen gas. PtNPs were added into the electrolyte solution; when a PtNP strikes and sticks on the supporting Au electrode, current ‘spikes’ and ‘steps’ are observed in the chronoamperograms.

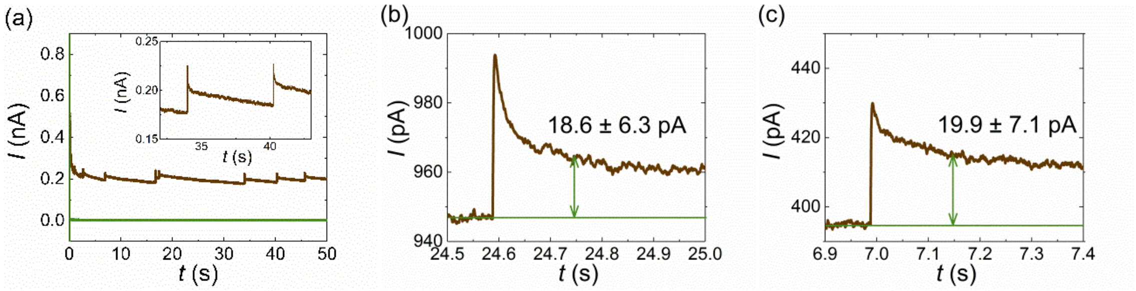

Figure 5.5 (a) chronoamperograms for a 5.0 μm Au microelectrode in 20 mM KNO_3 saturated with H_2; (b) and (c) are typical individual PtNP signals seen at 0.34 V and 0.44 V (vs SHE), respectively.

Figure 5.5 shows a typical current-time profile corresponding to the HOR on individual PtNPs. Figure 5.6a provides the chronoamperograms of 50 s duration at an overpotential of 0.44 V versus the standard hydrogen electrode, SHE. The brown line is the chronoamperogram measured in the presence of 20 pM PtNPs, while the green line shown for comparison is the blank chronoamperogram where no PtNP was added to the electrolyte. As shown in the inner panel of Figure 5.5a, current "steps" are recorded in the chronoamperogram in the presence of PtNPs. In the 'blank' chronoamperogram, no signal steps are visible. In the chronoamperogram with PtNPs added, current "steps" are only observed in the presence of H_2, indicating that steps are related to the oxidation of hydrogen on the PtNPs. For the case where both H_2 and PtNPs are present, the stepped nature of the responses suggests that the PtNPs are irreversibly adsorbed on the Au electrode.

Figures 5.5b and 5.5c show two representative current steps for HOR on individual PtNPs recorded at 0.34 V and 0.44 V (vs SHE), respectively. The current difference between the point at 150 ms from the starting point and the background (illustrated by the green lines in Figure 5.5b and 5.5c) is regarded as the steady-state current for HOR to an individual PtNP at a certain potential. By averaging the currents measured from several steps, the influence of the noise level on the signal caused by potentiosat is minimised. The average steady-state current is thus measured as 18.6 ± 6.3 pA at 0.34 V and 19.9 ± 7.1 pA at 0.44 V, where the standard deviation somewhat reflects not only the possible experimental noise/error but also the distribution of nanoparticle sizes. As the reacting current does not increase with the potential from 0.34 V to 0.44 V, the assumption that the current is indeed at steady state is reasonable and the steady-state current can be taken ca. 20 ± 7 pA. According to Eqn.(5.4), if the HOR on an individual PtNP is diffusion-controlled, the diffusional steady-state current I_{diff} would be expected to be 164 pA. The measured steady-state current on isolated PtNPs is clearly smaller than the diffusion-controlled value, showing that even on nano-size Pt, the reaction rate of the HOR is kinetically limited probably by the slow adsorption kinetics. Eqn.(5.5) describes the relationship between the adsorption rate constant k_{a} and the adsorption-limited steady-state current I_{ad}. The adsorption rate constant for HOR on an individual PtNP can be therefore calculated as 0.020 ± 0.008 m s^{-1}.

In Chapter 3, the adsorption rate constant k_{a} for HOR measured on polycrystalline Pt microdisc electrodes is measured to be 5×10^{-4} m s^{-1}. The steady-state current in Figure 5.5 implies an approximate k_{a} value of 0.02 m s^{-1} for HOR on the nano-size platinum. k_{a} thus approximately increases by 40 times from the polycrystalline Pt electrodes to the PtNPs. This may be because that compared to bulk Pt, the PtNP has much higher effective surface area. The k_{a} defined in the Tafel-Volmer mechanism is a “combined” adsorption rate constant, which is not only dependent on the property of the catalyst but also related to the maximum surface coverage Γ_{max}. For the same material, when Γ_{max} increases, the value of the “combined” k_{a} increases as a function of the square of Γ_{max}. Thus, the enhancement of k_{a} from 5×10^{-4} m s^{-1} to 0.02 m s^{-1} may suggest an increase of Γ_{max}. The simulation constant $\Gamma_{\mathrm{max}} = 2.2\times10^{-5}$ mol m^{-2} is only valid if the surface of the PtNP can be regarded as smooth as the poly-crystalline surface. However, as can be seen from the TEM images in Figure 5.1, the surface of the PtNP is composed of many smaller nanoparticles and is likely much ‘rougher’ than a polished poly-crystalline Pt surface. Therefore, a PtNP with a rough surface likely has a larger surface density of active sites for HOR than the smooth Pt electrode, indicating why the combined adsorption rate constant changes by ca. 40 times from the poly-crystalline Pt to the PtNP.

5.4 Hydrogen Oxidation Reaction on Drop-casted Platinum Nanoparticles

5.4.1 Drop-casting Experiments

The drop-casting experiment was performed by Miss Xue Jiao. A three electrode system in a Faraday cage was used for all drop cast electrochemical experiments. A μAutolab III from Metrohm Autolab B.V., Utrecht, The Netherlands, was employed as a potentiostat. The working electrode was a gold macrodisk electrode of radius 1.01 mm from BASi, West Lafayette, IN, U.S.A and the electrode was polished with alumina powders from Buehler, Lake Bluff, IL, U.S.A in a size sequence: 1.0 μm, 0.3 μm and 0.05 μm. The reference electrode was a standard mercury/mercurous sulfate electrode (MSE) [Hg/Hg_2SO_4, K_2SO_4 (saturated; + 0.64 V vs standard hydrogen electrode, SHE)] from BASi, West Lafayette, IN, U.S.A. The counter electrode was a graphite rod of diameter 6 mm from Sigma-Aldrich, Dorset, U.K. All experiments were conducted under a hydrogen atmosphere. All electrochemical and UV/Vis spectroscopy measurements were thermostatted at 25 ± 0.5 °C.

Nanoparticle modification of the gold macroelectrode was achieved through drop casting 1 μL of the stock PtNP suspension, directly from the manufacturer, onto the electrode surface. The electrode was subsequently allowed to dry under flowing nitrogen prior to experimentation.

5.4.2 Kinetics Influencing the Current-Potential Responses

For the hydrogen oxidation reaction (HOR) on the drop-casted PtNP clusters, there are four variables determining a voltammogarm: the centre-to-centre distance d_{NP}, the adsorption rate constant k_a, the desorption rate constant k_d and the standard heterogeneous rate constant k_0. The centre-to-centre distance can be calculated from the nanoparticle coverage used in the experiment and the adsorption rate constant k_a is measurable from the steady-state current. Therefore, the only two unknown kinetic parameters k_d and k_0 and their influence on the current-potential responses are explored via simulation, as shown in Figure 5.6.

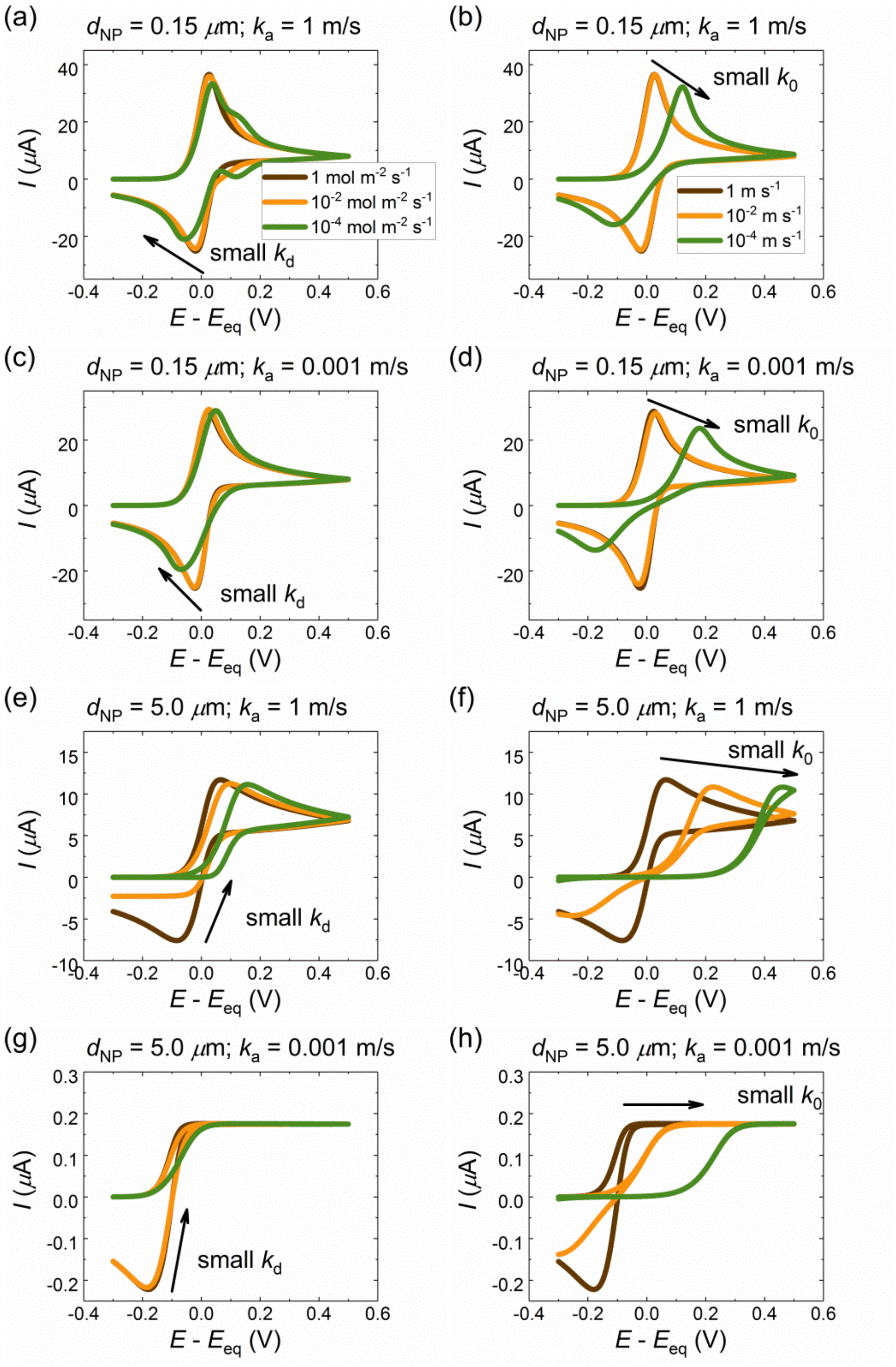

Figure 5.6 Voltammetric responses to the kinetic parameters k_d and k_0 with different particle coverages on the supporting substrate. In panels (a), (c), (e) and (g), k_0 = 1m s^{-1} and k_d = 1(brown), 0.01(orange) and 0.0001(green) mol m^{-2} s^{-1}. In panels (b), (d), (f) and (h), k_d = 1m s^{-1} and k_0 = 1(brown), 0.01(orange) and 0.0001(green) m s^{-1}. E – E_{eq} is the overpotential applied in the simulation.

Figure 5.6 shows example voltammograms with various kinetic parameters. The influences of k_d and k_0 are studied with two PtNP coverages (the large PtNP coverage where d_{NP} = 0.15 μm and the small PtNP coverage where d_{NP} = 5.0 μm) and two various adsorption rate constants (the fast adsorption process where k_a = 1 m s^{-1} and the slow adsorption one where k_a = 0.001 m s^{-1}). From Figure 5.6 a, c, e and g, it is found that a slow desorption rate constant k_d, corresponding to the process from H(ads) to H_2, can apparently decrease the backward peak current, especially under a small particle coverage or a slow adsorption process. From Figure 5.6 b, d, f and h, the decrease of the standard heterogeneous rate constant, k_0, can lead to an observable potential shift in the voltammogram and the peak-to-peak separation increases due to the irreversibility of the electron transfer step. Similarly to the influences caused by k_d, the voltammogram is affected more by k_0 when the PtNP coverage is small or the adsorption process is slow.

5.4.3 Variability of Drop-casted Nanoparticle Modified Electrode

To further explore the kinetics of the hydrogen oxidation reaction on nano-sized Pt, the HOR was next studied using PtNPs drop-casted on a gold electrode with various coverages via both experiment and numerical simulation. In contrast to the nano-impact experiments, the PtNPs are first immobilized on the supporting Au macro-electrode (radius 1.01 mm) prior to experimentation. Eight drop-casted electrodes with different coverages of PtNPs were employed in this work. The coverage is the percentage of the area occupied by all the PtNPs in the overall area of the substrate:

$$\text{Coverage of PtNPs (\%)} = \frac{N_{\text{NP}} \times \left(\pi r_{\text{NP}}{}^{2}\right)}{\pi r_{\text{Au}}{}^{2}} \times 100 \qquad (5.6)$$

where N_{NP} is the number of PtNPs and r_{Au} is the radius of the substrate Au electrode. The kinetic study of the HOR on the drop-casted electrodes is more complicated than on individual PtNPs, as the voltammetric features (for instance, the peak current) cannot be described by a simple equation but have to be modelled by numerical simulation. Since the HOR on PtNPs is known to be adsorption-limited, the disc model is applied in the simulation of the PtNP ensemble for convenience.

The aggregation or loss of the drop-casted nanoparticles can affect the experimental results measured from the drop-casted electrodes.[9] For this reason, the reproducibility of the HOR on various drop-casted PtNPs was tested and two of them are taken as examples: one is the electrode with a relatively high coverage of PtNPs (ca. 4.0%) and the other has a low coverage (ca. 0.06%). Figure 5.7 shows the reproducibility of the cyclic voltammograms for the HOR on the two electrodes. For both coverages, three voltammograms were recorded independently. Reasonable reproducibility is observed, especially for high coverage. The variability likely arises from some loss of the material. Therefore, the cyclic voltammograms with the highest signals were taken as represented of the coverages expected.

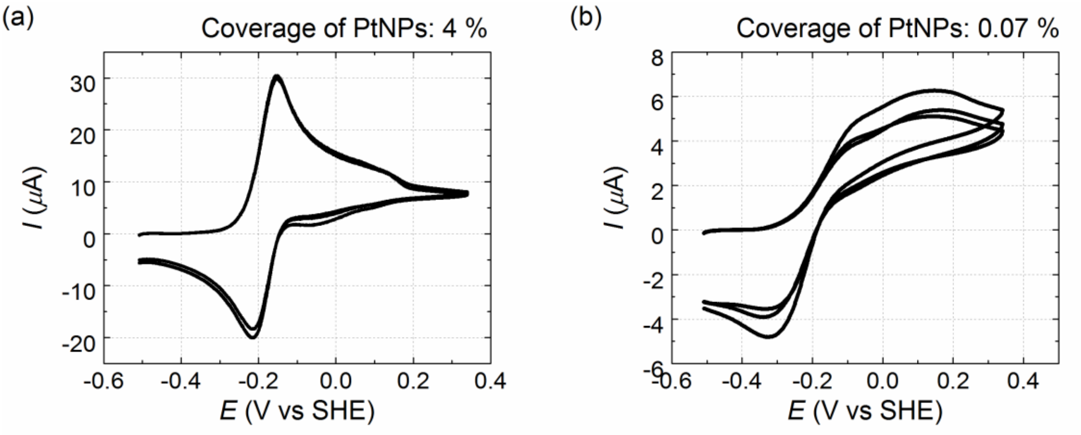

Figure 5.7 Cyclic voltammograms of the HOR on two drop-casted electrodes with different coverages of PtNPs: (a) 4.0 %; (b) 0.06 %. The electrolyte is 0.2 M KNO_3, the bulk concentration of hydrogen is 0.78 mM and the scan rate is 0.1 V s^{-1}. The substrate Au electrode has a 1.01 mm radius.

5.4.4 Cyclic Voltammetry on the Drop-casted Electrode

The experimental cyclic voltammograms for the HOR on various drop-casted electrodes are shown in Figure 5.8 a. The coverage of PtNPs varies from 0.03% to 4.0%. From Figure 5.8 a, for large PtNP coverages, the cyclic voltammogram shows an apparent peaked waveshape. When the coverage of the PtNP decreases, the peak becomes less observable. The voltammogram is nearly reversible when the PtNP coverage is high while it shows a quasi-reversible feature (the forward and backward peaks are not symmetric and the peak-to-peak separation becomes larger when the coverage decreases) especially under a small PtNP coverage, which indicates the value of k_0 cannot be either too small or too large. The back peaks are observed in all the experimental voltammograms, indicating that the desorption process cannot be ignored in the simulation.

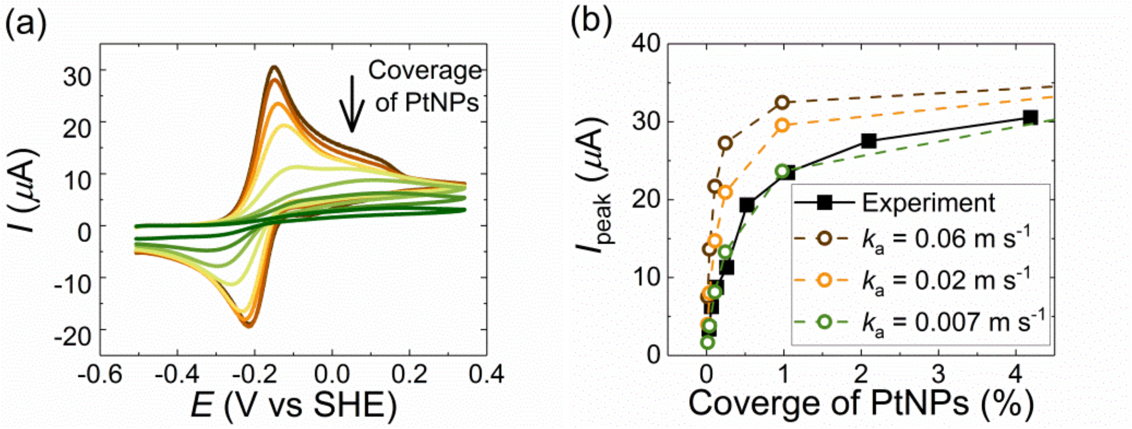

Figure 5.8 (a) Cyclic voltammograms for HOR on PtNPs drop-casted electrodes. The coverages of PtNPs from high to low are 4.0%, 2.0%, 1.0%, 0.50%, 0.25%, 0.12%, 0.06%, 0.03%. (b) Experimental and simulated forward peak currents varying as a function of the coverage of PtNPs. The black square points are from Figure 5.8a. The brown, orange and green circle points are from numerical simulations with k_a equal to 0.06, 0.02 and 0.007 m s^{-1}.

Figure 5.8 b shows the dependence of the forward peak current on the coverage of PtNP. The black line represents the experimental peak currents of Figure 5.8 a while the brown, orange and green lines are the peak currents obtained via the numerical simulation with different adsorption rate constants k_a, 0.06 m s^{-1}, 0.02 m s^{-1} and 0.007 m s^{-1}. In the simulation, when the value of k_a changed, we assigned the desorption rate constant k_d (unit: mol m^{-2} s^{-1}) and the standard heterogeneous rate constant k_0 (unit: m s^{-1}) the same number as k_a (unit: m s^{-1}). Among the simulated results shown in Figure 5.8 b, those shown for the 0.02 m s^{-1} k_a are the peak currents simulated with the adsorption rate constant measured in the nano-impact experiments. However, in Figure

5.8 b, the experimental peak currents for HOR on the drop-casted PtNPs clearly fit better with the simulated results of 0.007 m s^{-1} than 0.02 m s^{-1}, indicating the adsorption rate constant measured on the drop-casted PtNPs appears significantly less than that on the individual PtNPs.

It is now recognized that the drop-casting method leads to aggregation on surfaces and also that electrical contact between the nanoparticles and the substrate electrode cannot be guaranteed.[9] The disagreement between the kinetic data inferred from the two techniques likely, again, points to the limitation of the drop-casting approach. Applying the idealised nanoparticle coverages will thus lead to an underestimation for the kinetics of the electrochemical reaction. On the contrary, the nano-impact technique provides the opportunity to measure the reacting current occurring on an individual, active nanoparticle and thus the kinetic parameters determined from the nano-impact experiment are more likely to reflect the physical reality.

5.5 Summary

Two different electrochemical approaches, cyclic voltammetry on drop-casted electrodes and nano-impacts are used to determine the kinetics of the hydrogen oxidation reaction (HOR) on platinum nanoparticles (PtNPs). The adsorption rate constant for HOR on PtNPs can be quantified via the steady-state current measured on individual PtNPs in the nano-impact chronoamperometry or the voltammetric responses on the drop-casted PtNP ensembles with various PtNP coverages. In comparison with the adsorption rate constant measured on the bulk platinum electrodes, the adsorption rate for the HOR is larger on the PtNPs. This is likely a consequence of the high effective surface area of the nanoparticle as evidenced by the TEM data. At same time, the kinetic parameter obtained from the drop-casted PtNP ensembles (ca. 0.007 m s^{-1}) differs from the value on the individual PtNPs (ca. 0.02 m s^{-1}), reflecting that the kinetics of the electrocatalytic reaction can be misinterpreted and underestimated if the measurement is implemented on an ensemble of nanoparticles rather than at individual nanoparticles. The underestimation is attributed to aggregation or loss of the nanoparticle on the electrode surface in the drop-casting experiments. The nano-impact technique which allows the detection of individual nanoparticles has merits in the study of kinetics for electrocatalytic reactions.

References

1. X. Jiao, C. Lin, N. P. Young, C. Batchelor-McAuley and R. G. Compton, *The Journal of Physical Chemistry C*, 2016, **120**, 13148-13158.
2. T. Kim and T. Hyeon, *Nanotechnology*, 2014, **25**.
3. P. R. Bandaru, H. Yamada, R. Narayanan and M. Hoefer, *Materials Science and Engineering R: Reports*, 2015, **96**, 1-69.
4. F. Raimondi, G. G. Scherer, R. Kötz and A. Wokaun, *Angewandte Chemie - International Edition*, 2005, **44**, 2190-2209.
5. R. Tong, H. D. Hemmati, R. Langer and D. S. Kohane, *Journal of the American Chemical Society*, 2012, **134**, 8848-8855.
6. S. Mukerjee, *Journal of Applied Electrochemistry*, 1990, **20**, 537-548.
7. S. Chen and A. Kucernak, *Journal of Physical Chemistry B*, 2004, **108**, 13984-13994.
8. C. Batchelor-McAuley, J. Ellison, K. Tschulik, P. L. Hurst, R. Boldt and R. G. Compton, *Analyst*, 2015, **140**, 5048-5054.
9. H. S. Toh, C. Batchelor-McAuley, K. Tschulik, M. Uhlemann, A. Crossley and R. G. Compton, *Nanoscale*, 2013, **5**, 4884-4893.
10. H. S. Toh and R. G. Compton, *ChemistryOpen*, 2015, **4**, 261-263.
11. S. Gu, B. Xu and Y. Yan, *Annual Review of Chemical and Biomolecular Engineering*, 2014, **5**, 429-454.
12. T. J. Davies and R. G. Compton, *Journal of Electroanalytical Chemistry*, 2005, **585**, 63-82.
13. Y. Wang, K. R. Ward, E. Laborda, C. Salter, A. Crossley, R. M. J. Jacobs and R. G. Compton, *Small*, 2013, **9**, 478-486.
14. K. R. Ward, M. Gara, N. S. Lawrence, R. S. Hartshorne and R. G. Compton, *Journal of Electroanalytical Chemistry*, 2013, **695**, 1-9.
15. C. Amatore, J. M. Savéant and D. Tessier, *Journal of Electroanalytical Chemistry and Interfacial Electrochemistry*, 1983, **147**, 39-51.
16. O. Sliusarenko, A. Oleinick, I. Svir and C. Amatore, *Electroanalysis*, 2015, **27**, 980-991.
17. B. A. Brookes, T. J. Davies, A. C. Fisher, R. G. Evans, S. J. Wilkins, K. Yunus, J. D. Wadhawan and R. G. Compton, *The Journal of Physical Chemistry B*, 2003, **107**, 1616-1627.

18. R. G. Compton and C. E. Banks, *Understanding Voltammetry*, Imperial College Press, 2nd edn., 2011.

19. K. R. Ward, N. S. Lawrence, R. S. Hartshorne and R. G. Compton, *Journal of Physical Chemistry C*, 2011, **115**, 11204-11215.

20. E. Kätelhön, E. O. Barnes, K. J. Krause, B. Wolfrum and R. G. Compton, *Chemical Physics Letters*, 2014, **595–596**, 31-34.

21. I. Streeter and R. G. Compton, *Journal of Physical Chemistry C*, 2007, **111**, 18049-18054.

22. K. R. Ward, N. S. Lawrence, R. S. Hartshorne and R. G. Compton, *Journal of Electroanalytical Chemistry*, 2012, **683**, 37-42.

23. C. Lin, C. Batchelor-McAuley, E. Laborda and R. G. Compton, *The Journal of Physical Chemistry C*, 2015, **119**, 22415-22424.

24. R. M. Souto, *Electroanalysis*, 1994, **6**, 531-542.

Chapter 6 Redox Species Mediated Catalytic Reactions

In this chapter, a special catalytic process, in which the reactant species are either oxidized or reduced to form products exclusively via the electron transfer of the redox species, is investigated at individual and ensemble nanoparticles. The work has been published as part of two papers in the *Journal of Physical Chemistry C*.[1, 2] The experiment mentioned in section 6.4 was performed by Dr. Qianqi Lin.

6.1 Introduction

The heterogeneous EC' mechanism (E corresponds to an electron transfer step and C' to a catalytic step) is expressed as:

$$\mathrm{A(ads)} + e^- \rightleftharpoons \mathrm{B(ads)} \qquad \mathrm{(E)} \tag{6.1}$$

$$\mathrm{B(ads)} + \mathrm{R(sol)} \longrightarrow \mathrm{P(sol)} + \mathrm{A(ads)} \qquad (\mathrm{C}') \tag{6.2}$$

where A(ads) and B(ads) are the adsorbate redox couple, R(sol) and P(sol) are the reactant and product of the catalytic reaction. If the redox species is in the solution phase, a homogeneous EC' mechanism of the redox species mediated catalytic reactions can be written as:

$$\mathrm{A(sol)} + e^- \rightleftharpoons \mathrm{B(sol)} \qquad \mathrm{(E)} \tag{6.3}$$

$$\mathrm{B(sol)} + \mathrm{R(sol)} \longrightarrow \mathrm{P(sol)} + \mathrm{A(sol)} \qquad (\mathrm{C}') \tag{6.4}$$

The EC' reaction has a wide diversity of application and is the basis of many applicable techniques, such as the chemical etching for electrochemical etching with nanoscale accuracy[3] and the sensors for detecting glucose (diabetes testing),[4] ascorbic acid,[5] gases and alcohols.[6-8] The electrochemical response of the EC' reaction contains the contribution from the redox reaction and the cycling from the catalytic process. The existence of the catalytic reaction can significantly enhance the current signal and change the overpotential required for the electron transfer.[9] For this reason, EC' type reactions are also applied in the field of energy storage and transportation, as the advantage that high current densities can be achieved at low redox species concentration.[10] On the other hand, in the case where the additional catalytic process needs to be eliminated, the understanding of the kinetics for the whole system becomes very significant. In the electrochemical analysis, the detection of target analyte can be interfered by the coexistence of other reactive chemicals. For example, it is reported in the literature that the electrochemical detection of dopamine can be generally affected by ascorbic acid via a typical EC' reaction.[11] Therefore, it is important to explore the kinetics of this electrode reaction with the aim of revealing the kinetic factors which control the observed electrochemical response.

Recently nanoparticles have been widely used as efficient electrode materials in the electron conversion with the redox mediators A/B in such catalytic reactions.[12, 13] One approach to making nanoparticle electrodes is the surface modification, where a layer of nanoparticles is immobilized on the electrode surface. Often these function by conducting electrons to or from the electrode whilst also offering new active sites for reaction and hence promoting a catalytic reaction. In this way, at the very least, expensive materials on the supporting and inexpensive substrate electrodes (often carbon based) are used in minimal quantities but in other cases specific nano-effects are seen, most related with the small size of the nanoparticle.[14-16]

In this way the catalysis process is characterised via voltammetric techniques, to develop an understanding of the factors controlling catalysis at nanoparticle modified electrodes and in particular, consider particle size, particle shape and the inter-particle separation on the electrode surface.

6.2 Theoretical Model for EC' Reactions

In this section, the theoretical model and the numerical simulation applied for the homogeneous and heterogeneous catalytic reactions on nanoparticles is developed. To model the reaction on the nanoparticle modified electrode, the reaction is first simulated on a single nanoparticle located on a conductive, inert supporting electrode. The nanoparticle is treated as a nanoelectrode. Then an ensemble of nanoparticles immobilized on the supporting substrate is discussed. Two particle geometries for the nanoparticle, sphere and disc, are taken into consideration.

6.2.1 Theoretical Model for Heterogeneous EC' Reaction

Assuming the electron transfer step of the heterogeneous EC' reaction ((6.1)) is described by the Butler-Volmer equation, the reaction rate equations for the adsorbate A and the reactant R can be expressed as:

$$\frac{\partial \Gamma_{\mathrm{A}}}{\partial t} = -k_0 \exp\left(\frac{\beta F \eta}{RT}\right)\Gamma_{\mathrm{A}} + k_0 \exp\left(-\frac{\alpha F \eta}{RT}\right)\Gamma_{\mathrm{B}} + k_{\mathrm{c'}}\Gamma_{\mathrm{B}} c_{\mathrm{R(surf)}} \tag{6.5}$$

$$D_{\mathrm{R}} \left.\frac{\partial c_{\mathrm{R}}}{\partial z}\right|_{\mathrm{surf}} = -k_{\mathrm{c'}}\Gamma_{\mathrm{B}} c_{\mathrm{R(surf)}} \tag{6.6}$$

where Γ_{A} and Γ_{B} are the surface coverages of the adsorbates A and B (mol m^{-2}). Assuming that the nanoelectrode surface is covered by the redox species A (or the redox species A is actually the surface atoms) before the reactant is added into the solution, the sum of Γ_{A} and Γ_{B} during the reaction keeps constant, equal to the maximum surface coverage of the active sites Γ_{max}. k_0 is the standard electron transfer constant of reaction (6.1), α and β are the transfer coefficients ($\alpha + \beta = 1$).[17, 18] $\eta = E - E^{\mathrm{o}}_{\mathrm{f,\,(A(ads)/B(ads))}}$, E is the applied electrode potential and $E^{\mathrm{o}}_{\mathrm{f,\,(A(ads)/B(ads))}}$ is the formal potential (V) for the redox couple A(ads)/B(ads) defined under the condition $\Gamma_{\mathrm{A}} = \Gamma_{\mathrm{B}}$. $k_{\mathrm{c'}}$ is the catalytic rate constant of Eqn.(6.2) (mM^{-1} s^{-1}). For the redox reaction of adsorbates A and B, the electrode current is calculated by:

$$I = F\int \frac{\partial \Gamma_{\mathrm{A}}}{\partial t}\,\mathrm{d}S \tag{6.7}$$

Since the catalytic step is assumed irreversible, the concentration of P is not involved in the simulation. To simulate the electrode system, the mass transport of the solution-phase reactant R is described by the diffusion equation:

$$\frac{\partial c_{\mathrm{R}}}{\partial t} = D_{\mathrm{R}} \nabla^2 c_{\mathrm{R}} \tag{6.8}$$

Different from the homogenous case of (6.13), the catalytic reaction of the heterogeneous EC' reaction only happens at the electrode surface. By solving Eqn.(6.8) under the boundary conditions (6.5) and (6.6), the current response can be calculated via Eqn.(6.7).

6.2.2 Theoretical Model for a Homogeneous EC' Reaction

In the electron transfer step (6.3) of the homogeneous catalytic reaction, assuming the electron transfer is fast, the surface concentration of the redox couple can be described by the Nernst Equation:

$$\frac{c_{\mathrm{A,\ surf}}}{c_{\mathrm{B,\ surf}}} = \exp\left(\frac{F\eta}{RT}\right) \tag{6.9}$$

where F is the Faraday constant, R is the ideal gas constant, T is absolute temperature. The overpotential η equals to the difference between the applied potential E and the formal potential E_f. Note that no reaction is assumed on the supporting electrode where the overpotential required for reaction is assumed infinite. In contrast the use of Eqn.(6.9) presumes a negligible overpotential reflects the catalytic properties of the nanoparticle.

The reaction flux for A on the nanoparticle surface is expressed as:

$$j_{\mathrm{A}} = -D_{\mathrm{A}} \left.\frac{\partial c_{\mathrm{A}}}{\partial \vec{n}}\right|_{\mathrm{surf}} \tag{6.10}$$

where $\vec{n}$ is the vector perpendicular to the electrode surface, D is the diffusion coefficient. A reflective boundary condition is applied for the concentration gradient of R on both the nanoparticle and the inert supporting electrode surface:

$$\left.\frac{\partial c_{\mathrm{R}}}{\partial \vec{n}}\right|_{\mathrm{surf}} = 0 \tag{6.11}$$

In the theoretical model, it is assumed that the homogeneous catalytic reaction Eqn.(6.4) occurs only in the solution and the reactant R is inert on the electrode surface. Although the zero-gradient boundary condition for R on the electrode surface at first sight appears in contradiction to the fact that R can react in the solution layer just above the electrode, the zero-gradient boundary condition for species R has to be applied, otherwise the simulation deviates from our theoretical chemical model. In addition, the grid space in the simulation model between the first solution layer and the electrode surface is small enough to reduce any inaccuracy caused by the separation of the zero-gradient boundary condition on the electrode and the homogeneous reaction in the solution. The same reflective boundary condition is also applied for the redox species on the supporting electrode.

The change of the concentrations in the solution is driven by both diffusion and the homogeneous catalytic reaction:

$$\frac{\partial c_{\mathrm{A}}}{\partial t} = D_{\mathrm{A}} \nabla^2 c_{\mathrm{A}} + k_{\mathrm{cat}} c_{\mathrm{B}} c_{\mathrm{R}} \tag{6.12}$$

$$\frac{\partial c_{\mathrm{R}}}{\partial t} = D_{\mathrm{R}} \nabla^2 c_{\mathrm{R}} - k_{\mathrm{cat}} c_{\mathrm{B}} c_{\mathrm{R}} \tag{6.13}$$

k_{cat} is the homogeneous catalytic rate constant ($\mathrm{mM^{-1}\ s^{-1}}$).

Provided that $D_{\mathrm{A}} = D_{\mathrm{B}}$, the concentration of B in the above equations can be replaced by $c_{\mathrm{A}}^* - c_{\mathrm{A}}$, where c_{A}^* is the bulk concentration of A. By solving the partial differential equations (6.12) and (6.13), the concentrations of A and R can be derived. Therefore, the current can be calculated by:

$$I = \int F j_{\mathrm{A}} \mathrm{d}S \tag{6.14}$$

where S refers to the surface area of the electrode.

In order to discover the potential dependence of the current measured at the single nanoparticle, we simulate the current response to the potential which is swept over a range of interest. Note that in cyclic voltammetry, when the sweep rate of the potential is slow, a steady-state response is established on a time scale of $\tau = r_{\mathrm{el}}^2/D$ where r_{el} is the nanoparticle radius and $D \approx D_{\mathrm{ox}} \approx D_{\mathrm{red}}$. In particular for nanoparticles, the steady-state is established almost instantaneously but the treatment below allows in principle for application to particles of any size and any applied potential. To correspond to common electrochemical practice we also consider a reverse potential sweep and generate a cyclic voltammogram to characterise the homogeneous catalytic reaction on nanoparticles. To simulate this, the overpotential η is not a constant but varies as a function of the experimental time t:

$$\eta = \begin{cases} \eta_{\text{ini}} + vt & t \le \dfrac{|\eta_{\text{rev}} - \eta_{\text{ini}}|}{v} \\ \eta_{\text{rev}} + v\left(t - \dfrac{|\eta_{\text{rev}} - \eta_{\text{ini}}|}{v}\right) & t > \dfrac{|\eta_{\text{rev}} - \eta_{\text{ini}}|}{v} \end{cases} \tag{6.15}$$

where [η_{ini}, η_{rev}] is the sweeping window and v is the scan rate.

6.2.3 Numerical Simulation

Two different geometries of the nanoparticle are involved in the study of EC' reactions on nanoparticles: a sphere and a disc. As the diffusion is related with the geometry of the electrode system, both geometries are modelled and compared to explore the influence of the nanoparticle geometry on the catalytic reaction. As the simulation for a sphere which is located on the supporting substrate is more complex and time-consuming than that for a planar disc, the possibility of simplifying the geometry of a sphere into a disc is also examined. The illustration of the geometries and the simulation spaces for the two geometries are shown in Figure 6.1. As the geometry is symmetric, a two-dimension cylindrical coordinate system (r, z) is applied, where r is the radial direction parallel to the supporting substrate and z is perpendicular to r. Expanding grids are applied to reduce the computation time.[19]

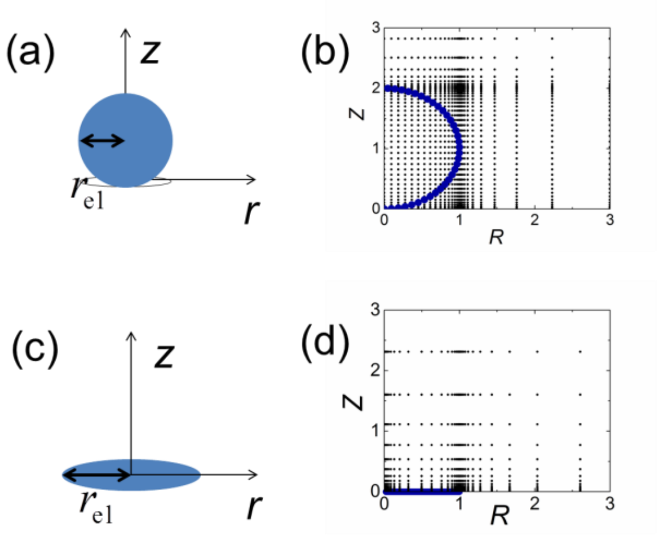

Figure 6.1 Illustration of the geometry and calculation grids for sphere (a, b) and disc (c, d) nanoparticles located on the supporting substrate. The blue lines in b and d show the position of the electrode surface. r_{el} is the radius of the electrode. In b and d, the normalized Z is equal to z/r_{el} and R is r/r_{el}.

The ensemble of nanoparticles modified on the supporting substrate is a nanoparticle array. Here the regular array is applied to simulate the nanoparticle modified electrode. For the regular array model, the inert substrate is split into a regular distribution of cells, where each cell contains one nanoparticle and, assuming close packing, each cell has the shape of a hexagon. As all the cells are equivalent, only one cell needs to be simulated in order to explore the electrochemical behaviour of the whole nanoparticle array. Figure 6.2 shows an illustration of the regular nanoparticle array and the diffusion domain approximation of one nanoparticle, where d is the average distance between two nearby nanoparticles and r_{domain} is the radius of the circle diffusion domain area. In the diffusion domain approximation, the hexagonal cell of Figure 6.2b has the same area with a circular cell.[20] Therefore, the coverage of nanoparticles are defined by $(r_{\mathrm{el}}/r_{\mathrm{domain}})^2$. The current measured from the array equals $n_{\mathrm{domain}}I$. I is the current detected from one nanoparticle. n_{domain} is the number of the nanoparticles and $n_{\mathrm{domain}} = (r_{\mathrm{sup}}/r_{\mathrm{domain}})^2$, where r_{sup} is the size of the substrate electrode. The simulation space for one nanoparticle in the array is the diffusion domain and similar calculation grids are built as applied in Figure 6.1. In contrast to the single nanoparticle, when simulating the array, as the two nearby cells are symmetric, there is no flux passing through the boundary of each simulation cell. The concentration gradient for solution species is zero at $r = r_{\mathrm{domain}}$.

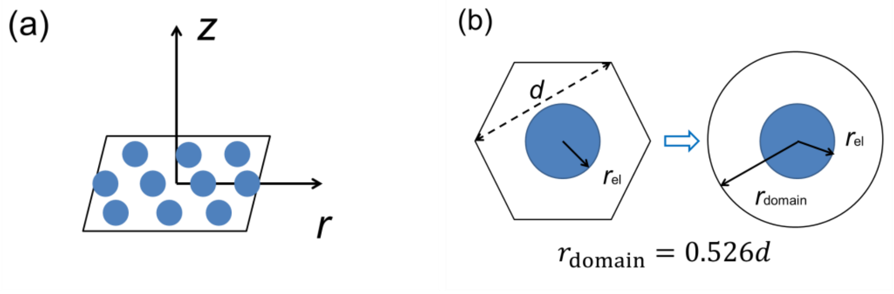

Figure 6.2 (a) Regular distribution of the nanoparticles on the supporting surface; (b) Diffusion domain approximation for one cell.

The resulting problem was solved numerically by means of the Newton-Raphson method and the alternating direction implicit (ADI) method as introduced in Chapter 2. The simulation programmes were written in Matlab R2016a and performed using an Intel(R) Xeon(R) 3.60G CPU. The convergence and validation of the results in this chapter were tested.

6.3 Heterogeneous EC' Reaction on Nanoparticle Modified Electrodes

The electrode system where the surface adsorbates mediate electron transfer to or from a species in solution via the heterogeneous EC' mechanism is studied on single nanoparticles and nanoparticle ensembles.

6.3.1 Heterogeneous EC' Reaction on the Single Particle

To understand the current-potential response of the EC' reaction, the voltammograms of an electron transfer in the simple oxidation of adsorbate A ("E reaction", Figure 6.3a) and a heterogeneous EC' reaction (Figure 6.3b) are simulated for various standard electrochemical rate constants, k_0. The current in Figure 6.3 is normalised by the peak current of one electron transfer reaction between the adsorbate and the electrode. Theoretically, the peak current can be calculated from the experimental conditions:[21]

$$I_{\text{peak, 1e}} = \frac{F^2}{4RT} vS\Gamma_{\max} \tag{6.16}$$

v is the scan rate, S is the electrode surface area, and $\Gamma_{\max}$ is the maximum surface coverage of the active sites. As shown in Figure 6.3, a peak is generated around the formal potential of the A(ads)/B(ads) redox couple and the current drops to zero at high overpotentials. This wave shape and the decrease to zero current are a consequence of the finite amount of electroactive species on the electrode surface. A decrease in k_0 causes changes in both the adsorption peak height and the peak position. For the EC' reaction, the concentration of R was selected as 1 mM, the catalytic rate constant as 1 M^{-1} s^{-1}, the diffusion coefficient of R as 1×10^{-9} m^2s^{-1}. The rest of simulation conditions are the same as those set for the E reaction. Figure 6.3b shows when the product of E reaction becomes the mediator of the following catalytic reaction, the current signal is enhanced and the voltammogram shows distinct and different waveshape. The peak vanishes and the current at high overpotentials is not zero but reaches a steady state. The effect of k_0 is reflected on the half-wave potential while the steady-state current is independent of k_0 as well as the overpotential is high enough to make the reaction fully driven.

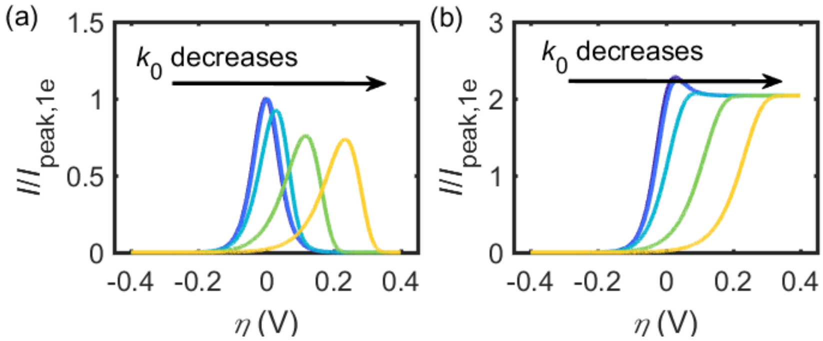

Figure 6.3 Influence of the electron transfer rate on the cyclic voltammograms. (a) E reaction. (b) Heterogeneous EC' mechanism. k_0 applied in the simulation are 100, 10, 1, 0.1, 0.01 s^{-1}, respectively. The rest of the simulation conditions can be found in the text.

For the case of microsize or even nanosize electrodes, the tiny size of the electrode that the steady-state diffusion of R is rapidly established. The analytical expression of the steady-state current can be derived on the basis of the steady-state approximation. At steady state, A is the intermediate between a slow catalytic reaction and a fast redox reaction. The reaction rate of the intermediate A of Eqns. (6.5) and (6.6) should be zero:

$$\frac{\partial \Gamma_{\mathrm{A}}}{\partial t} = -k_0 \exp\left(\frac{\beta F}{RT}\eta\right)\Gamma_{\mathrm{A}} + k_0 \exp\left(-\frac{\alpha F}{RT}\eta\right)\left(\Gamma_{\max} - \Gamma_{\mathrm{A}}\right) + k_{\mathrm{c'}}\left(\Gamma_{\max} - \Gamma_{\mathrm{A}}\right)c_{\mathrm{R(surf)}} = 0 \tag{6.17}$$

The current density at steady state can be then expressed as:

$$\frac{I}{FS} = k_{\mathrm{c'}}\left(\Gamma_{\max} - \Gamma_{\mathrm{A}}\right)c_{\mathrm{R(surf)}} \tag{6.18}$$

At the steady-state, the diffusion on the microelectrode surface can be approximated as linear and the concentration of R, as well as the surface coverage of A, is considered uniform in the radial direction. Therefore, the concentration difference only appears on the direction perpendicular to the electrode surface and the concentration gradient of R at the electrode surface can be calculated by:

$$D_{\mathrm{R}} \left.\frac{\partial c_{\mathrm{R}}}{\partial z}\right|_{\mathrm{surf}} = D_{\mathrm{R}} \frac{c_{\mathrm{R}}^{*} - c_{\mathrm{R(surf)}}}{\delta} = k_{\mathrm{c'}}\left(\Gamma_{\max} - \Gamma_{\mathrm{A}}\right)c_{\mathrm{R(surf)}} \tag{6.19}$$

where δ is the diffusion layer thickness. $\delta = r_{\mathrm{el}}/\delta_{\mathrm{geo}}$, δ_{geo} is a geometry factor dependent on the nanoparticle shape and location. δ_{geo} is $4/\pi$ for a planar nanoparticle on an inert supporting electrode and ln2 for the corresponding spherical case. For a microdisc electrode, the diffusion layer thickness equals to $\pi r_{\mathrm{el}}/4$. The surface coverage of the adsorbate A is zero at steady state. Combining Eqns. (6.18) with (6.19) gives the steady-state current for a heterogeneous EC' reaction on a microdisc electrode:

$$I_{\mathrm{ss}} = \frac{FSc_{\mathrm{R}}^{*}}{\dfrac{1}{k_{\mathrm{c'}}\Gamma_{\max}} + \dfrac{1}{4D_{\mathrm{R}}/\pi r_{\mathrm{el}}}} \tag{6.20}$$

Therefore, when the steady-state current is known, the catalytic reaction rate constant of the heterogeneous EC’ reaction ($k_{c'}$) can be determined.

From Eqn.(6.20), it is also found that at high overpotential, where the electron transfer does not limit the whole reaction rate, the reaction rate contains the contribution from the heterogeneous catalytic kinetics and the diffusion speed toward the electrode surface. The heterogeneous catalytic kinetics is reflected by the term $k_{c'}\Gamma_{\max}$ and the diffusion speed can be expressed by $\delta_{\text{geo}}D_{\text{R}}/r_{\text{el}}$. By comparing the magnitude of the two terms, we know the rate-determining factor of a heterogeneous EC’ system.

6.3.2 Heterogeneous EC’ Reaction at an Ensemble of Nanoparticles

For the heterogeneous E reaction, when the electron transfer is fast, the reaction current should be only related to the total surface area of the modified nanoparticles and will not be influenced by either the geometry of the nanoparticle or the distance between two adjacent nanoparticles. For the heterogeneous EC’ reaction, the catalytic kinetics and the diffusion of the solution-phase reactant can affect the reaction current. The catalytic kinetics $k_{c'}\Gamma_{\max}$ is only dependent on the total surface area of the nanoparticles while the diffusion mode of the reactant is related to the distribution of the nanoparticle on the supporting substrate.

In Figure 6.4, the distance between two adjacent nanoparticles d varies from $3r_{\text{NP}}$ to $100r_{\text{NP}}$. The disc-shape geometry is applied in Figure 6.4 and similar results can be observed in spherical nanoparticle ensembles. To study the influence of the nanoparticle distribution, the current in Figure 6.4 is divided by the total number of nanoparticles on the supporting substrate. Figure 6.4a corresponds to the case of single E reaction, where the current is proved to be independent of d. Figure 6.4b is the condition of relatively slow catalytic kinetics and Figure 6.4c is the slow diffusion. It is found in Figure 6.4a that the current-response at each nanoparticle is identical for the E reaction at different nanoparticle ensembles. For the EC’ reaction, if the heterogeneous catalysis is the rate-determining step, as shown in Figure 6.4b, the reaction is not limited by the diffusion and the current measured from the whole electrode is only related to the amount of nanoparticles modified on the supporting substrate. However, when the diffusion speed becomes smaller, the current is not only proportional to the number of immobilized nanoparticles but also affected by the distance between two nearby nanoparticles. Higher current is observed at the nanoparticles which are closer to its neighbours, as the consequence of overlapped diffusion layers.

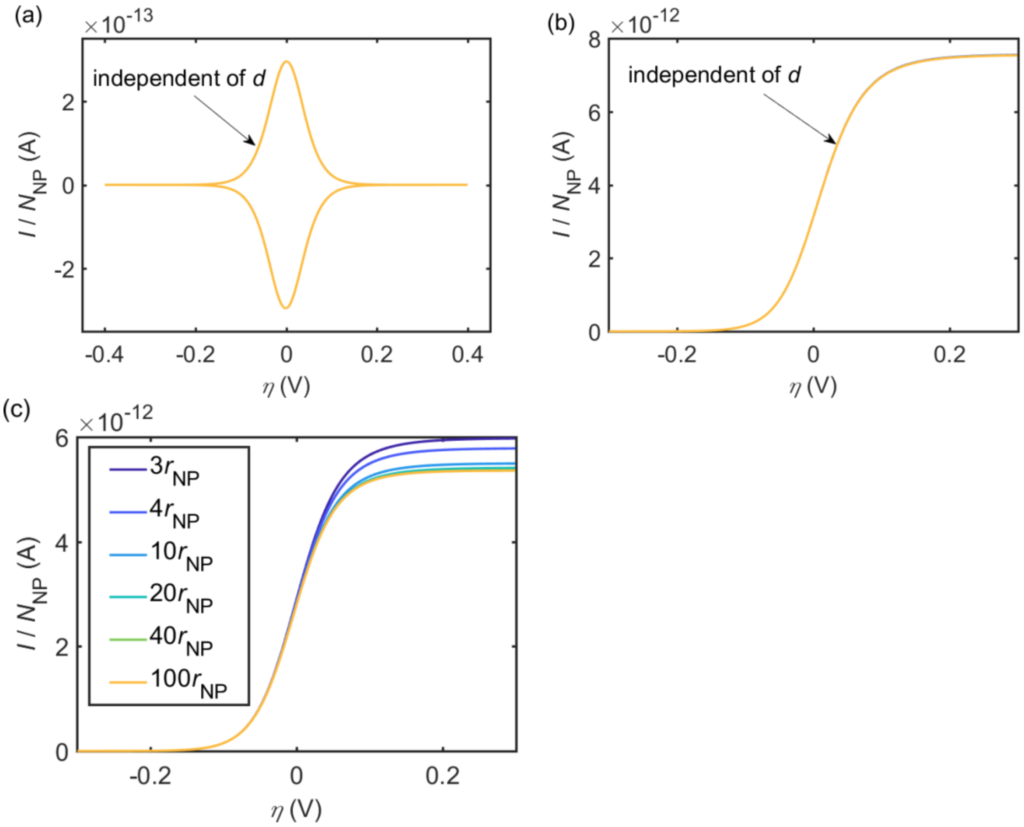

Figure 6.4 Current responses per nanoparticle at various nanoparticles modified electrodes with different distance *d* between two adjacent nanoparticles. (a) heterogeneous E reaction; (b) heterogeneous EC' reaction with fast diffusion; (c) heterogeneous EC' reaction with slow diffusion. The distances between two adjacent nanoparticles *d* are $3r_{NP}$, $4r_{NP}$, $10r_{NP}$, $20r_{NP}$, $40r_{NP}$, $100r_{NP}$. In the simulation $c_R^* = 1$ mM, $\Gamma_{max} = 2*10^{-6}$ mol m^{-2}, $r_{el} = 1$ μm, $k_{c'} = 5$ mM^{-1} s^{-1}, $D_R = 10^{-9}$ m^2 s^{-1} in 6.4b and 10^{-11} m^2 s^{-1} in 6.4c.

6.4 Example: Poly(vinylferrocene) Modified Graphene Nanoplatelet Mediated L-Cysteine Oxidation

In this section, the kinetics of the oxidation of L-Cysteine mediated by poly(vinylferrocene) modified graphene is studied with the combination of the nano-impact experiment and the numerical simulation.

6.4.1 Experimental procedure

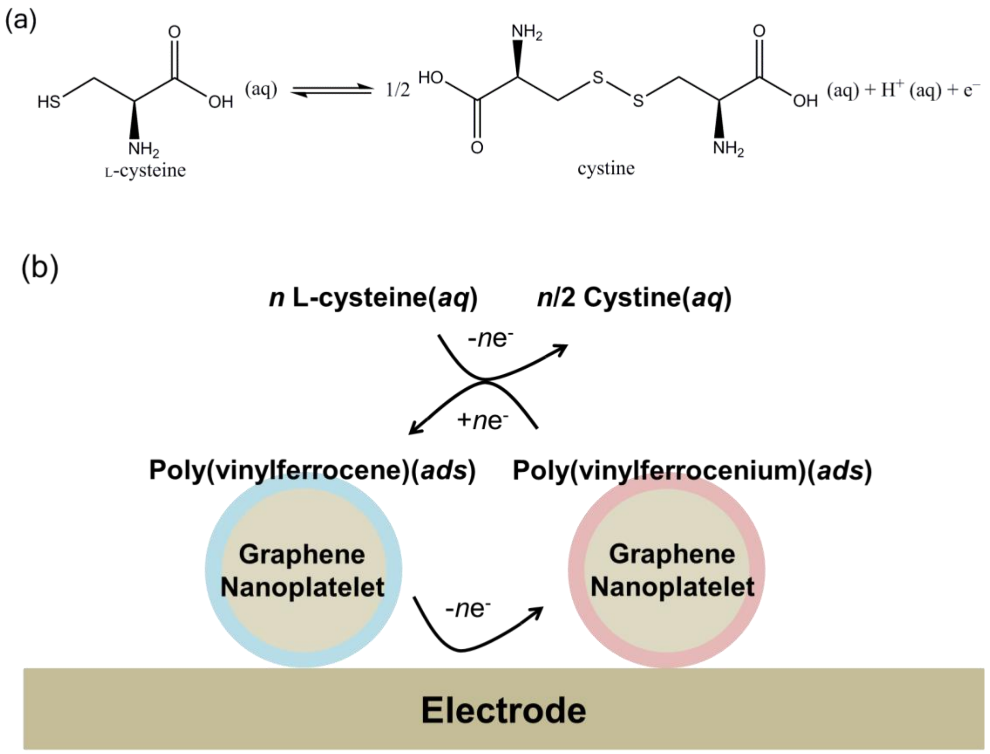

Figure 6.5 (a) Scheme of the oxidation reaction of L-cysteine. (b) Illustration of the PVF-GNP mediated L-cysteine oxidation.

The experiment was performed by Dr. Qianqi Lin. A standard three electrode cell was employed to conduct all the electrochemical experiments. An edge-plane pyrolytic graphite (EPPG) electrode (radius 2.0 mm) was used for preliminary voltammetric measurements, while a carbon fibre micro wire electrode (radius 3.5 μm and length 1 mm) was used for the nano-impact measurements, both acting as the working electrode.

The in-house EPPG was fabricated using highly ordered pyrolytic graphite (Le Carbone, Sussex, U.K.). A saturated calomel electrode (SCE, ALS distributed by BASi, Tokyo, Japan) and a platinum wire (99.99% GoodFellow, Cambridge, U.K.) were used as the reference and counter electrode respectively. Voltammetry was recorded using a μAutolab III potentiostat (Autolab, Utrecht, Netherlands) and nano-imapct chronoamperometry was conducted using an in-house built low noise potentiostat.[22] All the experiments were completed in a Faraday cage thermostated at 25 ± 1 °C.

For cyclic voltammetry, the EPPG electrode was cleaned by polishing in an alumina slurry of decreasing particle size (1.0-0.05 μm, Buehler, IL, U.K.). A cyclic voltammogram in a blank pH 7 aqueous solution was run with 0.1 M KCl to confirm the cleanliness of the electrode. After the EPPG electrode was rinsed and nitrogen (N_2) blown dried, it was transferred to a filter paper (70 mm, Fisherband, Loughborough, U.K.) with the prepared PVFc-GNPs. The particles were abrasively modified onto the electrode surface for at least 100 cycles of figure of eight. After the electrode modifications, a cyclic voltammogram was recorded in 25 mL of either blank or 10 mM L-cysteine pH 7 aqueous solution with 0.1 M KCl at a scan rate of 50 mV s^{-1}. The oxidation reaction of L-Cysteine is shown in Figure 6.5a and the mediated catalytical reaction is illustrated in Figure 6.5b.

For nano-impact chronoamperometry, the prepared PVFc-GNPs were suspended in 5 mL of various concentrations of a L-cysteine pH 7 aqueous solution supported with 0.1 M KCl. The concentration of the GNPs was *ca.* 3×10^{-14} M.[23, 24] The mixture was sonicated to achieve a good suspension, and bubbled with N_2 to remove the dissolved oxygen. Nano-impact chronoamperometry was run at the same time as degassing. As a control experiment, another chronoamperometry was run while degassing in the same electrolytic solution but with the absence of the GNPs. Two potentials, +0.20 and +1.00 V, were applied to the electrode for 20 s to generate a chronoamperogram.

6.4.2 Electrochemistry of L-cysteine Oxidation

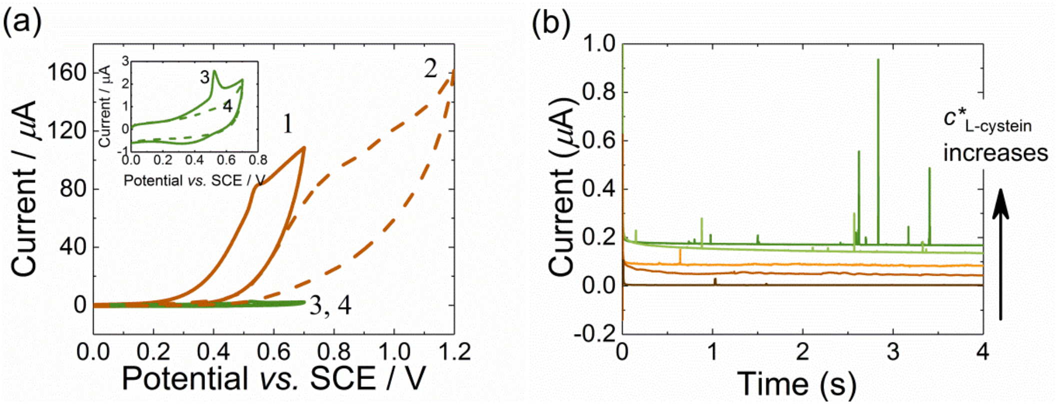

Figure 6.6 (a) Voltammogram in a N_2 degassed pH 7 aqueous solution supported with 0.1 M KCl at PVFc-GNPs modified EPPG electrodes *via* abrasive modification (1 and 3), and at unmodified EPPG electrodes (2 and 4). 10 mM L-cysteine is presence in 1 and 2. L-cysteine is absence in 3 and 4. Scan rate = 50 mV s^{-1}. (b) Nano-impacts chronoamperograms of 3 × 10^{-14} M GNPs suspension at carbon fibre micro wire electrodes potentiostatted at +1.00 V (*vs.* SCE), in a N_2 degassed pH 7 aqueous solution supported with 0.1 M KCl. Various concentrations of L-cysteine are used: 0, 5, 10, 15 and 20 mM. Baselines are shifted vertically for clarity.

The cyclic voltammetry of the L-cysteine oxidation is shown in Figure 6.6a. The solid brown line 1 is the oxidation of L-cysteine mediated by the PVFc-GNPs modified EPPG electrode, while the dash brown line 2 is the oxidation of L-cysteine with an unmodified electrode. The solid green line 3 and the dash green line 4 are measured in the absence of the reactant L-cysteine. Line 3 is the redox reaction of PVFc-GNP at the modified electrode, where the redox reaction of ferrocene is observed at around + 0.54V. Line 4 is the blank experiment with the unmodified electrode. Comparing line 1 and line 2, it is found that at the unmodified electrode, the oxidation of L-cysteine occurs at around +0.8 V, which is consistent with the literature for the *direct* oxidation of L-cysteine in a pH 7 buffer solution.[25] In contrast, when the electrode is modified with the catalyst PVFc-GNPs, the reaction occurs at *ca.* 0.54 V, close to the oxidation potential of the ferrocene moiety as shown in line 3. This can be ascribed to the oxidation of L-cysteine mediated by the ferrocenium cation. The mediated oxidation of L-cysteine is proposed via the heterogeneous EC' catalytic mechanism:

$$\mathrm{Cp_2Fe\left(ads\right)} \underset{}{\overset{k_0}{\rightleftharpoons}} \mathrm{Cp_2Fe^+\left(ads\right) + e^-} \tag{6.21}$$

$$\mathrm{Cp_2Fe^+\left(ads\right) + L\text{-}cysteine(sol)} \xrightarrow{k_{c'}} \mathrm{Cp_2Fe\left(ads\right) + product(sol)} \tag{6.22}$$

where the Cp_2Fe/Cp_2Fe^+ couple serves as the catalyst for the oxidation of L-cysteine, k_0 is the standard electrochemical rate constant of the Cp_2Fe/Cp_2Fe^+ couple at the GNPs surface, and $k_{c'}$ is the heterogeneous rate constant.

Figure 6.6b shows the study of the nano-impacts of PVFc-GNPs in L-cysteine containing solutions at carbon fibre micro wire electrodes. According to the cyclic voltammetry at the PVFc-GNPs modifed EPPG electrodes, the mediated oxidation of L-cysteine is expected to commence when the potential applied to the electrode is at least *ca.* +0.54 V (*vs*. SCE). The electrode was potentiostatted at +1.00 V (*vs*. SCE) to allow a large overpotential to fully drive the reaction. As discussed in the context of Figure 6.3b, at high overpotentials the oxidation of L-cysteine at an individual PVFc-GNP can reach a steady state, allowing the characterisation of the catalytic mechanism and kinetics. The prepared PVFc-GNPs were first suspended in 5 mL of pH 7 / 0.1 M KCl aqueous solution with the absence of L-cysteine. A chronoamperometry was run using a carbon fibre microwire electrode. When there is no L-cysteine in the solution (the black line at the bottom in Figure 6.6b), nano-impact spikes of PVFc-GNPs were observed. The charge passed per spike can be estimated by taking the integrated area under the individual spike, with the average value denoted as $\bar{Q}$. For the absence of L-cysteine, $\bar{Q}$ is 6 $^{+8}_{-6}$ pC. The PVFc-GNPs was then suspended in 5 mL of 20 mM L-cysteine / 0.1M KCl solution. The top line of Figure 6.4b shows the nano-impacts signals are significantly enhanced, with the value for $\bar{Q}$ as 180 ± 172 pC. Further, the experiment was repeated for various concentrations of L-cysteine, 5 mM, 10 mM and 15 mM (middle lines in Figure 6.4b). The corresponding $\bar{Q}$ for the three concentrations is 13 $^{+45}_{-13}$ pc, 62 ± 31 pC and 131 ± 105 pc, respectively. The variation is shown in Figure 6.7 (squares), where $\bar{Q}$ is plotted against the concentration of L-cysteine ($c^*_{\text{L-cysteine}}$).

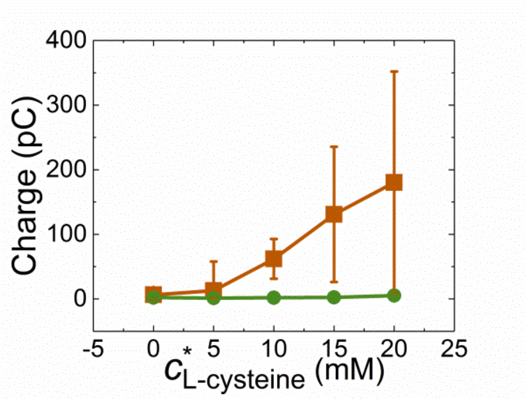

Figure 6.7 The average charge ($\bar{Q}$) passed per nano-impacts spike dependence of L-cysteine concentration ($c^{*}_{\text{L-cysteine}}$), at +1.00 V (squares) and +0.20 V (dots) *vs*. SCE. The error bars are obtained from SD/(n')$^{1/2}$, where SD is the standard deviation and n' is the number of spikes.

In order to demonstrate that the switch on/off of the mediated L-cysteine oxidation corresponds to the redox reaction of the ferrocene moieties, a potential +0.20 V was applied to the electrode to run the chronoamperometry of PVFc-GNPs in the same series of solutions varying the concentration of L-cysteine. The corresponding $\bar{Q}$ is plotted against $c^{*}_{\text{L-cysteine}}$, as shown as dots in Figure 6.7. Despite of the change in $c^{*}_{\text{L-cysteine}}$, $\bar{Q}$ remains constant at 2 ± 1 pC.

There are two possible physical origins of the charge transfer involved in the nano-impacts: a catalytic response following the Faradaic process as demonstrated above, or a capacitative response.[22-24] In the former case, Faradaic charge transfer first takes place between PVFc and the electrode, the resulting ferrocenium cation then undergoes further electron transfer with L-cysteine in the solution to produce cystine. The overall charge transfer should relate to the concentration of L-cysteine. Herein a threshold potential is required to drive the redox reaction (6.21) and the subsequent catalytic reaction (6.22). In the latter case, a nanoparticle becomes charged upon collision with the potentiostatted electrode. To maintain the charge neutrality, electrons move in or out of the electrode when the applied potential deviates from the potential of zero charge (PZC). The charge transfer should be independent on the reactions. Figure 6.7 shows at +0.20 V (*vs*. SCE), $\bar{Q}$ remains unchanged at different $c^{*}_{\text{L-cysteine}}$, hence only capacitative impacts likely occur. At +1.00 V (*vs.* SCE), $\bar{Q}$ increases with $c^{*}_{\text{L-cysteine}}$, inferring impacts arise due to the catalysis of L-cysteine following the Faradaic electron transfer between PVFc and the GNPs.

6.4.3 Derivation of the Catalytic Rate Constant from Nano-impacts Signals

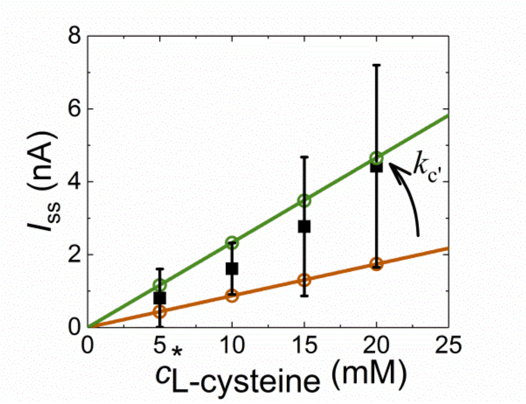

Figure 6.8 L-cysteine concentration ($c^{*}_{\text{L-cysteine}}$) variation of the steady-state current (I_{ss}) per nano-impacts spike. Black squares: experimental I_{ss}. The error bars are obtained from SD/$(n')^{1/2}$. Circles: simulated I_{ss}, with catalytic reaction rate (k_{c}) of 1.3 M^{-1} s^{-1} (red) and 3.6 M^{-1} s^{-1} (blue). Lines: calculated I_{ss} from Eqn.(6.20) to fit experimental I_{ss} within its error bars. The gradient change between the red and blue lines corresponds to a range of k_{c}. In the simulation, parameters used are $\Gamma_{\text{max}} = 2 \times 10^{-6}$ mol m^{-2}, $k_0 = 2$ m s^{-1}, $r_{\text{el}} = 7.5$ μm and $D_{\text{L-cysteine}} = 7.9\times10^{-10}$ $m^2 s^{-1}$.

As discussed in the context of Eqn.(6.20), a steady-state current can be used to infer kinetic information for the catalytic reaction of L-cysteine on PVFc-GNPs. However, due to the short residence time of the colloid, direct measurement of the steady-state current (I_{ss}) on an individual GNP is not easy.[26] Instead, an average I_{ss} is obtained implicitly from the reaction charge (Q) and duration (t_{impact}) per nano-impacts spike, *via* $I_{\text{ss}} = Q / t_{\text{impact}}$. Q and t_{impact} are collected at high overpotentials where the steady-state current is reached. After analysis of the nano-impacts spikes, the experimental I_{ss} is plotted as a function of $c^{*}_{\text{L-cysteine}}$ varying from 5 mM to 20 mM (Figure 6.8, black squares with error bars). The experimental I_{ss} is shown to be proportional with $c^*_{\text{L-cysteine}}$, which consistent with Eqn.(6.20). This supports the choice of mechanism used in analysing the experimental data.

In Figure 6.8, the red and blue lines are the theoretical prediction for the largest and the lowest steady-state currents, according to the distribution of the experimental value of I_{ss}. The gradient of the two lines is used to derive the boundary of the catalytic rate constant (k_{c}). A range of k_{c} can hence be determined by considering the distribution of the experimental I_{ss}. According to Eqn.(6.20), after plotting I_{ss} against $c^*_{\text{L-cysteine}}$, the gradient can be expressed as:

$$\frac{\mathrm{d}I_{\mathrm{ss}}}{\mathrm{d}c^*_{\text{L-cysteine}}} = FS\frac{k_{\mathrm{c'}}\Gamma_{\max}}{1+\dfrac{\pi k_{\mathrm{c'}}\Gamma_{\max} r_{\mathrm{el}}}{4D_{\text{L-cysteine}}}} \tag{6.23}$$

where the maximum surface coverage ($\Gamma_{\max}$) and the standard electrochemical rate constant (k_0) were measured from the redox reaction of PVFc/PVFc$^+$ in the previous work, as *ca.* 2×10^{-6} mol m^{-2} and k_0 is *ca.* 3 s^{-1}, respectively.[24] The diffusion coefficient of L-cysteine ($D_{\text{L-cysteine}}$) was reported as 7.9×10^{-10} m^2 s^{-1}.[27] The radius of GNP (r_{el}) is 7.5 μm. The catalytic rate constant (k_{c}) can thus be derived from the blue and red line, as 1.3 M^{-1} s^{-1} and 3.6 M^{-1} s^{-1}, respectively. Moreover, the values for $k_{\mathrm{c'}}$ are used to simulate the I_{ss} (Figure 6.8, circles). The simulated results match with the analytical lines, demonstrating the validity of Eqn.(6.20) in derivation of $k_{\mathrm{c'}}$.

6.5 Homogeneous EC' Reactions on Nanoparticle Modified Electrodes

For the homogeneous catalytic reaction, as both the redox catalyst A and the reactant R are assumed to be solution phase species, the reaction rate is determined by both the diffusion from the bulk solution to the nanoparticle surface and the homogeneous catalytic kinetics. In this section, current-potential responses of the homogeneous catalytic reaction on both individual nanoparticles and nanoparticle ensembles are simulated. The size effects on the electron transfer efficiency and mechanism are explored, providing information on the interplay between the diffusion and the kinetics in the homogeneous catalytic system.

6.5.1 Electron Transfer Efficiency of the Homogeneous EC' Reaction

Due to the convergent diffusion, the current-potential dependence for an electron-transfer reaction on a nanoparticle is an S-shape curve with the limiting current controlled by diffusion. The apparent (or 'effective') number of electrons transferred in the reaction n_e can be determined from I_{ss} / $I_{ss,1e}$, where I_{ss} is the measured steady-state current at high overpotentials and $I_{ss,1e}$ is the theoretical value of the diffusion-limited, one-electron-transfer reaction seen in the absence of any catalysis. Dependent on the nanoparticle geometry, $I_{ss,1e}$ can be expressed as:

$$I_{\text{ss, 1e}} = \begin{cases} 4FD_{\text{A}}c_{\text{A}}^{*}r_{\text{el}} & \text{disc nanoelectrode} \\ 4\pi \ln 2FD_{\text{A}}c_{\text{A}}^{*}r_{\text{el}} & \text{sphere nanoelectrode} \end{cases} \tag{6.24}$$

When the electron transfer process is followed by a chemical step catalysed by the redox species, the current measured on the electrode will be promoted due to the cycling of the redox catalyst. Therefore, the steady-state current as well as the effective number of electrons n_e will be affected as well. Figure 6.9 shows the influence of the catalytic process (Eqn.(6.4)) on the current-potential dependences of the catalytic reaction on a spherical nanoparticle. In Figure 6.9a and 6.9b, the current-potential dependences are simulated with various catalytic rate constants k_{cat} and concentrations of the reactant in the bulk solution c_R*. It is observed in Figure 6.9a that with the increase of k_{cat}, the "half-wave potential" (defined as the potential where I = ½ I_{ss}) shifts positively and the maximum steady-state current increses. Figure 6.9b shows that the amount of the reactant added in the solution has a significant effect on the value of I_{ss}, which alters the effective number of electrons transferred in the homogeneous catalytic reaction. In the simulation of various k_{cat}, it is found that the steady-state current cannot infinitely increase with k_{cat}. When the catalytic process is ultrafast and the steady-state current shows independence of k_{cat}, the diffusion of A and R becomes the rate-determining factor for such a reaction and the homogeneous catalytic reaction can be approximated as a two-step electron-transfer reaction:

$$\begin{aligned} \text{A} + \text{e}^{-} &\rightleftharpoons \text{B} \\ \text{R} + \text{e}^{-} &\rightleftharpoons \text{P} \end{aligned} \tag{6.25}$$

The steady-state current of (6.25) is the sum of the diffusion limited steady-state currents for the electron transfer steps A/B and R/P:

$$I_{\mathrm{ss}} = I_{\mathrm{ss,A/B}} + I_{\mathrm{ss,R/P}} \tag{6.26}$$

Therefore, the effective n_{e} for the fast (k_{cat} >> 1 and I_{ss} is independent of k_{cat}) homogeneous catalytic reaction becomes:

$$n_{\mathrm{e,max}} = 1 + \frac{D_{\mathrm{R}} c_{\mathrm{R}}^{*}}{D_{\mathrm{A}} c_{\mathrm{A}}^{*}} \tag{6.27}$$

This value is also the maximum number of transferring electrons that can be detected for a homogeneous catalytic reaction on any size of the nanoparticle.

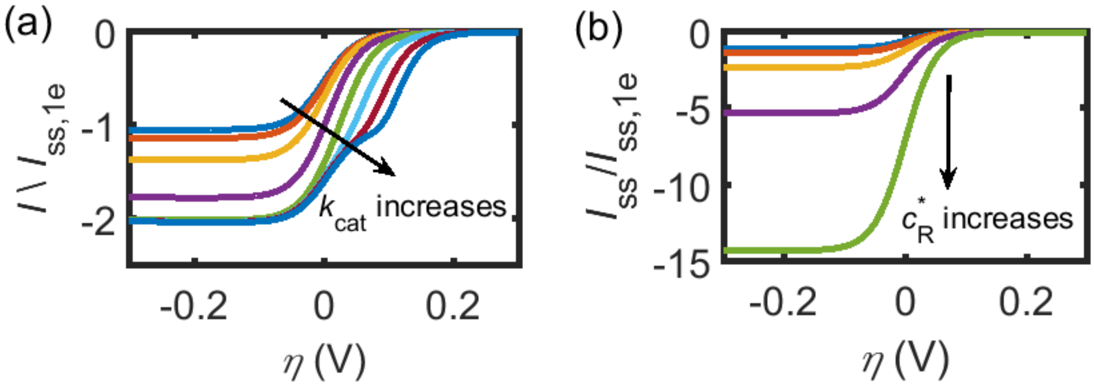

Figure 6.9. Current-potential dependences of homogeneous catalytic reactions on a spherical nanoparticle: (a) under various k_{cat}. From top to bottom, the value of k_{cat} for each plot increases from 0.1 to 10^6 mM^{-1}s^{-1}. In the simulation, c_{A}*=c_{R}*=1 mM, D_{A} = D_{R} = 10^{-10} m^2 s^{-1}, r_{el} = 1000 nm, k_0 = 10^3 m s^{-1} and α = β = 0.5; (b) under various c_{R}*. From top to bottom, the value of c_{R}* for each plot increases from 0.1 to 10^3 mM. k_{cat} is 10 mM^{-1}s^{-1} and other simulation conditions are the same as above. The sweep of the overpotential starts from 0.3 V.

On the other hand, when the mass transport of the reactant R is much faster than the redox species A, the concentration change of R can be ignored and in the solution $c_{\mathrm{R}} \approx c_{\mathrm{R}}^{*}$. At steady state, the diffusion equation of the redox catalyst A then becomes:

$$\frac{\partial c_{\mathrm{A}}}{\partial t} = D_{\mathrm{A}} \nabla^2 c_{\mathrm{A}} + k_{\mathrm{cat}} \left(c_{\mathrm{A}}^* - c_{\mathrm{A}} \right) c_{\mathrm{R}}^* = 0 \tag{6.28}$$

To simplify the equation, we first solve the equation on an isolated sphere nanoelectrode where only the radial direction r needs to be taken into consideration. The concentration variation on the radial direction is:

$$c_{\mathrm{A}}(r) = c_{\mathrm{A}}^* - \frac{c_{\mathrm{A}}^* r_{\mathrm{el}}}{r} \exp\left(-\sqrt{\frac{k_{\mathrm{cat}} c_{\mathrm{R}}^*}{D_{\mathrm{A}}}} \left(r - r_{\mathrm{el}} \right) \right) \tag{6.29}$$

According to Eqn.(6.10) and Eqn.(6.14), the steady-state current then can be solved:

$$I_{\mathrm{ss}} = -FSD_{\mathrm{A}} \left. \frac{\mathrm{d}c_{\mathrm{A}}}{\mathrm{d}r} \right|_{r=r_{\mathrm{el}}} = -FSD_{\mathrm{A}} \left(\frac{c_{\mathrm{A}}^*}{r_{\mathrm{el}}} + c_{\mathrm{A}}^* \sqrt{\frac{k_{\mathrm{cat}} c_{\mathrm{R}}^*}{D_{\mathrm{A}}}} \right) \tag{6.30}$$

where $S = 4\pi r_{\mathrm{el}}^2$ is the surface area of a spherical nanoparticle. Thus the effective n_{e} in this case are limited by the catalytic rate and the electrode size:

$$n_{\mathrm{e}} = 1 + r_{\mathrm{el}} \sqrt{\frac{k_{\mathrm{cat}} c_{\mathrm{R}}^*}{D_{\mathrm{A}}}} \tag{6.31}$$

Note that Eqn.(6.31) only works for isolated sphere electrodes and the geometry of the electrode will also affect the value of n_{e}, which will be discussed later.

For more general cases, combining our simulation work with reports in the literature, the number of transferring electrons for the catalytic reaction is found to be dependent on two combined parameters: γ_{AR} and K_{cat}

$$\gamma_{\mathrm{AR}} = \frac{c_{\mathrm{R}}^* D_{\mathrm{R}}}{c_{\mathrm{A}}^* D_{\mathrm{A}}} \tag{6.32}$$

$$K_{\mathrm{cat}} = \frac{k_{\mathrm{cat}} c_{\mathrm{R}}^* r_{\mathrm{el}}^{2}}{D_{\mathrm{A}}} \tag{6.33}$$

where γ_{AR} is related to the excess of the reactant relative to the redox catalyst and K_{cat} reflects the size effects on the catalytic reaction rate. The variation of the nanoparticle size is reflected in the parameter K_{cat}.

Taken the geometry influence into consideration, the number of electrons transferred, n_e, can be approximated as a function of γ_{AR} and K_{cat}:

$$n_e = \frac{I_{ss}}{I_{ss,1e}} \approx 1 + \frac{\sqrt{K_{cat}}}{\delta_{geo} + \frac{\sqrt{K_{cat}}}{\gamma_{AR}}} \tag{6.34}$$

From this approximate expression, it is apparent that both the size and the geometry of the nanoparticle can affect the apparent number of electrons transferred of the homogeneous catalytic reaction.

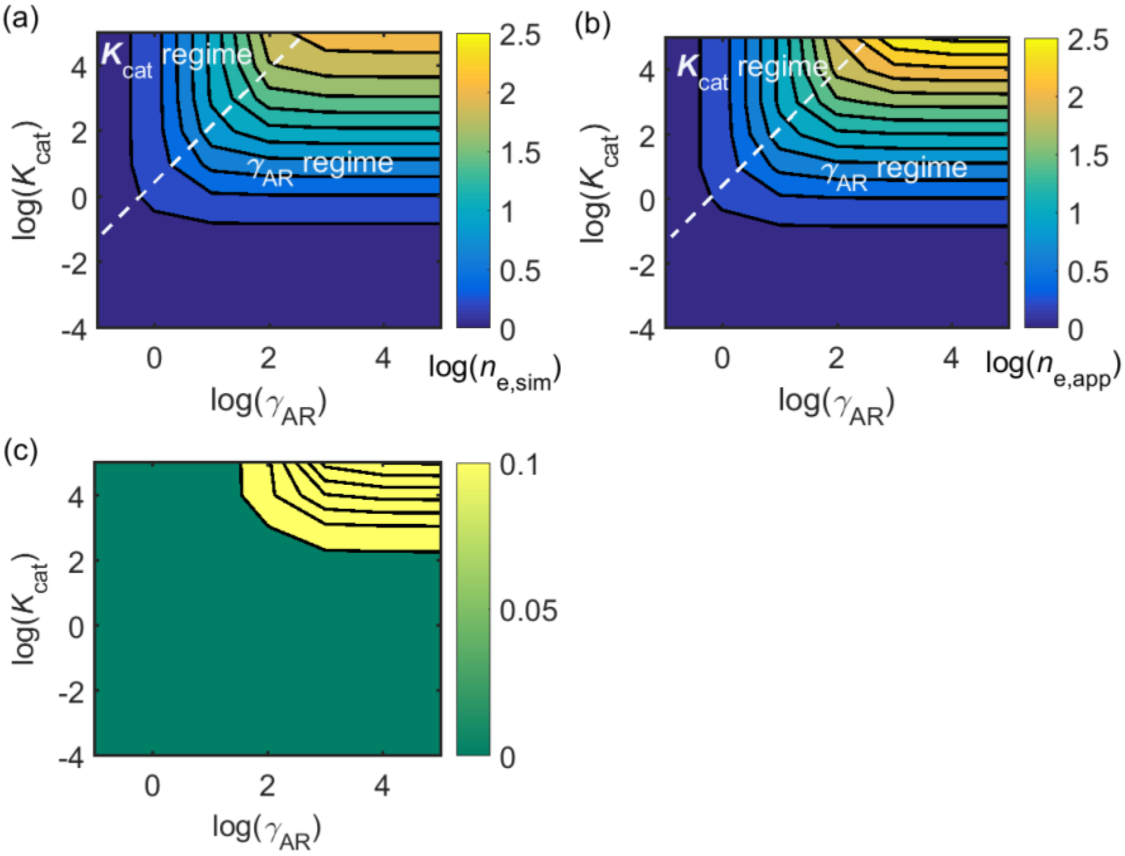

Figure 6.10 n_e of homogeneous catalytic reactions on a nanosphere: (a) Simulation $n_{e,sim}$ under various K_{cat} and γ_{AR}. (b) Approximation $n_{e,app}$ under various K_{cat} and γ_{AR}. (c) Difference between the simulation and approximation results $\left|n_{e,sim} - n_{e,app}\right| / n_{e,sim}$ **.**

The kinetic diagrams of n_e from both disc and sphere nanoparticles are calculated as the function of K_{cat} and γ_{AR} from both the simulation programme and the approximation equation (Eqn.(6.34)). Figure 6.10 shows the diagrams from the sphere nanoparticle of simulated $n_{e,sim}$ (Figure 6.10a), $n_{e,app}$ calculated from Eqn.(6.34) (Figure 6.10b), and the difference between the simulation and the approximation results $\left|n_{e,sim} - n_{e,app}\right| / n_{e,sim}$ (Figure 6.10c). The approximation fits the simulation results well when K_{cat} and γ_{AR} are not large. In the kinetic diagrams Figure 6.10a and 6.10b, a dashed line divides the diagram into two, corresponding to different dominant processes for the catalytic reaction on a nanoparticle. In the K_{cat} regime, as the catalytic process is relative fast, the number of electrons transferred in the reaction is limited by the mass transport of the reactant R; whereas in the γ_{AR} regime, the supply of the reactant is sufficient and the limiting factor becomes the catalytic reaction rate. When the nanoparticle is so tiny that $K_{cat} << 1$, even under rather large value of γ_{AR}, only one electron corresponding to the redox step (the E step) is seen. As the catalytic rate depends on the square of the nanoparticle size, r_{el}^2, the variation of the nanoparticle size can dramatically affect K_{cat} and hence the reaction as a whole. It can be observed from the diagrams that compared to the mass transport, the catalytic kinetics is very sensitive the variation of the nanoparticle size.

Figure 6.11 shows the simulation and approximation results for the catalytic reaction on the disc-shape nanoparticle. The kinetic diagram of $n_e(\gamma_{AR}, K_{cat})$ simulated from a nanodisc also can be divided into two regimes: K_{cat} and γ_{AR}, where the catalytic rate and the diffusion dominate. However, even though the kinetic diagrams show similar trends in Figures 6.10 and 6.11, the difference in geometry affects the value of the steady-state current and the measured n_e for the homogeneous catalytic reaction on the individual nanoparticle, as indicated in Eqn.(6.34). Therefore, for the homogeneous catalytic reaction on individual nanoparticle, the geometry factor cannot be ignored and the electron-transfer efficiency is affected by the shape of the nanoparticle.

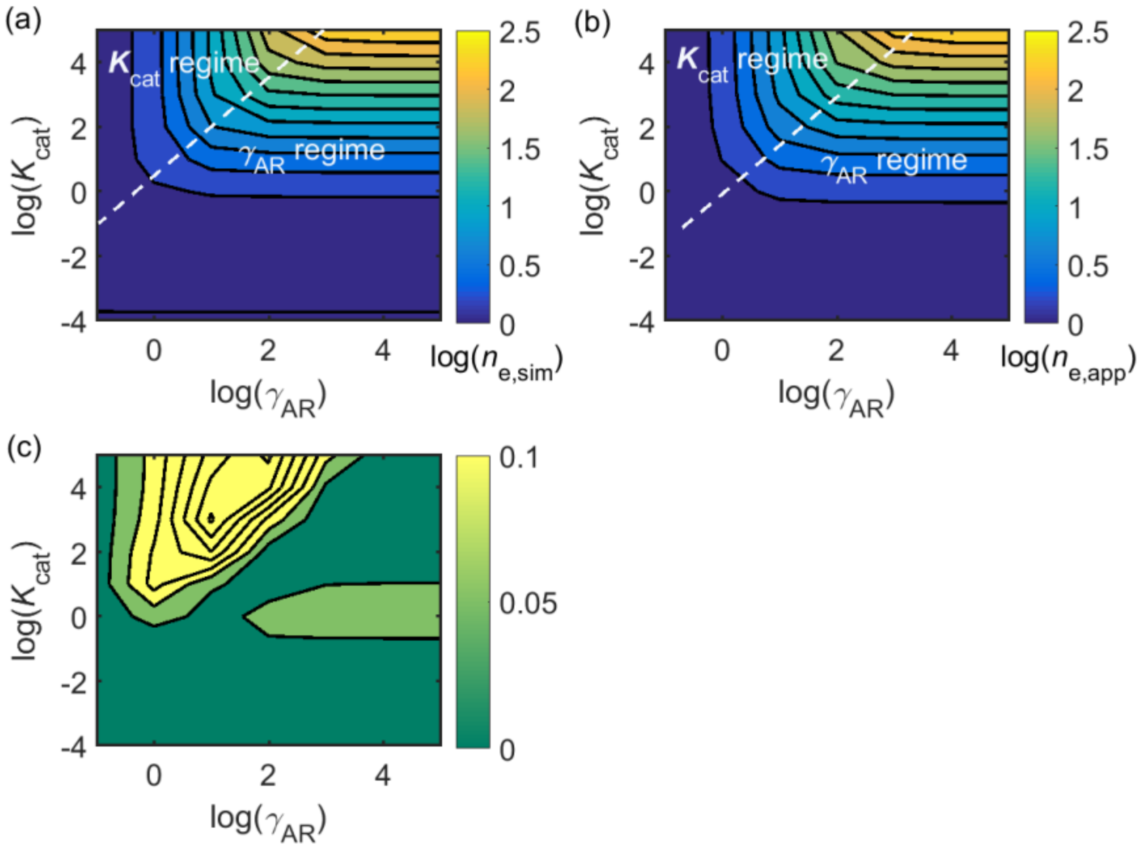

Figure 6.11 n_e of homogeneous catalytic reactions on a nanodisc: (a) Simulation $n_{e,sim}$ under various K_{cat} and γ_{AR}. (b) Approximation $n_{e,app}$ under various K_{cat} and γ_{AR}. (c) Difference between the simulation and approximation results $\left|n_{e,sim} - n_{e,app}\right| / n_{e,sim}$ **.**

6.5.2 Electron Transfer Steps of The Homogeneous EC' Reaction

As discussed above, the catalytic reaction with an ultrafast catalytic process (large K_{cat}) can be regarded as two one-electron-transfer reactions and the effective number of transferring electrons varies as a function of γ_{AR}. Figure 6.12 shows the current-potential dependence of the catalytic reaction on the nanosphere with large values of K_{cat} under various γ_{AR}. The values of K_{cat} used in the examples are 10^3 (blue lines), 10^4 (red lines) and 10^5 (yellow lines) and γ_{AR} are 5.0 (Figure 6.12a), 1.0 (6.12b) and 0.1 (6.12c), respectively. As shown in Figure 6.12, when the value of K_{cat} is large enough that the steady-state current is determined by the diffusion of the redox catalyst and the reactant, the value of the normalized steady-state current equals $1 + \gamma_{AR}$, as predicted in Eqn.(6.27).

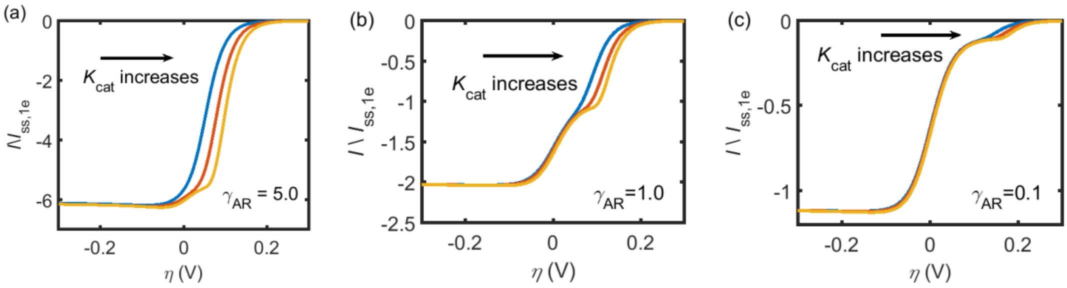

Figure 6.12 Voltammograms of the catalytic reaction on the nanosphere under various γ_{AR}. (a) $\gamma_{AR} = 5.0$; (b) $\gamma_{AR} = 1.0$; (c) $\gamma_{AR} = 0.1$. For each γ_{AR}, the simulation is implemented with Kcat equal to 10^3 (blue lines), 10^4 (red lines) and 10^5 (yellow lines). The voltage sweep starts from 0.3 V.

Moreover, similar to a double electron transfer reaction (a so-called 'EE' reaction), a split in the current-potential curve can be observed for large values of K_{cat} in Figure 6.12, indicating the two separate electron-transfer processes, with that at lower overpotentials reflects the full amount of reactant R in solution with the second wave reflects the concentration of A. The separation of the two electron-transfer steps on the voltammogram is related to the value of K_{cat}: for larger K_{cat}, there is more difference between the positions of the two split waves. It is also found that the current where the separation appears depends on the value of γ_{AR}: when γ_{AR} is 5.0 (Figure 6.12a), the split of wave appears at $I / I_{ss,1e}$ = 5.0 and when γ_{AR} = 1.0 (Figure 6.12b), the split is at $I / I_{ss,1e}$ = 1.0. Figure 6.13 shows the voltammograms for the reaction on the nanodisc, with the same simulation conditions as applied in Figure 6.12. Similarly, the split of wave in Figure 6.13 is more noticeable when K_{cat} increases and the split position is determined by the value of γ_{AR}.

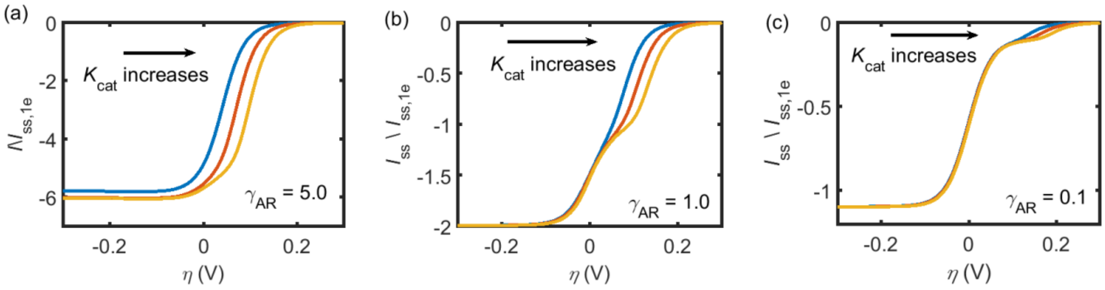

Figure 6.13 Voltammograms of the catalytic reaction on the nanodisc under various γ_{AR}. (a) γ_{AR} = 5.0; (b) γ_{AR} = 1.0; (c) γ_{AR} = 0.1. For each γ_{AR}, the simulation is implemented with *K*cat equal to 10^3 (blue lines), 10^4 (red lines) and 10^5 (yellow lines). The voltage sweep starts from 0.3 V.

When the catalytic reaction is treated as a two-step electron-transfer reaction under the condition of ultrafast catalytic rate (where $n_e = 1 + \gamma_{AR}$), the split of wave provides information about the nature of the two electron-transfer steps and the number of electrons transferred in each step. From Figures 6.12 and 6.13, it is found that on both nanosphere and nanodisc, the potential dependence of the first electron-transfer process varies with K_{cat} whereas the potential dependence for the second step is always constant, indicating that the first step is the consequence of the catalytic process R → P while the second one corresponds to the reversible redox reaction of A + e → B. It is also observed that the effective number of electrons transferred in the first step $n_{e,1st}$ is γ_{AR} and that in the second step $n_{e,2nd}$ is 1. Given that the total number of electrons transferred in the fast catalytic reaction equals $1 + \gamma_{AR}$, the same conclusion is obtained that the first electron-transfer is caused by the fast catalytic process and the second step reflects the redox step. In this case, the variation of the nanoparticle size, involved in K_{cat}, changes the overall thermodynamics of the electron transfer induced by the catalytic process and thus affects the number of electrons transferred in each step of the homogeneous catalytic reaction.

6.5.3 Homogeneous EC' Reaction on the Ensemble of Nanoparticles

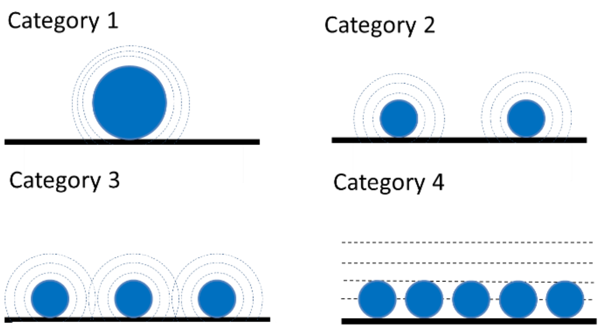

Figure 6.14 The four diffusion modes for nanoparticle modified electrodes.

The above text considered the catalytic response from an isolated single nanoparticle. In experimental reality, electrode surfaces are more commonly modified with ensembles of nanoparticles. In this section we consider how the presence of many nanoparticles can alter the response seen from the single particle as a result of mutually overlapping diffusion fields. Dependent on the diffusion domain size r_{domain} and the diffusion layer thickness, there are four diffusion modes on a nanoparticle modified electrode, as illustrated in Figure 6.14. Categories 1-4 in Figure 6.14 correspond to 1) the linear diffusion to a large particle surface and the diffusion condition of each particle is independent; 2) the convergent diffusion to the particle surface and the diffusion layer of each particle is independent; 3) the convergent diffusion layers of neighbouring particles overlap partly with adjacent particles; 4) the diffusion layers strongly overlap and the diffusion to the entire electrode is linear.

In the above sections, the case of independent diffusion layers (category 2) is discussed. For a nanoparticle modified electrode, when the coverage of nanoparticles is high (categories 3 and 4), the cyclic voltammogram (the current-potential response as a triangular voltage scan is applied to the electrode) will differ from those measured from category 2, due to the overlap of the diffusion layers. However, note that in contrast to the case of single nanoparticles, significant hysteresis develops (which is only seen for extreme scan rates for a single nanoparticle). The cyclic voltammograms on the nanoparticle ensembles then become more complicated and difficult to analyse, as more variables (i.e. scan rate and nanoparticle coverage) are introduced in the system. But the key point is still to understand the interplay between the diffusion and the kinetics, which is achieved by the variation of the nanoparticle size and the catalytic rate constant in the examples of Figure 6.15.

Figure 6.15 shows the cyclic voltammograms of the catalytic reactions with various nanoparticle sizes, catalytic rates and geometries. To focus on the size effects of the nanoparticle on the nanoparticle array with different diffusion categories, the coverage of the nanoparticle is fixed while the nanoparticle size is altered. In Figure 6.15, a, b and c are simulated with the disc model and the size of nanoparticles in each panel are 10, 100 and 1000 nm, respectively. Therefore, the diffusion mode varies from category 4 (fully overlapped diffusion layers) to category 3 (partly overlapped diffusion layers). In addition, to explore how the interplay between the diffusion and the homogeneous catalysis can influence the electrochemical responses collected from the nanoparticle array, two catalytic rate constants are used in the simulation: 10^2 (blue lines) and 10^4 (red lines) mM^{-1} s^{-1}. Figures 6.15 d-f are similar to a-c but simulated with the sphere model. To examine the electron transfer efficiency for the homogeneous catalytic reaction on the nanoparticles modified electrodes, the current-potential responses are compared with those simulated from the one-electron-transfer redox reaction, which are shown by the dashed black lines in Figure 6.15. The current for the catalytic reaction on the nanoparticle ensemble is normalized by the forward peak current of the redox reaction $I_{\text{peak,1e}}$ in each panel.

Without the catalytic process, the diffusion mode alters when the nanoparticle size increases, as indicated by the waveshape of the redox-only cyclic voltammograms in Figure 6.15. As the coverage is constant, the increase of the nanoparticle size leads to larger distance between two adjacent particles and thus changes the diffusion mode from category 4 to category 3 in this case. On the other hand, the increase of the catalytic rate leads to an enhancement of the current and a shift to low overpotential in the forward sweeping, improving the electron transfer efficiency as it does on individual nanoparticles. When the catalytic process is fast, the split of waves can be observed with small nanoparticles, while the first and second split peaks correspond to the catalytic process and the mass transport limitation, respectively. The split of wave is less apparent with the increase of the nanoparticle size, because of the variation of the diffusion mode.

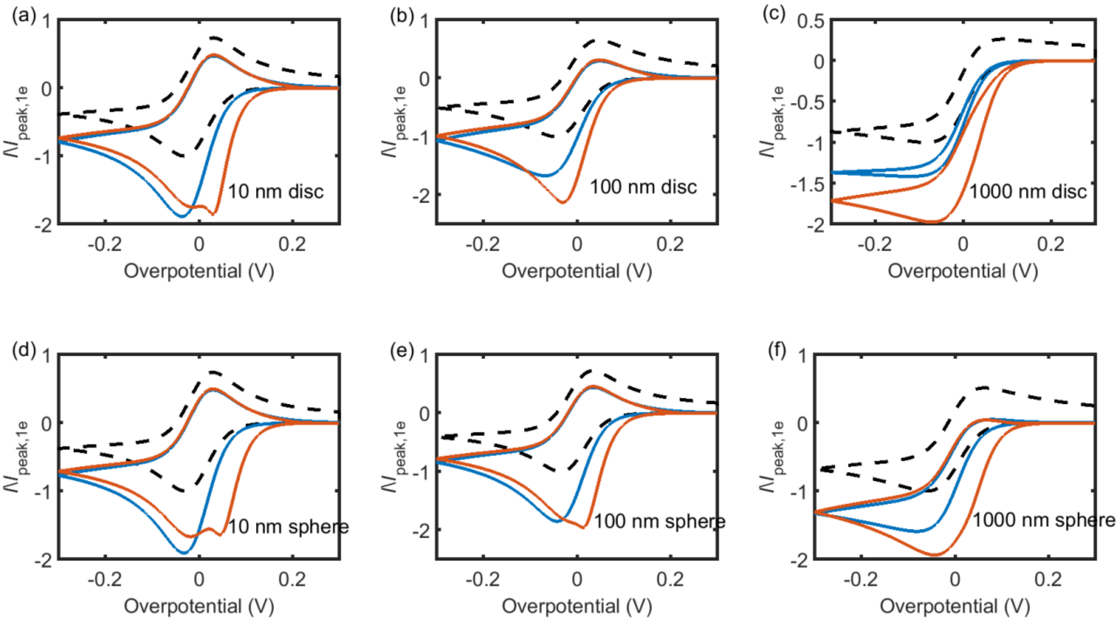

Figure 6.15 Current-potential responses of the catalytic reactions on nanoparticle modified electrodes. a, b and c are simulated on disc nanoparticles while d, e and f are on sphere nanoparticles. The radii of the nanoparticles are 10(a, d), 100(b, e), 1000(c, f) nm. The catalytic rate constants applied are 10^2 (shown by blue lines) and 10^4 (red lines) mM^{-1}s^{-1}. In the simulation, $c_R^* = c_A^*$ =1 mM, $D_R = D_A = 10^{-10}$ m^{2}s^{-1}, v = 1 V s^{-1}, r_{sup} = 1 mm. The coverages of the nanoparticles is 4% on the supporting electrode. The dashed black lines are the current-potential responses only from the redox reaction A/B. The voltage scan starts at 0.3 V.

Figures 6.15 a-c and d-f are the simulation results from the disc and sphere models. In the diffusion mode of category 4, due to the overlapped diffusion layer, there is no significant difference on the cyclic voltammograms of disc and sphere geometries, as shown in Figure 6.15a and 6.15d. However, under the same coverage, when the size of the nanoparticle increases, the geometry influence becomes more significant, indicated by the difference on the waveshape between Figures 6.15 b, c and e, f. For the limiting case of individual nanoparticles, the geometry can affect the measured number of electrons transferred in the homogeneous catalytic reaction. Therefore, unless the coverage of the nanoparticle is high in the ensemble, the influence of the geometry cannot be ignored. Moreover, unlike the case of a single isolated particle, for an ensemble, a sustained, steady current cannot be realised as a consequence of the overlapping diffusion fields destroying the local convergent diffusion and hence it is essential to track spatial and temporal concentration profiles of all species if the catalytic process is to be understood. At low coverages and short time scales, different shaped particles will respond according to their surface area. But at long time scales, the diffusion layers either overlap or at least become convergent, and the electrochemical responses are not influenced much by the morphology of the nanoparticle.

The effects of changing the particle size cannot be separated from those of the particle coverage (or inter-particle separation) in an ensemble immobilized on an electrode surface. This is because the net catalytic reaction flux reflects both the chemistry and the mass transport; the latter is profoundly sensitive to the absolute inter-particle distance since this controls the overlapping or not of adjacent diffusion layers. Accordingly, experimentalists are advised to consider coverage effects as well as particle size effects when assessing the catalytic properties of new nanomaterials.

6.6 Summary

The redox species mediated catalytic reaction (also called an EC' reaction) at the nanoparticle modified electrodes is studied via simulation. The two types of EC' reaction, homogeneous and heterogeneous, differing by the state of the redox mediator, are simulated in the cases of single nanoparticles and nanoparticle ensembles. For the heterogeneous EC' reaction, the steady-state current observed at high overpotential is related to the catalytic kinetics and the diffusion of the reactant. The conclusion is applied to the oxidation of cysteine mediated with ferrocene modified graphene nanoplatelets and a rate constant estimated.

The influence of the nanoparticle size is explored on the homogeneous EC' reaction. For the homogeneous catalytic reaction on an isolated individual nanoparticle, the steady-state current I_{ss} and the apparent number of electrons transferred in the reaction n_e are determined by γ_{AR}, the excess of the reactant to the redox catalyst, and K_{cat}, the size effects on the catalytic reaction rate. From the kinetic diagram $n_e(\gamma_{AR}, K_{cat})$, the catalytic process is found to be more sensitive to the size influence than the diffusion. On the nanoparticle arrays, under the same coverage, the increase of nanoparticle size leads to the change of the diffusion mode and the catalytic process improves the electron transfer efficiency; the response is size dependent due to the overlapping diffusion layers. For both single nanoparticles and nanoparticle arrays, the influence of geometry on the homogeneous catalytic reaction is that the disc and sphere nanoparticles have different and size-dependent current-potential responses, especially at low surface coverages.

References

1. Q. Lin, C. Lin, H. Wu, C. Batchelor-McAuley and R. G. Compton, *The Journal of Physical Chemistry C*, 2016, **120**, 20216-20223.
2. C. Lin and R. G. Compton, *The Journal of Physical Chemistry C*, 2017, **121**, 2521-2528.
3. L. Zhang, H. Chen, X. Zhao, Q. Zhai, D. Yin, Y. Sun and J. Li, *Applied Catalysis B: Environmental*, 2016, **193**, 47-57.
4. K. E. Toghill and R. G. Compton, *International Journal of Electrochemical Science*, 2010, **5**, 1246-1301.
5. B. Lertanantawong, A. P. O'Mullane, J. Zhang, W. Surareungchai, M. Somasundrum and A. M. Bond, *Analytical Chemistry*, 2008, **80**, 6515-6525.
6. A. Badalyan and S. S. Stahl, *Nature*, 2016, **535**, 406-410.
7. S. D. Ahn, A. C. Fisher, A. Buchard, S. D. Bull, A. M. Bond and F. Marken, *Electroanalysis*, 2016, **28**, 2093-2103.
8. H. Ozawa, T. Hino, H. Ohtsu, T. Wada and K. Tanaka, *Inorganica Chimica Acta*, 2011, **366**, 298-302.
9. J. M. Savéant, *Elements of Molecular and Biomolecular Electrochemistry: An Electrochemical Approach to Electron Transfer Chemistry*, Wiley, 2006.
10. M. A. Vorotyntsev, D. V. Konev and Y. V. Tolmachev, *Electrochimica Acta*, 2015, **173**, 779-795.
11. S. Pang, J. Yan, F. Zhu, D. He, B. Mao, A. Oleinick, I. Svir and C. Amatore, *Electrochemistry Communications*, 2014, **38**, 61-64.
12. Y. Nie, L. Li and Z. Wei, *Chemical Society Reviews*, 2015, **44**, 2168-2201.
13. W. Jin and G. Maduraiveeran, *Trends in Environmental Analytical Chemistry*, 2017, **14**, 28-36.
14. B. E. Hayden, *Accounts of Chemical Research*, 2013, **46**, 1858-1866.

15. Y. Tang and W. Cheng, *Nanoscale*, 2015, **7**, 16151-16164.

16. Y. Wang, E. Laborda, K. Tschulik, C. Damm, A. Molina and R. G. Compton, *Nanoscale*, 2014, **6**, 11024-11030.

17. R. Guidelli, R. G. Compton, J. M. Feliu, E. Gileadi, J. Lipkowski, W. Schmickler and S. Trasatti, *Pure and Applied Chemistry*, 2014, **86**, 245-258.

18. R. Guidelli, R. G. Compton, J. M. Feliu, E. Gileadi, J. Lipkowski, W. Schmickler and S. Trasatti, *Pure and Applied Chemistry*, 2014, **86**, 259-262.

19. D. J. Gavaghan, *Journal of Electroanalytical Chemistry*, 1997, **420**, 147-158.

20. H. Reller, F. Kirowa-Eisner and E. Gileadi, *Journal of Electroanalytical Chemistry and Interfacial Electrochemistry*, 1982, **138**, 65-77.

21. R. G. Compton and C. E. Banks, *Understanding Voltammetry*, Imperial College Press, London, U.K., 2nd edn., 2011.

22. C. Batchelor-McAuley, J. Ellison, K. Tschulik, P. L. Hurst, R. Boldt and R. G. Compton, *Analyst*, 2015, **140**, 5048-5054.

23. H. Wu, Q. Lin, C. Batchelor-McAuley and R. G. Compton, *ChemElectroChem*, 2016, DOI: 10.1002/celc.201600296, In press, DOI: 10.1002/celc.201600296.

24. H. Wu, Q. Lin, C. Batchelor-McAuley, L. M. Goncalves, C. F. R. A. C. Lima and R. G. Compton, *Analyst*, 2016, **141**, 2696-2703.

25. J. B. Raoof, R. Ojani and M. Kolbadinezhad, *Bulletin of the Chemical Society of Japan*, 2005, **78**, 818-826.

26. E. Kätelhön, A. Feng, W. Cheng, S. Eloul, C. Batchelor-McAuley and R. G. Compton, *The Journal of Physical Chemistry C*, 2016, **120**, 17029-17034.

27. J. B. Raoof, R. Ojani, H. Beitollahi and R. Hosseinzadeh, *Analytical Sciences*, 2006, **22**, 1213-1220.

Chapter 7 Electrochemical Detection of Single Enzymes

In this chapter, the kinetics of the single enzyme catalysis at the electrode-electrolyte interface is studied. To evaluate the possible detection of single enzyme activity via electrochemical methods, a combined finite difference and random walk simulation is used to model individual enzyme-electrode collisions where such events are monitored amperometrically via the measurement of products formed by the enzyme in solution. The example of single catalase measurement is analysed and discussed in section 7.4. This chapter contains the work published in Chemical Science.[1] The experimental part was performed by Dr. Lior Sepunaru.

7.1 Introduction

The nano-impact technique investigates stochastic current signals ("spikes") that reflect the approach of individual nanoparticles to an electrode and has evolved to become a powerful tool in the analysis of the physical properties as well as the catalytic activity of individual nano-scale particles or macromolecules.[2-4] In the latter case, a catalyst particle collides with the electrode or is located at or close to the electrode surface and a reaction involving electron transfer is detected, from which the catalytic ability of the particle can be inferred.[5-7] To study of enzyme catalysis, the nano-impact technique in principle might enable the observation of enzyme activity at the single-molecule scale while the target enzyme is investigated in its natural environment preserving its original activity and reactivity during the detection.[8-12] In this respect, the electrochemical method potentially holds an advantage over the conventional spectroscopic methods[13, 14] for studying single enzyme activity, since no enzyme modification is needed. The latter methods, can resolve single catalytic turnover using a single photon counting apparatus. In the 'nano-impacts' method the current is the observable. Although electrochemical single electron counting is currently far from realization, information on the flux of charge at variable time scales (in the range μs – s) can be gained, limited by the noise level of the system and the time resolution.

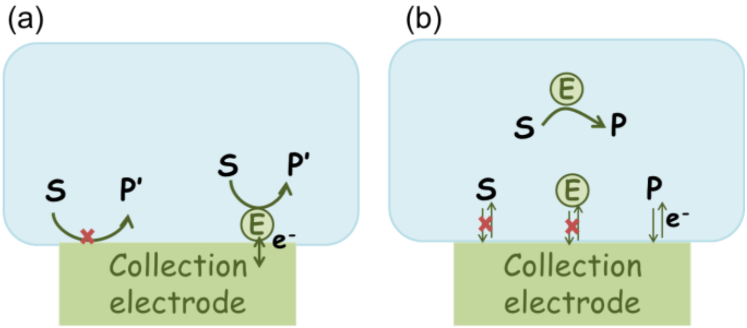

Figure 7.1 Illustration of two possible enzyme detection methods via the nano-impact technique. (a) The enzyme collides with the electrode with which it undergoes direct electron transfer. (b) The catalytic reaction of the enzyme occurs in solution and the product is detected electrochemically.

In the investigation of the activity of an enzyme via the nano-impact technique, the detection approach can be classified into two categories: As illustrated in Figure 7.1, on the one hand the enzyme activity is measured via electron transfer when the enzyme collides with the electrode (Figure 7.1a) and on the other it is detected via the electrochemical reaction of redox species generated by the enzyme's catalytic reaction in the solution (Figure 7.1b). In the first case of an enzyme collision, the catalytic reaction is mediated probably via the active site of the enzyme, and the enzyme effectively works as a "nano-electrode" attached to the supporting substrate.[10, 15] The mechanism of the whole process then follows:

$$\begin{aligned}&\mathrm{E(ads)} \pm \mathrm{e}^{-} \rightleftharpoons \mathrm{E'(ads)}\\&\mathrm{E'(ads)} + \mathrm{S(sol)} \rightleftharpoons \mathrm{E'S(ads)} \longrightarrow \mathrm{E(ads)} + \mathrm{P'(sol)}\end{aligned} \tag{8.1}$$

or alternatively:

$$\begin{aligned}&\mathrm{E(ads)} + \mathrm{S(sol)} \rightleftharpoons \mathrm{ES(ads)}\\&\mathrm{ES(ads)} \pm \mathrm{e}^{-} \longrightarrow \mathrm{E(ads)} + \mathrm{P'(sol)}\end{aligned} \tag{7.2}$$

where E and E' are the original and the reduced/oxidised forms of the active site, and S and P' are the substrate and the product of the heterogeneous catalytic reaction, respectively. In the second case, the current signal is caused by the electrochemical reaction of the redox species generated by the enzyme. The enzyme is assumed to not necessarily interact adsorptively with the electrode surface but to be solely detected via products formed by its reaction with the substrate. Therefore, the overall process including the catalysis in solution and the detection at the electrode can, assuming Michaelis-Menten kinetics,[16] be described as:

$$\begin{aligned} &\mathrm{E(sol)} + \mathrm{S(sol)} \rightleftharpoons \mathrm{ES(sol)} \longrightarrow \mathrm{P(sol)} + \mathrm{E(sol)} \\ &\mathrm{P(sol)} \pm e^{-} \rightleftharpoons \mathrm{X(sol)} \end{aligned} \tag{7.3}$$

where E is the active site transforming the substrate S into the product P in the solution phase. P is the redox species that reacts at the electrode and X is the reduced/oxidised form of P.

Although current signals corresponding to enzyme activities were observed via both methods,[10, 12] the second is probably more suitable for exploring the activity of authentic solution-phase enzyme catalysis as the enzyme does not interact with the electrode surface and any influence of the electrode potential on its active sites can be avoided. Moreover, the product P’ formed by the direct electron transfer to the active site can at least in principle be quite different to that of the solution-phase catalysis P. As the enzyme catalysis was reported to significantly rely on the dynamics of the enzyme and the surrounding reaction environment,[17, 18] it is important to understand the kinetics of the process as otherwise the analysis of corresponding stochastic signals recorded from the electrode remains obstructed and results concluded can at best be exclusively of a qualitative nature.

In this work, a two-dimensional simulation is developed to describe the solution-phase catalysis of the single enzyme. Stochastic current signals (“spikes”) of the detection of the activity of a single diffusing enzyme are simulated. Through comparison of different enzyme-electrode systems, the key factors influencing the measured signal are explored and it is determined under which experimental conditions such experiments may succeed.

7.2 Electrode Response to a Stationary Enzyme

Due to the complexity of the enzyme-electrode-electronics system, the simulation contains two parts: 1) the current corresponding to the catalytic reaction of a stationary solution-phase enzyme; 2) the mass transport of a single enzyme at the electrode-electrolyte interface. The kinetics of the single enzyme catalysis is first explored with the model of a stationary enzyme in this section. The simulation of a freely-diffusing enzyme will be discussed in section 7.3.

7.2.1 Theoretical Model of Single Enzyme Detection

The reactions involved in the detection of the solution-phase catalytic reaction of a single enzyme are expressed in Eqn.(7.3), where the catalytic activity is examined via the reduction or oxidation of the product at the electrode. To simplify the problem, the amount of the substrate S in solution is herein always assumed to be present in excess. The product P is generated from S and the reaction is assumed to follow the Michaelis-Menten kinetics as shown in Eqn.(7.4).[16] The amount of product generated per single enzyme n_{P} (mol) is determined by the turnover number k_{cat} of the enzyme (s^{-1}), the Michaelis-Menten constant K_{M} (M), the concentration of the substrate c_{S}^* (M), and the reaction time t (s). It is noted that Michaelis-Menten kinetics relate to enzyme ensembles dispersed in the solution and expressed as:

$$\frac{\mathrm{d}c_{\mathrm{P}}}{\mathrm{d}t} = k_{\mathrm{cat}} c_{\mathrm{enzyme}} \frac{c_{\mathrm{S}}^*}{K_{\mathrm{M}} + c_{\mathrm{S}}^*} \tag{7.4}$$

where c_{enzyme} is the concentration of the enzyme. We further note that as a starting point, the effect of fluctuations in enzyme activity is not taken into consideration in this model. In the absence of dynamic disorder, the average activity over time and the average activity of an ensemble of enzymes are hence equivalent.[19] Application of Eqn.(7.4) to the catalysis of a single enzyme then yields:

$$\frac{\mathrm{d}n_{\mathrm{P}}}{\mathrm{d}t} = \frac{k_{\mathrm{cat}}}{N_{\mathrm{A}}} \frac{c_{\mathrm{S}}^*}{K_{\mathrm{M}} + c_{\mathrm{S}}^*} \tag{7.5}$$

where N_A is the Avogadro constant (6.022×10^{23} mol^{-1}). Through the application of Fick's First Law, it is found that the concentration of P c_P (mM) is determined by the catalytic ability of the enzyme and the mass transport of P:

$$\int D_\mathrm{P} \frac{\partial c_\mathrm{P}}{\partial \vec{l}_\mathrm{enzyme}} \mathrm{d}S_\mathrm{enzyme} = \frac{k_\mathrm{cat}}{N_\mathrm{A}} \frac{c_\mathrm{S}^*}{K_\mathrm{M} + c_\mathrm{S}^*} \tag{7.6}$$

where D_P is the diffusion coefficient (m^2 s^{-1}) of P, $\vec{l}_\mathrm{enzyme}$ is the unit vector pointing from the enzyme surface, $\frac{\partial c_\mathrm{P}}{\partial \vec{l}_\mathrm{enzyme}}$ is the concentration gradient (M m^{-1}) of P on and perpendicular to the enzyme surface, and S_enzyme is the surface area of the enzyme (m^2).

If the reaction environment contains enough supporting electrolyte and the detection time is relatively short, only diffusion needs to be considered when modelling the mass transport.[20, 21] Here we assume that a single enzyme generates enough product so that the distribution of product molecules can be properly described as a concentration rather than individual molecule positions. The diffusion of the product is then described via Fick's Second Law:[22]

$$\frac{\partial c_\mathrm{P}}{\partial t} = \nabla^2 c_\mathrm{P} \tag{7.7}$$

Assuming the over- or under-potential applied at the collection electrode is high enough to immediately consume all product species reaching the electrode surface, the concentration of P at the electrode surface is regarded to be effectively zero during the experiment. The current arising from the reduction or oxidation of P can then be calculated from the concentration gradient at the electrode surface:

$$I = Fn_\mathrm{e} \int D_\mathrm{P} \frac{\partial c_\mathrm{P}}{\partial \vec{l}_\mathrm{el}} \mathrm{d}S_\mathrm{el} \tag{7.8}$$

where F is the Faraday constant (96485 F mol^{-1}), n_e is the number of electrons transferred per product (in this work, n_e is set to be 1), $\vec{l}_\mathrm{el}$ is the unit vector pointing from the electrode surface, and S_el is the surface area of the electrode.

7.2.2 Simulation of the Electrode Response to a Stationary Enzyme

For simulating the catalysis of a stationary enzyme, the finite difference approach is applied. As the size of the enzyme is small compared to the size of the detecting electrode, the enzyme is treated as a point in the simulation space. To simplify the problem, the orientation of the enzyme is not taken into consideration and a micro-size spherical electrode is first selected as the detecting electrode. The simulation space can then be described in two-dimensional cylindrical coordinates (r, z). As shown in Figure 7.2a, the z axis is located on the line linking the enzyme and the centre of the spherical electrode, and the r axis is set perpendicular to the z axis. In addition and to further simplify the enzyme-electrode system as explained below, in a second simulation the spherical electrode is replaced by a disc electrode in the same coordinate system, as illustrated in Figure 7.2b.

For the numerical simulation via the finite difference method, meshes of both the sphere- and the disc model are built, of which two examples are shown in the Figures 7.2c and 7.2d. More details on the calculation mesh can be found in section 7.2.3. The conditions and equations used to describe the enzyme-electrode system are listed in Table 7.1.

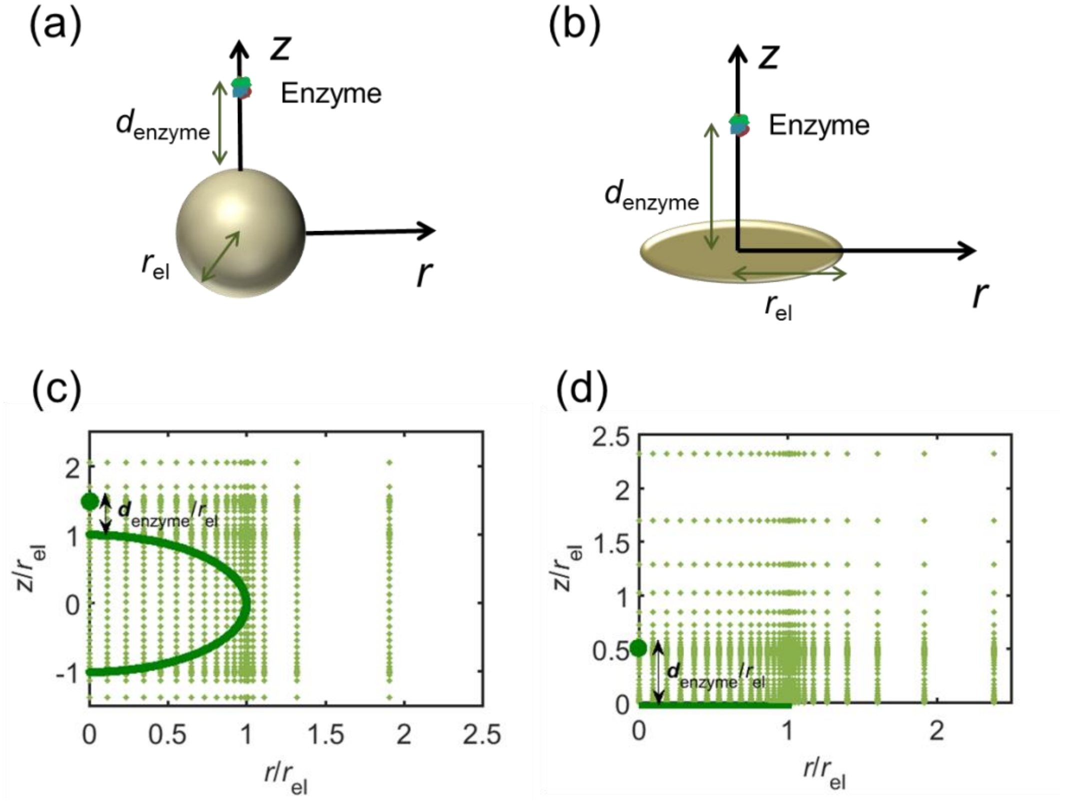

Figure 7.2 Simulation model for the detection of single enzymes. a) Illustration of a single enzyme near a sphere electrode; b) Illustration of a single enzyme near a disc electrode; c) Simulation mesh for the model in (a); d) Simulation mesh the model in (b).

To numerically simulate the enzyme catalysis based on the theoretical model Eqn.(7.6), the enzyme is treated as a point and the process can be described as:

$$D_{\mathrm{P}} \left. \frac{\partial c_{\mathrm{P}}}{\partial r} \right|_{\mathrm{enzyme}} \left(2\pi \Delta r_{\mathrm{enzyme}} \Delta z_{\mathrm{enzyme}} \right) = \frac{k_{\mathrm{cat}}}{N_{\mathrm{A}}} \frac{c_{\mathrm{S}}^{*}}{K_{\mathrm{M}} + c_{\mathrm{S}}^{*}} \tag{7.9}$$

where $\Delta r_{\mathrm{enzyme}}$ and $\Delta z_{\mathrm{enzyme}}$ are the space intervals between the enzyme point and the adjacent grid points in r and z direction, respectively. We note that as the enzyme is assumed to be a point source, the homogeneous product flux $\frac{\partial c_{\mathrm{P}}}{\partial \vec{l}_{\mathrm{enzyme}}}$ can be approximated to be $\left| \frac{\partial c_{\mathrm{P}}}{\partial \vec{l}_{\mathrm{enzyme}}} \right| \approx \left. \frac{\partial c_{\mathrm{P}}}{\partial r} \right|_{\mathrm{enzyme}}$ and only one direction is evaluated as shown in Eqn.(7.9).

Through the finite difference method, the enzyme catalysis can be expressed as:

$$\begin{gathered}
-D_{\mathrm{P}}\frac{c_{\mathrm{P}}\left(\Delta r_{\text{enzyme}}, z\left(d_{\text{enzyme}}\right)\right)-c_{\mathrm{P}}\left(0, z\left(d_{\text{enzyme}}\right)\right)}{\Delta r_{\text{enzyme}}-0}\left(2\pi\Delta r_{\text{enzyme}}\Delta z_{\text{enzyme}}\right)=\frac{k_{\text{cat}}}{N_{\mathrm{A}}}\frac{c_{\mathrm{S}}^{*}}{K_{\mathrm{M}}+c_{\mathrm{S}}^{*}} \\
z\left(d_{\text{enzyme}}\right)=\begin{cases}1+d_{\text{enzyme}} & \text{sphere} \\ d_{\text{enzyme}} & \text{disc}\end{cases}
\end{gathered} \qquad (7.10)$$

With the above definition the simulation is convergent as the choice of Δr_{enzyme} and Δz_{enzyme} does not influence the results.

Current responses as a function of reaction time are simulated for the two electrode models shown in Figure 7.2. To avoid the interference from the simulation conditions such as c_{S}^*, r_{el}, parameters are expressed in a dimensionless way. For instance, the reaction time is expressed as $tD_{\mathrm{P}}/r_{\text{el}}^2$ and the coordinates (r,z) are normalized by r_{el}. In this work, we define three dimensionless properties to characterise the single-enzyme catalysis: The flux at the electrode J, the total amount of product generated by the enzyme N_{P}, and the “collection efficiency” of the electrode σ:

$$J=\frac{I}{FDc_{\mathrm{S}}^{*}r_{\text{el}}} \qquad (7.11)$$

$$N_{\mathrm{P}}=N_{\mathrm{P,sol}}+N_{\mathrm{e}}\quad\left(N_{\mathrm{P,sol}}=\frac{2\pi}{c_{\mathrm{S}}^{*}r_{\text{el}}^{3}}\int_{r}\int_{z}rc_{\mathrm{P}}\mathrm{d}z\mathrm{d}r;\ N_{e}=\frac{1}{c_{\mathrm{S}}^{*}r_{\text{el}}^{3}F}\int_{0}^{t}I\left(\tau\right)\mathrm{d}\tau\right) \qquad (7.12)$$

$$\sigma=\frac{N_{\mathrm{e}}}{N_{\mathrm{P,sol}}+N_{\mathrm{e}}} \qquad (7.13)$$

where $N_{\mathrm{P,sol}}$ is the amount of the product in the solution and N_{e} is the amount of product consumed at the electrode until the time t.

The finite difference problem is solved numerically by means of the LU decomposition method and the alternating direction implicit (ADI) method. The simulation is written in Matlab R2016a and run on an Intel(R) Xeon(R) 3.60G CPU. The validation of the simulation program is examined via the convergence tests.

Table 7.1 List of the initial condition, boundary conditions and the partial differential equations for the enzyme-electrode model.

Condition	Equation
$t = 0$	$c_{\mathrm{P}} = 0$
$r \to \infty$	$c_{\mathrm{P}} = 0$
$z \to +\infty / -\infty$	$c_{\mathrm{P}} = 0$
Spherical electrode: $z^2 + r^2 = r_{\mathrm{el}}^2$ Disc electrode: $r \le r_{\mathrm{el}},\ z = 0$	$c_{\mathrm{P}} = 0$
Spherical electrode: $r = 0, \lvert z/r_{\mathrm{el}} \rvert > 1$ Disc electrode: $r = 0$	$\frac{\partial c_{\mathrm{P}}}{\partial r} = 0$
Disc electrode: $z = 0,\ r/r_{\mathrm{el}} > 1$	$\frac{\partial c_{\mathrm{P}}}{\partial z} = 0$
Spherical electrode: $r = 0,\ z = r_{\mathrm{el}} + d_{\mathrm{enzyme}}$ Disc electrode: $r = 0,\ z = d_{\mathrm{enzyme}}$	$D_{\mathrm{P}} \left. \frac{\partial c_{\mathrm{P}}}{\partial r} \right\vert_{\mathrm{enzyme}} \left(2\pi \Delta r_{\mathrm{enzyme}} \Delta z_{\mathrm{enzyme}} \right) = \frac{k_{\mathrm{cat}}}{N_{\mathrm{A}}} \frac{c_{\mathrm{S}}^*}{K_{\mathrm{M}} + c_{\mathrm{S}}^*}$
r, z in the solution	$\frac{\partial c_{\mathrm{P}}}{\partial t} = D_{\mathrm{P}} \left(\frac{\partial^2 c_{\mathrm{P}}}{\partial r^2} + \frac{1}{r} \frac{\partial c_{\mathrm{P}}}{\partial r} \right)$

7.2.3 Calculation Mesh for the Sphere- and Disc- Electrode Model

As the enzyme-electrode system is symmetric to the z-axis, only the simulation space $r \ge 0$ needs to be taken into consideration. Figure 7.3a shows the spherical electrode in the two-dimensional cylindrical coordinate system.

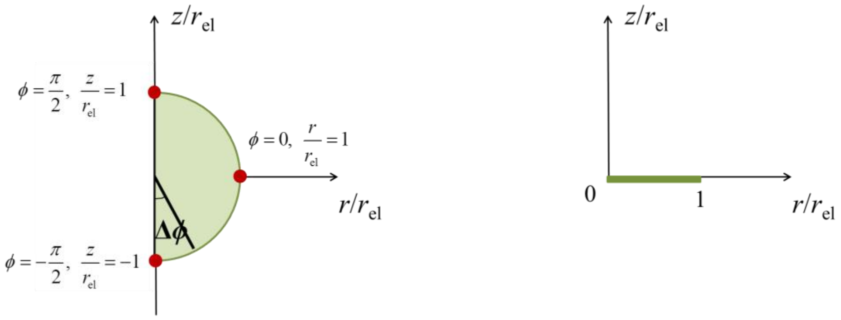

Figure 7.3 Illustration of the micro-sphere (a) and micro-disc (b) in two-dimensional cylindrical coordinates.

In the finite difference method, the half circle representing the sphere electrode in the simulation space is evenly divided into n_ϕ parts. To make the simulation simple, n_ϕ is usually selected to be an even value. The angle ϕ of the half circle is distributed evenly over the range $\left[-\frac{\pi}{2},\frac{\pi}{2}\right]$:

$$\phi_j=-\frac{\pi}{2}+(j-1)\Delta\phi,\ \Delta\phi=\frac{\pi}{n_\phi},\ j=1,2,\ldots,n_\phi,n_\phi+1 \tag{7.14}$$

The mesh for the area $\{z/r_{\mathrm{el}}\in[-1,\ 1],r/r_{\mathrm{el}}\in[0,\ 1]\}$ is then determined by:

$$\frac{r_{\mathrm{i}}}{r_{\mathrm{el}}}=-\sin(\phi_{\mathrm{i}}),\ i=1,2,\ldots,\frac{n_\phi}{2},\frac{n_\phi}{2}+1 \tag{7.15}$$

$$\frac{z_{\mathrm{j}}}{r_{\mathrm{el}}}=\cos(\phi_j),\ j=1,2,\ldots,n_\phi,n_\phi+1 \tag{7.16}$$

In r direction, for the region $r/r_{\mathrm{el}}>1$, the expanding grid is:

$$\frac{r_{\mathrm{i}}}{r_{\mathrm{el}}}-\frac{r_{\mathrm{i-1}}}{r_{\mathrm{el}}}=\Delta r\cdot w^{i-\left(\frac{n_\phi}{2}+1\right)-1},\Delta r=\sin(\Delta\phi),i=\frac{n_\phi}{2}+2,\frac{n_\phi}{2}+3,\ldots \tag{7.17}$$

where w is the expanding factor.

In z direction, a similar expanding grid is built for the region $z/r_{\mathrm{el}}<-1$:

$$\frac{z_{\mathrm{j}}}{r_{\mathrm{el}}}-\frac{z_{\mathrm{j+1}}}{r_{\mathrm{el}}}=-\Delta z\cdot w^{-j},\Delta z=1-\cos\left(\Delta\phi\right),\, j=0,-1,\ldots \tag{7.18}$$

Due to the presence of the enzyme, the grids built in positive z direction are more complex. In the region $z\in\left(r_{\mathrm{el}},r_{\mathrm{el}}+d_{\mathrm{enzyme}}\right]$, as the concentration gradient changes dramatically at the enzyme location, the grid is built as follows:

$$\frac{z_{\mathrm{j}}}{r_{\mathrm{el}}}-\frac{z_{\mathrm{j\text{-}1}}}{r_{\mathrm{el}}}=\begin{cases}\Delta z\cdot w^{j-\left(n_\phi+1\right)-1},r_{\mathrm{el}}<z_{\mathrm{j}}\le r_{\mathrm{el}}+\dfrac{d_{\mathrm{enzyme}}}{2}\\ \Delta z\cdot w^{n_{\mathrm{e}}-\left(j-\left(n_\phi+1\right)\right)},r_{\mathrm{el}}+\dfrac{d_{\mathrm{enzyme}}}{2}<z_{\mathrm{j}}\le r_{\mathrm{el}}+d_{\mathrm{enzyme}}\end{cases} \tag{7.19}$$

where n_{e} is the index of z_{j} corresponding to $z_{\mathrm{j}} = r_{\mathrm{el}} + d_{\mathrm{enzyme}}$.

For the rest of z direction $z > r_{\mathrm{el}} + d_{\mathrm{enzyme}}$, an expanding grid is applied:

$$\frac{z_{\mathrm{j}}}{r_{\mathrm{el}}}-\frac{z_{\mathrm{j\text{-}1}}}{r_{\mathrm{el}}}=\Delta z\cdot w^{j-n_{\mathrm{e}}-1},\, j=n_{\mathrm{e}}+1,n_{\mathrm{e}}+2,\ldots \tag{7.20}$$

An illustration of the disc electrode in (r, z) coordinates is shown in Figure 7.3b. To keep consistency with the spherical model, the calculation grid of the enzyme-disc system in r direction is the same as that of the enzyme-sphere system, determined by Eqn.(7.15) and Eqn.(7.17). In the z direction, when $z < r_{\mathrm{el}}$, the grid is calculated as:

$$\frac{z_{\mathrm{j}}}{r_{\mathrm{el}}}-\frac{z_{\mathrm{j\text{-}1}}}{r_{\mathrm{el}}}=\begin{cases}\Delta z\cdot w^{j-2},0<z_{\mathrm{j}}\le\dfrac{d_{\mathrm{enzyme}}}{2}\\ \Delta z\cdot w^{n_{\mathrm{e}}-(j-1)},\dfrac{d_{\mathrm{enzyme}}}{2}<z_{\mathrm{j}}\le d_{\mathrm{enzyme}}\end{cases},\ z_1=0 \tag{7.21}$$

For the grids in the region $z > d_{\mathrm{enzyme}}$, Eqn.(7.20) is applied.

7.2.4 Convergence Test

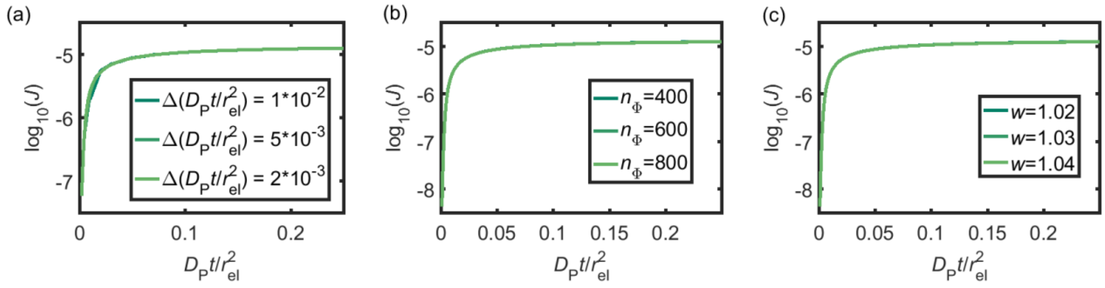

Figure 7.4 Convergence check of (a) the simulation time interval, (b) the number of grid points on the half sphere, (c) the expanding factor for the enzyme-microdisc model. D_P is 10^{-9} m^2 s^{-1} and r_{el} is 1 μm. The curves with different simulation parameters in each panel all overlap.

In Figure 7.4 and Figure 7.5, the reaction flux (*J*) caused by the redox reaction of the enzyme product P at the microdisc (Figure 7.4) and the microsphere (Figure 7.5) electrode are calculated with a series of simulation time intervals $\Delta(D_P t/r_{el}^2)$ and simulation grids. The simulation girds are determined by two parameters: the number of grid points on the half sphere surface [-π/2, π/2] n_Φ and the expanding factor *w*. It is proved that for both the enzyme-microdisc and the enzyme-microsphere models, the simulation results are independent on the value of n_Φ when these simulation parameters are small enough to reach convergent states. *w* is selected to be 1.03 in the following simulations.

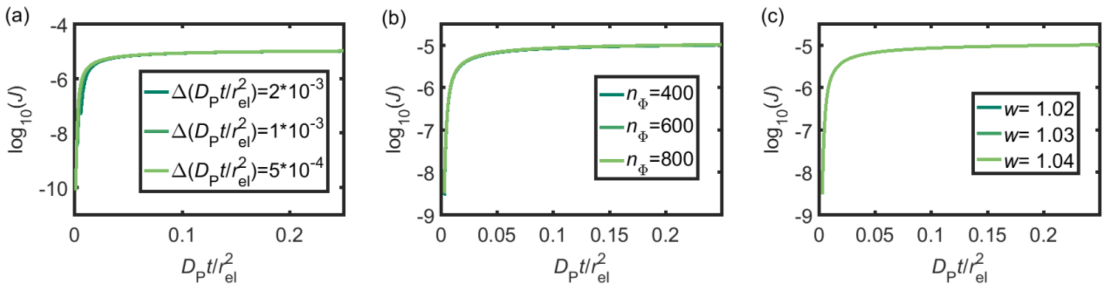

Figure 7.5 Convergent check of (a) the simulation time interval, (b) the number of grid points on the half sphere, (c) the expanding factor for the enzyme-microsphere model. D_P is 10^{-9} m^2 s^{-1} and r_{el} is 1 μm. The curves with different simulation parameters in each panel all overlap.

7.2.5 Catalytic Current of a Stationary Enzyme

We characterise the enzyme-electrode system by the flux J (defined in Eqn.(7.11)), the total amount of product generated by the enzyme N_P (Eqn.(7.12)), and the collection efficiency of the electrode σ (Eqn.(7.13)). To illustrate the catalysis-collection process, three dimensionless quantities affecting the current collected by the electrode are further introduced: The enzyme catalytic ability, K_{cat}, the relative distance between the enzyme and the centre of the electrode d, and the normalized reaction time T. The dimensionless parameter K_{cat} is defined as:

$$K_{\mathrm{cat}} = \frac{k_{\mathrm{cat}} r_{\mathrm{el}}^2}{D_{\mathrm{P}}} \left(\frac{c_{\mathrm{S}}^*}{K_{\mathrm{M}} + c_{\mathrm{S}}^*} \right) \approx \frac{k_{\mathrm{cat}} r_{\mathrm{el}}^2}{D_{\mathrm{P}}} \tag{7.22}$$

In this paper, where it is assumed that the enzyme is always exposed to an excess concentration of the substrate, $c_{\mathrm{S}}^* >> K_{\mathrm{M}}$ and thus $\frac{c_{\mathrm{S}}^*}{K_{\mathrm{M}} + c_{\mathrm{S}}^*} \approx 1$. The relative distance between the enzyme and the centre of the microdisc electrode is normalized with respect to the size of the electrode:

$$d = \frac{d_{\mathrm{enzyme}}}{r_{\mathrm{el}}} \tag{7.23}$$

where d_{enzyme} (m) is the absolute distance from the centre of the electrode to the enzyme location. d reflects the mass transport of the enzyme product from the enzyme to the electrode. T refers to the reaction time, normalized to the radius of the electrode r_{el} and the diffusion coefficient of the product D_P:

$$T = \frac{D_{\mathrm{P}} t}{r_{\mathrm{el}}^{2}} \tag{7.24}$$

The advantage of using these "combined" parameters is that all variables, such as r_{el}, c_S^* and D_P, are grouped according to their influence on the enzyme-electrode system. It is then clearer to describe the characteristics of the whole process.

Figure 7.6 illustrates how the enzyme-electrode system is affected by these factors. Figures 7.6a, 7.6b and 7.6c show the flux J, the amount of product N_P, and the collection efficiency σ varying as a function of T at different enzyme catalytic abilities K_{cat}. It can be seen that J and N_P are determined by K_{cat} while σ is independent on the value of K_{cat}. In Figures 7.6d, 7.6e and 7.6f, the influence of the relative enzyme location d is examined. J and σ are found to be affected by the value of d while N_P remains constant when the enzyme changes its location. When the reaction time is long enough, the enzyme-electrode system is able to reach steady state, where the flux no longer increases with time. The *total* amount of the enzyme product N_P at the steady state is determined only by the catalytic ability $N_P = f(K_{cat})$, the collection efficiency is only related to the enzyme location $\sigma = f(d)$, and the reaction flux is a function of both factors $J = f(K_{cat}, d)$.

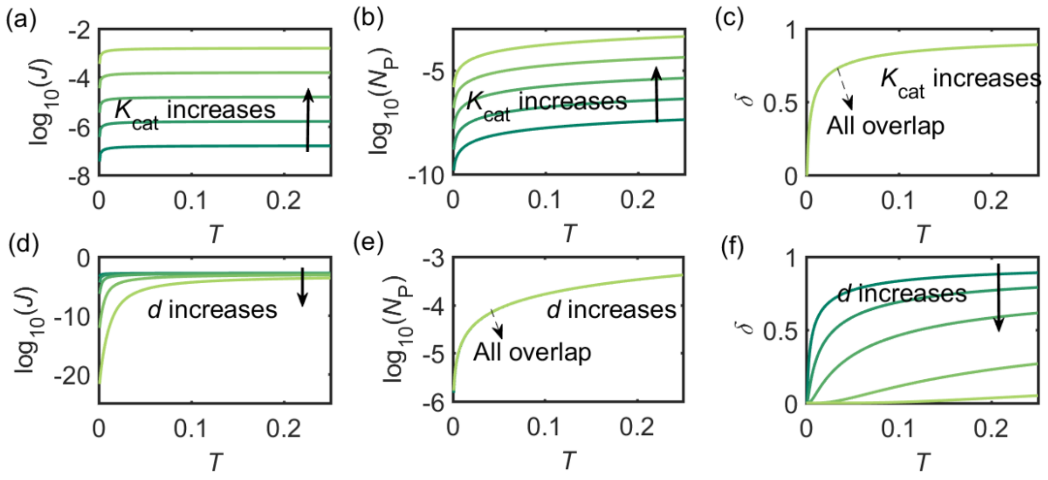

Figure 7.6 Characterisation of the enzyme-microdisc system. (a), (b) and (c) are the current flux J, the total amount of product N_P, and the collecting efficiency σ varying with the reaction time T at different catalytic abilities K_{cat} from 10 to 10^5. d = 0.05. (d), (e) and (f) depict the current flux J, the total amount of product N_P, and the collecting efficiency σ varying with the reaction time T at different enzyme locations d. d varies from 0.05 to 1.0. K_{cat} = 10^5.

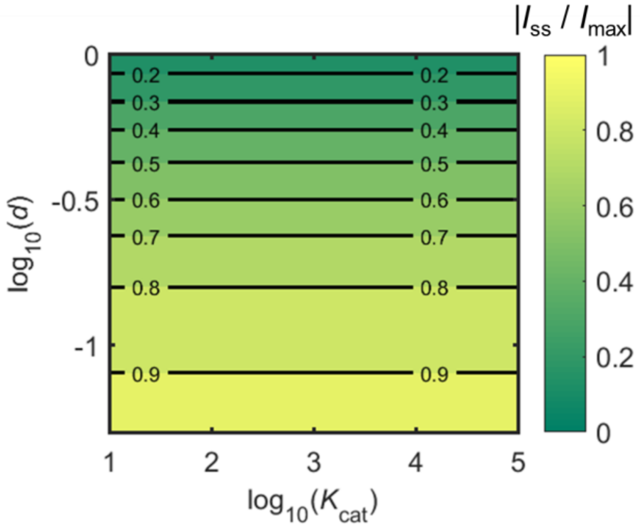

Figure 7.7 Normalized steady-state current (defined as the current at T = 0.25) as a function of d and K_{cat} for the enzyme-microdisc system.

Figure 7.7 shows a working curve of the normalized current at the steady state varying as a function of d and K_{cat}. For clarity, the steady-state current I_{ss}, which is defined as the current value at T = 0.25, is normalized by I_{max}. I_{max} is the maximum current that can be collected by the electrode and is limited by enzyme catalysis, corresponding to the case where the enzyme locates exactly at the electrode surface and each product molecule generated is immediately consumed by the electrode. Thus I_{max} can be predicted by the turnover number of the enzyme:

$$I_{max} = k_{cat} e_0 \tag{7.25}$$

where e_0 is the charge on an electron, 1.602×10^{-19} C. It can be seen from Figure 4 that after the normalization, I_{ss} / I_{max} is independent from the catalytic kinetics but only influenced by the distance from the electrode, indicating that compared to the fast catalysis of the enzyme, the diffusion of the product is the rate-limiting process in the enzyme-electrode system.

7.2.6 Microdisc and Microsphere Electrodes

Figure 7.2 illustrates the two microelectrode geometries that are considered in the simulation of the enzyme-electrode system. To examine the possibility of replacing the enzyme-microsphere model by the enzyme-microdisc model, the same simulations are implemented with the microsphere electrode. As shown in Figures 7.8 and 7.9, similar trends are observed in the microsphere model.

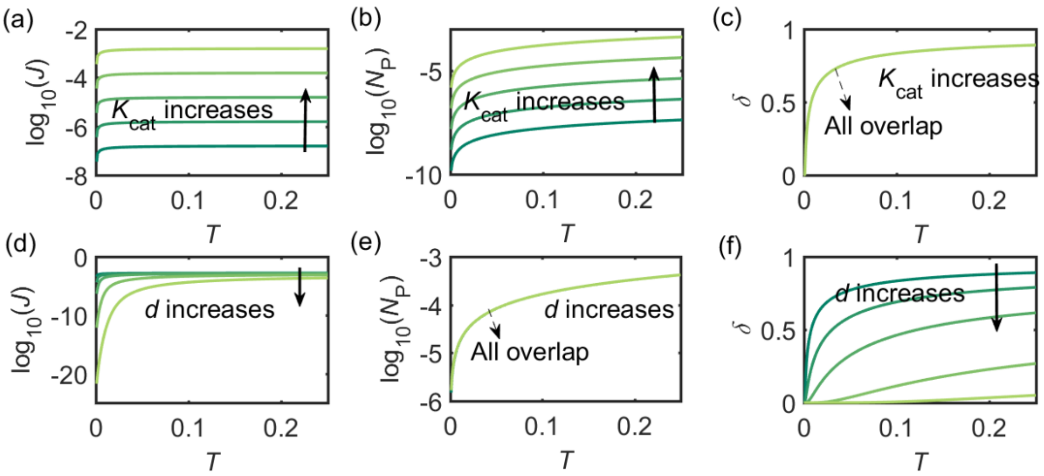

Figure 7.8 Characterisation of the enzyme-microsphere system. (a), (b) and (c) are the current flux *J*, the total amount of product N_P, and the collecting efficiency σ varying with the reaction time *T* under different catalytic ability K_{cat}. K_{cat} varies from 10 to 10^5. *d* = 0.05. (d), (e) and (f) are the current flux *J*, the total amount of product N_P, and the collecting efficiency σ varying with the reaction time *T* under different enzyme location *d*. *d* varies from 0.05 to 1.0. $K_{cat} = 10^5$.

Numerical results reveal that, although absolute values of the currents collected from the two microelectrodes are not identical; their responses are similar. The computationally more efficient enzyme-microdisc system can therefore be treated as an excellent approximation for the enzyme-microsphere electrode and, in the following, all simulation results are based on the enzyme-microdisc model, while similar conclusions can be drawn with regard to the enzyme-microsphere system.

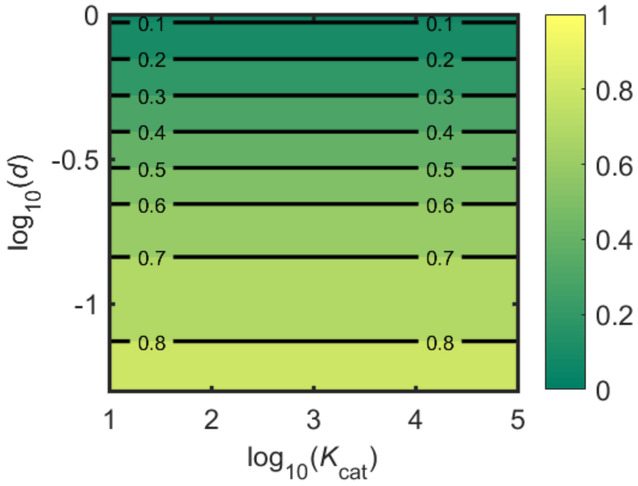

Figure 7.9 Normalized steady-state current (defined as the current at T = 0.25) as a function of d and K_{cat} for the enzyme-microsphere system.

7.3 Electrode Response to a Freely-Diffusing Enzyme

7.3.1 Simulation of the Enzyme Diffusion

In the above finite difference model, which focusses on the diffusion of the product, the enzyme is treated as a stationary point at a fixed distance d_{enzyme} from the electrode. However, due to its Brownian motion, the enzyme does not remain at a fixed position but randomly moves in solution. The enzyme is therefore treated as a random walker when modelling its movement in the electrolyte. When it enters the region close to the electrode, the enzyme can be detected via its catalytic product, which partly diffuses towards to the electrode where it may be oxidised or reduced, and a corresponding current "spike" may be observed in the chronoamperogram.[11, 12] The diffusion of the enzyme is herein dependent on the distance between the enzyme and the electrode surface, which is due to the effect of near-wall hindered diffusion.[23-25]

If we only consider the diffusion of the enzyme perpendicular to the electrode surface, the random walk of the enzyme can be simulated in one direction x, defined as the dimension perpendicular to the electrode surface. In the hindered diffusion theory, the distance-dependent diffusion coefficient of the enzyme can be expressed as:[25]

$$D_{\mathrm{enzyme}}(x)=\frac{6x^2+2xr_{\mathrm{enzyme}}}{6x^2+9xr_{\mathrm{enzyme}}+2r_{\mathrm{enzyme}}{}^2}D_{\mathrm{enzyme},\infty} \tag{7.26}$$

where r_{enzyme} is the radius of the enzyme and $D_{\mathrm{enzyme},\infty}$ is its diffusion coefficient in bulk solution. Here it needs to be noted that when focusing on the movement of a single enzyme, the enzyme is no longer regarded as a point but treated as a nano-sphere with certain volume, where the radius of the enzyme can be approximated from the volume of the enzyme. We further note that the above equation only applies to the diffusion towards a plane and is here used as an approximation.

The diffusion of the enzyme follows Fick's second law:

$$\frac{\partial p(x,t)}{\partial t}=\frac{\partial}{\partial x}\left(D_{\mathrm{enzyme}}(x)\frac{\partial p(x,t)}{\partial x}\right) \tag{7.27}$$

where $p(x, t)$ is the probability distribution of the enzyme position. The probability distribution at the beginning of each random walk step is described by a Dirac delta function:

$$p(x)=\delta(x-x_0) \tag{7.28}$$

where x_0 is the initial location of the enzyme. By solving Eqn.(7.27), the probability distribution after one random walk step $p(x,\Delta t_{\mathrm{rw}})$ (Δt_{rw} is the time interval between two random movements) can be determined. The average displacement Δx_0 is then calculated as:

$$\Delta x_0=\langle x\rangle-x_0=\int_{-\infty}^{+\infty}(x-x_0)p(x,\Delta t_{\mathrm{rw}})dx \tag{7.29}$$

and the average absolute displacement $\Delta x_{\pm}$ is calculated from the standard deviation:

$$\Delta x_{\pm}=\sqrt{\left\langle\left(x-\langle x\rangle\right)^2\right\rangle}=\sqrt{\int_{-\infty}^{+\infty}\left(x-\langle x\rangle\right)^2p(x,\Delta t_{\mathrm{rw}})dx} \tag{7.30}$$

The direction of the movement after each random walk is herein set randomly and the total displacement hence:

$$\Delta x_{\text{total}} = \begin{cases} \Delta x_0 + \Delta x_{\pm}, \text{ at a probability of } 0.5 \\ \Delta x_0 - \Delta x_{\pm}, \text{ at a probability of } 0.5 \end{cases} \tag{7.31}$$

The location of the enzyme after the *k*th random walk step is then determined as:

$$x_0^k = x_0^{k-1} + \Delta x_{\text{total}} \tag{7.32}$$

However, although the random walk step length Δx_{total} can be calculated via solving the mass transport equation Eqn.(7.27), the simulation is very time-consuming, especially when the level of accuracy required is high and the modelled time period is long. Therefore, in order to optimise the simulation procedure, an approximation to the random walk is used.

If the diffusion is homogeneous, that is $D(x) = D_{\text{enzyme, }\infty}$, the probability distribution after each random walk step is a Gaussian function and the step length of each random step is $\sqrt{2D_{\text{enzyme, }\infty}\Delta t_{\text{rw}}}$ .Taking hindered diffusion into account, the Gaussian step length for the one-dimensional random walk however needs to be corrected. It is reported in the literature that the corrected Gaussian step length Δx_{total} for the case of anisotropic diffusion can be expressed as:[26, 27]

$$\begin{aligned} \Delta x_{\text{total, p}}(x) &= L(x) + \frac{1}{2} L(x) L'(x) \\ \Delta x_{\text{total, m}}(x) &= L(x) - \frac{1}{2} L(x) L'(x) \end{aligned} \tag{7.33}$$

with the corresponding probabilities

$$\begin{aligned} P_{\text{p}}(x) &= \frac{1}{2} + \frac{1}{4} L'(x) \\ P_{\text{m}}(x) &= \frac{1}{2} - \frac{1}{4} L'(x) \end{aligned} \tag{7.34}$$

where the subscripts p and m refer to the two directions of the one-dimensional random walk. $L(x) = \sqrt{2D(x)\Delta t_{\text{rw}}}$ is the uncorrected step length and $L'(x) = \mathrm{d}L(x)/\mathrm{d}x$.

7.3.2 Simulation of the Electrode Current to a Diffusing Enzyme

For a time series of enzyme locations $\left\{d_{\text{enzyme}}^{i}\right\}=\left\{d_{\min},\ldots d_{\max}\right\}$, the corresponding catalytic currents $\left\{i_{\text{enyzme}}^{i}\left(d_{\text{enzyme}}^{i},t\right)\right\}$ can be calculated from the enzyme catalysis model introduced in section 7.2, where the discretised i_{enzyme} signify the average current between two sampling points. For each $i_{\text{enyzme}}^{i}\left(d_{\text{enzyme}}^{i},t\right)$, which is the current arising from an enzyme located at a fixed position and being active within the time interval [0, Δt_{rw}], the catalytic reaction is modelled, while significantly longer time period is considered as the electrode corresponding to the products generated within this time period is at least partly observed after $t = \Delta t_{\text{rw}}$. On the basis of these $\left\{i_{\text{enyzme}}^{i}\left(d_{\text{enzyme}}^{i},t\right),d_{\text{enzyme}}\in\left[d_{\min},d_{\max}\right]\right\}$, the current contribution of each random walk step can be approximated via:

$$i_{\text{rw}}^{k}=\left|\frac{d_{\text{enzyme}}^{r}-x_{0}^{k}}{d_{\text{enzyme}}^{r}-d_{\text{enzyme}}^{r+1}}\right|i_{\text{enzyme}}^{r}+\left|\frac{d_{\text{enzyme}}^{r+1}-x_{0}^{k}}{d_{\text{enzyme}}^{r}-d_{\text{enzyme}}^{r+1}}\right|i_{\text{enzyme}}^{r+1} \tag{7.35}$$

where i_{rw}^{k} is the current during the kth random walk step, x_{0}^{k} is the enzyme location determined after the kth random walk step. d_{enzyme}^{r} and d_{enzyme}^{r+1} are the pre-defined enzyme position adjacent to the simulated enzyme location x_{0}^{k}, $d_{\text{enzyme}}^{r}\le x_{0}^{k}<d_{\text{enzyme}}^{r+1}$. i_{enzyme}^{r} and i_{enzyme}^{r+1} correspond to the enzyme positions d_{enzyme}^{r} and d_{enzyme}^{r+1}. The total current at the electrode that includes the contributions from every former enzyme position can be calculated as:

$$I_{\text{electrode}}^{k}=\sum_{s=1}^{k}i_{\text{enzyme}}^{s} \tag{7.36}$$

It is herein noted that the recorded spike shape is also determined by the measurement sampling frequency and the filter built into the potentiostat.[28] The filter is of particular relevance as it may lower the height of the observed peak currents if the electrode signal exceeds the filter bandwidth. To model a more realistic experimental condition, the current calculated from the random walk of the enzyme is therefore filtered via a first-order Butterworth filter.[29] The simulation of the digital filter in the circuit is implemented by the Butterworth filter design in Matlab R2016a.

7.3.3 Catalytic Current of a Diffusing Enzyme

When the enzyme movement is additionally taken into consideration, the generated product does not fully reach the electrode before the enzyme moves on to its next position and both processes, the product diffusion and the enzyme movement, are modelled separately. The enzyme is herein treated as a random walker, while the step length Δt_{rw} of the random walk is determined by convergence tests to ensure that Δt_{rw} is small enough in comparison with the bandwidth of the simulated measurement electronics ($1/f_{\mathrm{cutoff}}$). Please note that below dimensional variables (i.e. r_{el}, D_{P}, d_{enzyme}) are depicted in the modelling of real nano-impact experiments, while the above Figures 7.6 and 7.7 employ dimensionless parameters (i.e. J, K_{cat}, d) to better illustrate the kinetics of the stationary enzyme.

To simulate the chronoamperogram for a diffusing enzyme, the electrode's current responses to stationary enzymes are collected for a series of enzyme locations as discussed in Section 7.3.2 and exemplarily shown Figure 7.10 where the current responses to an enzyme at locations d_{enzyme} ranging from 0.05 to 1.5 μm are modelled. The enzyme herein features a size r_{enzyme} of 5 nm and a bulk diffusion coefficient $D_{\mathrm{enzyme},\infty}$ of 5×10^{-11} m^2 s^{-1}, while the microdisc radius is set to 0.5 μm and the diffusion coefficient of the product D_{P} is set to 10^{-9} m^2 s^{-1}. To generalise the results, the collected current is normalized to the maximum catalytic current I_{max}. For each current response in Figure 7.10, the catalytic reaction only occurs within the time period $0 < t \leq \Delta t_{\mathrm{rw}}$ in which the enzyme is stationary. The current at $t > \Delta t_{\mathrm{rw}}$ is caused by the fraction of the product which is not fully consumed during the time $0 < t \leq \Delta t_{\mathrm{rw}}$. It can be found in Figure 7.10 that the closer the enzyme is located to the electrode, the larger is the catalytic current and the sharper is the drop of the current amplitude after Δt_{rw} is reached. For all further simulations the stationary current response was modelled in a time interval t_{max} of 10^{-4} s via the finite difference simulation, while the response in the range $t_{\mathrm{max}} < t < 2t_{\mathrm{max}}$ is interpolated linearly to $i_{\mathrm{enzyme}}(2t_{\mathrm{max}}) = 0$. t_{max} needs to be long enough to ensure the convergence of the output current signals.

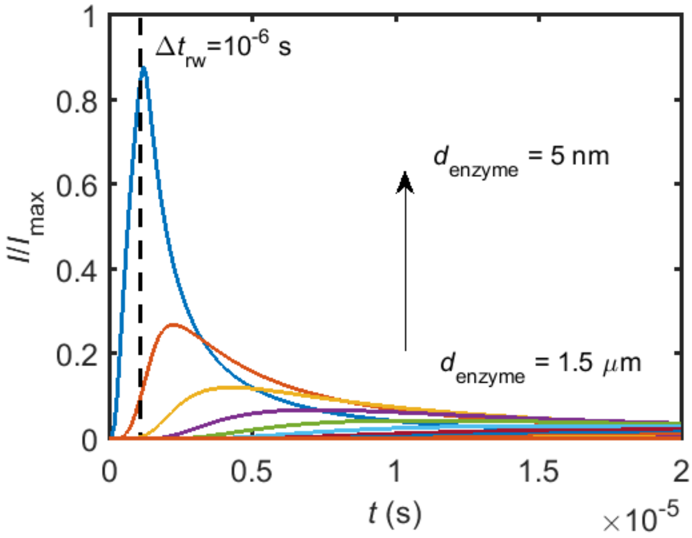

Figure 7.10 Collection of the normalised current-time response to a single enzyme at a series of enzyme positions. The dashed line shows the random walk step length Δt_{rw} = 10^{-6} s. The enzyme positions d_{enzyme} shown in the figure range from 5 nm to 1.5 μm. r_{el} = 0.5 μm, D_P = 10^{-9} m^2 s^{-1}.

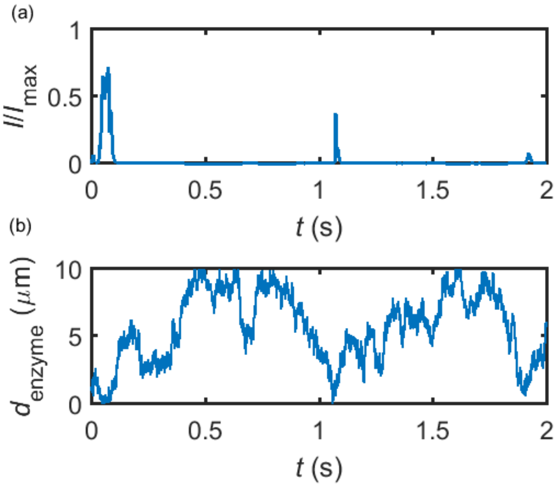

Figure 7.11 Example of a simulated random walk current (a) and the corresponding pathway in the solution (b). The space, in which the enzyme moves freely, ranges from 5 nm to 10 μm. Other simulation parameters are the same as applied in Figure 7.10.

Based on the normalized current-time responses shown in Figure 7.10, the chronoamperogram of the diffusing enzyme is simulated in Figure 7.11 and the corresponding pathway of its movement is presented. Two current "spikes" can be observed, while each spike indicates an approach of the enzyme towards the electrode and the spike shape infers the details of each approach. When the enzyme immediately leaves the electrode after an approach, a sharp spike is measured in the chronoamperogram such as that at around 1.1 s in Figure 7.11. On the other hand, if the enzyme moves forward and backward several times near the electrode, a long spike with noisy current fluctuations will be recorded, such as the one at 0-0.1 s.

Figure 7.11 proves that the solution-phase enzyme catalysis can in principle be observed experimentally. It is also shown that each approach of the enzyme can be distinguished as the current is very sensitive to changes in the distance between the enzyme and the electrode, which enables a further analysis of the spike data and the extraction of information on both the enzyme catalysis and the enzyme diffusion. This two dimensional result differs significantly from the one-dimension case discussed in the previous work:[11] In the two-dimensional case, convergent diffusion leads to a collection efficiency that depends sharply on the distance between the enzyme and the electrode. When the enzyme diffuses towards or away from the microelectrode, sharp current *on- and offsets* can be observed in the chronoamperometry that are due to the dependency of the collection efficiency on the enzyme location as shown in Figures 7.6 and 7.7. This sensitivity of the microelectrode in principle enables the detection of single enzyme activity via its product in the nano-impact technique, which is obscured in the case of a macroelectrode. The semi-infinite diffusion field at the macroelectrode resulting from linear diffusion and coupled to the marked mismatch of the diffusion coefficients of the enzyme and its product means that the 'collection' of the product is much less sensitive to the motion of the enzyme.

7.3.4 Current Signals with Various Electrodes and Electronics

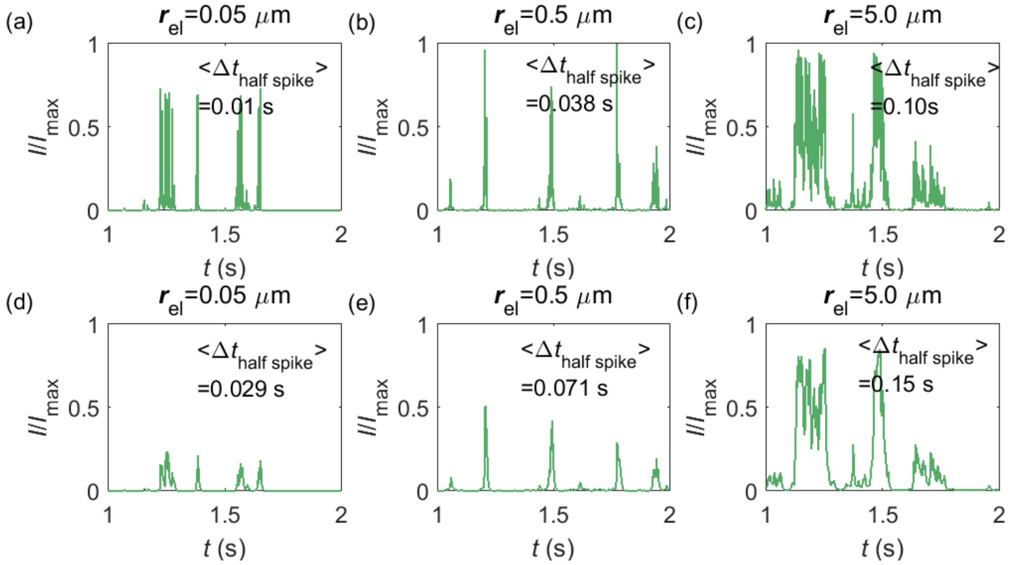

Figure 7.12 Chronoamperograms of single enzyme detection at microdisc electrodes featuring radii of 0.05, 0.5 and 5.0 μm. Figures (a)-(c) are the modelled potentiostat signals after passing a 4 kHz filter, while (d)-(f) depict the same data filtered via a 50 Hz filter. The average spike duration time for each system is listed on the plot. In the simulation, r_{enzyme} = 5 nm, D_{enzyme} = $5*10^{-11}$ m^2 s^{-1}, D_P = $1*10^{-9}$ m^2 s^{-1}, Δt_{rw} = 10^{-6} s. The simulation space of d_{enzyme} is from 5 nm to 5 μm and the total simulation time is 5 seconds.

Having shown that spikes can only be observed at micro-sized electrodes, the influence of the electrode size needs to be taken into consideration. Figure 7.12 shows the current responses to a freely-diffusing enzyme at microdisc electrodes of various radii. Figures 7.12 a-c are the chronoamperograms (normalized to the maximum possible current, I_{max}) at electrodes featuring radii of 0.05, 0.5 and 5.0 μm and the cut-off frequency of the measurement filter is set to 4 kHz; d-f are the same simulations as shown in a-c but with a different cut-off frequency of 50 Hz. The spike durations in each chronoamperogram are analysed and indicated in the corresponding figure. The spikes are recognized via a threshold value that is set to distinguish a spike from the background. In the analysis in Figure 7.12, the threshold value for spike duration is selected to be 0.5% of the maximum spike current. In addition, considering the noise level in the real experiment, spikes featuring a small current height are unrecognizable and are here removed if the peak current is less than 10% of the maximum spike current. To avoid any influence from the background noise, the spike duration is characterised by the width at half of the spike height $\Delta t_{\text{half-spike}}$.

From Figures 7.12 a-c, it is found that the spike features a height close to the maximum possible current $I_{\max}$ at the electrodes with 0.05, 0.5 and 5.0 μm radii. The current signal at the 0.05 μm is slightly smaller than the other two due to the finite closest approach of the enzyme applied in the simulation. The closest approach $d_{\min}$ is defined as the radius of the enzyme (5 nm) for all the three electrode systems but the magnitude of the current spike is determined by the relative closest approach $d_{\min}/r_{\text{el}}$ as explained in Figures 7.6 and 7.7. Therefore, the spikes recorded at the 0.05 μm electrode ($d_{\min}/r_{\text{el}}$ = 0.1) are slightly lower than that at the 5.0 μm one ($d_{\min}/r_{\text{el}}$ = 0.001). More discussion on the selection of the simulation space can be found in the Supporting Information. It is also found in a-c that the spike length varies significantly with the electrode size. The average half-spike widths of 0.05, 0.5 and 5.0 μm electrodes are 0.01, 0.038 and 0.10 s under the 4 kHz cut-off frequency. Sharper spikes are observed at the 0.05 μm electrode than the 5.0 μm electrode, reflected by a 5 fold decreases in the spike duration. This is because the current is more sensitive to the variation of the enzyme location at the smaller electrode. The spikes last for longer at larger electrodes, showing the transition from the two-dimensional to the one-dimensional system as discussed above.

In Figures 7.12 d-f, with a 50 Hz cut-off frequency, a similar dependency of the current signal on the electrode size is still observed as shown in a-c. The spikes recorded at larger electrodes have longer duration time. However, the spike height in d-f is smaller than $I_{\max}$, especially at the smallest 0.05 μm electrode. This is because that a low cut-off frequency is employed and the current response recorded from the electrode is largely distorted. Comparison of the chronoamperograms in a-c and d-f reveals that the spike currents in a-c are larger than those in d-f and the spikes are sharper, as a low-pass filter with higher cut-off frequency retains more information of the original current recorded.

7.3.5 Convergence Test

The simulation of this enzyme-electrode-electronics system is tested under different simulation parameters: the random walk step length Δt_{rw}, during which the enzyme is regarded stationary and the catalytic reaction occurs at a certain location; the maximum simulation time for one enzyme location t_{max}; and the simulation space d_{enzyme} = [d_{min}, d_{max}]. In addition, to simulate the experimental situation, a low-pass filter with a cutoff frequency f_{cutoff} is applied, which influences the convergence of a simulation. The high cutoff frequency applied in this work is set as 4 kHz and the low cutoff frequency is 50 Hz. To obtain similar accuracy when simulating the same enzyme-electrode system, more delicate parameters are needed with the high cutoff frequency, where more details can be recorded as shown in Figure 7.12. Therefore, the convergence tests are all under the condition of a 4 kHz cutoff frequency.

Here the average half-spike width is selected to characterize the random current signals collected in the chronoamperogram. An example is shown in Figures 7.13 and 7.14 depicting the convergence test for the 0.5 μm electrode. Figure 7.13 compares the simulation results at different t_{max} and Δt_{rw}. It shows that when the random walk step length is short and the maximum simulation time for one position is long, similar stochastic spikes are obtained. Figure 7.14 studies the influence of the simulation space. The expansion of the simulation space does not make much difference on the spike duration for the 0.5 μm electrode.

To simulate the experimental data, the results are required to be independent of t_{max} and Δt_{rw}, which we have examined. However, the influence of the simulation space remains an input parameter, as the closest approach d_{min} is limited under real experimental conditions. For instance, as the enzyme undergoes a solution-phase catalytic reaction, the closest approach should be larger than the size of the enzyme but the exact distance cannot be determined. The value of the upper boundary d_{max} determines the frequency of observed spikes. Considering the simulation time it may cost, the upper boundary cannot be selected as far as possible. When comparing the current signal simulated for various electrode sizes in Figure 7.12, the range of enzyme diffusion space is always defined identically from 5 nm to 5 μm. It can be found in Figure 7.14 that this range of space is large enough to describe the movement of the enzyme around a 0.5 μm electrode. But as the collecting efficiency is determined by the relative distance $d_{\mathrm{enzyme}}/r_{\mathrm{el}}$ rather than d_{enzyme}, the closest approach 5 nm may be too large for smaller electrodes to be convergent and the upper boundary 5 μm may be too small for larger electrodes. When theoretically investigating the difference between the electrodes of various sizes, it is however necessary to keep the simulation space consistent for all the enzyme-electrode systems. When simulating real experimental conditions, the simulation space tough needs to be carefully selected to make the results converge, where a greater value was modelled.

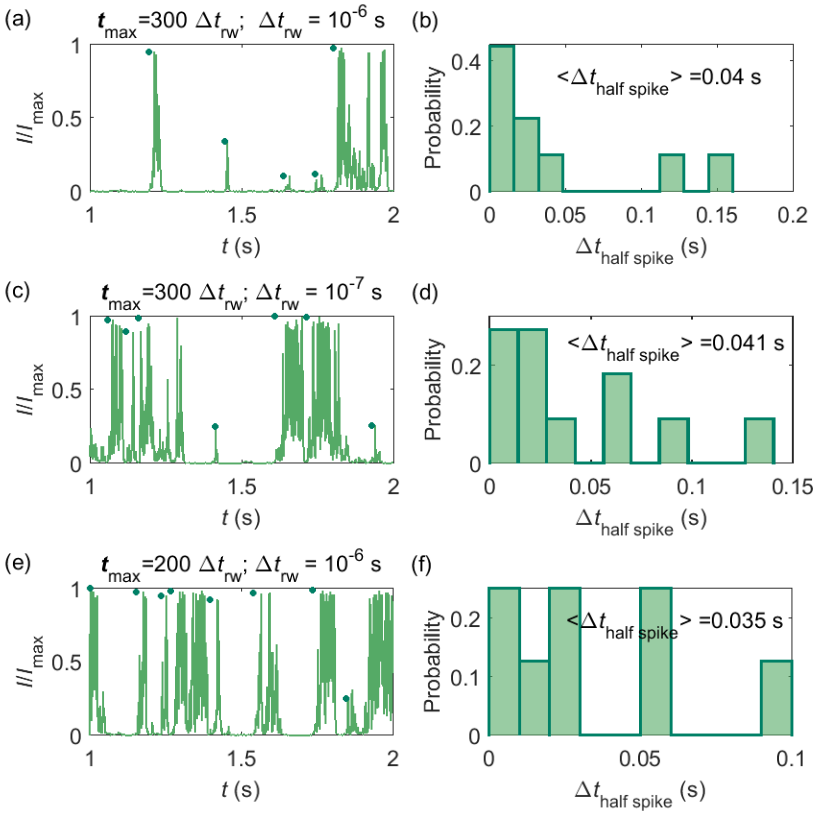

Figure 7.13 Convergence test of t_{max} and Δt_{rw} for the 0.5 μm electrode. The range of the enzyme diffusion space is from 5 nm to 5 μm. Other simulation parameters are the same as applied in Figure 7.12.

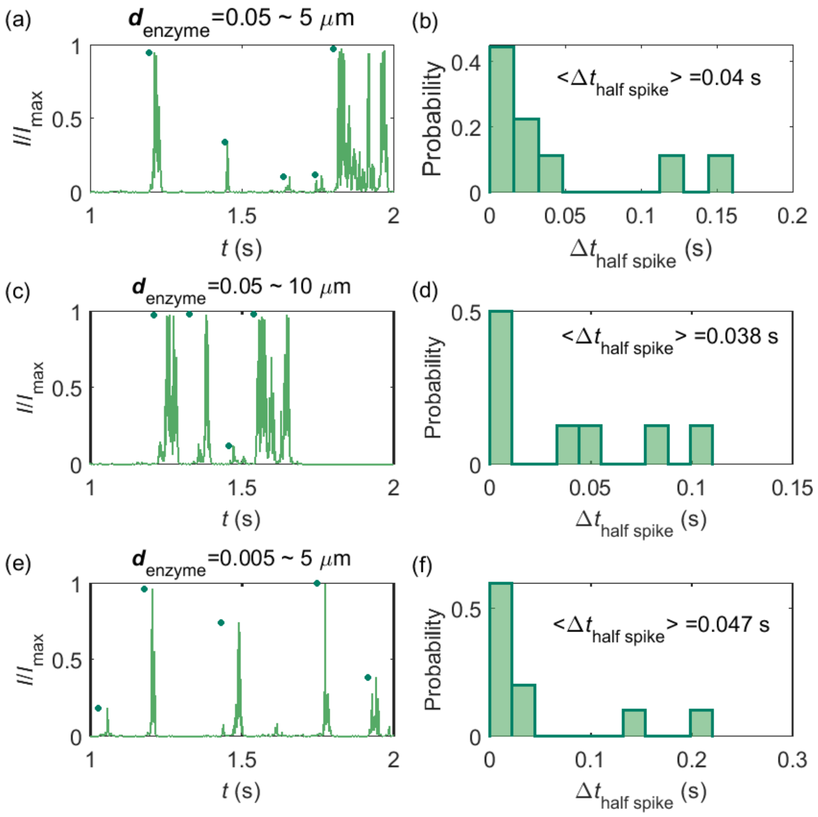

Figure 7.14 Convergence test of the simulation space for the 0.5 μm electrode. Other simulation parameters are the same as applied in Figure 7.12.

7.4 Example: Electrochemical Detection of Single Catalases

Single catalases in the solution phase are detected via the nano-impact technique. The experimental data is analysed and examined by the theoretical model. The single catalase experiment was performed Dr. Lior Sepunaru.

7.4.1 On the Possible Electrochemical Detection of Single Catalase Enzymes

Based on the model developed in this work, the electrochemical detection of single catalase enzymes is simulated. To this end, the experimental parameters of the catalase-microdisc system are modelled: $D_{\mathrm{P(O2)}} = 10^{-9}$ m^2 s^{-1},[30] $r_{\mathrm{el}} = 5$ μm,[11] $D_{\mathrm{enzyme(catalase)}} = 5\times10^{-11}$ m^2 s^{-1},[31] $k_{\mathrm{cat(catalase)}} = 10^6$ s^{-1},[32] $r_{\mathrm{enzyme(catalase)}} = 5$ nm,[33] $f_{\mathrm{cutoff}} = 4$ kHz.[11] In reported work of this group,[11] single catalase impact experiments were conducted in a 9 pM catalase solution with chronoamperograms recorded at a 5 μm radius microdisc electrode. The reason for choosing catalase is mainly due to its high turnover number[32] which is at the upper limit of known enzymatic catalytic rates. In addition, the oxygen product is easy to detect electrically.

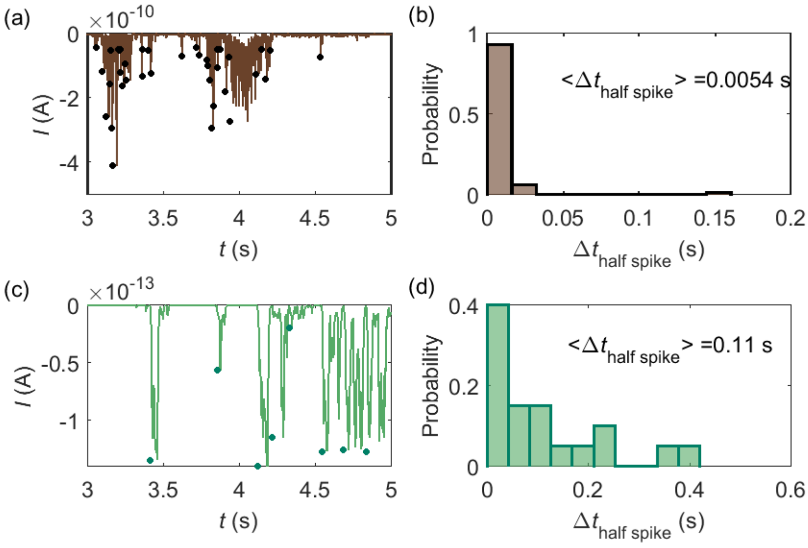

Figure 7.15 (a) is an experimentally found chronoamperogram of 9 pM catalase in a 100 mM hydrogen peroxide solution at an applied potential of -1.0 V versus SCE, measured at a 5 μm radius microdisc electrode; (b) is the corresponding histogram of the half-spike width of the current spikes in (a); (c) and (d) are the simulated chronoamperograms (see text) referring to single catalase detection at a microdisc electrode and the corresponding histogram of the half-spike width. The total recording time is 50 s for both experiment and simulation. The simulation space is from 5 nm to 10 μm.

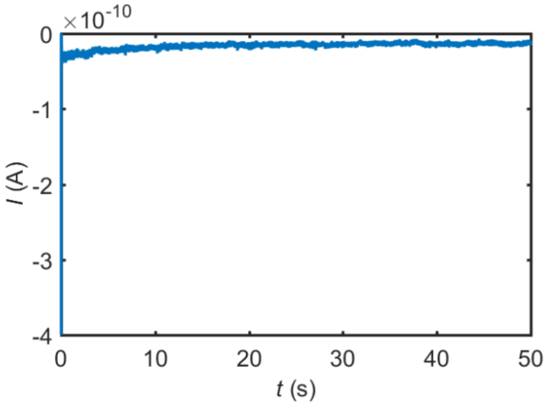

Figure 7.16 Control experiment relating to Figure 7.15a.

Some typical current spikes collected from the experiment are shown in Figure 7.15a and the analysis of the spikes is presented in Figure 7.15b. The control experiment of Figure 7.16 in the absence of catalase does not show any spikes in the chronoamperometric measurements, indicating that the spikes relate to the catalase catalysis. From the experimental results, the magnitude of the spike height is approximately 10^{-10} A and the average half-spike width is 0.0054 s. For direct comparison, a simulation of the same catalase-microdisc system is shown in Figure 7.15c and 7.16d. The simulated spikes feature a height of ca. 10^{-13} A and an average half-spike width of 0.11 s.

To compare the experimental and the simulated current responses, we consider both the duration and shape of the spike. First, the simulated half-spike width $\Delta t_{\text{half-spike}}$ is significantly longer than that of the experiment. According to the simulation in Figure 7.12, only broad spikes are anticipated to be observed at the relatively large 5 μm electrode, which contradicts experiment. Secondly, as the magnitude of the spike height is mainly determined by the turnover number and the reported turnover number (10^6 s^{-1}) measured from an ensemble of catalases leads to spike heights of the order of 10^{-13} A, the simulated spikes are much too small to be distinguished from the background noise in any real experiment using broad bandwidth. That said, in contrast to the kinetics averaged over an ensemble as reflected in the classical Michaelis-Menten kinetics, single enzyme activity is thought to be dynamically fluctuating and the turnover number for individual enzymes can deviate from the average value.[18, 34] *Hypothetically*, if the turnover number of a single catalase is temporarily near 10^9 s^{-1} at the moment of detection, a current spike of 10^{-10} A can be observed, which is experimentally feasible to measure. However, the activity of single catalase is yet to be reported by optical or other experimental means and the fact that the enzyme contains four catalytic heme centres probably slightly averages any dynamic disorder of the enzyme catalytic rate. Comparison of the experimentally measured current (Fig 7.15a) and the theoretical calculated current spikes (Fig 7.15c) reveals a three orders of magnitude difference in the current magnitude. This discrepancy might be explained by experimental artefacts such the formation of electrochemically active oxygen bubbles.[11] Alternatively, the experimental spikes may reflect enzymatic activity operating ‘transiently’ at catalytic rates that are three orders of magnitude higher than the ensemble averaged rate and consequently with substantially lower observed “impact” frequency. However, this process can be further complicated by contribution from surface adsorbed enzymes and is out of the scope of this theoretical investigation. In either case, full information on the enzyme turn-over rate cannot be gained.

7.4.2 Implications for the Design of Experiments

The possibility of experimentally detecting the activity of an individual enzyme in solution is mainly determined by the maximum current and the duration time of the signal. If under experimental conditions a 10 pA current spike is the minimum current that can still be observed at a microelectrode, according to Eqn.(7.25), the turnover number needs to be of the order of magnitude of 10^8 s^{-1} in the case of one electron being transferred per consumed substrate molecules, which means the detection of the activity for an individual enzyme is feasible for enzymes exhibiting a fast turnover number or an agglomerate or aggregate of enzymes.[12] In addition, the spike duration determines whether a signal can be distinguished from the background noise. Only sharp spike onsets can be identified, while slow spike on- and off-sets will be indistinguishable from (the typically slow) changes in the background current. Although the electrical signal attributed to the enzyme activity can be observed at both micro- and macro-electrodes, the spikes can be only identified at nano- and micro- electrodes, as the sensitivity of the current to the variation of the enzyme distance is related to the size of the detection electrode. At macroelectrodes, the spike is too broad to be identified and hence it is difficult to observe spikes from the background.

In addition, the characterisation of the spikes is also influenced by the bandwidth of the measurement electronics. Figures 7.12 a-c and d-f are calculated for different filter models (for instance, different potentiostats), which feature different transfer characteristics and different bandwidths. If the same series of impact events was recorded simultaneously with both potentiostats, different current responses would hence be observed and the average spike duration and the number of spikes detected may alter between the measurements. The filter response to signals in the high frequency regime is herein particularly interesting as series of signal fluctuations in this regime may be resolved through some potentiostats and then be identified as individual spikes, while a different potentiostat may show the same series of fluctuations as a single longer spike. The application of a low-pass filter operated at a cut-off frequency of 4 kHz therefore leads to a shorter average spike length and a larger number of spikes being detected if compared to a measurement using a low-pass filter set at 50 Hz.

7.5 Summary

It is computationally shown that in principle the nano-impact method enables the electrochemical characterisation of freely-diffusing enzymes if a small electrode is used, the potentiostats bandwidth is sufficient, and the enzyme features a large average turnover number. These findings apply to an enzyme operating at a constant turnover number, while fluctuations in the enzyme activity will further enhance its detectability. The model presented provides understanding of the enzyme-electrode system and useful predictions for experimentalists: We demonstrate that current responses corresponding to single catalase activity can in principle be observed at electrodes with radii varying from a few nanometres to a few micrometres. However, the simulated current spikes are too small to be distinguished from the background noise in any real experiment using a broad bandwidth. Enzymes with faster turnover numbers than catalase lead to larger current signals that can be experimentally observed and electrodes with smaller sizes better detect the signals. Again, the influence of the measurement electronics cannot be ignored. The electronics with a short bandwidth keeps more information than that of a broad bandwidth and is more favourable in the detection of the single enzyme activity.

The model is applied to simulate current signals that could possibly be attributed to single catalase at a 5.0 μm electrode measured at a cut-off frequency of 4 kHz. The simulation and the experiment show however significant discrepancy in the magnitude and the duration time of the current signal, revealing that without further consideration of the enzyme catalysis kinetics and the influence of the experiment environment, the experimental phenomena cannot be explained as the detection of product generated by the activity of a single catalase enzyme in solution.

References

1. C. Lin, E. Katelhon, L. Sepunaru and R. G. Compton, *Chemical Science*, 2017, DOI: 10.1039/C7SC02084H.

2. X. Xiao, F.-R. F. Fan, J. Zhou and A. J. Bard, *Journal of the American Chemical Society*, 2008, **130**, 16669-16677.

3. W. Cheng and R. G. Compton, *TrAC, Trends in Analytical Chemistry*, 2014, **58**, 79-89.

4. S. V. Sokolov, S. Eloul, E. Kätelhön, C. Batchelor-McAuley and R. G. Compton, *Physical Chemistry Chemical Physics*, 2017, **19**, 28-43.

5. X. Xiao, S. Pan, J. S. Jang, F. R. F. Fan and A. J. Bard, *Journal of Physical Chemistry C*, 2009, **113**, 14978-14982.

6. J. Kim, B.-K. Kim, S. K. Cho and A. J. Bard, *Journal of the American Chemical Society*, 2014, **136**, 8173-8176.

7. J. M. Kahk, N. V. Rees, J. Pillay, R. Tshikhudo, S. Vilakazi and R. G. Compton, *Nano Today*, 2012, **7**, 174-179.

8. J. E. Dick, C. Renault and A. J. Bard, *Journal of the American Chemical Society*, 2015, **137**, 8376-8379.

9. A. N. Sekretaryova, M. Y. Vagin, A. P. F. Turner and M. Eriksson, *Journal of the American Chemical Society*, 2016, **138**, 2504-2507.

10. L. Han, W. Wang, J. Nsabimana, J.-W. Yan, B. Ren and D. Zhan, *Faraday Discussions*, 2016, **193**, 133-139.

11. E. Kätelhön, L. Sepunaru, A. A. Karyakin and R. G. Compton, *ACS Catalysis*, 2016, **6**, 8313-8320.

12. C. Chan, L. Sepunaru, S. V. Sokolov, E. Kätelhön, N. P. Young and R. G. Compton, *Chemical Science*, 2017, **8**, 2303-2308.

13. X. S. Xie, *Accounts of Chemical Research*, 1996, **29**, 598-606.

14. S. Weiss, *Science*, 1999, **283**, 1676-1683.

15. J. A. Cracknell, K. A. Vincent and F. A. Armstrong, *Chemical Reviews*, 2008, **108**, 2439-2461.

16. L. Michaelis and M. M. L. Menten, *FEBS Letters*, 2013, **587**, 2712-2720.

17. R. M. Daniel, R. V. Dunn, J. L. Finney and J. C. Smith, *Annual Review of Biophysics and Biomolecular Structure*, 2003, **32**, 69-92.

18. B. P. English, W. Min, A. M. van Oijen, K. T. Lee, G. Luo, H. Sun, B. J. Cherayil, S. C. Kou and X. S. Xie, *Nat Chem Biol*, 2006, **2**, 87-94.

19. S. C. Kou, B. J. Cherayil, W. Min, B. P. English and X. S. Xie, *The Journal of Physical Chemistry B*, 2005, **109**, 19068-19081.

20. E. J. F. Dickinson, J. G. Limon-Petersen, N. V. Rees and R. G. Compton, *The Journal of Physical Chemistry C*, 2009, **113**, 11157-11171.

21. K. Ngamchuea, S. Eloul, K. Tschulik and R. G. Compton, *Analytical Chemistry*, 2015, **87**, 7226-7234.

22. R. G. Compton and C. E. Banks, *Understanding Voltammetry*, Imperial College Press, 2nd edn., 2011.

23. E. Kätelhön and R. G. Compton, *Chemical Science*, 2014, **5**, 4592-4598.

24. S. Eloul, E. Kätelhön and R. G. Compton, *Physical Chemistry Chemical Physics*, 2016, **18**, 26539-26549.

25. M. A. Bevan and D. C. Prieve, *Journal of Chemical Physics*, 2000, **113**, 1228-1236.

26. L. Farnell and W. G. Gibson, *Journal of Computational Physics*, 2004, **198**, 65-79.

27. L. Farnell and W. G. Gibson, *Journal of Computational Physics*, 2005, **208**, 253-265.

28. E. Kätelhön, E. E. L. Tanner, C. Batchelor-McAuley and R. G. Compton, *Electrochimica Acta*, 2016, **199**, 297-304.

29. S. Butterworth, *Experimental Wireless & Wireless Engineer*, 1930, **7**, 536-541.

30. R. T. Ferrell and D. M. Himmelblau, *Journal of Chemical & Engineering Data*, 1967, **12**, 111-115.

31. S. Sengupta, K. K. Dey, H. S. Muddana, T. Tabouillot, M. E. Ibele, P. J. Butler and A. Sen, *Journal of the American Chemical Society*, 2013, **135**, 1406-1414.

32. J. Switala and P. C. Loewen, *Archives of Biochemistry and Biophysics*, 2002, **401**, 145-154.

33. E. Sim and R. B. Sim, *European Journal of Biochemistry*, 1979, **97**, 119-126.

34. R. B. Liebherr, M. Renner and H. H. Gorris, *Journal of the American Chemical Society*, 2014, **136**, 5949-5955.

Chapter 8 Conclusions and Future Works

In this thesis, the kinetics of electrochemical reactions at the metal-water interface has been studied via both simulation and experiment. New theories and analytical methods were developed for a variety of electrode systems.

The hydrogen oxidation reaction (HOR) on platinum (Pt) microelectrodes was studied to explore the role of chemical adsorption and solvent reorganization in the electrochemical reaction with a surface-bonded intermediate. For a fully reversible reaction, the steady-state current was limited by the diffusion of the reactant towards the electrode. It was found that slow pre-adsorption process led to a decrease of the steady-state current value at microdisc electrodes, even in the case of reversible electron transfer. In the Butler-Volmer electron transfer model, the electron transfer rate always increases with overpotential. But if the reorganization energy is significantly large, the electron transfer rate at high overpotential is limited by the slow solvent or ligand reorganization, which can also cause the steady-state current smaller than expected. The theoretical model was applied to explain experimental data for the HOR on Pt microdisc electrodes and the adsorption rate constant of this system deduced from the steady-state current.

Surface-bonded intermediates and adsorption coupled electron transfers were further investigated. It is known that in a sufficiently supported electrolyte solution, the electrical double layer is compressed to a thin layer, where the potential in the solution phase quickly drops to zero and does not affect the electron transfer, that is, the plane of electron transfer is outside the region of double layer. However, in the case of electron transfer coupled with surface adsorption, due to the strong chemical interaction, the electron transfer occurs over a very short distance from the electrode and the influence of the electrical double layer *must* be taken into consideration. A model was developed to calculate the Gibbs energy surface of the reaction and determine the reaction path. It was found that the presence of the electrical double layer reduced the apparent transfer coefficient of the electron transfer process, especially for the case of neutral species reacting to form a charged species $X(sol) \rightarrow X^{+/-}(ads)$, which was also indicated by experiments on the oxygen reduction reaction at carbon electrodes of different sizes.

In addition to electron transfer across the interface, solution-phase processes, such as diffusion and homogeneous chemical (or catalytical) reaction, may also affect the overall kinetics of an electrochemical reaction. The hydrogen oxidation reaction, homogeneous EC' reaction, and heterogeneous EC' reaction were studied at nano- or micro- electrodes. Both single nano/micro-electrodes and nano/micro-electrode arrays were considered. The adsorption rate constant of HOR on platinum nanoparticles was investigated showing that the measurement was more reliable via the nano-impact approach than a drop-casting method, as the nanoparticle distribution and coverage is not predictable on a drop-casted electrode. For EC' reactions at single nano-/micro-electrodes, the steady-state current was used to characterise the catalytic kinetics and the diffusion of the reactant. Theoretical equations and kinetic diagrams were derived to describe the competition of the two rate-determining factors. The voltammetric responses of EC' reactions at nanoelectrode ensembles were found to be related to the nanoelectrode coverage, size and geometry. Clear merits the nano-impact technique used in our experiments were established.

The nano-impact technique allows not only the measurement of mediated electrochemical reaction, but also the detection of single enzymes. The thesis has shown computationally the possibility of electrochemically detecting a freely-diffusion single enzyme in the solution phase via the nano-impact method. The overall enzyme-electrode system was modelled via a combination of the random walk model and the finite difference method. The kinetics of the overall system were investigated and the conditions needed to generate a measurable current signal in the experiment were predicted: a high turnover number, sufficient substrates, a small detection electrode and a narrow electronics bandwidth. The simulation results were used to examine the measurement of single catalase enzymes. In this case the observed discrepancy between the experiment and simulation in terms of both the magnitude and the duration of the current signal allowed the inference that the experimental phenomena could *not* be explained by single enzyme catalysis.

Kinetics studies allow us to understand electrode systems and make useful predictions in real applications. Future work will likely continue exploring the varied kinetics of the electrode-electrolyte interface via the nano-impact technique. On the one hand, basic theories of electron transfer across the interface can be studied. The structure of the inner Helmholtz layer and its influence on an overall electrochemical reaction are of particular interest. On the other hand, there can be focus on applications of the nano-impact technique. Thus electroanalytical methods could be implemented to investigate single enzyme dynamics in combination with the theoretical models and simulations.